Atomic relaxation upon multiphoton absorption of soft X-rays

Dissertation
zur Erlangung des Doktorgrades
an der Fakultät für Mathematik, Informatik und Naturwissenschaften
Fachbereich Physik
der Universität Hamburg

vorgelegt von

Aljoscha Rörig

Hamburg

2024

Preface

Parts of the results of this dissertation have been published in Nature Communications volume 14, Article number: 5738 (2023)
(`https://doi.org/10.1038/s41467-023-41505-1`).

All calculations in Chapter 5 were performed by Sang-Kil Son from the Center for Free-Electron Laser Science (CFEL) in Hamburg using the XATOM toolkit.

The calculations in Chapter 6 using JAC were performed by Stephan Fritzsche from the Helmholtz Institute Jena, and calculations using FAC were done by the author.

Throughout this thesis, the term "Auger-Meitner" will be used in place of the commonly used term "Auger", representing a synthesis of Richard Sietmann's proposal to acknowledge Lise Meitner [1], given that she was the first to observe the effect in 1922 [2], and Olivier Duparc's conclusion that Pierre Auger had published his findings already in 1923 [3] (not in 1925) and centred his doctoral thesis [4] on this subject, providing an atomic description [5]. Since Auger's doctoral research primarily addressed the Auger-Meitner effect, his name appears first, while Meitner is mentioned second, as it was not the principal focus of her work. This ordering carries pragmatic implications, as the well-established "Auger" effect is effectively augmented by the inclusion of "Meitner", which may be omitted according to personal preference without distracting from the subject matter. The explanation mentioned above diverges slightly from the proposal put forward by Matsakis et al. [6] as Duparc's conclusion [5] are inadequately addressed in their argument.

This thesis used ChatGPT 4 omni mini, provided by the University of Hamburg, to assist the academic writing process through rephrasing.

Abstract

This thesis explores the atomic relaxation processes following multiphoton absorption of soft X-ray free-electron laser pulses within the M shell of xenon at photon energies ranging from 700 to 1700 eV, employing ion time-of-flight spectroscopy and within argon's $2p$ subshell to form a double-core-hole state, using electron time-of-flight spectroscopy.

The investigation sheds light on the multiphoton multiple ionisation processes of isolated xenon atoms interacting with ultraintense soft X-ray free-electron laser pulses, elucidating the dependence on photon energy across three fluence (photons per unit area) regimes. A map of resonant features as a function of photon energy and charge state is rendered, facilitating the identification of transition energy lines linked to specific resonant excitations through comparison with theoretical calculations. Analysing the calculated ionisation pathways reveals the significance of multiple-core-hole states, shifting the energies where a specific photon energy becomes resonant. The findings further indicate that ion yields in resonance spectra remain constant beyond a specific saturation point, making it possible to study resonances in a pure form and setting the stage for future investigations into pulse duration effects.

Furthermore, the thesis presents evidence of a resonant $2p$ double-core-hole state in singly charged argon induced by two-photon absorption, with calculations confirming the transition of a $2p$ electron to a $3d$ orbital. The observed relaxation processes align with theoretical predictions, and further analysis demonstrates that the second step of the double-core-hole decay cascade emits electrons within the same energy range as the first step, enhancing consistency between theory and experiment. A single-core-hole feature in doubly charged argon is also identified through theoretical calculations.

Zusammenfassung

Diese Arbeit untersucht die atomaren Relaxationsprozesse nach Multiphotonenabsorption von Freie-Elektronen-Laserpulsen im weichen Röntgenbereich in der M-Schale von Xenon bei Photonenenergien von 700 bis 1700 eV mithilfe der Ionenflugzeitspektroskopie und in der $2p$-Unterschale von Argon für die Entstehung von zwei Innerschalenlöcher mithilfe der Elektronenflugzeitspektroskopie.

Die Untersuchung betrachtet die Multiphotonen-Mehrfachionisationsprozesse von isolierten Xenonatomen, die mit ultraintensiven Freie-Elektronen-Röntgenlaserpulsen wechselwirken, und beleuchtet die Abhängigkeit von der Photonenenergie für drei verschiedene Photonenfluenzen. Die Resonanzen werden auf einer zweidimensionalen Karte als Funktion der Photonenenergie und des Ladungszustands dargestellt, welche die Identifizierung der Übergangsenergielinien für spezifische resonante Anregungen durch Vergleich mit theoretischen Berechnungen ermöglicht. Die Analyse der berechneten Ionisierungspfade zeigt die Bedeutung von Zuständen mit mehrfachen Innerschalenlöchern, welche die resonanten Bedingungen verschieben, bei denen eine bestimmte Photonenenergie resonant wird. Die Ergebnisse deuten ferner darauf hin, dass die Ionenausbeute in Resonanzspektren ab einer spezifischen Photonenfluenz konstant bleibt, was die unverzerrte Untersuchung von Resonanzen ermöglicht und gleichzeitig die Voraussetzungen für künftige Untersuchungen der Auswirkungen der Pulsdauer schafft.

Darüber hinaus wird in dieser Arbeit ein resonanter $2p$-Doppel-Innerschalenloch-Zustand in einfach geladenem Argon nachgewiesen, der durch Zwei-Photonen-Absorption induziert wird. Die theoretischen Berechnungen bestätigen den Übergang eines $2p$-Elektrons in ein $3d$-Orbital und die beobachteten Relaxationsprozesse stimmen mit theoretischen Vorhersagen überein. Darüber hinaus zeigt die Analyse, dass der zweite Schritt der Zerfallskaskade des Doppel-Innerschalenlochs Elektronen im gleichen Energiebereich wie der erste Schritt emittiert und die Übereinstimmung zwischen Theorie und Experiment verbessert. Ein Innerschalenloch in doppelt geladenem Argon konnte ebenfalls mithilfe von theoretischen Berechnungen identifiziert werden.

Contents

List of Figures

List of Tables

Acronyms

ADC   analogue-to-digital converter

ADU   analogue-to-digital unit

AQS   atomic-like quantum systems

a.u.   atomic units

BPMs   beam position monitors

CFD   constant fraction discriminator

CSD   charge-state distribution

DAQ   data acquisition system

DCH   double-core-hole

FAC   flexible atomic code

FEL   free-electron laser

FWHM   full width at half maximum

GATT   gas attenuator

HBT   Hanbury Brown and Twiss

HE   high-energy

HFS   Hartree-Fock-Slater

IR   infrared

JAC   Jena atomic calculator

KB   Kirkpatrick-Baez

KEE   Kinetic electron emission

LCLS   Linac Coherent Light Source

LE   low-energy

LOPT   leading-order perturbation theory

LSS   Lindhard, Scharff, and Schiott

MBES	magnetic bottle electron spectrometer
MCDHF	multiconfigurational Dirac-Hartree-Fock
MCH	multiple-core-hole
MCP	microchannel plate
NIR	near-infrared
NQS	nano-sized quantum systems
PCS	photoionisation (photoabsorption) cross section
PED	pulse-energy distribution
PEE	Potential electron emission
PHD	pulse-height distribution
PLL	phase-locked loop
QED	quantum electrodynamic
REMI	reaction microscope
REXMI	resonance-enabled or resonance-enhanced X-ray multiple ionisation
RF	radio-frequency
SASE	self-amplified spontaneous emission
SCADA	supervisory control and data acquisition
SCH	single-core-hole
SNR	signal-to-noise ratio
SQS	small quantum systems
SRA	synchrotron radiation aperture
TOF	time-of-flight
UV	ultraviolet
VLS	variable line spacing
VMI	velocity map imaging
XFEL	X-ray free-electron laser
XGM	X-ray gas monitor
XREMPI	X-ray resonance-enabled multiphoton ionisation

Chapter 1

Introduction

Nearly a century ago, Lise Meitner [2] and Pierre Auger [3] independently discovered the Auger-Meitner effect in the early 1920s – a phenomenon that Auger termed the "composed photoelectric effect" [7]. This effect constitutes a fundamental relaxation mechanism through electron ejection in light–matter interaction. While Meitner focused on the characteristic emission spectrum of β-rays resulting from the decay of radioactive lead isotopes, Auger investigated the photoexcitation of atoms, including argon and xenon, induced by the absorption of X-ray photons emitted by an X-ray tube.

The present thesis aligns with Auger's initial objective [8] of capturing X-ray-induced relaxation processes in atoms. However, it focuses on the sequential absorption of multiple X-ray photons rather than a single photon per atom. This approach is facilitated by a bright fourth-generation light source, specifically the European X-ray free-electron laser (XFEL) [9], which is approximately 10^{26} times brighter than the first X-ray tubes [10]. XFELs have brought forward unprecedented experimental conditions, which facilitate investigations of ultrafast timescales that were previously not accessible, such as ultrafast X-ray scattering [11] or X-ray absorption spectroscopy [12]. Unlike Auger, who utilised a cloud chamber [13] to track charged particles, this study employs high-precision ion and electron time-of-flight (TOF) spectroscopy, which can keep pace with the rapid particle generation of the XFEL, allowing for the detection of more than thousand particles per second.

An understanding of the multiphoton absorption process and its associated relaxation mechanisms is essential for elucidating radiation damage in biological samples during interactions with intense, femtosecond X-ray pulses [14, 15]. Particularly heavy atoms within protein molecules exhibit greater susceptibility to X-ray-induced damage [16, 17] due to their higher atomic photoionisation cross sections compared to lighter elements, such as carbon, nitrogen, and oxygen [18]. In the context of material structure and dynamics, the electronic response of individual atoms is critical in determining whether a significant diffraction signal can be captured in a single-shot coherent imaging experiment before radiation damage occurs. Furthermore, this knowledge could aid in interpreting unidentified astrophysical X-ray emission lines from unusual atomic species formed via collisions in outer space [19, 20] and contributes to the refinement of theoretical models by advancing the understanding of light–matter interaction into new regimes of electronic correlations within atoms [21].

Today, the Auger-Meitner effect or decay remains central to the atomic response following soft X-ray photoabsorption induced by XFELs [22–25], highlighting the

fundamental nature and significance of this effect. In addition to the "normal" case described in Auger's doctoral thesis [4], Brown et al. expanded this concept to encompass a "resonant" case [26], which is a recurring theme throughout this thesis. While the normal Auger-Meitner effect typically refers to the emission of a secondary electron following photoionisation, the resonant case is preceded by photoexcitation. Depending on the electronic shell of the atom, X-ray absorption can initiate a series of Auger-Meitner decays – termed cascades – that eject an electron at each decay step, ultimately resulting in the multiple ionisation of the atom. The high photon densities in XFEL pulses enable the atom to absorb additional photons between decay steps, thereby increasing the complexity of the possible atomic states. This results in ionisation occurring from the inside out rather than commencing with the atom's valence (outer) shell.

The thesis is structured into two parts, each featuring its own introduction and conclusion. The first part systematically investigates the influence of photon energy on the ionisation process of xenon atoms following multiphoton absorption in the M shell, induced by soft XFEL pulses across three fluence regimes, employing ion TOF spectroscopy. In contrast, the second part focuses on forming a double-core-hole (DCH) state in the L shell of argon using electron TOF spectroscopy. This latter section represents a step down in complexity from multiphoton absorption in the M shell, aiming to elucidate the underlying mechanisms of the involved processes. The main result of part one is rendered in a map of resonant features as a function of photon energy and charge state, facilitating the identification of transition energy lines linked to specific resonant excitations through comparison with theoretical calculations. Analysing the calculated ionisation pathways reveals the significance of multiple-core-hole (MCH) states, shifting the energies where a specific photon energy becomes resonant. The findings further indicate that ion yields in resonance spectra remain constant beyond a specific saturation point, making it possible to study resonances in a pure form and setting the stage for future investigations into pulse duration effects.
The second part provides experimental evidence of a resonant $2p$ DCH state in singly charged argon arising from two-photon absorption, with transition processes supported by Jena atomic calculator (JAC) calculations. Additionally, analysis via flexible atomic code (FAC) revealed that the second step of the DCH decay cascade emits electrons in the same energy range as the first, enhancing the alignment between theoretical predictions and experimental results while also identifying a single-core-hole (SCH) feature in doubly charged argon through JAC calculations.
In addition to the two main parts, the thesis provides a detailed description of the data analysis steps, illustrating the increasing complexity of evaluating the detected highly charged ions, which accompany the experimental challenges of operating an XFEL.

Chapter 2

Soft X-ray–atom interaction

This chapter briefly overviews the fundamental principles governing an atom's response to soft X-ray absorption, which are essential for understanding the interaction of atoms with ultraintense soft XFEL pulses.

2.1 Photoabsorption

Photons in the soft X-ray regime, typically defined as extending from just below the K edge of carbon ($\sim$250 eV) to the K edge of argon ($\sim$3 keV) [27], predominantly interact with atoms via photoabsorption rather than elastic or inelastic photon scattering [28–30]. This interaction effectively reduces to the absorption of photons by the atom's bound electrons, which are localised within orbitals characterised by specific binding energies E_{bind}. When a bound electron absorbs a photon of energy $\hbar\omega$, it may either be excited or ionised, contingent on the photon energy. Here, $\hbar$ denotes the reduced Planck constant, and ω represents the angular frequency of the photon. If $\hbar\omega > E_{\mathrm{bind}}$, the process results in ionisation, referred to as direct photoionisation [Fig. 2.1 **a**]. Conversely, if $\hbar\omega$ equals the energy difference between the current state and a higher-lying unoccupied orbital, the electron undergoes excitation, termed resonant photoexcitation [Fig. 2.1 **b**].
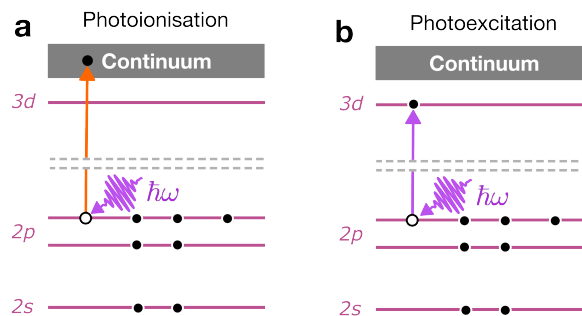
Figure 2.1: Schematic representation of the processes of **a** photoionisation and **b** photoexcitation, illustrated using the energy levels of argon. A black dot represents an electron, while a white dot denotes a vacancy. The horizontal dashed grey lines indicate a discontinuity, omitting the $3s$ and $3p$ energy levels for improved clarity. Upon reaching the continuum, electrons transition to an unbound state.

In the soft X-ray regime, inner-shell electrons, defined as those not located in the outmost (valence) shell, predominantly absorb photons owing to their higher cross sections [31]. When an electron absorbs a photon, the orbital angular momentum quantum number of the electron, denoted as l, must change, as the photon possesses an intrinsic angular momentum, termed spin, of one that must be conserved during the transition after absorption. Consequently, l must change by $\Delta l = \pm 1$ if $l \neq 0$ and by $\Delta l = +1$ if $l = 0$, following the selection rules for electric dipole transitions [32]. The orbital angular momentum quantum number l describes the subshell of an atomic shell defined by the principal quantum number n and is constrained by the condition $l \leq n - 1$ [33]. The shells corresponding to $n =$ 1–5 are designated as the K, L, M, N, and O shell, while the orbitals with $l =$ 0–3 are referred to as s, p, d, and f orbitals [27].

Alongside n and l, the magnetic quantum number m_l and the spin magnetic quantum number m_s uniquely define the state of an electron. m_l specifies the orbitals within a subshell and is related to the component of the orbital angular momentum onto the conventionally chosen z-axis, specifying the orbital's spatial orientation. m_l can have integer values ranging from $-l$ to $+l$, including zero, yielding a total of $2l + 1$ orbitals within a subshell. m_s similarly indicates the projection of the two possible orientations of the intrinsic electron angular momentum (spin s) onto the z-axis. For $s = \frac{1}{2}$, the values of m_s are $\pm\frac{1}{2}$, commonly referred to as "spin-up" and "spin-down". Each orbital can maximally hold two electrons, one with spin-up and one with spin-down, following the Pauli exclusion principle [27].

If the photon that ionises an inner-shell electron possesses significantly more energy than that required for photoionisation, monopole excitations or ejections may occur as second-order effects, as depicted in Fig. 2.2. Panel **a** illustrates a valence electron that is additionally excited during photoionisation, termed shake-up, while panel **b** illustrates a valence electron that is additionally ejected from the atom, referred to as shake-off. These monopole excitations or ionisations, characterised by the absence of angular momentum transfer between the initial and final states, can be interpreted as a consequence of the sudden change in the effective nuclear charge resulting from the reduced electronic screening following the removal of an inner-shell electron by photoionisation. As a result, only the electron's principal quantum number n changes after the monopole excitation [29, 34].
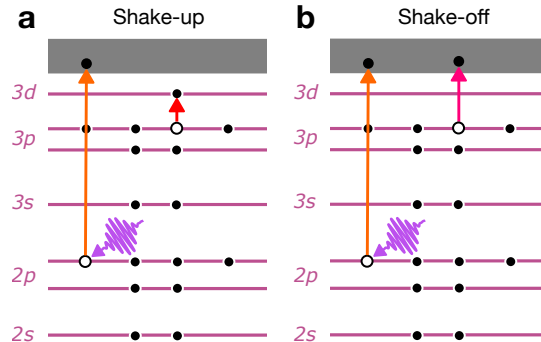
Figure 2.2: Schematic representation of the shake-up **a** and the shake-off process **b** during photoionisation.

2.2 Atomic relaxation

In the soft X-ray regime, energy deposited through photoabsorption predominantly relaxes via Auger-Meitner decay [2, 3] rather than radiative decay, termed fluorescence, due to the inaccessibility of the electronic K shell for atoms with atomic numbers greater than that of argon, beyond which fluorescence becomes significant [35]. Auger-Meitner decay is a second-order effect following photoabsorption, referring to the emission of an electron after filling an inner-shell vacancy by a higher-lying, less tightly bound electron. The energy difference between the orbital energy of the filling electron and the inner-shell vacancy is transferred to another electron within the same or an even higher-lying subshell, resulting in the ejection of that electron with a definite excess energy. Ultimately, Auger-Meitner decay represents an electron correlation effect, wherein energy is converted through electron-electron interactions within the electronic cloud [36, 37].
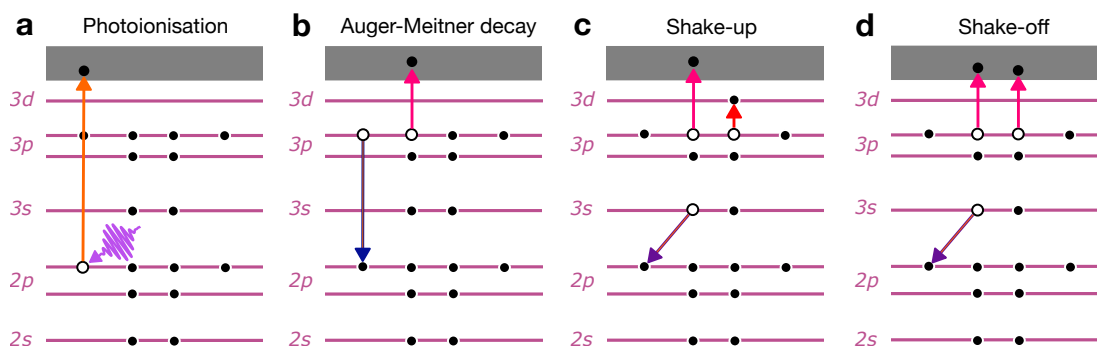
Figure 2.3: Schematic representation of the normal Auger-Meitner decay following the initial ionisation of an inner-shell electron by a single photon, along with potential accompanying shake-up or shake-off processes.

Fig. 2.3 illustrates in panel **a** the initial photoionisation and panel **b** the normal Auger-Meitner decay. If the inner-shell vacancy is filled by an electron from a higher-lying subshell within the same shell, the process is termed Coster-Kronig decay. If, in addition, the ejected electron originates from the same shell, the phenomenon is referred to as super Coster-Kronig decay [38]. This phenomenon represents a specific instance of Auger-Meitner decay and is encompassed within discussions of Auger-Meitner decay in this thesis. The Auger-Meitner decay may also involve shake-up (panel **c**) or shake-off processes (panel **d**). These shake processes manifest in the electron spectrum as lower-energy satellite peaks neighbouring the main peak [29, 34].

When the inner-shell vacancy is produced via photoexcitation, as illustrated in panel **a** of Fig. 2.4, the process is termed "resonant" Auger-Meitner decay. Shake processes cannot occur because no excess energy is available. A distinctive aspect of this scenario is that the excited electron may act as either a spectator (panel **b**), remaining uninvolved in the decay process, or as a participant (panel **c**), taking part in the decay process itself [39].
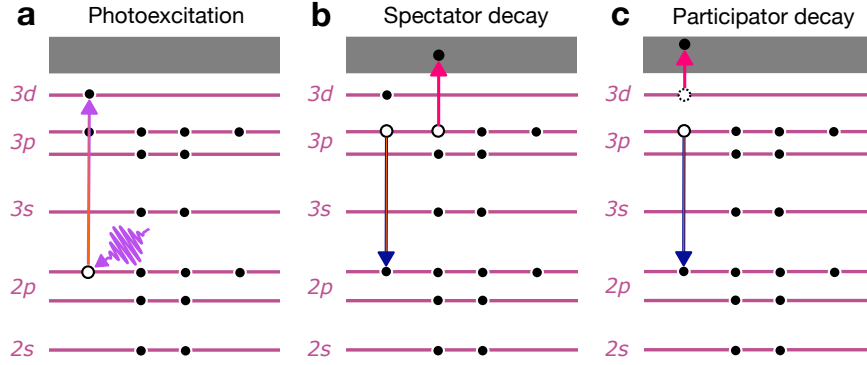
Figure 2.4: Schematic representation of the resonant Auger-Meitner decay. Panel **a** illustrates the initial photoexcitation. The resonant Auger-Meitner decay can be subdivided into **b** spectator decay and **c** participator decay.

The high photon energies of soft X-rays enable the excitation or ionisation of deep inner-shell electrons using a single photon [31, 40], resulting in a cascade of Auger-Meitner decays [41].
For instance, Ch. 5 is devoted to the photon-energy-dependent ionisation process of xenon within the energy range of 700 to 1700 eV, where photoabsorption predominantly occurs within the $3d$ subshell [31]. This leads to the formation of a $3d$ core hole, which subsequently evolves into an excited ion that decays through a series of Auger-Meitner decays.

$$\hbar\omega + \mathrm{Xe}^0 \xrightarrow{\mathrm{PI}} \mathrm{Xe}^+(3d^{-1}) + e^-$$
$$\mathrm{Xe}^+(3d^{-1}) \xrightarrow{\mathrm{AM}} \mathrm{Xe}^{2+}(4d^{-2}) + e^-$$
$$\mathrm{Xe}^{2+}(4d^{-2}) \xrightarrow{\mathrm{AM}} \mathrm{Xe}^{3+}(4d^{-1}5p^{-2}) + e^-$$
$$\mathrm{Xe}^{3+}(4d^{-1}5p^{-2}) \xrightarrow{\mathrm{AM}} \mathrm{Xe}^{4+}(5p^{-4}) + e^-$$
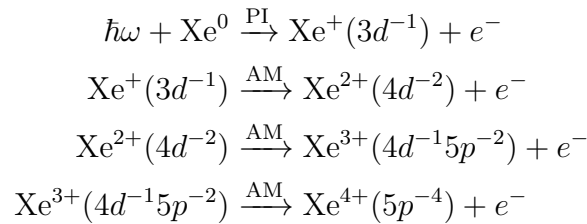
PI represents photoionisation, AM for Auger-Meitner decay, and e^- denotes an ejected electron. This decay cascade constitutes only the most probable route to Xe^{4+} and is an example taken from Ref. [41].

2.3 Photoionisation cross section

The total photoionisation (photoabsorption) cross section (PCS), σ_{tot}, represents the effective area characterising the probability a photon with energy $\hbar\omega$ ionises an atom. For inner-shell photoionisation, this cross section approximately scales with Z^5, away from any absorption edges, where Z denotes the atomic number [42]. Fig. 2.5 illustrates the calculated total PCS for the elements neon ($Z = 10$), argon ($Z = 18$), krypton ($Z = 36$), and xenon ($Z = 54$) for the photon-energy range 200–1500 eV. The discontinuities correspond to the absorption edges of specific subshells of an atom, after which σ_{tot} approximately decreases with $(\hbar\omega)^{-7/2}$ [42].
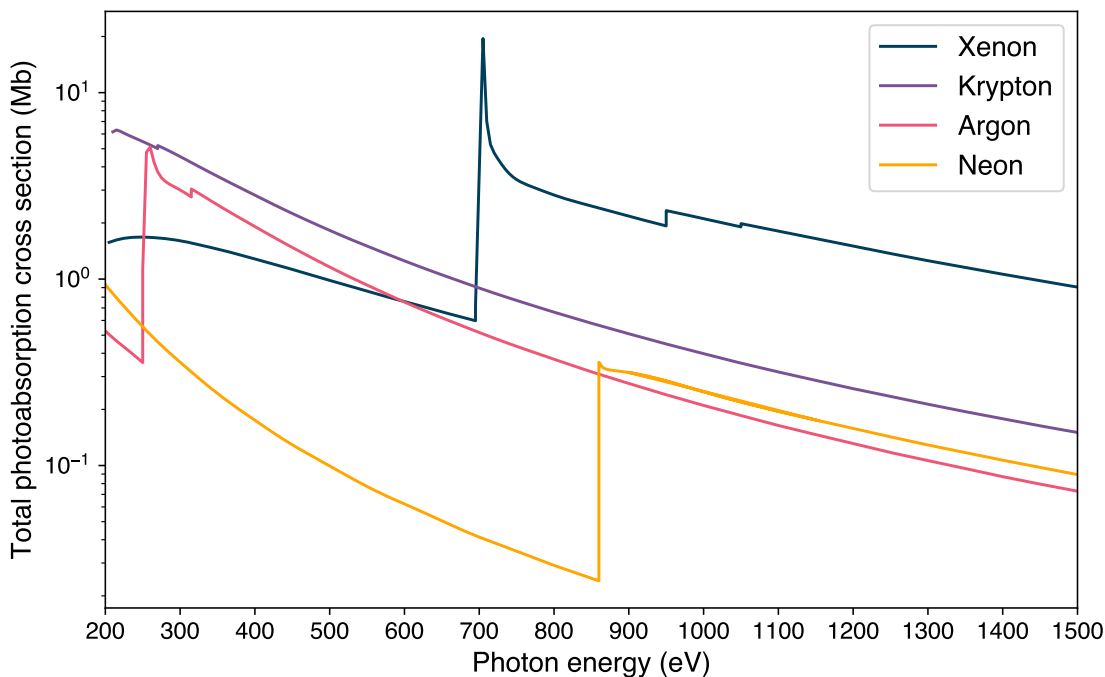
Figure 2.5: Calculated total photoabsorption cross sections as a function of photon energy for neon, argon, krypton and xenon. The data is taken from Ref. [31].

2.4 Strong-field effects

In the infrared infrared (IR) to the near ultraviolet (UV) regime [43], ionisation via a single photon is unattainable. Nevertheless, ionisation can still occur in these regimes through tunnelling, known as tunnel ionisation, or by the simultaneous absorption of multiple photons, termed direct multiphoton ionisation [44]. Both processes necessitate high intensities I of laser-like light. For tunnel ionisation of a valence electron, the ponderomotive energy U_{p} – the cycle-averaged kinetic energy of a free electron in an electromagnetic field – must exceed the binding energy, indicating the onset of the strong-field regime. In atomic units (a.u.), the ponderomotive energy is given by:

$$U_{\text{p}} = \frac{I}{4\omega^2}$$

For direct multiphoton ionisation, the intensity I must remain high, as the cross section for the simultaneous absorption of multiple photons diminishes rapidly with the required number of photons [44]. However, the ponderomotive energy U_p should be significantly smaller than the binding energy E_bind to avoid perturbing the atomic potential [45–47].

An explicit calculation of U_p for soft X-rays follows, demonstrating that no strong-field effects are anticipated in the present studies. With a photon energy of $\hbar\omega = 1300$ eV, a pulse duration of $\tau_\mathrm{pulse} = 25$ fs and a pulse energy of $E_\mathrm{pulse} = 1879$ µJ, the intensity is $I = 1.11 \times 10^{18}$ W/cm^2. With I and $\hbar\omega$ the ponderomotive energy is:

$$U_\mathrm{p} = \frac{2e^2\hbar^2}{4c\epsilon_0 m_\mathrm{e}} \frac{I}{(\hbar\omega)^2} = \frac{1.11 \times 10^{18} \ \mathrm{W/cm}^2}{(1300 \ \mathrm{eV})^2} = 0.09 \ \mathrm{eV} \ll 1300 \ \mathrm{eV}.$$

According to Ref. [44], even a pulse duration of $\tau_\mathrm{pulse} = 10$ fs is "sufficiently long", with $\nu \times \tau_\mathrm{pulse} = 3143$ cycles of the electromagnetic field and $\nu = \frac{1300 \ \mathrm{eV}}{h}$, for the definition of a cross section to hold.

2.5 Sequential multiphoton absorprtion

Both studies on xenon and argon in this thesis investigate ultraintense ($\sim 10^{18}$ W/cm^2) and ultrashort ($\sim$fs) XFEL pulses, which provide 10^{12}-10^{13} photons per pulse. This results in the sequential absorption of multiple photons by the atoms within the pulse duration. Unlike direct multiphoton absorption, sequential absorption involves the interaction of photons with different electrons rather than multiple photons being absorbed by a single electron. Furthermore, sequential absorption does not require simultaneous photon absorption. In the soft X-ray regime, although direct (non-sequential) multiphoton ionisation is theoretically possible, it is negligible compared to sequential photoionisation, which possesses a significantly larger PCS and requires only a single photon to ionise an inner-shell electron [23–25, 48–50].

2.6 Angular distribution of photoelectrons

In general, ejected electrons following photoionisation are not emitted isotropically; instead, they depend on the angle θ between their emission direction and the polarisation of the interacting photons [29]. For the investigation of DCH formation in the $2p$ subshell of argon, an electron TOF spectrometer [Sec. 3.5] was employed at a fixed angle, allowing detection solely of electrons emitted at this specific spectrometer angle. In contrast, a magnetic bottle electron spectrometer (MBES) can capture electrons emitted over the whole sphere of 4π [51]. As the photons generated by the XFEL pulses are linearly polarised, the following expression for the photoelectron differential cross section can be used [52]:

$$\frac{\mathrm{d}\sigma}{\mathrm{d}\Omega} = \frac{\sigma_\mathrm{tot}}{4\pi}[1 + \beta P_2(\cos\theta)],$$

where σ_tot denotes the total cross section, β the asymmetry parameter, which depends on l, and $P_2(\cos\theta) = \frac{1}{2}(3\cos^2\theta - 1)$ is the second order Legendre polynomial.

2.7 Theoretical calculations

2.7.1 XATOM toolkit

Analysing multiphoton absorption in xenon and its complex relaxation dynamics necessitates a theoretical framework to investigate the underlying mechanisms and dynamic pathways. For this purpose, the XATOM toolkit was employed, which calculates ionisation dynamics *ab initio* for any specified electronic configuration of neutral atoms and atomic ions interacting with ultraintense XFEL pulses [53, 54]. This toolkit is based on a nonrelativistic quantum electrodynamic (QED) and leading-order perturbation theory (LOPT) framework, using the Hartree-Fock-Slater (HFS) approach [55]. It has been augmented to include first-order relativistic energy corrections and resonance effects [21, 56], the latter is detailed in Ch. 5. The toolkit computes photoabsorption cross sections, Auger-Meitner rates, and fluorescence rates, which are integrated into a rate equation approach to simulate the X-ray multiphoton ionisation dynamics by solving a massive set of coupled rate equations. Given that the number of coupled rate equations exceeds 10^{60} [57], a Monte Carlo on-the-fly approach was employed for the calculations [58].

The calculations employed a temporal Gaussian profile with a pulse duration of 10 fs full width at half maximum (FWHM) and a photon-energy bandwidth of 1%. A single Gaussian spatial profile was assumed to model the fluence distribution for volume integration. Both will be detailed in Section 5.3.

2.7.2 JAC

The JAC program is a versatile tool for executing atomic structure calculations on arbitrary open-shell atoms and atomic ions using the relativistic multiconfigurational Dirac-Hartree-Fock (MCDHF) method. In addition to calculating atomic-level structures and properties, as well as transition amplitudes between bound-state levels, it is capable of determining transition probabilities, Auger-Meitner rates, and PCS [59]. These calculations are instrumental in the investigation of DCH formation in argon, as discussed in Ch. 6.

2.7.3 FAC

The FAC is a widely used software package for calculating atomic data of radiation and collision processes and is based on the relativistic Dirac equation [60]. In this study, it is employed to investigate DCH states in argon by calculating electron energy levels, partial PCS, and Auger-Meitner transition rates.

Chapter 3

Experiment

This chapter provides the foundational knowledge necessary for the experiments conducted. It encloses the free-electron laser (FEL) operational principles, the beam transport system, the experimental chamber, photon diagnostic techniques, and the data acquisition system (DAQ). The FEL section only treats the basic knowledge based on G. Margaritondos's "A simplified description of X-ray free-electron lasers" [61]. For a detailed introduction to 1D FEL theory, the reader is advised to Ref. [62] or Ref. [63].

The present study comprises two experimental configurations to investigate the photon-energy-dependent ionisation of xenon and the formation of double-core holes in argon. Both experiments were performed using the small quantum systems (SQS) instrument at the SASE3 branch of the European XFEL in Schenefeld, Germany.

3.1 European XFEL

Since 2017, the European XFEL research facility has been dedicated to generating ultraintense, spatially coherent (laser-like) soft and hard X-ray pulses spanning the photon-energy range from 250 eV up to 25 keV outperforming the most brilliant synchrotron light sources in terms of pulse energy (typically several mJ) and pulse duration (typically 10–30 fs). This capability facilitates a wide range of scientific topics, including studying ultrafast processes and extreme states of matter, three-dimensional imaging of viruses and proteins, and observing chemical reactions. The facility can produce up to 27,000 electron bunches per second, with pulse durations of less than 100 fs (FWHM) [9].

The European XFEL has a length of 3.4 km and mainly consists of three parts: the linear electron accelerator, the undulator systems, and the experimental endstations. These components facilitate the acceleration of electrons to near the speed of light to send them through special magnetic arrangements, known as undulators, which induce the emission of laser-like X-ray radiation [64, 65]. Each component is briefly described below, focusing on the SASE3 undulator and the SQS beamline.

3.1.1   Electron injector and linear accelerator
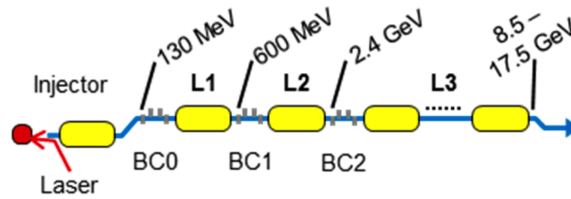
Figure 3.1: Layout of the linear accelerator of the European XFEL. This figure is an edited version of Fig. 1 in Ref. [65].

The first objective is to form electrons into bunches confined to small volumes with similar velocities before they enter the accelerator. The quality of this initial electron beam is crucial as every minor imbalance in the electron bunches is amplified during acceleration.

Electron generation is initiated by a photocathode radio-frequency (RF) gun, which produces free electrons through the interaction of UV-laser pulses with a Cs_2Te photocathode via the photoelectric effect [66, 67]. After generation, the electrons are formed by a magnetic field and pre-accelerated to 6 MeV before entering the accelerator [65]. The injector generates ten trains of electron bunches per second, each comprising up to 2,700 short electron bunches within one 600-µs-long RF pulse in burst mode, yielding an effective repetition rate of 4.5 MHz. The injector encompasses a 43-meter-long beamline section, which includes a diagnostic section for assessing various properties of the electron bunches, such as charge, trajectory, and timing [68].

The linear accelerator comprises 96 twelve-metre-long superconducting modules distributed over 1.7 km. The modules follow a TESLA-type design [69] and are constantly cooled to 2.2 K for superconductivity. Each module comprises eight niobium cavities, each of nine cells. A 10 MW multi-beam klystron supplies RF power to four modules, coupling to each cavity to facilitate the necessary energy transfer to the electrons.

Furthermore, the 96 modules are organised into three sections L1, L2, and L3, as shown in Fig. 3.1. Before each section, electrons pass through one of three bunch compressors (BC0, BC1, and BC2 in Fig. 3.1), which compress the initial bunch duration from 20 ps to less than a few femtoseconds. The maximum electron beam energy of the accelerator reaches 17.5 GeV [65].

Following the accelerator, electrons are directed into two electron beamlines using a fast-rise-time, high-precision, flat-top strip-line kicker [9]. Additionally, an upstream kicker diverts not-needed electron bunches to a dump beamline, allowing for individual bunch patterns in the two electron beamlines.

When writing this thesis, the European XFEL features three operational undulators: SASE1, SASE2, and SASE3, with SASE1 and SASE2 dedicated to hard X-rays and SASE3 to soft X-rays. The SASE3 undulator is situated downstream of the SASE1 undulator in the south electron beamline, necessitating that electron bunches used for lasing in SASE3 first pass the SASE1 undulator, as illustrated in Fig. 3.2. This configuration results in coupled operational conditions for the two undulators, which can be mitigated through various techniques [70, 71].
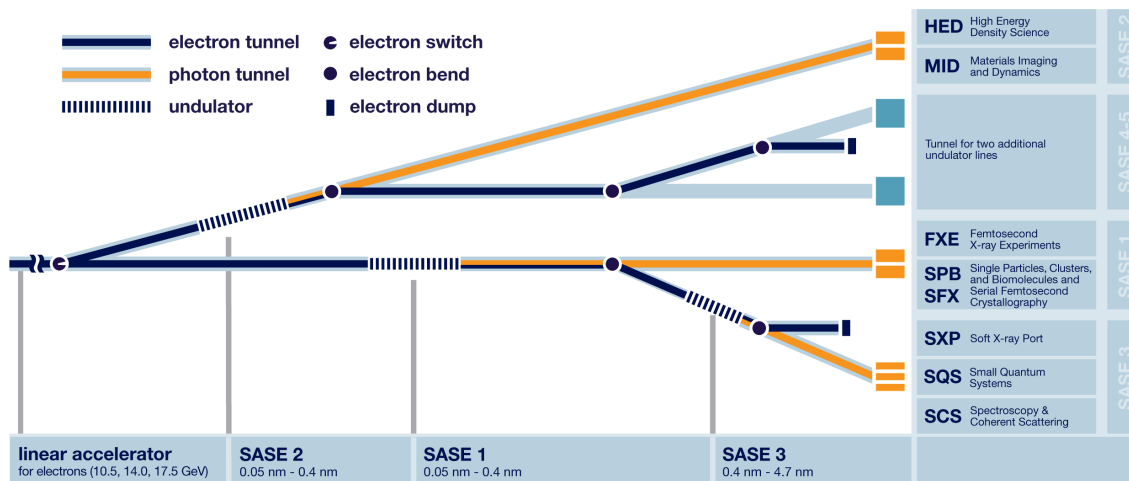
Figure 3.2: Undulator beamlines at the European XFEL[1].

The SASE3 undulator, with a total length of 128.1 m, consists of 21 modules, each having a length of 5 m and a period length of 68 mm. Between the modules with a spacing of 1.1 m, air coils, permanent magnet phase shifters, quadrupole magnets, and electron beam position monitors (BPMs) are located [9]. The resultant photon energy is influenced by both the electron beam energy and the tuning of the undulator gap, which can be adjusted within a range of 10 to 25 mm [70]. In the present experiments, the electron energy is held constant while the undulator gap varies the photon energy. The SASE3 undulator can deliver photon energies ranging from 250 to 3000 eV, with a pulse energy of up to 10 mJ, depending on photon energy, and a pulse duration varying from 10 to 25 fs.

In the experiments described below, the electron beam energy was set at 14 GeV to investigate the photon-energy-dependent ionisation of xenon. A specific machine mode with tailored tuning achieved high intensities (10^{13} photons per pulse) within the photon-energy range of 700–1700 eV. For studying double-core hole formation in argon, the electron beam energy was tuned to 8 GeV for the argon study to facilitate photon energies below 500 eV.

---

[1]https://www.xfel.eu/facility/beamlines/index_eng.html

3.1.2   SASE3 undulator

An undulator comprises a periodically alternating structure of permanent magnets, creating a sinusoidal magnetic field with a periodic length λ_U. The SASE3 undulator has a planar configuration featuring two opposing symmetric arrays separated by the undulator gap. The magnetic field of a single magnet is in the order of 0.5 T [72]. Fig. 3.3 illustrates an undulator and how the electrons interact with it.
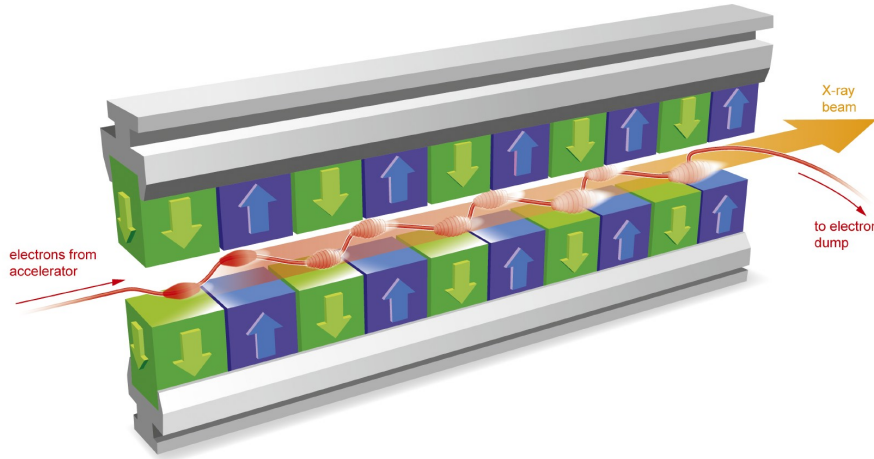
Figure 3.3: Schematic representation of an undulator and the progression of its lasing process.[2].

As accelerated electrons traverse the undulator, they are pushed onto a slalom trajectory due to the Lorentz force, resulting in transverse acceleration that leads to photon emission. With a kinetic energy of 14 GeV in standard operation mode, the electrons attain a longitudinal velocity approaching the speed of light. While the emitted photons propagate at light speed, the electrons lag behind, facilitating interactions between electrons and photons.

The electron bunches exhibit a velocity distribution; thus, the electromagnetic field of the photons causes selective acceleration and deceleration of various electrons based on their velocities. This interaction results in the formation of thin slices, or microbunches, as the transverse magnetic component of the electromagnetic field couples with the undulator-induced transverse velocities of the electrons, exerting a Lorentz force in the direction of propagation. Consequently, microbunching develops along the undulator path, with spacing corresponding to the photon wavelength.

Ultimately, this process yields a correlated emission (in phase) of photons from the electrons, with intensity scaling as N^2, where N represents the number of electrons. The total intensity of the XFEL pulse is continuously amplified during its passage through the undulator until saturation occurs. This amplification mechanism is initiated by the spontaneous emission of electrons, known as shot noise, and is referred to as self-amplified spontaneous emission (SASE).

The electrons propagate at relativistic velocities v approaching the speed of light c, resulting in a Lorentz-contracted undulator period $\frac{\lambda_U}{\gamma}$ in their rest frame, where the Lorentz factor γ is defined as $\gamma = \frac{1}{\sqrt{1-\beta^2}}$ with $\beta = \frac{v}{c}$. In this frame, the

___
[2]https://www.xfel.eu/facility/overview/how_it_works/index_eng.html

wavelength of the emitted photons corresponds to $\frac{\lambda_{\mathrm{U}}}{\gamma}$, as the electron's oscillation may be conceptualised as that of an electric dipole antenna. To determine the wavelength of the emitted photons λ in the laboratory frame, the Lorentz-contracted undulator period must be further adjusted by the longitudinal Doppler effect using a factor of $\frac{1}{2\gamma}$. However, due to the oscillation perpendicular to the propagation direction of the electrons, the effective longitudinal velocity v is reduced and must be accounted for [61]. Finally, the emitted fundamental wavelength viewed without an observer angle is:

$$\lambda = \frac{\lambda_{\mathrm{U}}}{2\gamma^2}\left(1 + \frac{K^2}{2}\right).$$

The undulator parameter is given by $K = \frac{e}{2\pi m_e c}\lambda_{\mathrm{U}} B_0$, where e denotes the elementary charge, m_e mass of the electron, and B_0 the maximum undulator field strength [72]. In general, higher harmonics, which scale λ by $\frac{1}{n}$ with $n \in \mathbb{N}^+$ are produced together with the fundamental ($n = 1$) in FELs [73]. They are typically suppressed and exhibit a reduced intensity. Only the fundamental will be considered for the remainder of this chapter.

In a real undulator, the emitted light is not monochromatic but exhibits a specific bandwidth $\Delta\lambda$ around the central wavelength λ, which inversely scales with the number of undulator periods N_{U} [61].

Fig. 3.4 displays an arbitrarily chosen single-shot spectrum of a SASE pulse, characterised by a bandwidth of 19.5 eV centred at 1390 eV, alongside the averaged spectrum derived from over 1000 shots. Furthermore, this figure highlights the statistical nature [9] of individual SASE pulses, which are composed of a random distribution of intensity spikes [48]. The average spectrum is fitted with a Gaussian profile to determine the bandwidth (FWHM). This analysis was also conducted at selected photon energies ranging from 700 to 1500 eV, as summarised in Fig. 3.5. The spectral distributions at different photon energies were measured using the SASE3 monochromator with an attenuated beam.

The conversion of absolute bandwidth (in eV) to relative bandwidth (in %) indicates a trend of decreasing relative bandwidth with increasing photon energy. This observation aligns with 1D FEL theory [62], wherein the relative bandwidth approximates the Pierce parameter ρ at saturation, which approximately scales nonlinearly with the undulator parameter by $K^{2/3}$ [74].
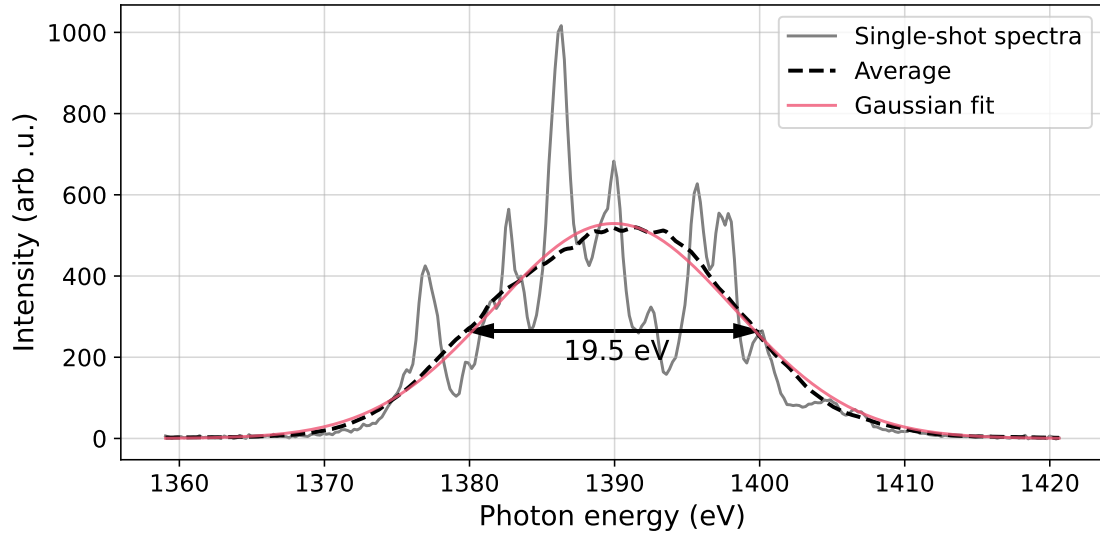
Figure 3.4: Single-shot and average SASE spectrum obtained using the SASE3 monochromator with an electron energy of 14 GeV and a bunch charge of 250 pC. The red curve represents the Gaussian fit of the average spectrum.
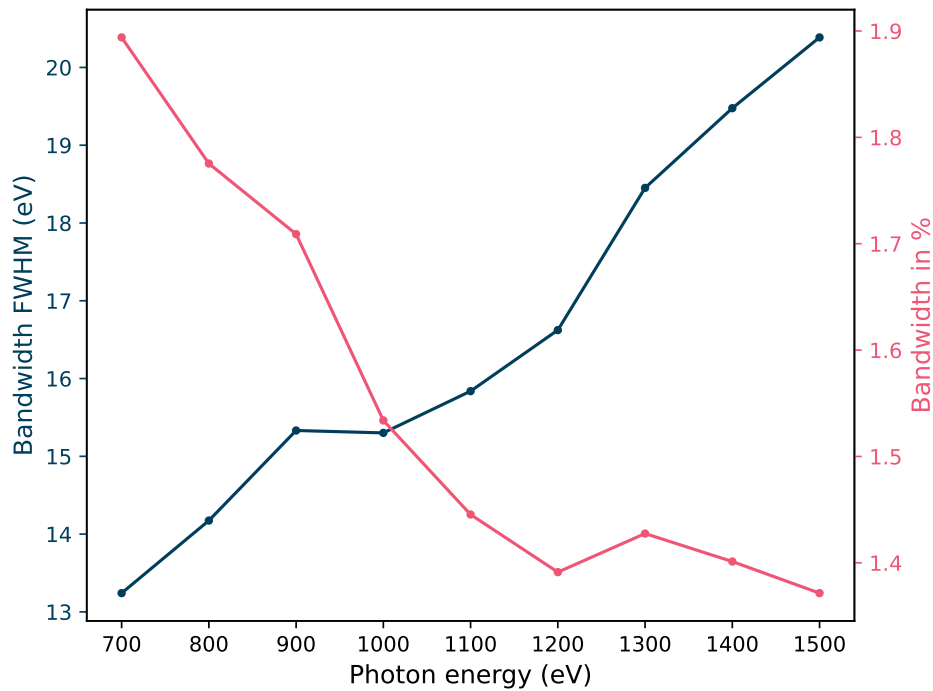
Figure 3.5: Absolute (FWHM) and relative spectral bandwidth as a function of photon energy.

3.2 SQS instrument

The SQS instrument investigates fundamental light-matter interactions involving atoms, ions, small molecules, clusters, and large biomolecules in the gas phase under soft X-ray radiation. It is one of seven operational instruments (status of 2024) at the European XFEL, having commenced user operations in 2018. The primary focus is on nonlinear phenomena such as multiple ionisation and multiphoton processes, time-resolved experiments that probe dynamical processes on the femtosecond timescale, strong-field phenomena including electron dynamics in the near-infrared (NIR) regime, and scattering experiments, all employing spectroscopic techniques. These techniques include detecting ions, electrons, and photons via TOF spectroscopy, angle-resolved kinetic energy spectroscopy, X-ray emission spectroscopy, X-ray imaging, and single-photon detection [75–78]. Furthermore, the instrument has diverse sample delivery systems, including a gas needle, a supersonic molecular beam source, a state-selected molecular source, a rare gas aggregation cluster source, a pulsed microplasma cluster source, and an aerosol source. For the techniques mentioned above, three specific, interchangeable experimental end stations are available: the atomic-like quantum systems (AQS), the nano-sized quantum systems (NQS), and the reaction microscope (REMI) end station. Two end stations can be operated simultaneously, featuring two distinct focus set points (F_1 and F_1') at the first end station and a single focus point (F_2) at the second end station [79]. Additionally, time-resolved pump-probe experiments can be conducted using a synchronised optical laser [65, 80–83] or via X-ray pump/X-ray probe in two-colour mode employing the magnetic chicane in the SASE3 undulator [84]. In this study, the AQS end station was employed exclusively, and the gas needle was used for sample injection of xenon and argon.

X-ray photon beam transport
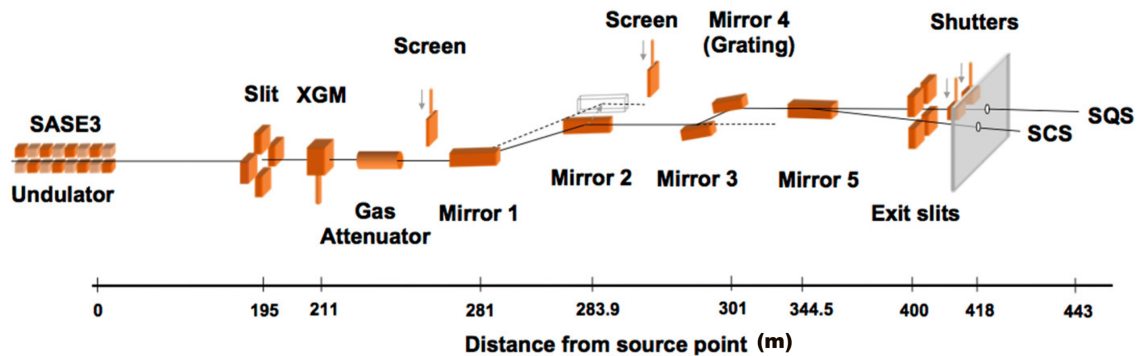
Figure 3.6: Optical layout of the SASE3 photon transport system. This figure is an edited version of Fig. 3 in Ref. [65].

Generally, the sample can be irradiated with either a direct broadband SASE beam from the undulator or a narrowband beam produced by the soft X-ray monochromator, which typically has reduced pulse energy. Fig. 3.6 illustrates the optical layout of the SASE3 beamline in the tunnel. Following the undulator, parts of the FEL beam can be tailored by a double-slit system known as the synchrotron radiation

aperture (SRA) before it reaches the X-ray gas monitor (XGM) detector [85] and the gas attenuator (GATT) [86], both of which will be described in the subsequent sections.

After the GATT, the beam enters the first of four high-quality grazing-incidence mirrors (M1–M4). The initial two mirrors, M1 and M2, form a horizontal chicane designed to suppress high-photon-energy backgrounds and contributions from higher FEL harmonics. Mirrors M3 and M4 create a vertical chicane, with M3 capable of accommodating either a low-energy or high-energy pre-mirror. M4 serves as a plane mirror, which can be replaced with a variable line spacing (VLS) device, thus working in conjunction with a vertical slit positioned at the focal point of M3 to constitute the soft X-ray monochromator [87].

After passing through the monochromator, the beam exits the tunnel and enters the experimental hutch of SQS, traversing a photon diagnostic section, which includes an additional XGM. The beam continues onward to a pair of bendable X-ray mirrors arranged in a Kirkpatrick-Baez (KB) configuration, which focus the FEL to micron level at three distinct focal spots in the experimental end stations, achieving intensities of up to 10^{18} W/cm^2 [79].

3.3   X-ray gas monitor detector

The XGM detector [85] measures the FEL's pulse energy and beam position on a shot-to-shot basis and can operate at MHz repetition rates. The acquired data is used in real-time during experiments to monitor pulse energy and is also employed in offline data analysis for sorting pulse energies, rendering it one of the most valuable diagnostic tools at FEL facilities.

The XGM consists of a chamber filled with a diluted rare gas, through which the FEL beam passes, resulting in the photoionisation of neutral rare gas atoms. An electrostatic field extracts the generated ions and electrons, which subsequently are detected by two Faraday cups [88]. The detected electric current is directly proportional to the number of photons, while the gas concentration is sufficiently low to prevent perturbations of the photon beam [85, 89].

Because of specific ionisation edges or resonances, the use of a specific gas depends on the experiment's photon-energy range. In the xenon investigation, the XGM within the tunnel was filled with krypton gas, while the XGM close to the experiment used xenon gas. The argon investigation used krypton gas for both XGMs in the experimental hutch and the tunnel.

3.4   Gas attenuator

The SASE3 GATT [86] is a fast-responding, 15-meter-long gas cell filled with nitrogen gas, designed to precisely regulate the pulse energy of the FEL beam by varying the gas pressure. The attenuation happens via photoabsorption of the neutral nitrogen gas, which is suitable as it has no ionisation edges in the soft X-ray regime. Beam attenuation using gas serves as an alternative to solid foils, which are too thin to withstand the heat load generated by high-intensity FEL beams at the SASE3 beamline. The GATT effectively dissipates absorbed energy between single FEL pulses within the pulse train, making it suitable for MHz repetition rates [86, 90].

3.5 AQS end station
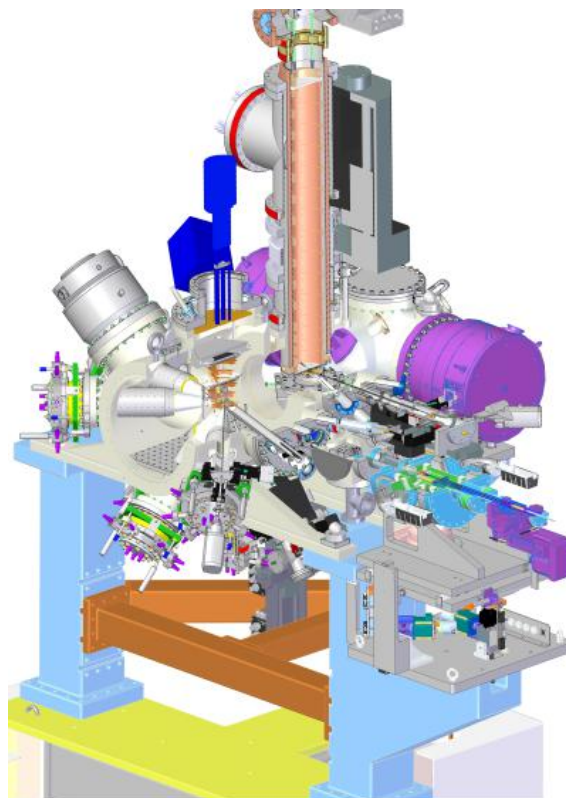
Figure 3.7: Layout of the AQS end station[3].

One of the experimental end stations at the SQS instrument is the AQS end station. It is primarily used to investigate free atoms and small molecules. The background pressure within the integrated vacuum chamber, where these atoms and molecules are introduced, can reach vacuum levels as low as 10^{-10} mbar to minimise the interaction of residual gases with the tightly focused FEL beam [80]. Figure 3.7 depicts the layout of the AQS end station. As of 2024, the station has six identical electron TOF spectrometers, a velocity map imaging (VMI) spectrometer, and a MBES (magnetic bottle electron spectrometer). Three electron TOF spectrometers are positioned in the dipole plane, perpendicular to the beam propagation direction, while the remaining three are situated in the non-dipole plane. Each dipole-plane spectrometer is set at distinct angles: 0°, 54.7°, and 90°. An angle of 54.7° defines the "magic angle", at which the differential cross section is independent of the asymmetry parameter β [Sec. 2.6]. Additionally, the vertical (90°) electron TOF spectrometer can function as an ion TOF spectrometer by reversing the polarity of the applied voltages and using the VMI extraction electrodes to direct the low-kinetic-energy ions towards the spectrometer. The VMI spectrometer is installed coaxially with the vertical TOF spectrometer [81].

---

[3]`https://www.xfel.eu/facility/instruments/sqs/instrument/aqs_end_station/index_eng.html`

Figure 3.8 shows one of the six identical high-resolution electron TOF spectrometers at AQS [77]. Electrons or ions enter the spectrometer from the left side, where they are electrostatically focused by the electrodes before entering the field-free drift tube, ultimately reaching the microchannel plate (MCP) detector. A negative bias can be applied on the drift tube to retard electrons to improve the energy resolution. The acceptance angle of the spectrometer is 0.14% of 4π. Additionally, a positive or negative potential can be applied to the front of the MCP detector to enhance gain.
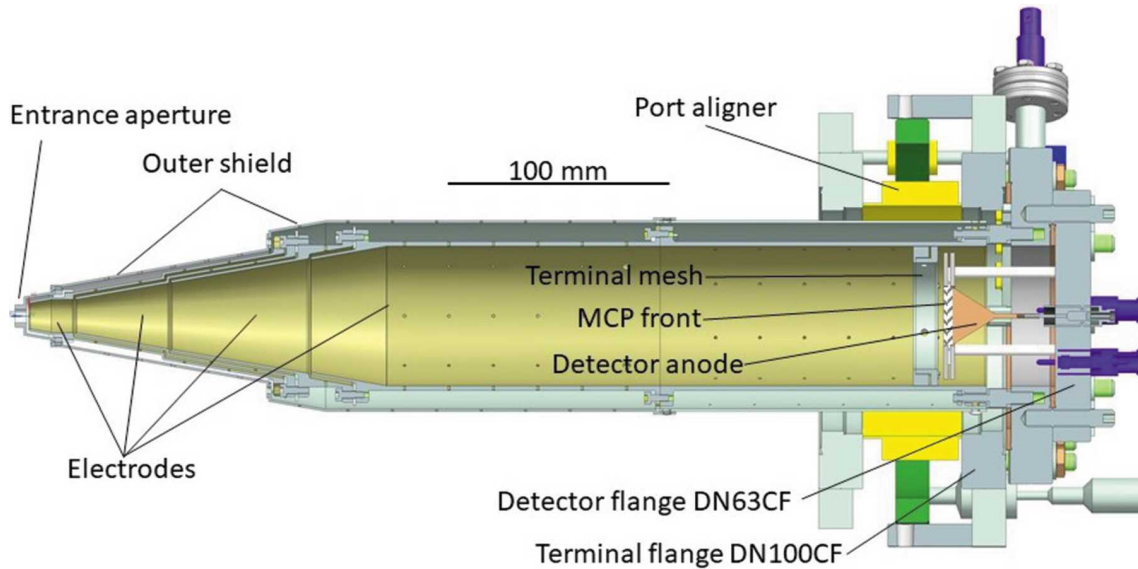
Figure 3.8: Layout of the electron TOF spectrometer. This figure is adapted from Ref. [77].

MCP detectors mainly detect individual particles, including photons, electrons, and ions. When an incident particle strikes the surface of an MCP detector, it generates secondary electrons, which are registered as output. An MCP consists of a planar lead glass plate embedded with millions of thin, conductive pores (channels). Each channel is an independent secondary electron multiplier, with gains exceeding $> 10^6$. Upon entry into a channel, a particle collides with its wall, resulting in a cascade of secondary electrons accelerated by the electric field created by the applied voltage at either end of the MCP.

The detector used here is the *F9890-31* model by *Hamamatsu*, which comprises two stacked MCPs arranged in a Chevron configuration. This type of MCP stack assembly amplifies each incident particle into a variable output pulse of electrons. A histogram of these variable output pulses yields a characteristic pulse-height distribution [91].

3.6 Data aquisition

The European XFEL employs the Karabo supervisory control and data acquisition (SCADA) framework [92] as the primary user interface for conducting experiments and processing recorded data. Karabo can manage significant data volumes at up to 20 GB/s while preserving global time correlation.
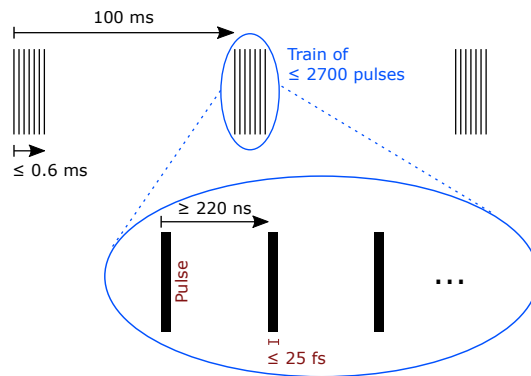
Figure 3.9: European XFEL's Pulse delivery structure[4].

The European XFEL can generate ten trains per second, each comprising up to 2700 pulses, with a minimum temporal spacing of 220 ns, as illustrated in Fig. 3.9. All DAQ systems at the European XFEL are synchronised to this pulse pattern, ensuring that each pulse is associated with a correlated dataset, including parameters such as pulse energy and TOF spectrum. The frequency of the master clock at the European XFEL, which synchronises all devices, is twice the accelerator repetition rate, resulting in a frequency of 9.028 MHz.

The analogue signals from the MCP detector are processed using a 12-bit analogue-to-digital converter (ADC) digitiser, the *ADQ412-4G* manufactured by *SP Devices*. The digitiser is triggered at a frequency of 10 Hz, acquiring data over the initial 600 µs of the 100 ms time frame, thereby ensuring comprehensive signal capture during the ion generation period induced by the X-rays. Both xenon and argon studies employed a sampling rate of 4 GHz to attain optimal temporal resolution.

To systematically study light-matter interactions in the soft X-ray regime, selecting rare gas atoms free from environmental disturbances is preferable. The used xenon and argon gas have a purity of 5.0, which means that the gases contain 99.999% xenon or argon atoms, respectively and are obtained through separation from the earth's atmosphere by liquefying air using the Hampson–Linde cycle [93]. The gases are injected into the chamber by gas expansion through a needle at room temperature. The needle is mounted a few millimetres away from the interaction volume with the FEL.

---

[4]https://rtd.xfel.eu/docs/data-analysis-user-documentation/en/latest/overview/

Chapter 4

Data Analysis

This chapter outlines the essential procedures for extracting the observables from the experimental raw data, which primarily consist of TOF spectra for ions and electrons. Ions are detected using the vertical TOF spectrometer operated as an ion TOF, while electrons are detected by the spectrometer positioned at the magic angle of the AQS end station.

In the experiment focused on the photon-energy-dependent ionisation process of xenon, several additional analysis steps were implemented beyond standard TOF mass spectrometry. These steps included the deconvolution of the signal arising from xenon's seven isotopes and the compensation for the charge-state dependence of the MCP detector signal. An overall systematic error estimate is performed for each analysis step, while for each experimental ion yield a statistical error is estimated. Both error analyses are essential for evaluating the validity of the observed phenomenon. Furthermore, for each xenon TOF spectrum corresponding to a specific photon energy and pulse energy, a corresponding argon TOF spectrum was measured, which is used for calibrating the theoretical fluence distribution.

The data analysis pertaining to the investigation of DCH formation in argon's $2p$ subshell is more straightforward and adheres to a standard evaluation of the electron TOF spectra.

4.1 Extracting charge-state distribution

4.1.1 Extracting time-of-flight spectrum

The raw trace is a time series comprising a total of 2.1×10^6 samples obtained from the digitiser, encompasses all pulses of the pulse train and must be segmented into individual pulse chunks corresponding to single TOF spectra. In this context, the raw trace reflects the negative analogue signal of the MCP detector represented in integer values. Fig. 4.1 illustrates the average pulse train trace along with its 35 TOF spectra (dark blue) recorded at a photon energy of 1325 eV. The purple dashed line denotes the average baseline of the trace. The grey dotted lines indicate the boundaries marking the beginnings and ends of the TOF spectra and, thus, the positions on the time axis where the trace is segmented into single TOF spectra. The first grey dashed line represents the start of this segmenting process and must be set manually, approximately in the vicinity of the time position where the photons of the first bunch reach the detector, which can be identified in the trace as a small peak, dubbed "prompt".

The time interval between the pulses is set during the experiment by selecting the electron bunches that are effectively used for photon generation provided by the electron accelerator. In the experiment using xenon, every 32nd bunch was used at an accelerator repetition rate of 2.25 MHz, yielding a time interval of 14.22 μs between the pulses. The digitiser operated in interleaved mode with a sampling rate of 4 GSPS (Gigasample/s), with each sample representing a time interval of approximately 0.25 ns. Consequently, each TOF spectrum has a length of 56,320 samples.
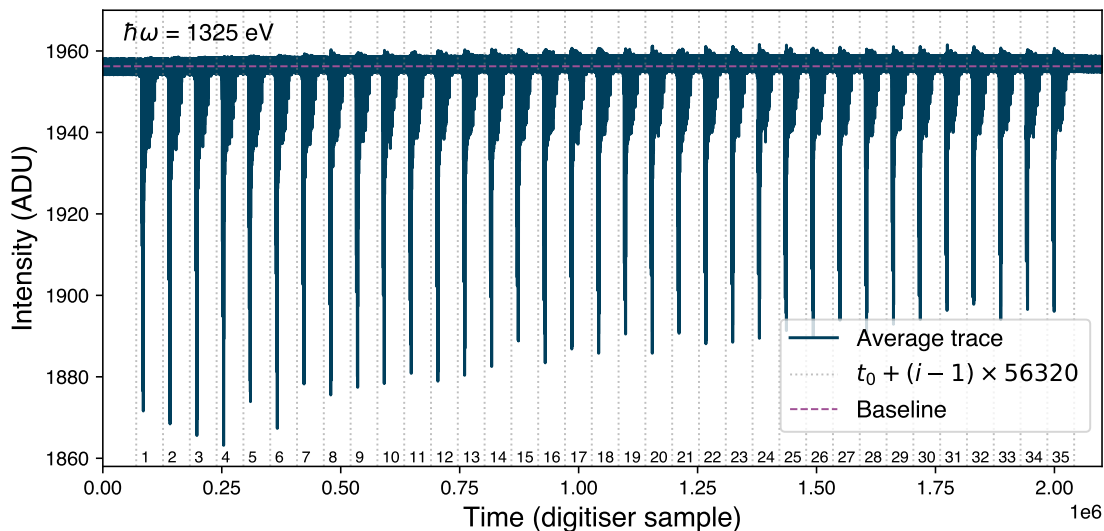
Figure 4.1: Raw data of the average pulse train with 35 numbered (i=1–35) pulses at 1325 eV. The grey dotted vertical lines indicate the beginning of each TOF spectrum, with their positions determined by the formula provided in the legend.

Examination of the baseline in Fig. 4.1 reveals variability across each pulse in the train. For subsequent analysis, the average trace is segmented into 35 individual TOF spectra and compared among them. Fig. 4.2 presents four averaged TOF spectra (1, 5, 10, and 15) corresponding to different positions within the train. The inset additionally illustrates the baselines in the signal-free regions, highlighting that the baseline deviates across various positions within the train. The digitiser's dynamic range extends from -2048 to 2047 analogue-to-digital unit (ADU), corresponding to a 12-bit resolution (4096). Throughout the experiment, the baseline was set at 1956 ADU to utilise the dynamic range effectively and prevent saturation of the negative signal.
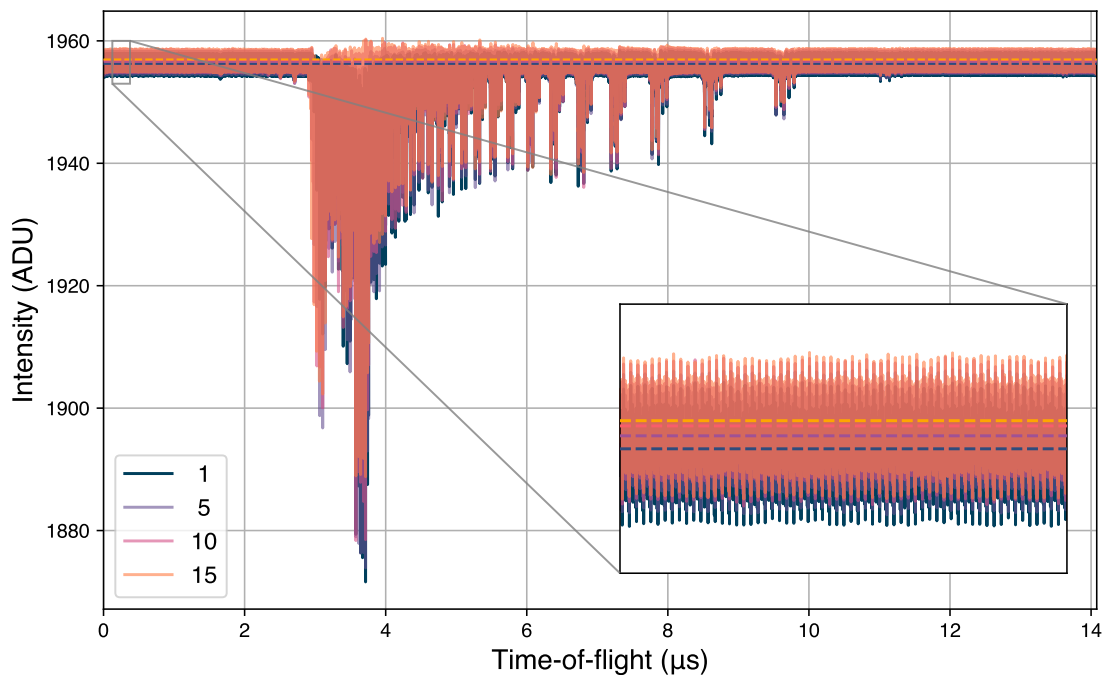
Figure 4.2: Averaged TOF spectra for different pulse positions in the pulse train.

A discernible trend of increasing baseline values with later pulse positions is evident in Fig. 4.3, which displays the average baseline of a TOF spectrum for each pulse position. In this context, "baseline" refers to the initial signal-free 4960 samples of a TOF spectrum ranging from 320 to 5280 samples, with the average baseline defined as the mean value of these samples. The baseline of 1956 ADU is subtracted in Fig. 4.3.
Within the pulse train, the baseline progressively increases until saturation is reached, indicating a charge accumulation between the charge-collecting MCP anode and the AC-coupled readout between pulses. The noise level is recorded at 15 ADU, which also serves as the lower bound for the signal. The difference between the minimum and maximum baseline values, 0.8 ADU, represents approximately 5% of the lowest signal and is, therefore, significant. This finding underscores the necessity of performing baseline subtraction for each individual TOF spectrum rather than applying a global baseline correction to the entire pulse train trace.
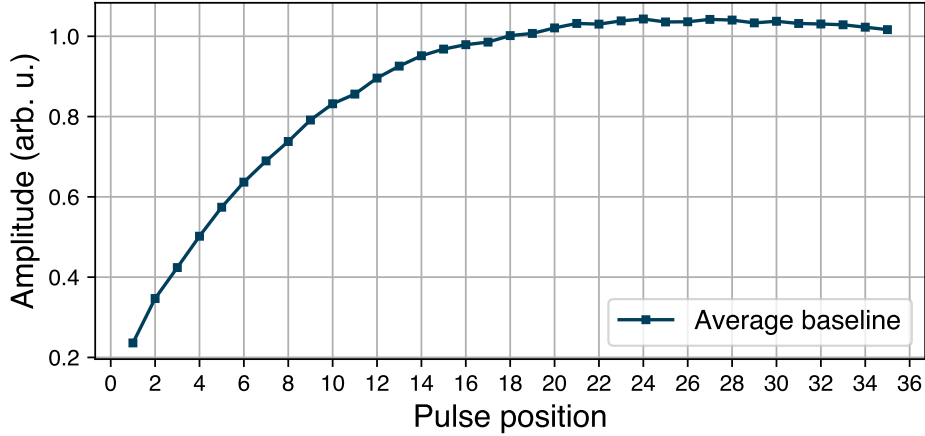
Figure 4.3: Baseline amplitude as a function of the pulse position in the pulse train.

Further, the inset of Fig. 4.2 shows a periodic noise pattern. The timing system at the European XFEL supplies a 9.02 MHz clock, which is input into the phase-locked loop (PLL) chip of the digitiser. This clock is multiplied multiple times by several internal chips with sampling rates significantly lower than the target to achieve the effective sampling rate of 4 GSPS. Additionally, these chips exhibit slightly different bias settings, resulting in the observed period noise pattern. Panel **a** of Fig. 4.4 illustrates this in greater detail, presenting an example of 55 samples of the averaged signal, with markers for every 1st (red squares) and 8th (blue triangles) sample. This identified pattern exhibits a periodicity of 16 and can be addressed by establishing 16 distinct baselines for each ith sample within the TOF spectrum.

Panel **b** of Fig. 4.4 displays the intensity of the Fourier transformation of 5000 signal-free samples of the uncorrected TOF signal as a function of frequency, pinpointing seven frequencies that contribute to the periodic noise (dark blue) alongside the corresponding corrected TOF signal (purple), wherein these frequencies nearly vanish. The lowest detected frequency of 0.25 GHz determines the periodicity of 16 due to its period of 4 ns equivalent to 16 samples.

In order to correct for periodic noise, an iteration is executed for i ranging from 1 to 16. For each i, every 16th digitiser channel, beginning from the ith channel, is selected, and the corresponding ith baseline is subtracted. The ith baseline is calculated as the average of approximately 5000 signal-free samples, starting from the ith channel. Furthermore, the beginning of this average is offset by a multiple of 16 to ensure that the average excludes the prompt. This procedure is conducted pulse-wise, automatically accounting for the position-dependent offset within the pulse train.

Finally, panel **c** of Fig. 4.4 shows the average corrected baseline as a function of pulse position within the train, demonstrating compensation for both the drifting baseline and periodic noise. The average baseline now constitutes less than 1‰ of the lowest signal. Additionally, Fig. 4.5 present histograms of the corrected and uncorrected noise values. The histograms in panel **b** and **c** reveals a Gaussian distribution following the correction procedure, indicating a purely stochastic nature of the noise, in contrast to the discrete distributions evident in panel **a**.
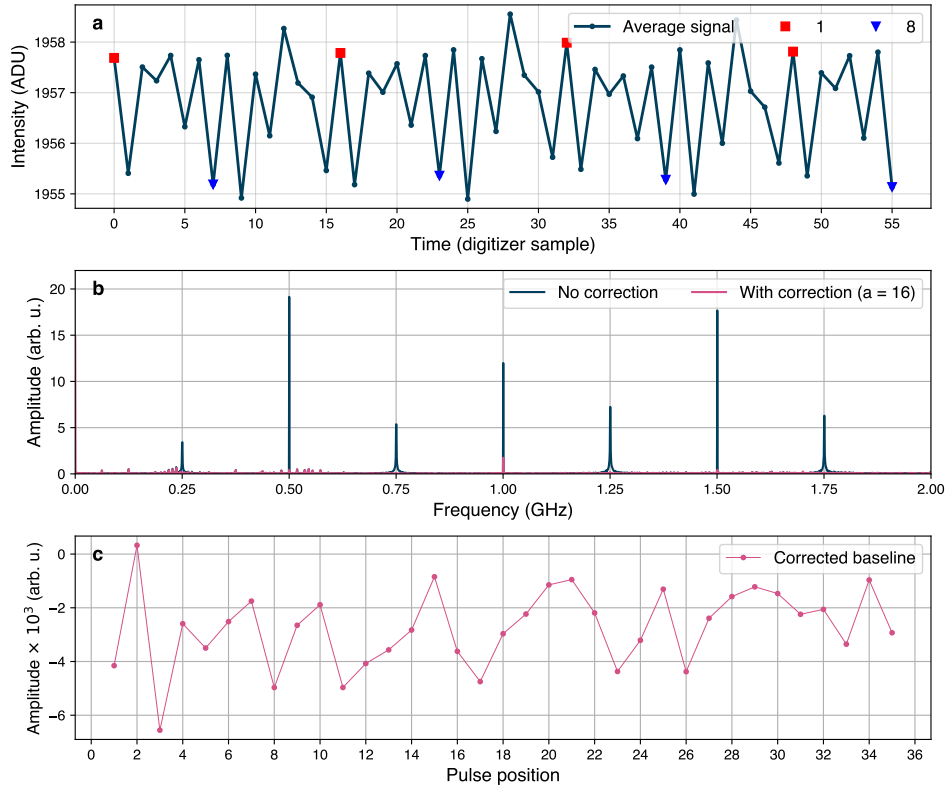
Figure 4.4: Periodic noise of the averaged trace.
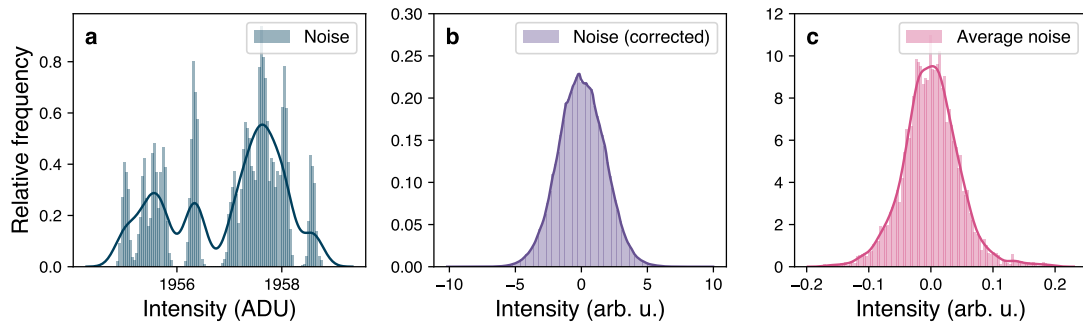
Figure 4.5: Histogram of the noise: Panel **a** presents the uncorrected background noise. Panel **b** displays the corrected noise recorded in each individual spectrum. Panel **c** illustrates the noise distribution of the averaged spectrum.

4.1.2 Theoretical background of ion TOF spectroscopy

Before detailing the calibration procedure, a brief theoretical background on TOF spectrometry is presented. A TOF spectrum reflects the travel times of an ensemble of charged particles, such as xenon ions, which traverse a field-free drift tube after being accelerated by an electric field and before reaching the detector, facilitating the determination of their mass-to-charge ratio $\frac{m}{q}$. Fig. 4.6 shows a SIMION simulation of the used TOF spectrometer (s. Sec. 3.5) and is segmented into three regions. Section I is the interaction zone, section II the field-free drift tube and section III belongs to the post acceleration of the detector assembly.
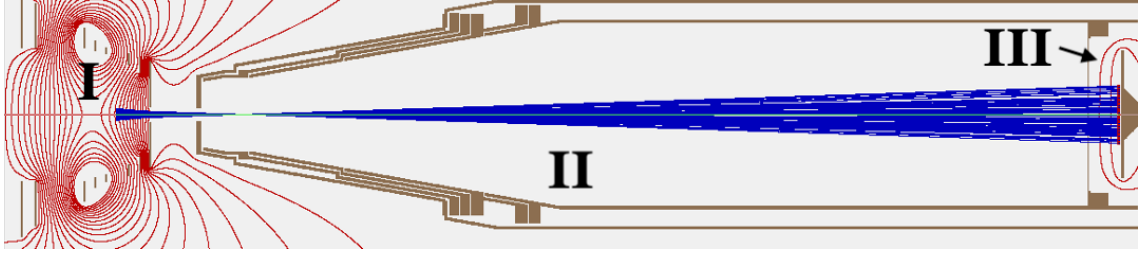
Figure 4.6: SIMION simulation of the spectrometer. The blue streams reaching from the interaction zone to the detector correspond to a beam of singly charged xenon ions [Courtesy A. De Fanis 2020].

As outlined in Sec. 3.5, the electric field generated by the VMI electrodes in Section I accelerates the ions from the interaction zone towards the entrance of the spectrometer. This configuration, along with the drift tube and grounded electrodes of the spectrometer, is analogous to the widely employed Wiley-McLaren design [94]. Each charged particle, characterised by charge q (in units of the elementary charge e) and mass m (in units of atomic mass unit u), is accelerated by the effective longitudinal electric potential difference U between the interaction zone and the detector, leading to a gain in kinetic energy expressed as $E_{\text{kin}} = qU$. Assuming that $v \ll c$ (where v denotes the velocity of the charged particle and c represents the speed of light), the classical expression for kinetic energy may be employed:

$$E_{\text{kin}} = \frac{1}{2}mv^2 = qU.$$

By substituting v with the relation $v = \frac{d}{t-t_0}$, where d represents the length of the drift tube and $t - t_0$ denotes the TOF (with t_0 is the time offset), the calibration formula $\frac{m}{q}$ can be derived:

$$t = t_0 + k'\sqrt{\frac{m}{q}} \Leftrightarrow \frac{m}{q} = \frac{(t-t_0)^2}{k}. \tag{4.1}$$

Let k represent a scaling factor, defined as $k = k'^2$ with $k' = \frac{d}{\sqrt{2U}}$, which will be determined during the calibration procedure. When transforming the t-axis, it is essential to transform the intensity I to ensure that the magnitudes of the integrals remain equivalent, as dictated by the Jacobian determinant.

$$\left| \int I(\tfrac{m}{q}) \mathrm{d}\tfrac{m}{q} \right| \overset{!}{=} \left| \int I(t) \mathrm{d}t \right|$$

From that $\left|I(\tfrac{m}{q})\mathrm{d}\tfrac{m}{q}\right| = \left|I(t)\mathrm{d}t\right|$ can be derived, which yields the necessary correction:

$$I(\tfrac{m}{q}) = I(t)\cdot\left|\frac{\mathrm{d}t}{\mathrm{d}\tfrac{m}{q}}\right| = I(t)\cdot\frac{1}{\left|\frac{\mathrm{d}\tfrac{m}{q}}{\mathrm{d}t}\right|} = I(t)\frac{k}{2(t-t_0)}.$$

It is important to note that due to this quadratic behaviour and the digitizer's constant sampling frequency (time steps), a reduction in peak width results in fewer sample points within an interval of a given charge state. Specifically, lower charge states exhibit better temporal resolution than higher charge states.
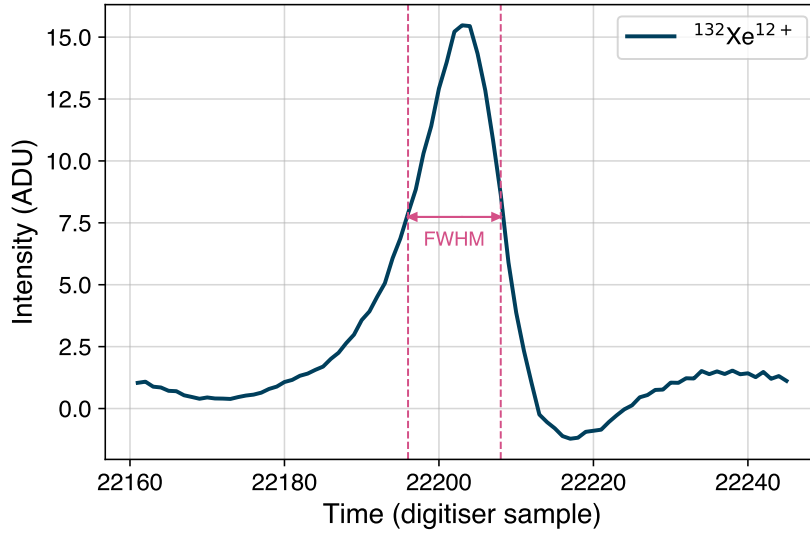
Figure 4.7: Mass peak of isotope $^{132}\mathrm{Xe}^{12+}$ to determine the FWHM.

Fig. 4.7 shows the isotope peak of $^{132}\mathrm{Xe}^{12+}$ alongside its corresponding FWHM. Following the final calibration, which will be detailed in the subsequent section, the mass resolution can be calculated using the formula $\frac{m}{\Delta m} = 880$ with $\Delta m = 0.15$ u (FWHM) and $m = 132$.

For completeness, the initial velocity v_0 of the ions can be approximated by the mean v_{th} derived from the Maxwell–Boltzmann distribution, corresponding to the average velocity of an atom at a temperature T:

$$v_0 \equiv v_{\mathrm{th}} = \sqrt{\frac{8k_{\mathrm{B}}T}{\pi m}}.$$

k_{B} is the Boltzmann constant. With the values $m = 132$ u, $T = 293.15$ K, $U = 500$ V, and $q = e$, where e is the elementary charge, the ratio of v_0 to v reads:

$$\Rightarrow \frac{v_{\mathrm{th}}}{v} = \sqrt{\frac{4k_{\mathrm{B}}T}{\pi qU}} \approx 0.8\%,$$

meaning that v_0 is neglectable.

4.1.3 Calibration $t \mapsto \frac{m}{q}$
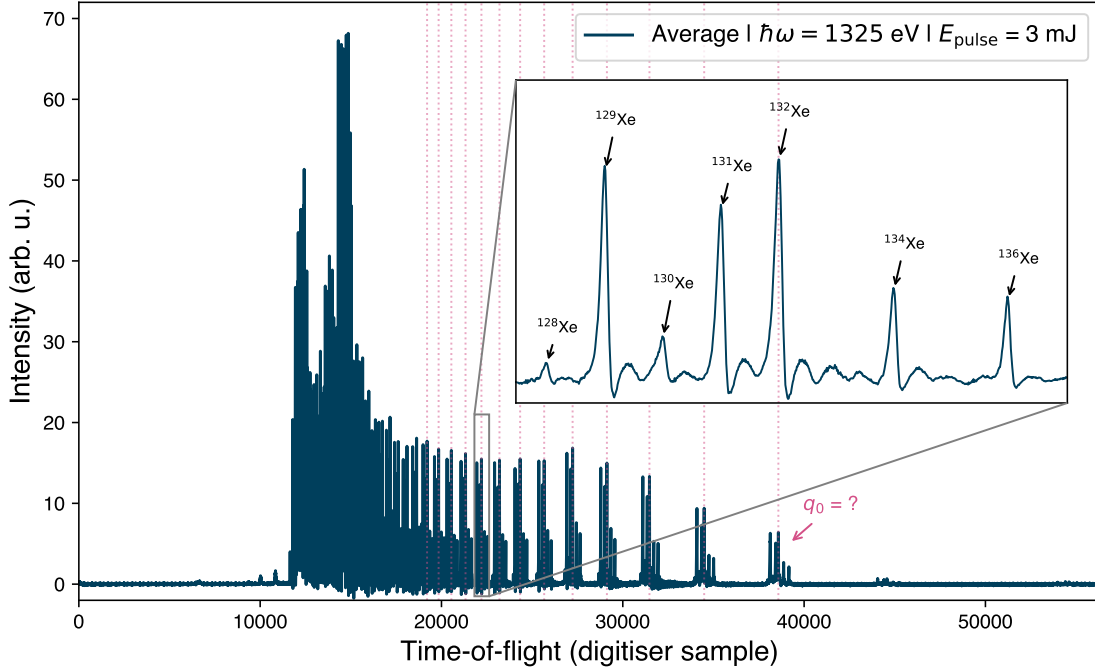
Figure 4.8: Analogue TOF spectrum averaged over all shots at 1325 eV with an average pulse energy of 3 mJ. The inset of Fig. 4.8 shows the distribution of the seven most common isotopes.

Following the background correction, an average TOF spectrum (dark blue) is obtained, as depicted in Fig. 4.8. In the subsequent analysis, the trace of the spectrum is inverted to a positive scale, as this format is more intuitive for interpretation. The spectrum shows distinct collections of peaks scaling down quadratically towards shorter flight times. Each collection corresponds to a different charge state with increases for shorter flight times, as stated by Eq. 4.1. One of the charge states (Xe^{12+}) is zoomed in in the inset, displaying seven distinct peaks, which correspond to the typical isotope distribution of atmospheric xenon. Atmospheric xenon atoms have a specific isotope distribution and compile the seven most common isotopes ^{128}Xe, ^{129}Xe, ^{130}Xe, ^{131}Xe, ^{132}Xe, ^{134}Xe, and ^{136}Xe differing in abundance. The two isotopes ^{124}Xe and ^{126}Xe each have an absolute abundance of less than 0.1% in the isotope composition and could not be observed in the present study. Therefore, the two isotopes will be neglected in the following [95].

For the calibration procedure, which aims to translate the TOF (digitiser samples) to mass-over-charge in a.u., no additional data set is needed since the xenon TOF spectrum provides sufficient mass peaks, which are well-known in the literature and which can clearly be identified. The calibration is crucial for the ion yield extraction to obtain equidistant boundaries for peak integration throughout the TOF spectrum. Furthermore, calibration is needed for preceding analysis steps, such as deconvolution of the isotope distribution and correction of the detection efficiency.

The rose dotted lines mark the manually determined positions on the TOF axis of isotope ^{132}Xe for 13 different charge states, each attributed to a specific mass-over-

charge ratio $\frac{132}{q}$ to perform a least square curve fitting based on Eq. 4.1 using the Levenberg-Marquardt algorithm [96] to retrieve the parameters k and t_0 for a coarse calibration curve $\frac{m}{q}(t)$. At this stage, it does not matter which of the seven isotopes is used for the coarse calibration. The preliminary calibration serves to identify the lowest charge state q_0 of the used peaks and as a base to make a more precise automated calibration. In practice, the process begins with $q_0 = 1$ and increments up until it matches with the data. Fig. 4.9 **a**–**c** presents three different fits for q_0 = 3, 4 or 5, meaning that the TOF peaks of isotope ^{132}Xe are either attributed to the charge states 3–15, 4–16 or 5–17. Here, it is already known that $q_0 = 4$ is the scouted starting charge state, and the figure is supposed to demonstrate how the fit deviates for $q_0 \pm 1$. Each fit is accompanied by a residuals plot, which exhibits the difference between the value of the fitted model and the experimentally determined value for the same data point to assess the quality of the fit model. In panel **a** and **c**, it can be seen that the residuals show a systematic, quadratic-like shape, indicating that the fit and the experimental data do not match. Panel **b** shows a stochastically distributed pattern of the residuals with no systematic dependencies, indicating a good match between fit and experimental values.
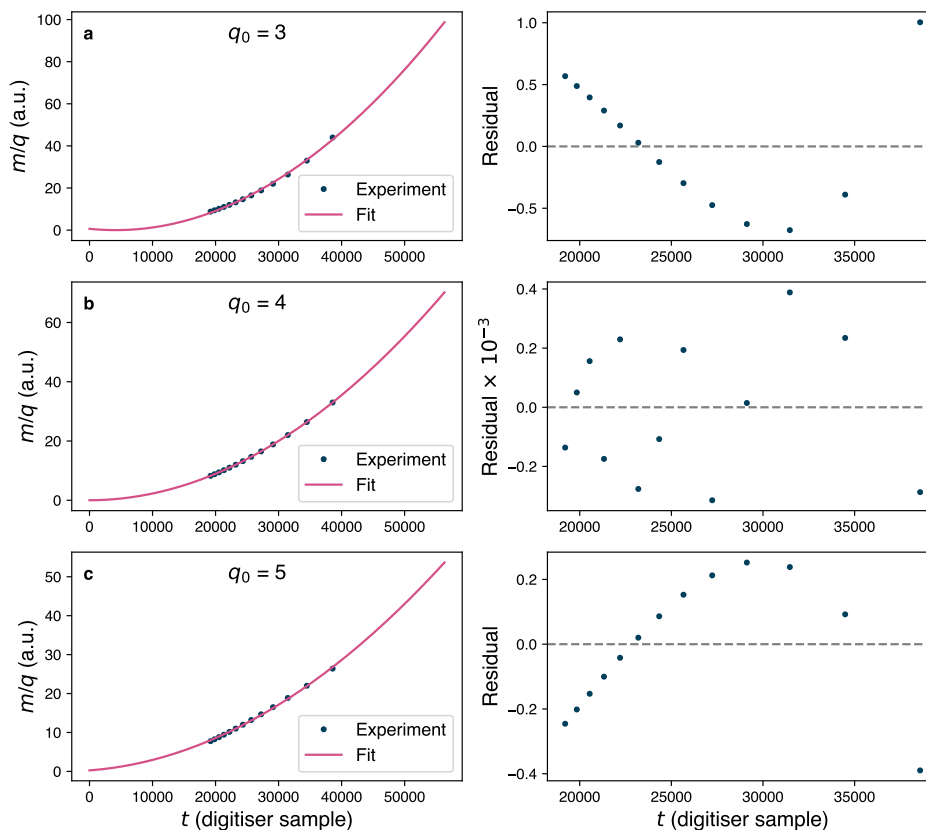
Figure 4.9: Time-to-mass-over-charge calibration with three different values for the lowest charge state q_0 based on Eq. 4.1.

Through the preliminary calibration, a time frame encompassing the peaks with $\pm \frac{0.15\ \mathrm{u}}{q}$ around the peak centre can be automatically defined, from which the time position of the peak maximum is extracted. To enhance the accuracy of the calibration curve, charge states up to Xe^{30+} were included. In addition to isotope ^{132}Xe, the isotopes ^{129}Xe, ^{131}Xe, ^{134}Xe and ^{136}Xe for the charge states Xe^{4+}–Xe^{9+} were used in the calibration, along with the two oxygen peaks $^{16}O^{6+}$ and $^{16}O^{7+}$. Isotope ^{132}Xe is selected as the reference peak for the charge states ≥ 10 due to its minimal overlap with isotope peaks from higher charge states. This will be discussed in greater detail in Sec. 4.1.5. Fig. 4.10 illustrates the final calibration curve, with an inset of its residuals, shown in the lower right corner. The maximum of the residuals is 0.006 a.u., indicating a deviation of less than 1%, which demonstrates strong agreement between the fit and experimental data. Additionally, it was found that using the position of the peak maximum provides a more accurate calibration than curve fitting with a skewed Gaussian model.
The calibration curve navigates the TOF spectra by returning its array indices, equivalent to the digitiser samples, upon input of a specific mass-over-charge ratio. When aiming for a specific mass-to-charge ratio with the final calibration, the resulting peak centre displays a maximum error of one index. Throughout the data analysis, the calibration procedure was done multiple times to accommodate changes in experimental conditions during the beamtime, such as the exchange of pre-mirrors or the transition of the sample gas between xenon and argon.
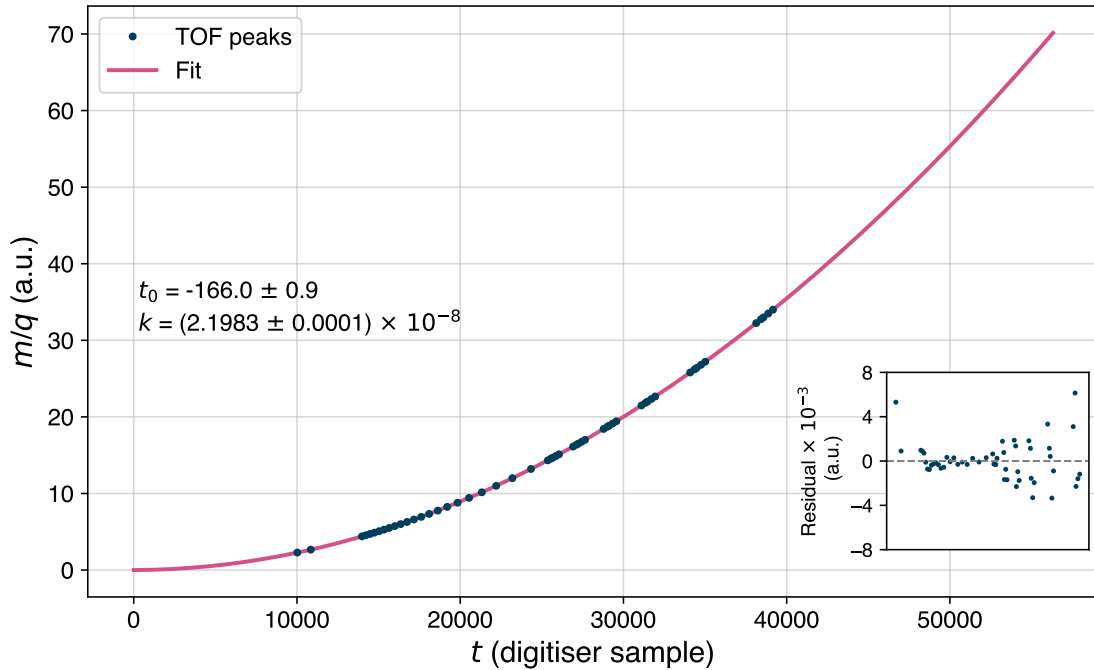
Figure 4.10: Final time-to-mass-over-charge calibration based on Eq. 4.1.

4.1.4   Deconvolution of xenon isotopes

The extraction of the ion yield of a charge state is facilitated by integrating the signal along its time axis. This can be done by integrating the isotope distribution of a certain charge state or by integrating a particular isotope peak, e.g., isotope ^{132}Xe, assuming that the abundances of the isotopes are equal for all charge states. Despite the fact that the temporal resolution is quite high in the experiment, it is inevitable that peaks with the same mass-over-charge ratio superimpose each other. This is inherent to TOF mass spectroscopy and is independent of the temporal resolution. For example, the two peaks belonging to ^{128}Xe^{16+} and ^{136}Xe^{17+} have the same ratio of 8.0, which cannot be separated by the TOF spectrum. The first question which arises is: Is there one isotope out of the seven which does not show any superposition with isotopes from other charge states? To address this question, the first thing to do is to define an overlap of two isotope peaks. Let μ_{12} be the magnitude of the distance between two mass-over-charge peaks on the mass-over-charge axis. For simplicity, one of these two peaks has a fixed isotope mass, e.g. $m_1 = 132$, but changing charge state q_1, and the other peak $\frac{m_2}{q_2}$ is kept variable in its mass m_2 and charge state q_2 to run over it. Considering the asymmetry of a mass-to-charge peak [Fig. 4.7], the width of each peak in the TOF spectra is defined as $\frac{2\Delta m}{q}$, where the constant mass width Δm scales with the charge state q. This means that μ_{12} must be smaller than the sum of the two halve peak widths $\frac{\Delta m}{q_{1,2}}$ for an overlap to occur.

$$\mu_{12} = \left| \frac{m_1}{q_1} - \frac{m_2}{q_2} \right| < \frac{\Delta m}{q_1} + \frac{\Delta m}{q_2}$$

$$\Rightarrow \frac{|m_1 q_2 - m_2 q_1|}{q_1 + q_2} < \Delta m \tag{4.2}$$

By systematically varying the three variables q_1, m_2, and q_2 with a fixed mass $m_1 = 132$ with $m_2 \in [128, 129, 130, 131, 132, 134, 136]$ and $q_1, q_2 \in [2, 41]$ (lowest and highest measured charge state), and $\Delta m = 0.15$ u, several superpositions that satisfy the above-mentioned relation could be identified. The findings are listed in Tab. 4.1, along with superpositions originating from oxygen ^{16}O with $m_2 = 16$ and $q_2 \in [1, 8]$, which will be ignored for the moment, but will become relevant in the further analysis.

^{132}Xe	^{128}Xe	^{129}Xe	^{136}Xe	^{16}O
25+	-	-	-	3+ (0.05)
31+	30+ (0.13)	-	32+ (0.15)	-
32+	31+ (0.58)	-	33+ (0.59)	-
33+	32+ (1.00)	-	34+ (1.00)	4+ (1.00)
34+	33+ (0.60)	-	35+ (0.61)	-
35+	34+ (0.23)	-	36+ (0.25)	-
41+	-	40+ (0.26)	-	5+ (0.42)

Table 4.1: Overlapping isotopes of other charge states in relation with the reference isotope ^{132}Xe at different charge states. The number in parenthesis displays the degree of overlap.

Given that condition 4.2 is true, the degree of overlap $\Omega \in (0, 1]$ is defined as follows:

$$\Omega = 1 - \frac{|m_1 q_2 - m_2 q_1|}{\Delta m(q_1 + q_2)},$$

whereas 1 equals a total overlap with $\frac{m_1}{q_1} = \frac{m_2}{q_2}$ and 0 no overlap of the two peaks. This analysis can be done for each of the seven isotopes. Tab. 4.2 displays the number of charge states affected by overlapping isotopes (xenon and oxygen) from other charge states for each isotope.

Xe isotope	Affected
128	10 + 2 = 12
129	9 + 4 = 13
130	7 + 1 = 8
131	5 + 1 = 6
132	6 + 1 = 7
134	11 + 1 = 12
136	16 + 0 = 16

Table 4.2: Number of charge states affected by overlapping isotopes (xenon and oxygen) from other charge states for each isotope. The second summand represents the number of superpositions, which are exclusively from oxygen.

The isotope ^{131}Xe exhibits the fewest overlaps across all charge states, which is shown in Tab. 4.3 in more detail.

^{131}Xe	^{128}Xe	^{134}Xe	^{136}Xe	^{16}O
25+	-	-	26+ (0.22)	-
26+	-	-	27+ (0.87)	-
27+	-	-	28+ (0.52)	-
33+	-	-		4+ (0.28)
40+	39+ (0.07)	41+ (0.09)	-	-
41+	40+ (0.34)	-	-	5+ (0.86)

Table 4.3: Overlapping charge states of isotopes different to isotope ^{131}Xe.

Generally, it is found that up to Xe^{15+}, none of the seven isotopes of xenon were affected by other xenon isotopes. However, Xe^{8+} is affected by $^{16}O^{+}$ at the isotopes ^{128}Xe and ^{129}Xe.

Fig. 4.11 displays two zooms into the average TOF spectrum at the photon energy of 1325 eV and pulse energy of 3 mJ to illustrate the overlapping nature of the xenon TOF spectrum. Panel **a** presents the barely separable charge state Xe^{15+} and the first occurring overlap of charge state Xe^{16+} of both isotopes $^{128}Xe^{16}$ and $^{136}Xe^{17}$, while panel **b** shows the overlapping isotopes corresponding to the exemplary charge states Xe^{28+}, Xe^{29+}, and Xe^{30+}. Each charge state in panel **b** is distinguished by a unique colour and hatching to emphasise the overlaps. To provide orientation, the red dotted lines mark the isotope peak of ^{132}Xe for different charge states.

As a result, no isotope of xenon remains unaffected by superpositions of other isotopes from different charge states. Nevertheless, it is crucial for the analysis to
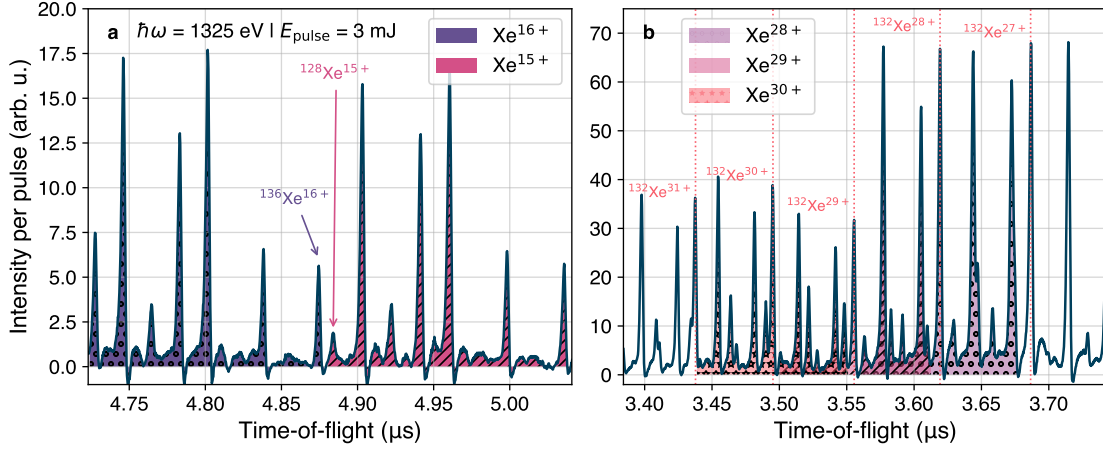
Figure 4.11: Superposition of isotope peaks from different charge states.

extract the ion yields of all charge states. To achieve this, a deconvolution procedure can be employed, utilising the isotope pattern as the response function for each charge state, given that the abundances of the isotope distribution remain consistent across charge states. In this context, it is assumed that the time series of the measured signal $S \equiv S(t)$ consists of unknown impulses $\xi \equiv \xi(t)$, which encapsulate the complete ion yield of a charge state that the deconvolution operation aims to extract. This signal is convolved ($*$ denote the convolution operator) with the impulse response function $R \equiv R(t)$, which encompasses the known xenon isotope pattern, in addition to noise $\varepsilon \equiv \varepsilon(t)$:

$$S = \xi * R + \varepsilon.$$

On the time axis, the isotope response function is not invariant as it depends on the charge state: The time difference between the peak positions of two isotopes m_1 and m_2, within a charge state scales with $\frac{1}{\sqrt{q}}$. Using Eq. 4.1 and defining $\tau = t - t_0$, the time difference can be expressed as follows:

$$\Delta\tau = \tau_{m_1}^{(q)} - \tau_{m_2}^{(q)} = \frac{k'}{\sqrt{q}}\left(\sqrt{m_1} - \sqrt{m_2}\right),$$

so that the isotope response function cannot be used for spectral deconvolution. Yet, on a logarithmic time axis, the time difference reads:

$$\Delta\log\left(\tau\right) = \log\left(\tau_{m_1}^{(q)}\right) - \log\left(\tau_{m_2}^{(q)}\right) = \log\left(\frac{\tau_{m_1}^{(q)}}{\tau_{m_2}^{(q)}}\right) = \log\left(\sqrt{\frac{m_1}{m_2}}\right),$$

and is the same for any charge state. Therefore, the TOF spectrum, expressed on a logarithmic time axis, can be deconvolved by the isotope distribution expressed on the same time axis [97]. When transforming $\tau \mapsto \log\left(\tau\right)$, the intensities modifies to $I(\tau) \mapsto I(\log\left(\tau\right)) = I(\tau) \cdot \tau$. Fig. 4.12 shows the intensity as a function of the logarithmic time axis for isotope distributions of charge states Xe^{8+}–Xe^{15+} overlaid to visualise the equidistant peak widths.
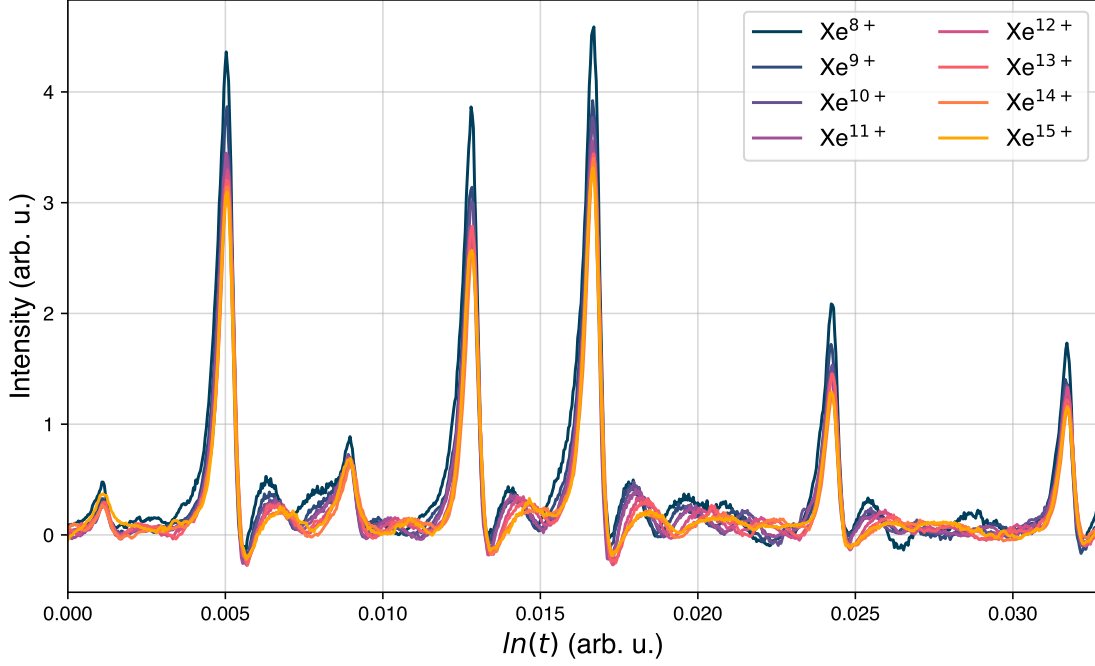
Figure 4.12: Isotope distribution for the charge states Xe^{8+}–Xe^{15+} on a logarithmic time axis.

The deconvolution is based on the convolution theorem, which states that the Fourier transform of the convolution of two functions is equivalent to the product of their respective Fourier transforms. Let $\mathcal{S} = \mathcal{F}\{S[\log(t)]\}$ represent the Fourier transform on a logarithmic time axis of the measured TOF signal S, where $\mathcal{F}$ denotes the Fourier transform operator. Additionally, let $\mathcal{R} = \mathcal{F}\{R[\log(t)]\}$ represent the Fourier transform on a logarithmic time of the known isotope pattern (response function) and $\Xi = \mathcal{F}\{\xi[\log(t)]\}$ the Fourier transform on a logarithmic time axis of the desired impulse spectrum. The Jacobian transformation is not necessary here because it cancels out in the further process due to the linearity of the Fourier transform, and the final inverse transforms to a linear time axis of ξ.

$$\mathcal{F}\{\xi * R\} = \mathcal{F}\{\xi\} \cdot \mathcal{F}\{R\} = \Xi \cdot \mathcal{R} = \mathcal{S}.$$

ξ can then be calculated as follows with $\mathcal{F}^{-1}$ denoting the inverse Fourier transform operator:

$$\xi = \mathcal{F}^{-1}\left\{\frac{\mathcal{S}}{\mathcal{R}}\right\}$$

The impulse spectrum ξ is still on a logarithmic time axis and must be transformed back to the linear time axis $\xi[\log(t)] \mapsto \xi[t]$. In practice, the response function is the isotope distribution at charge state Xe^{12+}, which is extracted from the averaged TOF spectrum. This means that the response function automatically includes the noise ε and that each averaged TOF spectrum has its unique response function. Charge state Xe^{12+} is chosen as suitable because of its occurrence in every spectrum of the photon-energy scan 700–1700 eV, the lack of oxygen superposition and intermediate temporal resolution due to the quadratic decrease with higher flight times. The

Fourier transform and inverse Fourier transform are carried out by using the Fast Fourier Transform (FFT) algorithm, making an instant deconvolution operation possible.

Fig. 4.13 shows the average TOF spectrum at 1325 eV in dark blue overlaid with the deconvolved spectrum in pink. The inset shows a zoom of charge state Xe^{12+}, along with the final Gaussian peak after deconvolution representing the ion yield of the charge state, which is centred at the highest peak of the isotope distribution at isotope ^{132}Xe and applies to all charge states.

Now, the ion yield of every charge state can be extracted by integrating the deconvolved peaks. However, two main problems remain. The first issue is the contamination with oxygen in the TOF spectrum, which influences deconvolution and distorts the ion yields of specific charge states. The second issue concerns the pulse height of the detector signal, which increases with the ion's charge state. The following sections will address these issues and how to treat them in the analysis.
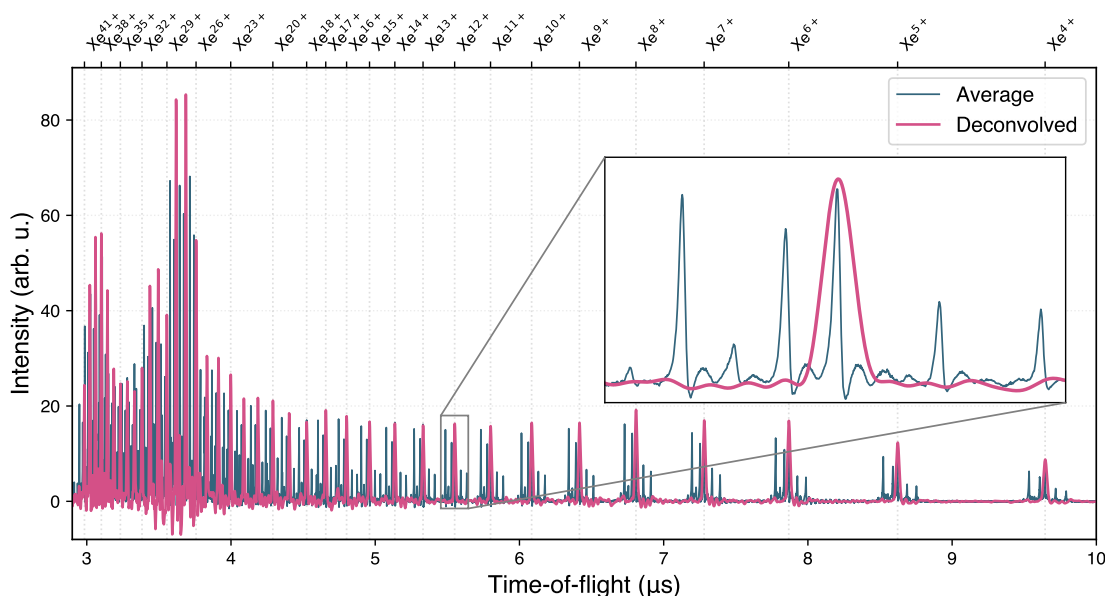
Figure 4.13: TOF spectrum overlaid with the deconvolved TOF spectrum of xenon at a photon energy of 1325 eV with a pulse energy of 3 mJ.

4.1.5 Detection efficiency

In general, MCP detectors exhibit a detection efficiency influenced by various parameters, including velocity, mass, ionic charge state, and post-acceleration (bias) voltage of the MCP [98]. The masses of the xenon isotopes are constant and span a limited range $m =$128–136 u. However, the charge state of the xenon ions varies significantly, resulting in a wide range of kinetic energies, increasing linearly with the charge state at a fixed potential difference. This charge-state dependence is reflected by the pulse heights of the analogue output signals corresponding to the detected ions. Typically, the analogue signal is processed by a constant fraction discriminator (CFD), which is unaffected by pulse height; a detailed explanation of CFD will be provided later in this section. At high ion hit rates (> 90 per pulse on average), the simultaneous incidence of two or more ions on the MCP detector results in an output pulse height that cannot be discriminated by the CFD ($\approx$ 1–7% of the counts per pulse), leading to erroneous counting.

In the context of this study, it is crucial to evaluate the analogue signal from the MCP to quantitively assess the charge-state distribution. Consequently, the analogue signal must be adjusted to normalise the varying pulse heights for different charge states of the corresponding ions. The aim is to determine a correction factor for each charge state, which can be applied to the respective ion yield. It is assumed that the pulse height linearly increases when multiple equivalent ions (having the same mass and charge state) simultaneously strike the detector.

In the present study, the bias voltage was set to -100 V throughout the experiment, resulting in a potential difference between the interaction regime and detector of 500 V [99]. This led to relatively low kinetic energies of ions with a low charge state impinging on the detector compared to a related study by Rudek et al. in 2018 [21], where they had a bias voltage of -2500 V[1]. Their study investigated the interaction of xenon with intense hard X-ray pulses and observed charge states as high as Xe^{42+}. The ion hits were identified using a CFD with an increasing threshold for higher charge states to account for the velocity-dependent MCP detection efficiency. To parametrise the velocity dependence of the detection efficiency ϵ, they employed the relation proposed by Sigaud et al. [100]:

$$\epsilon = A \ln(\gamma) + B,$$

where A acts as a scaling constant and B as an offset. The relation is based on the approach of Takahashi et al. [101], using the Lindhard, Scharff, and Schiott (LSS) [102] approximate formula for the electronic stopping power $\frac{\mathrm{d}E}{\mathrm{d}x}$ of ions in solids, possessing kinetic energies on the order of keV. This model is used to characterise the secondary electron emission yield γ generated following the impact of ions (atomic number Z_1) on the MCP surface (atomic number Z_2), which is typically composed of lead glass, a material commonly employed in MCP detectors:

$$\frac{\mathrm{d}E}{\mathrm{d}x} \propto \gamma = \frac{Z_1 Z_2}{\left(Z_1^{2/3} + Z_2^{2/3}\right)} \frac{v}{v_0},$$

where v is the velocity of the ion and v_0 the Bohr's velocity.

---

[1]Private email correspondence with Benedikt Rudek

However, the ion-induced secondary electron emission is generally determined by the contribution of two simultaneously happening processes [103]:

① Potential electron emission (PEE): The partial release of stored potential energy during the neutralisation of the ion, impinging on the MCP detector. In this process, an inner-shell electron from the MCP material tunnels into the ground state of the ion, providing that the ionisation potential of the ion exceeds twice the work function of the MCP material. Subsequently, the inner-shell vacancy in the MCP material relaxes via Auger-Meitner decay, triggering the electron avalance [98, 103–107].

② Kinetic electron emission (KEE): This process is mainly driven by the ejection of electrons from the MCP material due to the impact of the ion, whose kinetic energy supplies the needed energy [100–102, 108, 109].

Fig. 4.14 displays the kinetic (qU), accumulated ionisation potential [43] and total energy of an ion as a function of the charge state.
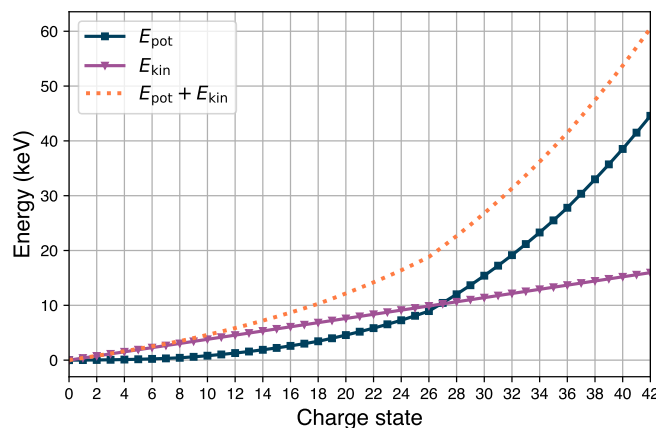
Figure 4.14: Kinetic and potential energy of an ion as a function of charge state.

As of Xe^{27+}, the potential energy surpasses the kinetic energy, leading to new conditions, which are way beyond the condition stated by Baragiola et al. [103] for singly charged ions, that the ionisation potential must be higher than twice the work function of the MCP material to trigger secondary emissions. Lead glass has a work function of 6.3 eV [110], meaning already Xe^+ can trigger PEE. Mróz et al. showed in their calibration procedure for analogue gains of an MCP stack in Chevron configuration by using xenon ions that the charges states Xe^{7+} up to Xe^{15+} are dominated by KEE and beyond Xe^{15+} PEE start to influence the secondary emission of the detector [111]. They could also confirm this with highly charged tantalum ions [112].
Finally, the detection efficiency was determined using an empirical approach [113] rather than estimating it based on the parameters of the MCP. The initial step in systematically examining the MCP response and establishing a compensation method for the charge-state-dependent pulse heights involves extracting the pulse heights of individual pulses using a CFD, as will be detailed in the subsequent section.

Constant fraction discriminator

A CFD is a signal-processing unit commonly used in precise timing measurements to extract the timestamp of an analogue pulse-shaped signal generated by a particle impinging on a detector. These pulse-shaped signals vary in amplitude due to the stochastic nature of the MCP's amplification process but have a common pulse shape and, thus, a constant rise time. The jitter in amplitude makes a threshold triggering of the signal pulse imprecise because of differing trigger times in the temporal course, as shown in panel **a** of Fig. 4.15.
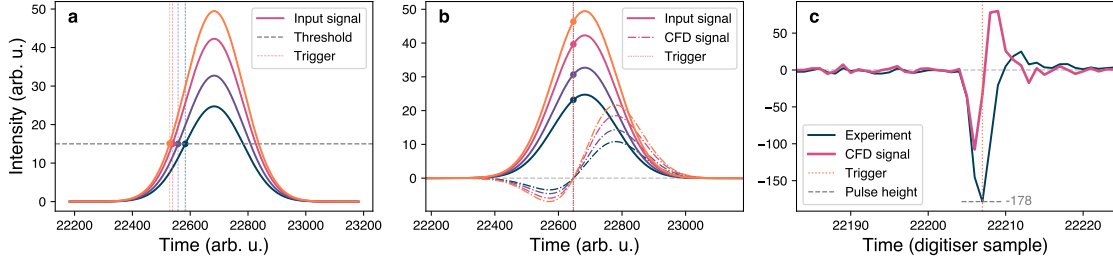
Figure 4.15: Illustration of the operational principles of a CFD. Panel **a** demonstrates threshold triggering, panel **b** depicts constant fraction triggering, and panel **c** presents an example pulse (not inverted) from the experiment alongside the corresponding CFD signal.

Using a CFD, the desired timestamp is triggered at a specific fraction of the pulse's peak height during the temporal evolution when passing a specific threshold set by one of the CFD parameters, as shown in panel **b** of Fig. 4.15. This fraction is constant for all pulses and is a CFD parameter that is set manually. The aim here is to retrieve the timestamp at the peak height of the pulse, which is equivalent to a fraction of 1.

The CFD splits the input signal into two branches: The first branch inverts the input signal and attenuates it by the set fraction. The second branch delays the input signal by the manually set delay parameter. Subsequently, the two signals are summed up, and the temporal position of the combined signal's zero crossing, equivalent to the desired timestamp (s. Fig. 4.15), is extracted by outputting a logic pulse. Panel **c** of Fig. 4.15 shows a single pulse of an ion impinging on the detector and the triggering of the timestamp and pulse height by the used software CFD. The delay parameter (= 1 digitiser sample) is selected so that the zero crossing aligns with the maximum of the pulse.

For the CFD to operate correctly, the rate at which the ions hit the detector (count rate) must be small enough to avoid overlapping pulses. Generally, the count rate can be adjusted by reducing the gas pressure (fewer neutral atoms) of the sample gas or by attenuating the intensity of the XFEL pulses (fewer photons) in the interaction zone. When an ion impinges on the detector, a pulse is generated with a fixed number of samples with the full width Δw. No overlap means that the peak heights of two pulses are more than Δw apart. Nevertheless, the CFD is still able to discriminate two pulses which partially overlap if their peak centre is not more than $\frac{\Delta w}{2}$ apart. The next step is to use a software-based CFD to extract the pulse-height distribution (PHD) for the individual pulses within the TOF spectra.

Pulse-height distribution

The PHD comprises the discriminated electronic output signals of the MCP by the CFD in a specific range of flight times. This range can cover the complete TOF spectrum or only the flight times of ions at a selected charge state.
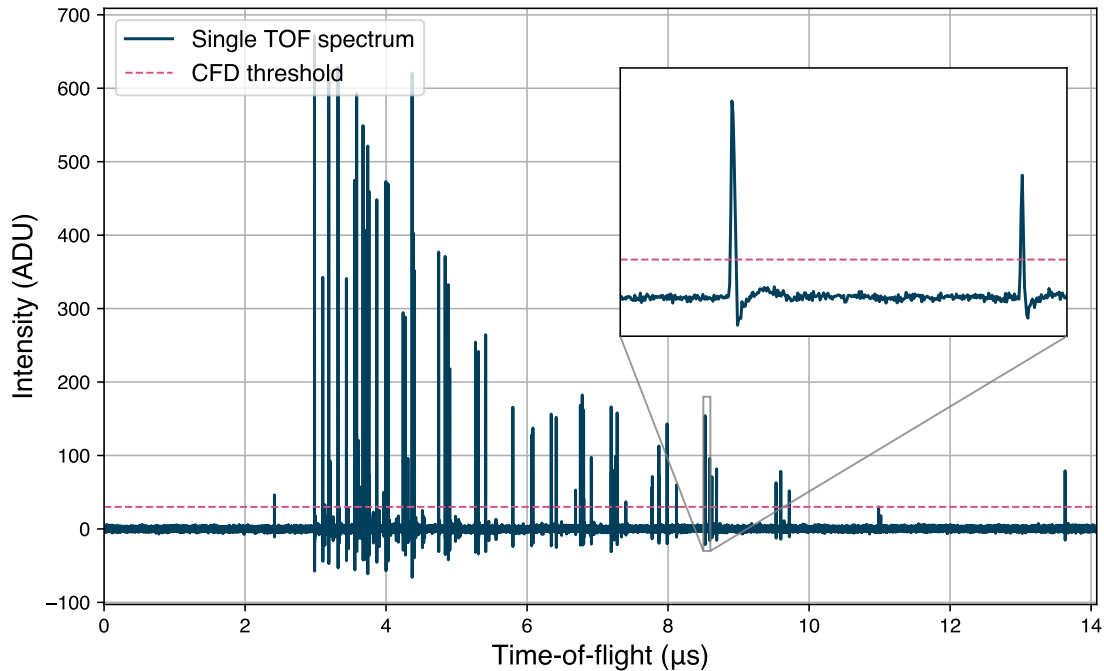
Figure 4.16: TOF spectrum of a single pulse.

Fig. 4.16 illustrates a TOF spectrum generated by a single pulse in dark blue to demonstrate the variation in pulse heights of individual impinging ions within the TOF spectrum. The rose dashed line indicates the pulse-height threshold of the CFD, which must be surpassed for a signal pulse to be registered as a hit.
An increasing trend in pulse height towards shorter flight times is already evident, indicating that higher charge states are associated with higher pulse heights. The inset provides a more detailed view of the pulses corresponding to a specific charge state.
To systematically investigate the PHD, it is suitable to employ a CFD on individual (non-averaged) TOF spectra to extract timestamps and pulse heights. For optimal CFD functionality, a data set with reduced gas pressure was used to ensure operation within the counting mode regime. The gas pressure was sufficiently lowered to minimise the occurrence of non-discriminable pulses, which constituted less than 1‰ of the total counts. Non-discriminable pulses refer to instances where the centres of two peaks are separated by less than $\frac{\Delta w}{2}$. Additionally, the pulses were pre-filtered by pulse energy, utilising only the first 12 pulses of the pulse train. The rationale for this approach will be detailed in Sec. 4.1.7. Following this pre-filtering, a second pulse energy filter was applied to retain only those pulses with energies centred around the peak of the pulse-energy distribution, as illustrated in Fig. 4.17.
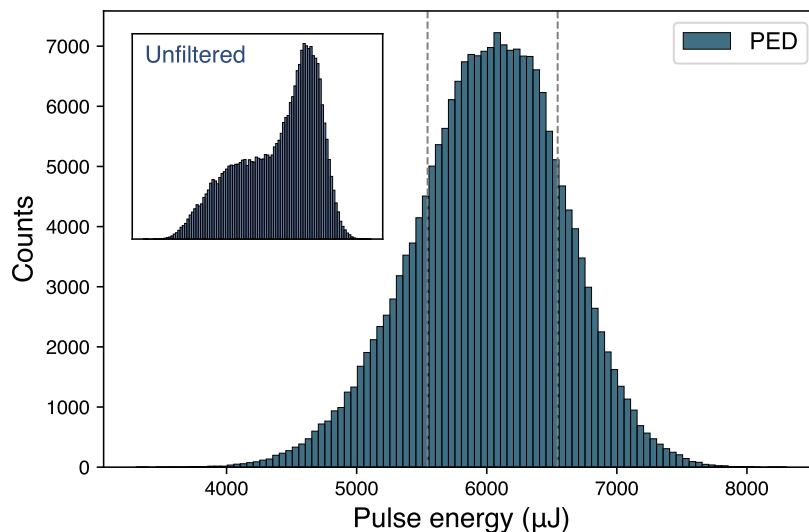
Figure 4.17: Pulse-energy distribution of the data set at low gas density.
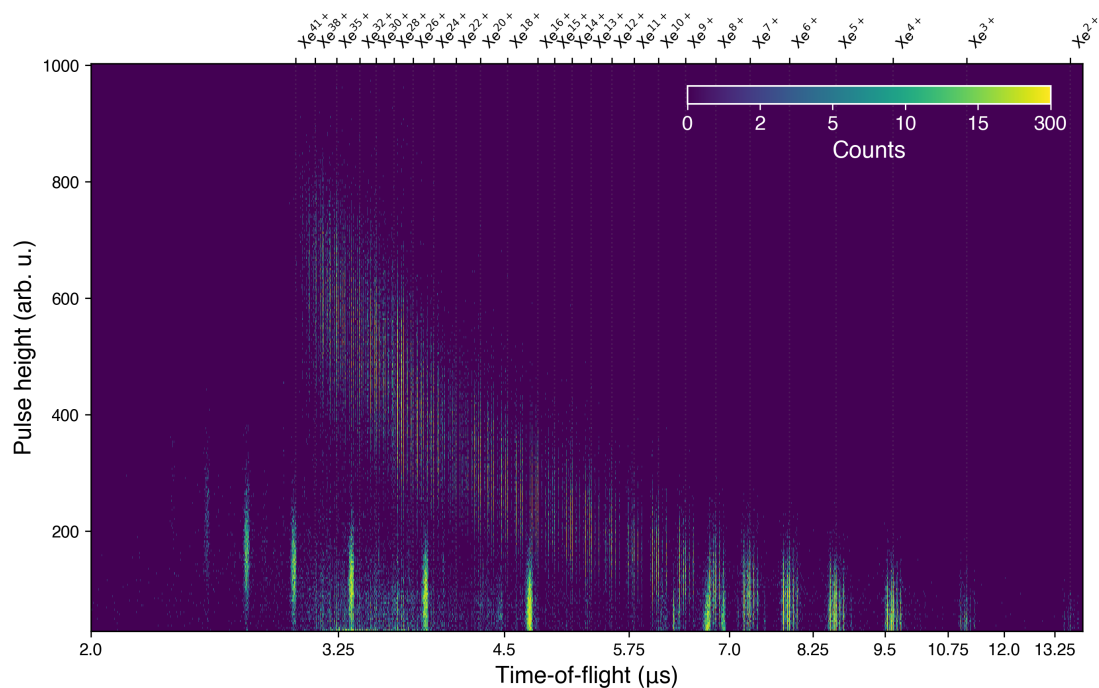
Figure 4.18: PHD as a function of the TOF at a photon energy of 1325 eV at a reduced sample gas pressure to ensure the counting regime. The TOF axis is on a logarithmic axis and the intensity (counts) is compressed to limit the dynamic range for better visualisation. The compression is explained in Sec. 4.5.

Fig. 4.18 displays the colour-coded histogram of the magnitude of the PHD as a function of the TOF for pulse heights slightly above the noise extracted by a software CFD. It has been observed that pulses exceeding a pulse height of 15 exhibit the characteristic pulse shape (s. inset of Fig. 4.16), indicating that pulses below 15 can be excluded from the analysis. Some xenon charge states are marked on the upper x axis to provide a better orientation.

In Fig. 4.18, the centre of gravity of the counts moves towards higher pulse heights as the charge state increases (flight times become shorter) on average. Besides the thin xenon isotope lines, slightly thicker lines are visible at Xe^{8+}, Xe^{16+}, Xe^{24+}, Xe^{32+}, Xe^{40+} and three lines beyond Xe^{41+} with significantly lower pulse heights and belong to the oxygen ions O^{+}, O^{2+}, O^{+3}, O^{4+}, O^{5+} and O^{6+}–O^{8+}. The centres of gravity of the pulse heights of these peaks are also increasing with a higher charge state. These observations indicate that the pulse height depends on the charge state and the mass of the ions.

As of Xe^{25+}, signals emerge above the noise level and increase with the charge state. A valley separates them from the centre-of-gravity signal. The temporal structure is identical to the centre-of-gravity signal, meaning it originates from xenon ions. It will be shown that these signals belong to PEE.

To further investigate this phenomenon, the PHD will be separated by setting a time frame into PHDs of single charge states (Xe^{2+}–Xe^{41+}) at the fixed isotope ^{132}Xe to investigate the properties of the obtained distributions. Isotope ^{132}Xe is the most abundant isotope of xenon, has the second least overlaps for all charge states [Tab. 4.2] and is almost unaffected until the charge states Xe^{30+} [Tab. 4.1] by overlaps.

Fig. 4.19 displays how a PHD of a charge state is extracted. The grey dashed lines in panel **a** represent the limits $\pm\Delta m$ around the isotope peak, where the pulse heights are selected for the charge state PHD. The pink lines represent a selection of randomly chosen single pulses from which the pulse heights are extracted. The dashed dark blue line indicates the average pulse, encompassing all 5301 pulses, for reference.
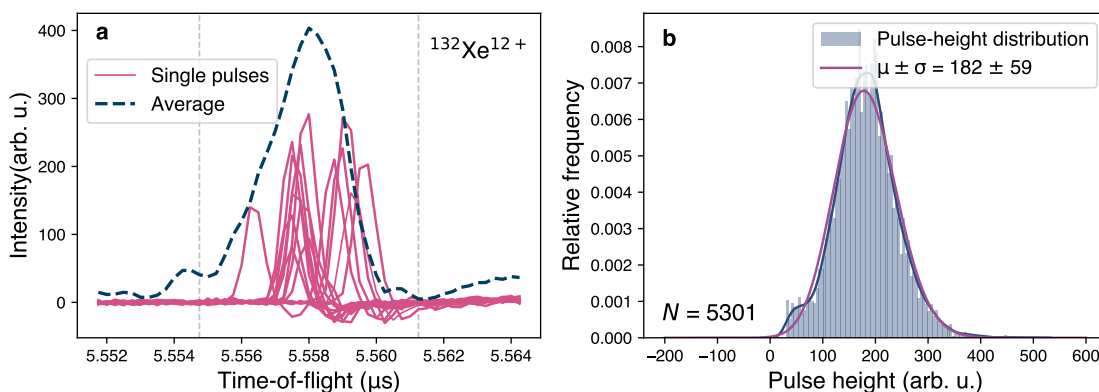
Figure 4.19: TOF spectra and PHD of $^{132}Xe^{12+}$. Panel **a** shows single pulses and the average isotope peak in the limits Δm around the isotope peak. Panel **b** shows the PHD of the isotope in the before-mentioned limits.

Panel **b** shows a histogram of 5301 pulses extracted within the limits marked in panel **a** and a corresponding distribution fit, done using a gamma distribution, where μ represents the mean and σ the standard deviation of the distribution. Similar to the approach by Gershman et al. [114], a two-parameter gamma distribution is appropriate for modelling the distribution of MCP gain because the average number of emitted secondary electrons is almost proportional to the average value of the pulse height [115] and the individual pulse heights are independent of each other. The gamma distribution reflects the probability $P(x)$ of the number of released electrons during the gain cascade of the MCP stack.

$$P(x) = \frac{x^{\alpha-1}\exp(-\frac{x}{x_0})}{x_0^\alpha \Gamma(\alpha, 0)}$$

Γ is the incomplete gamma function, x is the pulse height, x_0 describes the scale and α the shape parameter of the gamma distribution. For $\alpha \to \infty$, the distribution is Gaussian, and for $\alpha \to 1$, it is exponential.

A fit using the gamma distribution was performed for all charge states from Xe^{2+}–Xe^{41+} and for the isotopes $^{129}\mathrm{Xe}$, $^{131}\mathrm{Xe}$, $^{132}\mathrm{Xe}$, $^{134}\mathrm{Xe}$, and $^{136}\mathrm{Xe}$. Subsequently, isotopes exhibiting overlaps were excluded, as detailed in Tab. 4.4. For the charge states Xe^{2+}–Xe^{39+}, an average PHD mean and an average ion velocity are derived by averaging the available isotopes within each specific charge state. These data points can subsequently be employed in a fitting procedure to establish a general correction curve to compensate for each charge state's ion yield.

Isotope	Discarded charge states
$^{129}\mathrm{Xe}$	8, 16, 18, 19, 24, 25, 26, 27, 32, 36, 37, 38, 40
$^{131}\mathrm{Xe}$	25, 26, 27, 33, 40, 41
$^{132}\mathrm{Xe}$	25, 31, 32, 33, 34, 35, 41
$^{134}\mathrm{Xe}$	22, 23, 25, 26, 27, 28, 32, 33, 34, 35, 36, 41
$^{136}\mathrm{Xe}$	17, 19, 20, 22, 23, 26, 27, 28, 32, 33, 34, 35, 36, 38, 39, 40

Table 4.4: Discarded charge states at specific isotopes due to superposition.

Correction curve

For the fitting procedure, the approach by Gilmore and Seah [113] will be used, which relates the mean value of the PHD to the average gain of the MCP assembly as a function of ion velocity:

$$\tilde{\mu} = Av\left(1 - \left(\frac{1}{1+\left(\frac{v}{v_0}\right)^n}\right)^{\frac{1}{n}}\right) + \tilde{\mu}_0. \tag{4.3}$$

The variable $\tilde{\mu}$ represents the ion-induced secondary electron yield of the MCP detector in units of pulse height. The parameter A is a scaling factor specific to each element, while v denotes the ion's velocity, which is proportional to $\sqrt{\frac{q}{m}}$. The parameter v_0 indicates the straight-line threshold, n is a power, and $\tilde{\mu}_0$ serves as an offset, interpreted as the minimum signal response of the MCP assembly detector corresponding to the ion species.

The model proposed by Gilmore and Seah [113], published in 2000 as part of their investigation into ion detection efficiency in static secondary ion mass spectrometry (SIMS), is primarily empirical and lacks a strictly theoretical derivation. This model articulates the ion-induced secondary electron yield (gain) of individual microchannel plates and applies to stacked MCPs configured in a Chevron arrangement, as stacking can be viewed as an extension of the channels.

Through their model, Gilmore and Seah have built upon earlier approaches, including the LSS theory [102], as well as the Parilis-Kishinevskii approximation [108] and its adaptation by Meier and Eberhardt [109] for low velocities. In their work, Parilis and Kishinevskii introduced the concept of a straight-line threshold, v_0, which segments the velocity axis into two regions: a non-linear regime for velocities below v_0 and a linear regime for those above v_0. The linear behaviour exhibited above v_0 has been corroborated by numerous studies investigating MCP detection efficiency [100, 109, 116] and represents a fundamental component of the Gilmore-Seah model. However, the most significant aspect of this investigation lies in the non-linear region below v_0. The model offers greater flexibility compared to the Parilis-Kishinevskii approximation, allowing for the adaptation of detector specifications, such as gain offset and the non-linear increase in gain for low velocities.

In addition to the model by Gilmore and Seah, several other models were also examined in the current investigation. Liénard et al. [117] presented a model in 2005 based on the Parilis-Kishinevskii approach, specifically for Li^+ and Na^+ ions within an ion impact energy range of 0.5 to 7.5 keV. The model developed by Takahashi et al. [101], published in 2011, is based on the LSS formula [102] and is designed for neutral rare gas atoms. A comparable model proposed by Sigaud et al. [100] in 2016 investigated argon charge states up to Ar^{3+} and demonstrated a trend of increasing MCP detection efficiency as a function of charge state. However, none of these models provided a satisfactory fit to the available data, as they only aligned well at high velocities.

Fig. 4.20 illustrates the mean charge-state-dependent PHDs as a function of charge state q in panel **a** and as a function of velocity v in panel **c**. The PHDs and the corresponding fits of all xenon charge states can be found in Sec. A.2. In panel **a**, the means of the PHDs are fitted with a straight line, which reveals significant deviations from the data points, as shown in the residual plot (the difference between data points and the fitted line) in panel **b**, particularly for lower charge states. Panel **c** displays the data points fitted with the model of Gilmore and Seah, which exhibits the most minor deviations among all tested fitting models, as evidenced by the residuals plot in panel **d**. Nonetheless, the residuals in panel **d** demonstrate a periodic rather than a stochastic distribution around zero, indicating unresolved dependencies that could not be elucidated within the scope of this study. The compensation of ion yield for charge states is based on the Gilmore-Seah fit presented in panel **c**.
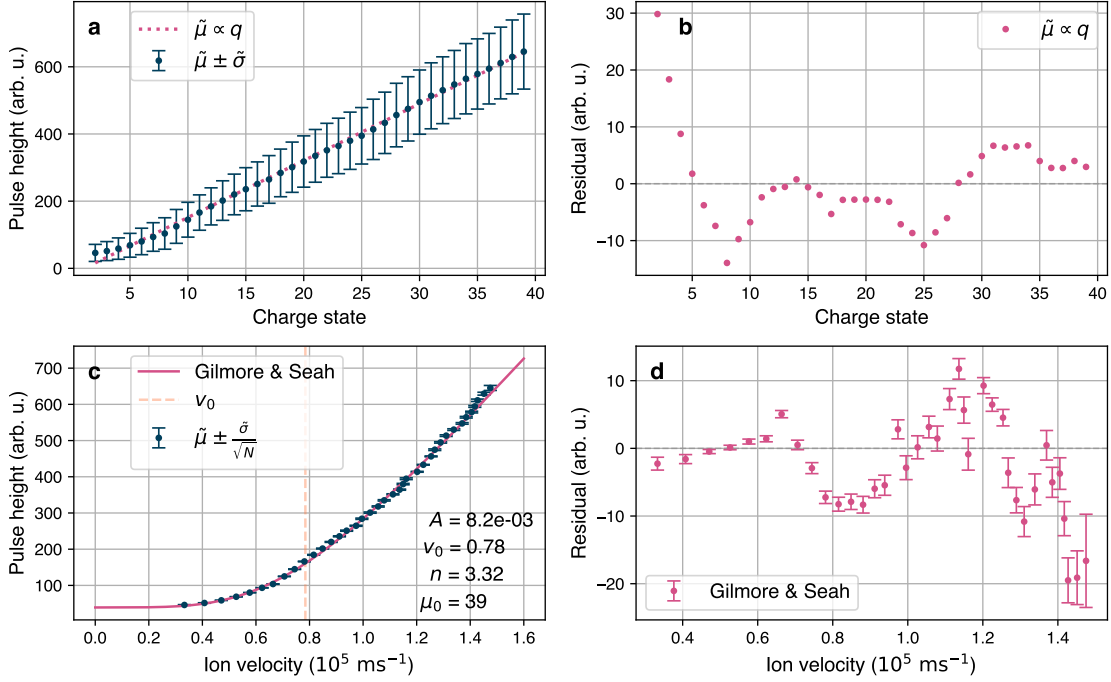
Figure 4.20: PHD means as a function of charge state q (panel **a**) with a straight-line fit and velocity v (panel **c**) with a fit with the Gilmore-Seah model. The fit residuals (deviation between fit and data points) are presented in panels **b** and **d**.

Fig. 4.21 shows, in panel **a**, the integrated ion yields of isotope ^{132}Xe from the TOF spectrum for charge states Xe^{2+}–Xe^{39+} of the corrected analogue signal and the reference digitised spectrum after applying a CFD. The deconvolution algorithm could not be applied to the TOF spectrum due to a low signal-to-noise ratio from reduced gas pressure. Panel **b** depicts the percentage deviation between the corrected and reference spectra. The mean deviation of 10% excludes charge states Xe^{25+} and Xe^{33+} due to their overlapping with oxygen signals.
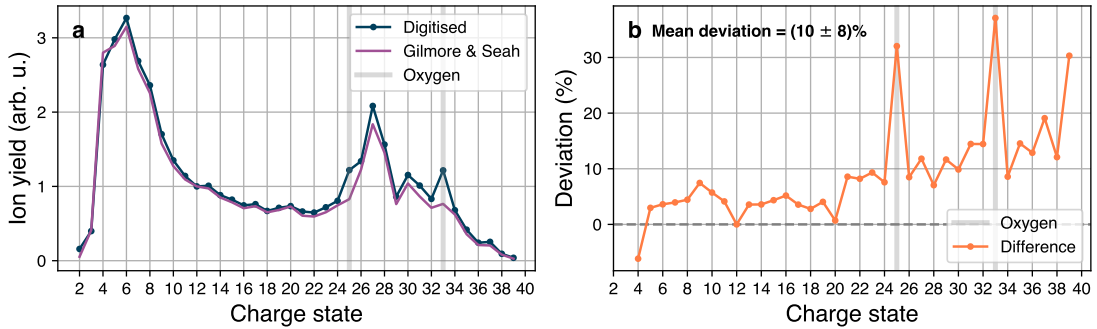
Figure 4.21: Comparison of the corrected analogue ion yield with the counted ion yield.

Potential electron emission

It can be observed that starting from the charge state Xe^{10+}, a secondary distribution emerges above the background noise. This phenomenon could be attributed to the process of PEE, as a reduced number of initial electrons facilitates the occurrence of a secondary electron avalanche following Auger-Meitner neutralisation. Further, this would mean that for charge states below Xe^{10+}, the Auger-Meitner electrons emitted are insufficient to initiate a detectable electron avalanche. Conversely, KEE produces a more significant number of initial electrons, resulting in increased pulse heights [107].
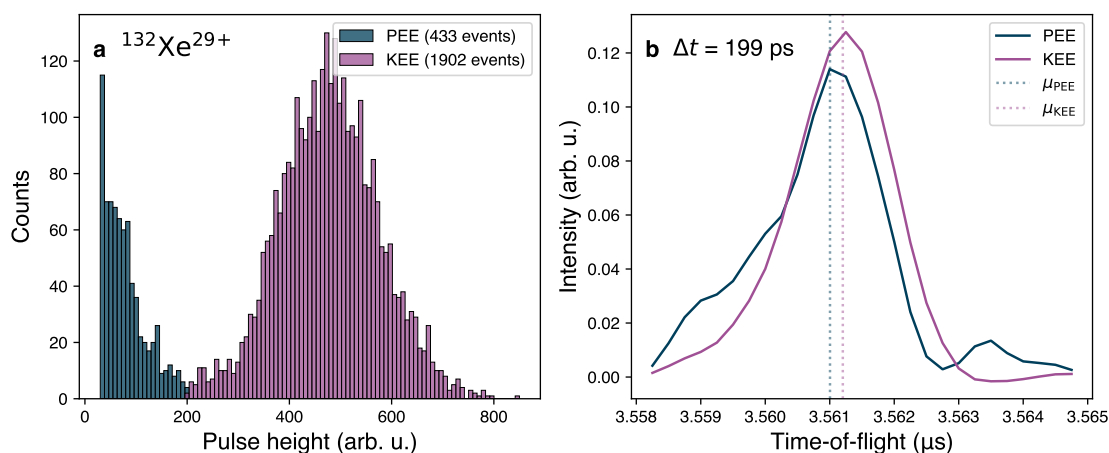
Figure 4.22: PHD histogram separated into PEE and KEE together with the separated TOF signal of $^{132}Xe^{12+}$. Panel **a** shows single pulses and the average isotope peak in the limits Δm around the isotope peak. Panel **b** shows the PHD of the isotope in the before-mentioned limits.

Fig. 4.22 presents the PHD of charge state Xe^{12+} in panel **a**, with distinct colourations to emphasise the contributions of PEE (dark blue) and KEE (purple). Panel **b** illustrates the TOF signal, delineated into PEE and KEE components, revealing that the PEE signal precedes the KEE signals by approximately 200 ps. This observation supports the notion that PEE occurs before ion impact on the surface, indicating that direct physical contact between the ion and the surface is unnecessary [104]. Nonetheless, the time difference is less than the experimental temporal resolution of 250 ps, thus preventing any possibility of double counting of the PEE and the KEE signal. Consequently, this suggests that a pulse generated by an ion can be considered as the sum of PEE and KEE.

Fig. 4.23 illustrates the evolution of the two-component PHD for different charge states. The pulse-height range varies with every charge state to better visualise the structure of the PHDs.
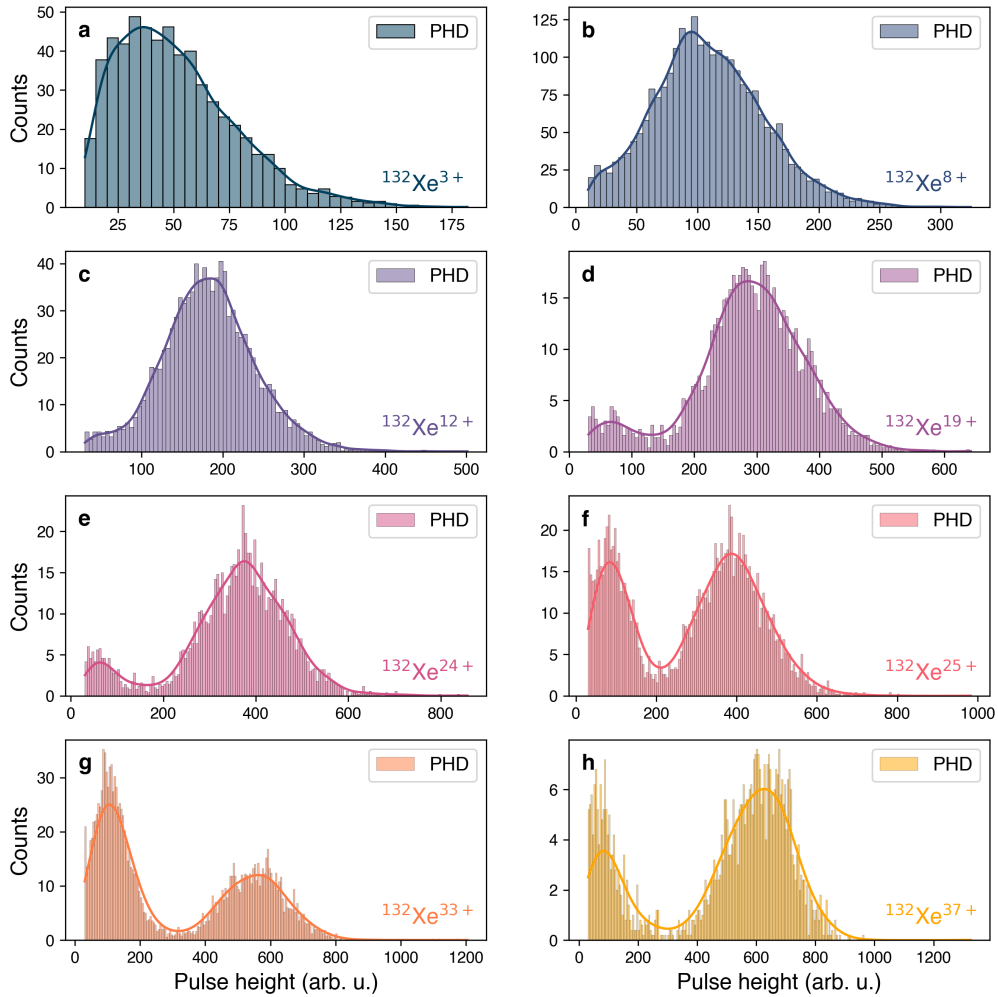
Figure 4.23: PHD of the charge states Xe^{3+}, Xe^{8+}, Xe^{12+}, Xe^{19+}, Xe^{24+}, Xe^{25+}, Xe^{33+}, and Xe^{37+}.

For the charge states Xe^{3+}, Xe^{8+}, and Xe^{12+} in panel **a**–**c**, the PHD seems to consist of one Gaussian-like peak, considered the main peak resulting from KEE, moving to higher pulse heights for higher charge states. As of Xe^{19+} in panel **d**, a small peak arises in the range 0–100 on the x axis, which is considered to result from PEE with a similar number of counts compared to panel **e** and **h**. For the charge states Xe^{25+} and Xe^{33+} in panel **f** and **g**, it can be seen that the first peak has a significantly higher number of counts, which results from the superposition with oxygen since oxygen is lighter than xenon causing a much smaller pulse height.

Similarly to KEE, the mean pulse height of PEE was extracted for the charge states Xe^{10+}–Xe^{39+}. Fig. 4.24 displays the PEE signal as a function of velocity in panel **a** and potential energy in panel **b**. The potential energy is the sum of ionisation energies I_i until the respective charge state q $(E_{\text{pot}}(q) = \sum_{i=1}^{q} I_i)$.
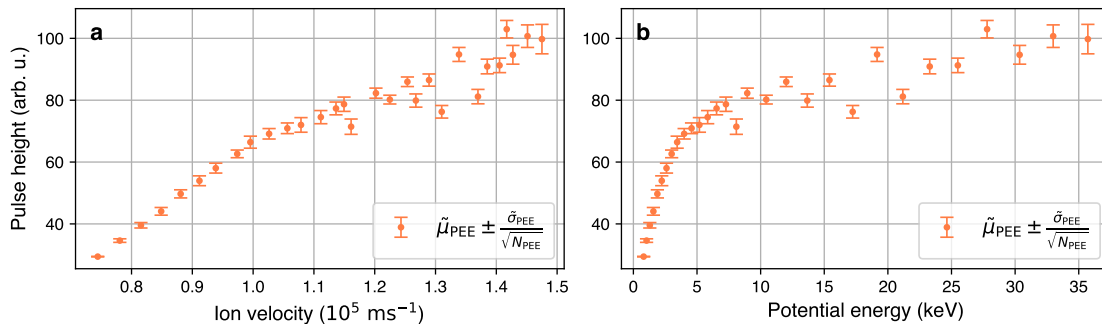
Figure 4.24: Means of the PEE signal distribution as a function of ion velocity and potential energy.

Overall, the PEE signal is small compared to KEE since its pulses are weaker weighted due to the smaller pulse heights. Furthermore, the dependence of the PEE could not be accurately modelled.

Given the ambiguity associated with the PEE signal, only the KEE signal will be used for the correction curve, analogous to the approach taken in Ref. [21], where the distribution below the KEE distribution was discarded by setting a velocity-dependent CFD threshold. Furthermore, fitting exclusively the KEE component results in the lowest deviation of the analogue TOF spectrum from the reference digitised TOF spectrum.

4.1.6 Signal from residual gas

Due to the ultraintense intensities of the XFEL pulses, they inevitably interact with the residual gas (mainly oxygen from water) in the experimental chamber. Since the xenon signals overlap with those of oxygen, it is essential to estimate the contribution of the oxygen background on the xenon ion yields.
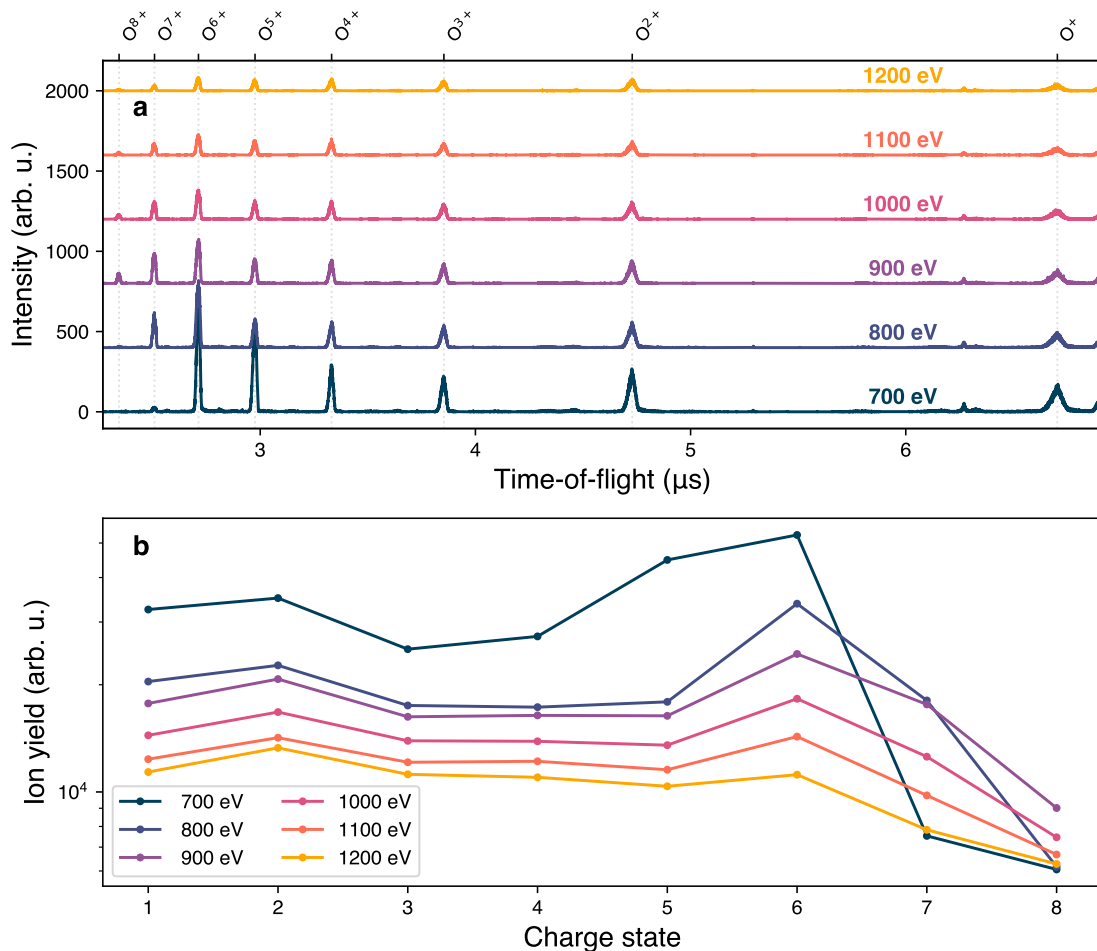
Figure 4.25: Residual gas background at different photon energies. Panel **a** shows the TOF spectrum and panel **b** shows the integrated ion yield.

Fig. 4.25 shows in panel **a** the digitised TOF spectrum of the residual gas in the experimental chamber with the markings of the oxygen charge states O^+-O^{8+}, and in panel **b** the integrated oxygen ion yields as a function of charge state for different photon energies. The variation in oxygen ion yields with photon energy indicates that each TOF spectrum obtained during the photon energy scan exhibits a different background.

Since oxygen has a much lower mass (mass 16 a.u.) than xenon, the PHD at the oxygen peak allows one to estimate the oxygen contribution for every photon energy.

Fig. 4.26 shows the PHDs of the oxygen peaks for the charge states charge states O^+–O^{8+}. The temporal limits of the PHD were set to encompass the complete oxygen peak ($\pm\Delta m$), which includes more than one isotope of xenon, as shown in Tab. 4.5.
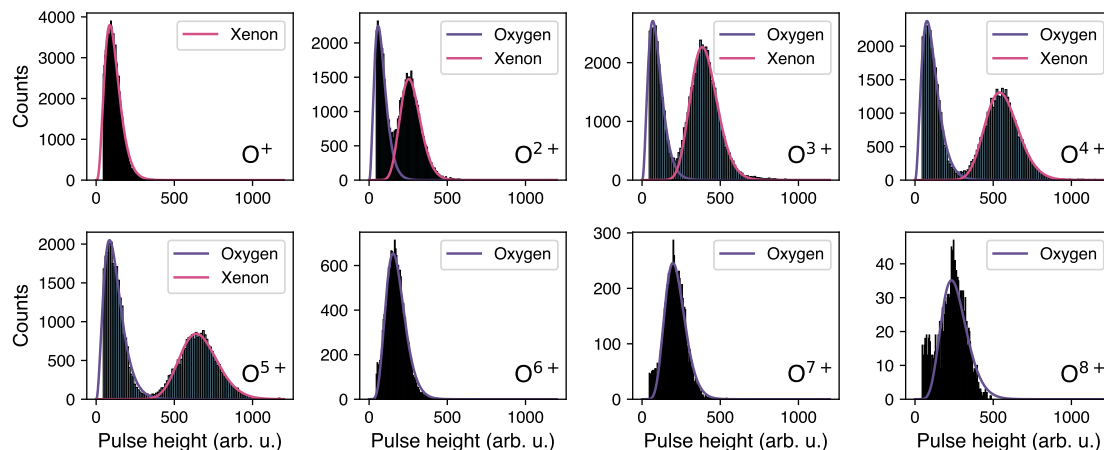
Figure 4.26: PHDs of the oxygen charge states O^+–O^{8+}, which span more than one isotope of xenon at the photon energy of 1325 eV.

	$^{16}O^+$	$^{16}O^{2+}$	$^{16}O^{3+}$	$^{16}O^{4+}$	$^{16}O^{5+}$
^{128}Xe	8+ (1.00)	16+ (1.00)	24+ (1.00)	32+ (1.00)	40+ (1.00)
^{129}Xe	8+ (0.26)	16+ (0.26)	24+ (0.26)	32+ (0.26)	40+ (0.26)
^{130}Xe	-	-	-	-	41+ (0.13)
^{131}Xe	-	-	-	33+ (0.28)	41+ (0.86)
^{132}Xe	-	-	25+ (0.05)	33+ (1.00)	41+ (0.42)
^{134}Xe	-	-	25+ (0.52)	-	-
^{136}Xe	-	17+ (1.00)	-	34+ (1.00)	-

Table 4.5: Superposition of the seven xenon isotopes with oxygen.

While oxygen and xenon manifest as distinct peaks in the PHD as of O^{2+}, accurately isolating the oxygen contribution proves challenging because the PEE occurs within the same pulse-height range. This issue was substantiated by comparing the integrated oxygen mass-over-charge peaks in the background TOF spectrum with the integrated contributions in the PHD of a xenon TOF spectrum, both recorded at a photon energy of 1200 eV. Fig. 4.27 illustrates a comparison of the two methods, revealing a notable discrepancy. Consequently, the isolation of oxygen peaks in the PHD as a means of estimating the oxygen contribution is deemed unsuitable.
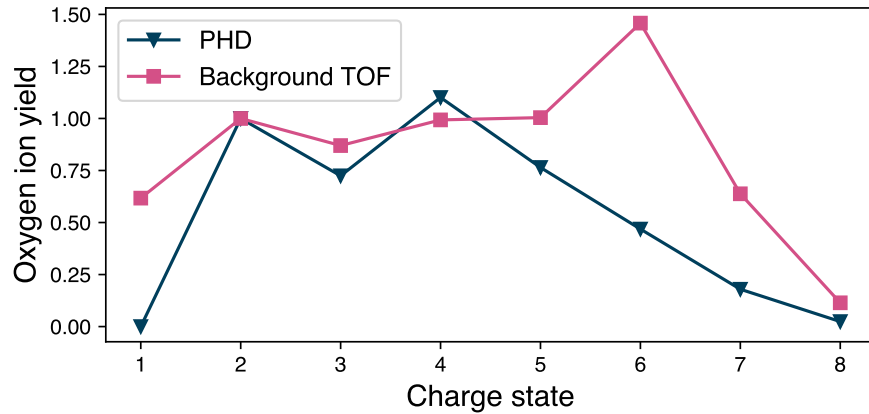
Figure 4.27: Comparison of the integrated oxygen ion yield from the background TOF spectrum with the oxygen contribution in the PHD of a xenon TOF spectrum at the photon energy of 1200 eV.
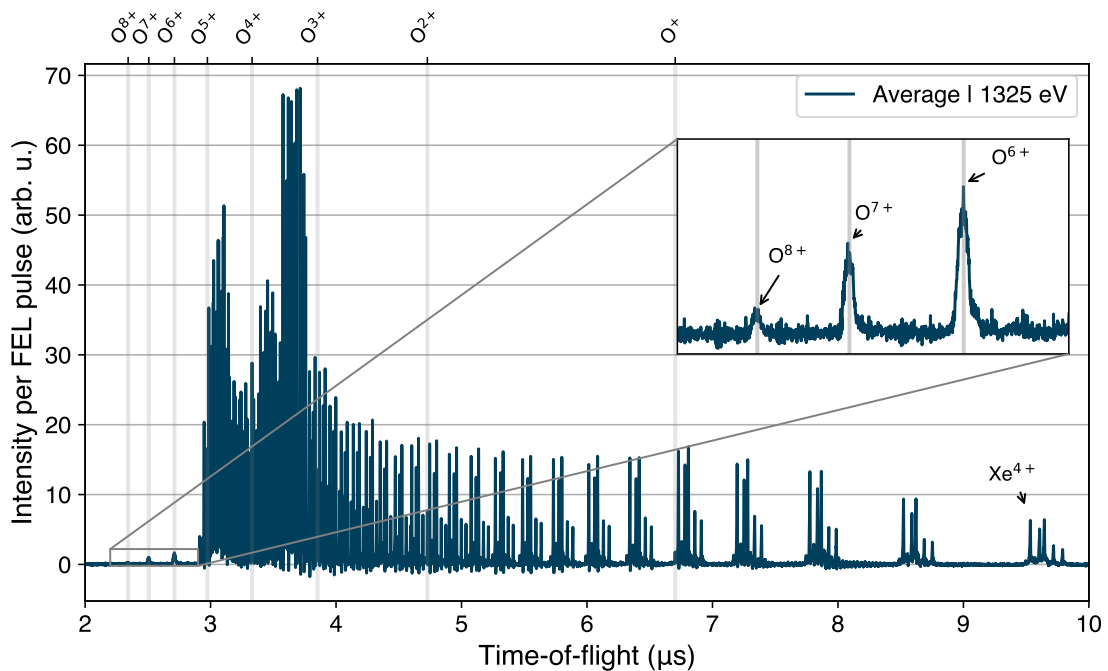
Figure 4.28: Truncated average analogue TOF spectrum with highlighted oxygen peaks.

Fig. 4.28 shows a truncated (2-10 µs) TOF spectrum with markings of all possible oxygen charge states O^+-O^{8+} to illustrate the superposition with the isotope peaks of xenon. With the hypothetical TOF of the highest possible charge state isotope $^{128}Xe^{44+}$ of 2.83 µs and with the flight time of O^{6+} of 2.71 µs, the charge states O^{6+}–O^{8+} in the inset are not relevant for the analysis as no superposition takes place. Further, the charge states O^+ and O^{2+} do not significantly contribute to the xenon TOF spectrum for all photon energies nor interfere with the deconvolution algorithm. Consequently, only the charge states O^{3+}–O^{5+} are of concern, as they

affect the deconvolution procedure.

For a pragmatic estimation, the contribution of oxygen in the PHD of isotope ^{132}Xe for the charge states Xe^{25+}, Xe^{33+}, and Xe^{41+} were used as isotope ^{132}Xe is the centre of the isotope pattern and exhibits the highest abundance. The contribution of the PEE in the oxygen peak was estimated by using the PEE-to-KEE ratio of the PHD of isotope ^{132}Xe at the precursor charge states Xe^{24+}, Xe^{32+}, and Xe^{40+} as they do not overlap with those of oxygen. Subsequently, the PEE contribution at the charge states Xe^{24+}, Xe^{32+}, and Xe^{40+} will be subtracted from the oxygen contribution of the PHD at the charge states Xe^{25+}, Xe^{33+}, and Xe^{41+}. Finally, the ratio of the adjusted oxygen contribution to that of the isotope ^{132}Xe contribution will be subtracted from the ion yield of the charge states Xe^{25+}, Xe^{33+}, and Xe^{41+} for each photon energy.
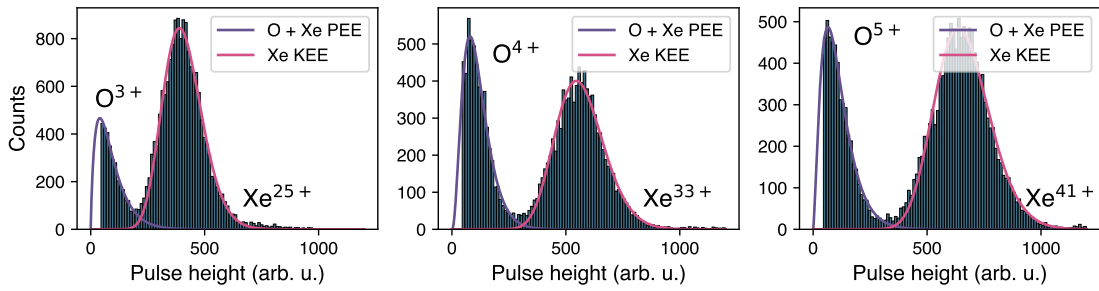
Figure 4.29: PHDs of isotope ^{132}Xe for the charge states Xe^{25+}, Xe^{33+}, and Xe^{41+}.

In conjunction with applying the deconvolution algorithm and compensation for the charge-state-dependent pulse heights, the oxygen correction enables the precise extraction of ion yields for each charge state. Consequently, the grouped ion yields for each charge state will be called charge-state distribution (CSD).

4.1.7 Pulse-energy dependence

It was observed that within the pulse train, the average pulse energy varies considerably, and pulses with comparable average pulse energies exhibit significant differences in ion yield. Fig. 4.30 **a** displays the CSDs derived exclusively from the TOF spectra generated by pulses at positions 5 and 32, which have similar average pulse energies. Notably, the two CSDs show marked differences. Panel **b** illustrates the relative deviation between the two CSDs, revealing an average deviation of 25%.
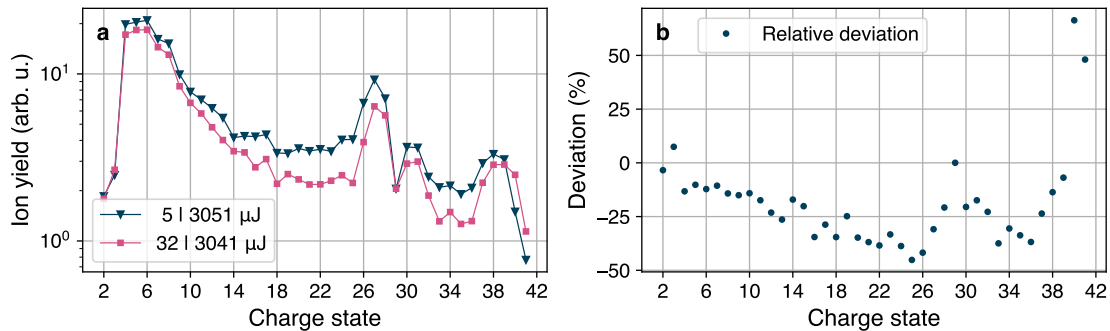
Figure 4.30: CSD of pulses with a similar pulse energy but varying positions within the pulse train at a photon of 1325 eV. Panel **a** compares the CSDs and **b** shows their relative deviation from each other.

This discrepancy is presumed to arise from variations in beam pointing within the pulse train, resulting in fluctuations in spatial positioning within the experimental chamber and on the mirrors. Such variations can lead to the beam interacting with differing target densities in the chamber, while changes in the mirrors' positioning may alter the focus, thereby reducing the number of photons reaching the chamber. The observed differences in beam pointing stem directly from the stochastic nature of the FEL and may be exacerbated by the specific operational mode employed to achieve ultraintense pulse energies during the experiment.
In the current study of xenon, two XGMs were employed. The first XGM (tunnel) was positioned in the XFEL tunnel before entering the beamline. In contrast, the second XGM (hutch) was installed behind the experimental chamber to assess the pulse energy within the chamber during the experiment. The rationale for employing both XGMs will be elaborated in Chapter 5, Section 5.1.1, and is not essential at this point.
Fig. 4.31 illustrates the correlation between the average pulse energy for both XGMs as a function of pulse position to investigate the pulse-position dependence. The error bars represent the standard deviation of the pulse-energy distribution (PED) at each specific pulse position. The inset presents the same data without error bars and includes additional pagination corresponding to the pulse position. This representation indicates that excluding the first four and the last four pulses (marked in pink in the inset) allows for a linear correlation to be established within the error margins.
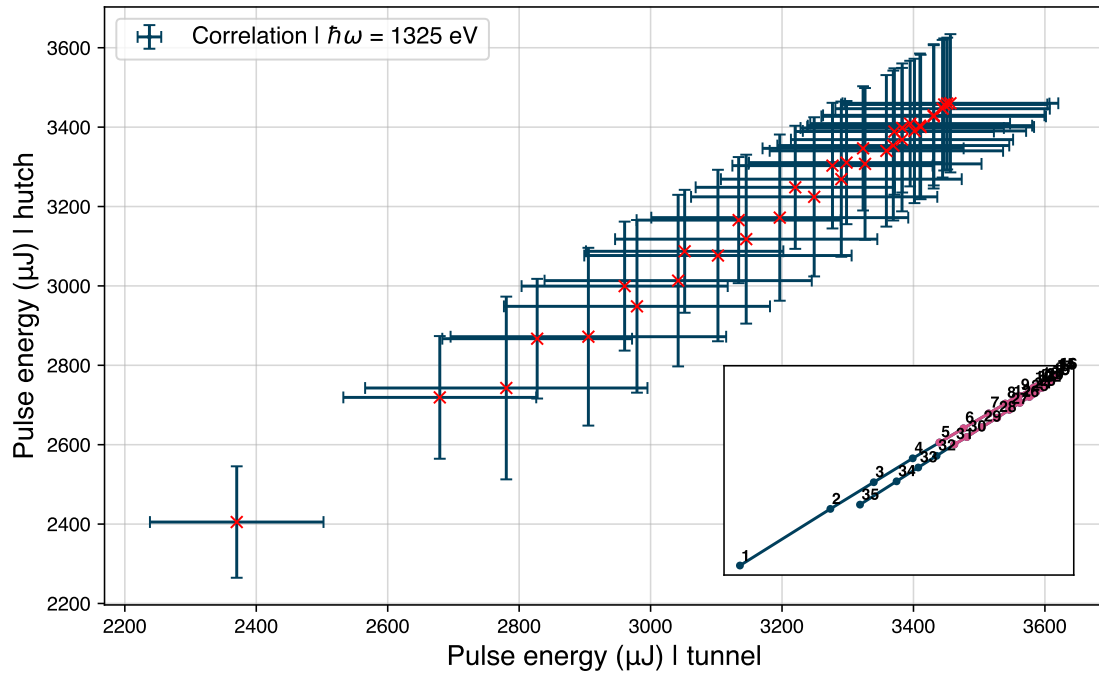
Figure 4.31: Correlation of the tunnel and the hutch XGM.

The pulse energy of the hutch XGM was obtained from the electrode signal after background subtraction similar to the TOF signal, as illustrated in Fig. 4.32, which was recorded for each pulse. The initial peak of the signal, indicated by the pink cross, exhibits a linear relationship with the pulse energy and is used for the correlation plot following the normalisation of the signal to the average pulse energy of the tunnel XGM. During the experiment, the slow signal of the hutch XGM was used, which is an average over several seconds. This slow signal is calibrated, whereas the fast signal is not.
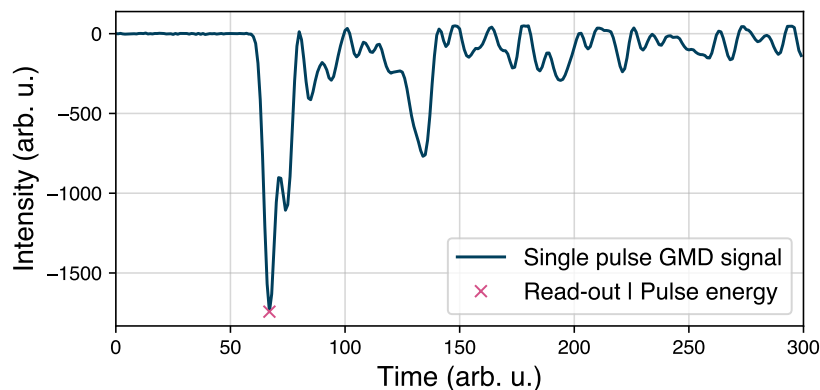
Figure 4.32: Electrode signal of the hutch XGM.

The linear correlation regime between the two XGMs is reached by considering only those pulse positions of the pulse train where the average pulse energy falls within the range of plus or minus one standard deviation around the median of the

average PED within a given pulse train. This filtering is illustrated in panel **a** of Fig. 4.33 and is applied to all pulse trains for every photon energy of the scan. For every photon energy, this leads to a different overall PED, as shown in panel **b**, which takes on a Gaussian-like shape.
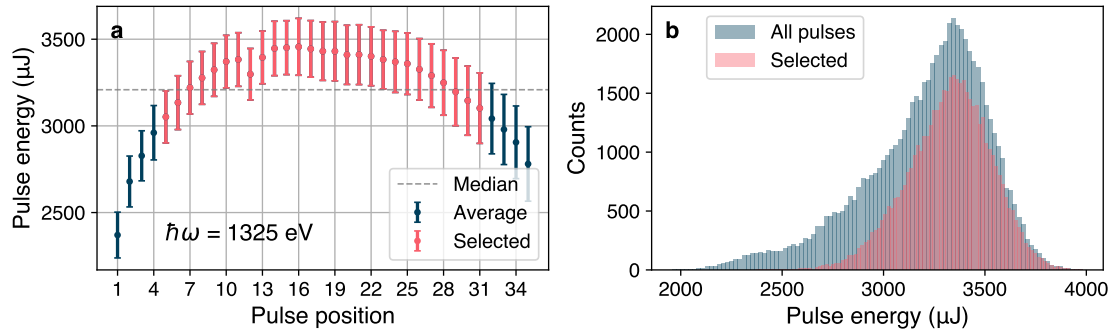
Figure 4.33: Pulse-position filtering applied to **a** the average pulse energy as a function of pulse position within the train and **b** the PED.

Following pulse-position filtering, the PED is segmented into distinct bins of pulse energies, from which a CSD is generated, to achieve finer data points for each photon energy rather than a single data point for all photon energies, as shown in Fig. 4.34. The individual pulse energies of the PED can be converted into the corresponding number of photons. The binning process aims to ensure that specific bins of the translated PEDs for different photon energies overlap or come as close as possible to one another. The nearest bins for a specified number of photons can be selected to maintain a constant number across all photon energies.
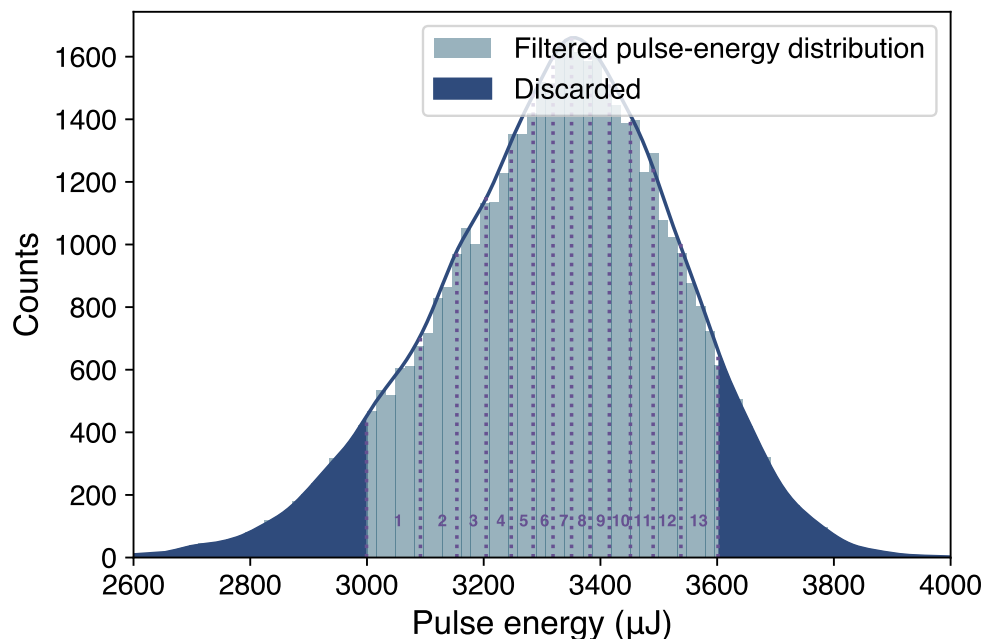
Figure 4.34: Binning of the pulse-energy distribution.

For the binning process, each bin incorporates a fixed number of spectra rather than an equidistant pulse-energy range. The latter approach could result in bins with excessively large spectra counts and others with insufficient counts. Due to the PED's Gaussian-like profile, the bins naturally become narrower in the pulse-energy range towards the centre, reducing the pulse-energy spread. Only the distribution's tails must be excluded, as their encompassing pulse-energy range is too broad to assign a single pulse energy reliably.

One essential question is the requisite number of pulses per bin necessary to produce a CSD whose sample mean approaches the true mean. This question will be approached by investigating the ion yield of the charge state Xe^{12+} as a function of the number of included TOF spectra, as illustrated in Fig. 4.35. It was determined that including 800 pulses represents a reasonable compromise between the available recorded pulse count and a stochastically stable average value.
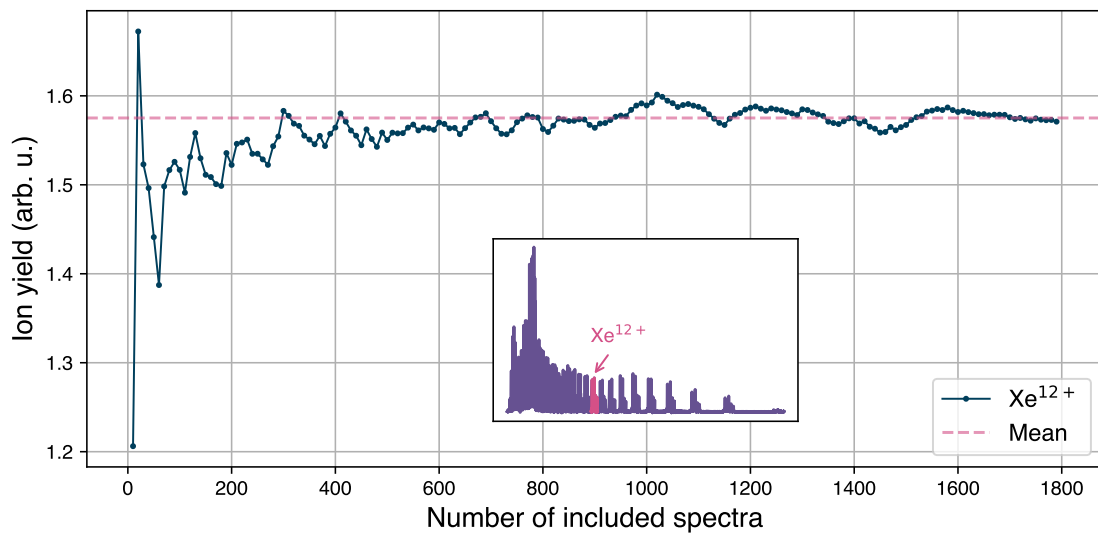
Figure 4.35: Ion yield of Xe^{12+} as a function of the number of included TOF spectra.

4.1.8 Error estimation

To account for random fluctuations of the ion yield and a possible drift of the beam affecting the ion yield, the bin size of included shots is extended to 3200 spectra. This yields four different CSDs for a pulse-energy bin. The standard deviation of the four values defines the statistical error ΔY_{stat}. The systematic error ΔY_{sys} comprises three parts:

① **Deconvolution error**

② **Ion-loss estimation**

③ **Pulse-height dependence correction error**

Deconvolution error

The deconvolution error will be estimated based on the deviation between the input of a modelled xenon TOF spectrum, characterised by known ion yields, and its corresponding output.

For the sake of simplicity, the peaks will be approximated as Gaussian distributions. The centres of the isotope peaks, denoted as μ, and their standard deviations, σ, vary with TOF and must be modelled as functions of the isotope mass m and charge state q. The experimentally determined integration limit of $\pm\Delta m$ from the centre encompasses approximately 45% of the peak's area; thus, $2\Delta m$ accounts for 90% of the total peak area. In the context of a Gaussian distribution, Δm corresponds to 1.645σ. Moreover, Δm is a function of m and q and can be calculated using the calibration parameters k' and t_0 [Sec. 4.1.2].

$$\sigma = \frac{\frac{k'}{\sqrt{q}}\left(\sqrt{m+\Delta m}-\sqrt{m}\right)}{1.645} \text{ and } \mu = t_0 + k'\sqrt{\frac{m}{q}}$$

The amplitude A of an isotope peak with mass m is determined by the relative abundance of the corresponding isotope, multiplied by the ion yield $Y(q)$ associated with the respective charge state.

Fig. 4.36 illustrates the distribution of the seven most prevalent isotopes of Xe^{12+} in counting mode. To derive the relative abundances, the individual isotope peaks are integrated, with their sum normalised to one. This process necessitates the integration of the digitised TOF spectrum, as ion hits on the detector generate ringing that does not cancel out in the average analogue signal. However, this is mitigated through the deconvolution procedure in the analysis (see Sec. 4.1.4).

A quantitative comparison of the isotope distributions between Ref. [118] and the experimental data is presented in Tab. 4.6, demonstrating a good agreement. The error bars represent the standard deviation of the integrated peaks, assuming a Gaussian distribution.

With A_x as the relative abundance of an isotope, the xenon isotope distribution at charge state q can be modelled as follows:

$$Y(q) \cdot \sum_{x \in \text{isotopes}} A_x \cdot \text{Gaussian}[\mu(m_x, q), \sigma(m_x, q)].$$
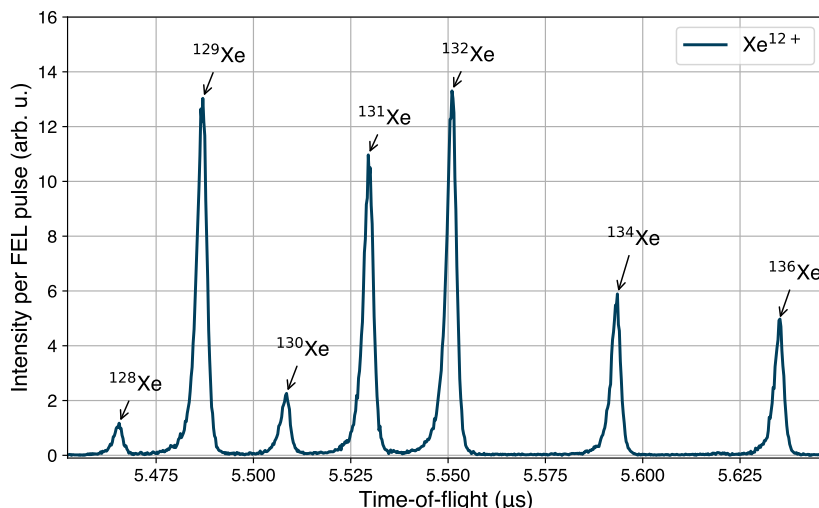
Figure 4.36: Isotope distribution of Xe^{12+} at 1300 eV with a pulse energy of 1.9 mJ in counting mode to determine the experimental isotope abundances within the isotope distribution of xenon.

Isotope	Literature [118]	Measurement
^{128}Xe	1.9%	2.1±0.1%
^{129}Xe	26.5%	26.0±0.6%
^{130}Xe	4.1%	4.3±0.1%
^{131}Xe	21.2%	21.3±0.5%
^{132}Xe	27.0%	26.4±0.6%
^{134}Xe	10.4%	10.8±0.3%
^{136}Xe	8.9%	9.1±0.2%

Table 4.6: Distribution of the seven most common isotopes of xenon, with both the literature and experimental values normalised to 100%.

The superposition of oxygen complicates the deconvolution process, as the oxygen peaks are not accounted for in the response function. To address this, the oxygen peaks are modelled using the oxygen ion yields obtained from the background scan at 1200 eV. The oxygen peaks are subsequently scaled to ensure that the ion yield of O^{6+} in the modelled spectrum corresponds to that of the O^{6+} in the TOF spectrum at 1325 eV. Moreover, the xenon ion yields $Y(q)$ for the modelled spectrum are adjusted to align with the yields at 1325 eV. Notably, the ion yields for both xenon and oxygen do not account for the pulse-height dependence, as the deconvolution occurs prior to this correction in the analysis; otherwise, the noise would disproportionately elevate lower charge states. Finally, random noise is added to the modelled spectrum to simulate the noise characteristics of a realistic TOF spectrum.
Fig. 4.37 presents the modelled spectrum in panel **a**, which comprises both the xenon and oxygen TOF spectra, while panel **b** depicts the deconvolved modelled TOF spectrum.

Fig. 4.38 illustrates in panel **a** the comparison between the deviations of the experimental input ion yields and the output ion yields extracted from the modelled spectrum. Panel **b** displays the deviation expressed as a percentage relative to the
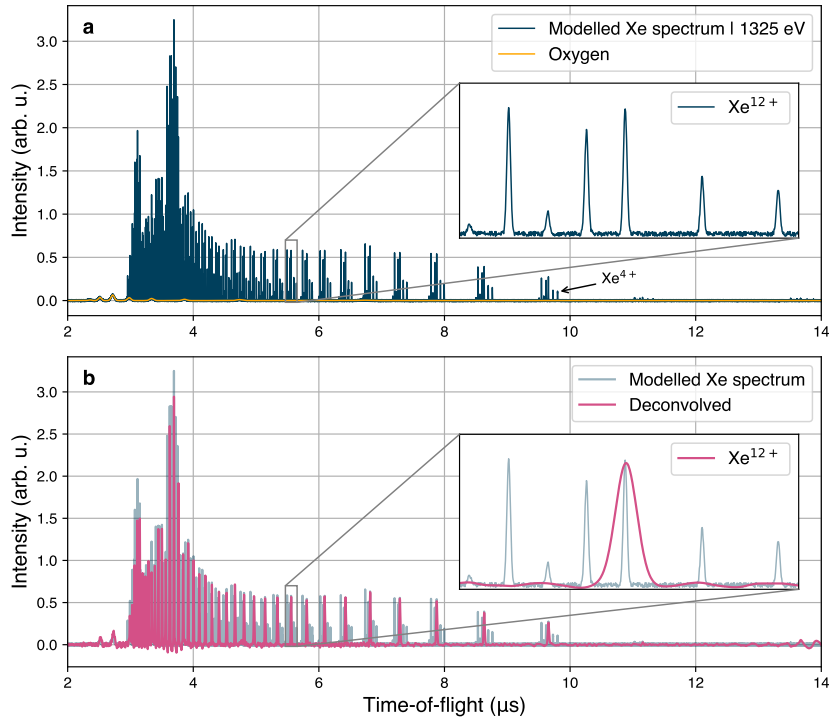
Figure 4.37: Modelled TOF spectrum. **a** Modelled TOF spectrum of xenon, scaled with the experimental ion yields measured at 1325 eV, superimposed with a modelled TOF spectrum of oxygen scaled by the ion yields extracted from the background spectrum at 1200 eV. **b** Deconvolution of the modelled spectrum. The inset in each panel shows charge state Xe^{12+}.

input ion yields. The standard deviation of the ion-yield deviations is 3.2%. Deviations for charge states Xe^{2+}, Xe^{3+}, and Xe^{41+} are omitted due to their substantial deviations of approximately 400%, 45%, and 85%, respectively, attributed to low signal-to-noise ratios at these charge states. The relative deviations constitute the deconvolution error.
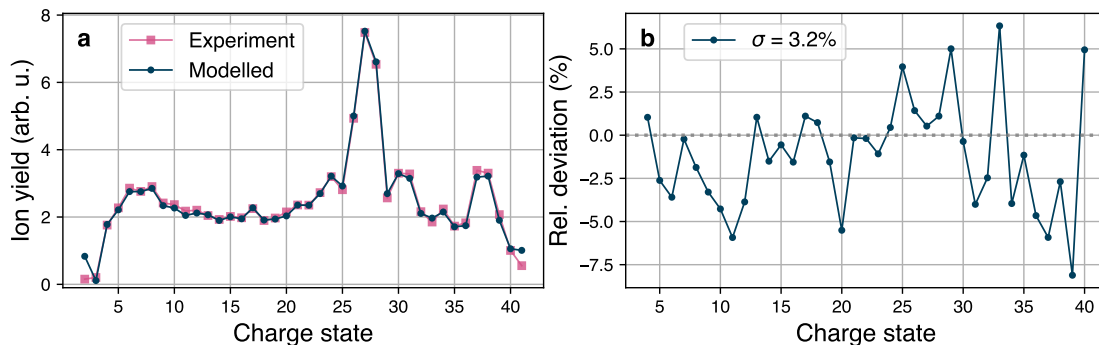
Figure 4.38: Comparison between the experimental input ion yields and the output ion yields from the modelled spectrum.

The signal-to-noise ratio (SNR) is different for each charge state. It depends on the number of covered samples and the pulse-height dependence. The number of samples $N_{\text{samples}}^{(q)}$ covering the full isotope peak with mass m at charge state q spans the interval $[\frac{m - \Delta m}{q}, \frac{m + \Delta m}{q}]$ and can be calculated by using Eq. 4.1:

$$N_{\text{samples}}^{(q)} = \frac{t_2 - t_1}{\delta t} = \frac{1}{\delta t} \cdot \frac{1}{\sqrt{q}} \cdot \frac{\sqrt{m + \Delta m} - \sqrt{m - \Delta m}}{\sqrt{k}} = \frac{N_0}{\sqrt{q}}.$$

δt is the time interval of a single sample and N_0 the number of samples for $q = 1$. Fig. 4.39 illustrates the SNR as a function of charge state, depicted in dark blue. The SNR increases with higher charge states due to the pulse-height dependence. However, this SNR requires correction for the decreasing number of samples for higher charge states. This correction is achieved by multiplying the SNR by $\sqrt{N}$, depicted in pink. This factor results from resolution scaling with N and noise scaling with $\sqrt{N}$, reflecting the accumulation of additional noise data points. Fig. 4.39 further demonstrates that the SNR is considerably low for charge states Xe^{2+} and Xe^{3+}, which accounts for the significant deviations observed post-deconvolution.
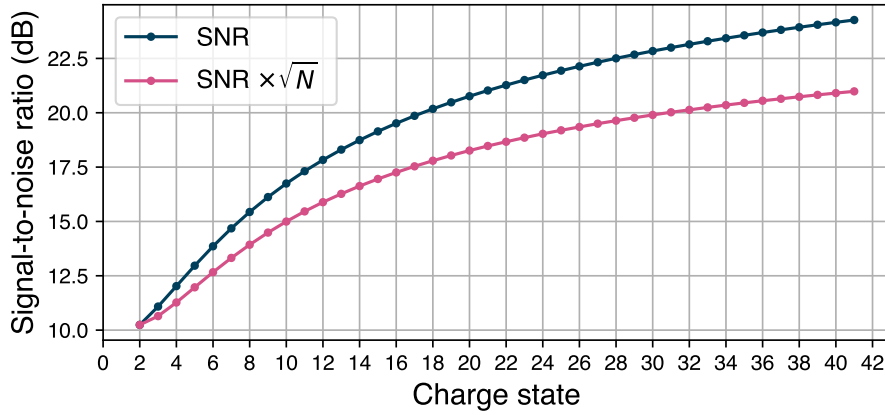
Figure 4.39: Signal-to-noise ratio as a function of charge state

Ion-yield loss

The charge states Xe^{2+}–Xe^{7+} exhibit a distinctive asymmetry in their PHDs, which, as noted by Liénard et al. [117], is attributed to the electronic threshold of the detector acting as a high-pass filter that attenuates low-energy ion signals. This suggests that the actual PHD follows a Gaussian distribution, which appears truncated at zero due to portions falling below the electronic threshold. As a consequence, ions generated below the threshold are not detected, leading to an ion deficiency or loss. It is assumed that this loss could be mitigated by increasing the post-acceleration voltage of the detector, which would enhance the kinetic energies of the ions, thereby resulting in higher pulse heights. However, this hypothesis is untested within the scope of this thesis, leaving the extent of ion loss speculative. Consequently, the subsequent estimation of ion loss, denoted as ΔY_{loss}, will not augment the ion yield but will contribute to the error bars.

To estimate the ion loss beneath the electronic threshold, the PHD is modelled as a Gaussian distribution that extends into negative pulse heights. The area of the extended PHD below zero represents the proportion of ion loss.

To determine the area of the extended PHD, the CFD threshold is adjusted to the lowest possible setting, enabling the collection of all available pulses while minimising noise interference. The unextended PHD is then normalised to one and fitted with a Gaussian distribution, as shown in Fig. 4.40 for the charge states Xe^{2+}–Xe^{9+}. The resulting amplitude, exceeding one, serves as the correction factor for enhancing the ion yield to account for the estimated ion loss.
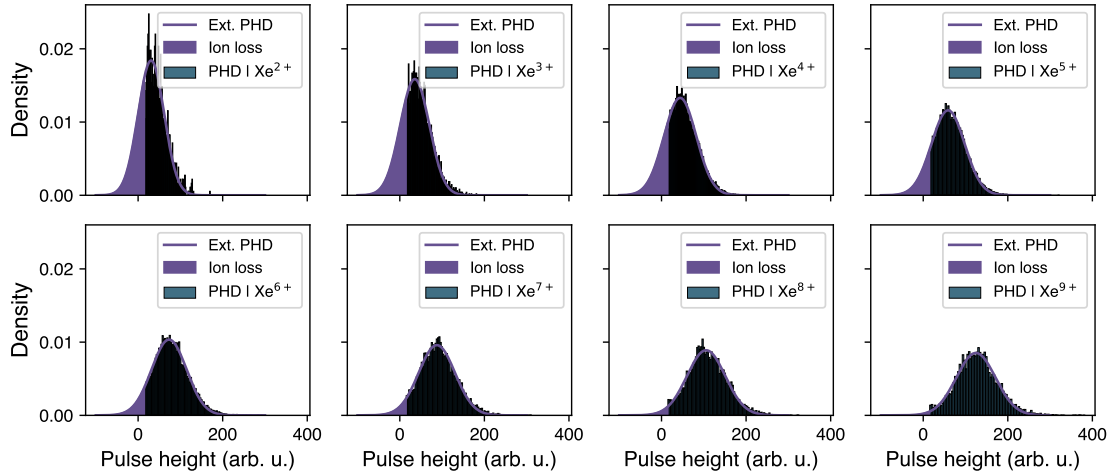
Figure 4.40: Estimation of the ion loss by extending the actual PHD to negative pulse heights.

Fig. 4.41 shows the ion-loss correction factors for the charge states Xe^{2+}–Xe^{9+}. The estimation for Xe^{9+} is one within the error bars, meaning no ion loss. The remaining correction factors for Xe^{2+}–Xe^{8+} are thus used to represent the relative error associated with the ion loss, denoted as ΔY_{loss}. For the remaining charge states $> Xe^{8+}$, the correction factor is one and does not contribute to the overall error.
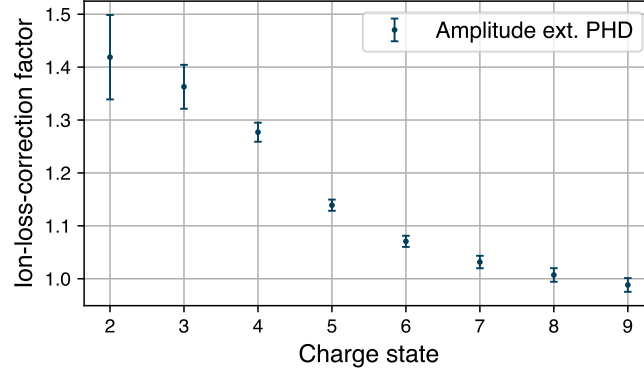
Figure 4.41: Ion-loss-correction factor.

The relative difference between the reference spectrum and the corrected analogue spectrum of the data at low gas density represents the pulse-height correction error, denoted as ΔY_{corr}.

For the estimation of the overall systematic error, it is assumed that all contributions are independent:

$$\Delta Y_{\text{sys}} = \Delta Y_{\text{loss}} + \Delta Y_{\text{corr}} + \Delta Y_{\text{decon}}$$

The overall error estimation reads:

$$\frac{\Delta Y}{Y} = \sqrt{(\Delta Y_{\text{sys}})^2 + (\Delta Y_{\text{stat}})^2}$$

Fig. 4.42 shows the CSD of xenon at 1325 eV with a pulse energy on target of 1.8 mJ and its corresponding errors.
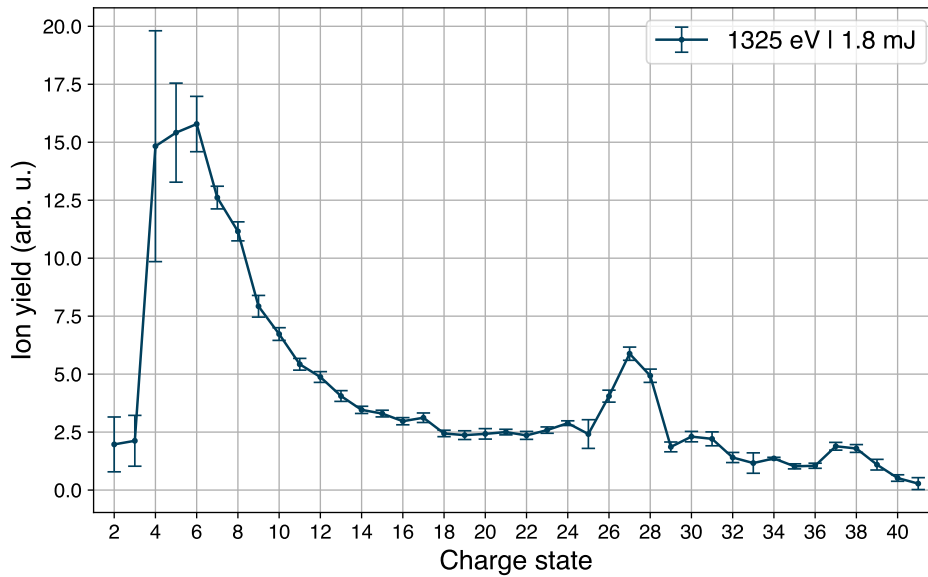
Figure 4.42: CSD with estimated errors at 1325 eV.

4.2 Acceptance length of ion TOF spectrometer

The spectrometer is oriented perpendicular to the beam propagation axis, with its entrance directed towards the beam focus to collect the generated ions. It is crucial to determine whether the spectrometer's acceptance length exceeds the beam's Rayleigh length, as this information is necessary for modelling the fluence distribution in theoretical calculations. If the acceptance length is shorter than the Rayleigh length, the fluence distribution can be approximated as uniform along the beam propagation direction.

To determine the acceptance length, a series of SIMION simulations were conducted by Alberto De Fanis to ascertain the precise positions of the FEL beam and the electronic focusing optics, which are integral to the VMI spectrometer mounted above the interaction point, opposite the ion TOF spectrometer. These two positions are critical in determining the acceptance length of the spectrometer. Generally, differing configurations influence the TOF of the ions. Given that the TOF is known from the experimental data, the objective is to identify the configuration that yields a simulated TOF matching the experimental value. This is achieved by minimising the time difference between simulated and experimental TOF, denoted as t_{sim} and t_{exp}, respectively. Fig. 4.43 presents a colour map of $(t_{\mathrm{sim}} - t_{\mathrm{exp}})^2$ for Xe^{12+} on a logarithmic scale, assisting in the identification of the pair of FEL position and VMI offset that exhibit the minimum. The colour map remains consistent across all charge states. With the values of -7 mm for the VMI offset and -4 mm for the FEL position, the acceptance length is estimated to be ± 1.5 mm.
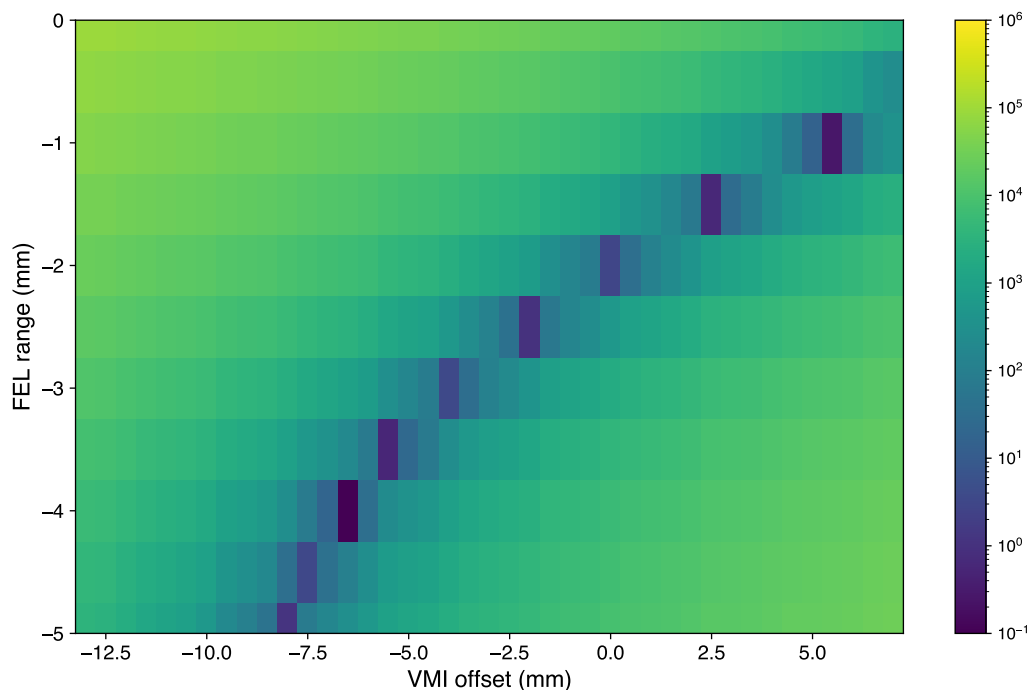
Figure 4.43: Colour map of $(t_{\mathrm{sim}} - t_{\mathrm{exp}})^2$ for different parameters of the SIMION simulation.

4.3 Argon data for fluence calibration

For each xenon, TOF spectrum analysed in Ch. 5, a corresponding argon TOF spectrum was recorded under identical experimental conditions. The argon TOF spectra require analogous evaluation to that of the xenon spectra in order to extract the argon ion yields. Deconvolution is unnecessary, as argon primarily consists of the isotope Ar^{40}. This section outlines the methodologies to evaluate the argon TOF spectra.

To determine the correction curve for compensating the MCP detection efficiency, a dataset for the photon energy 1100 eV, where the highest charge state Ar^{16+} was observed, is used. This dataset was acquired at reduced gas pressure, ensuring optimal operation of the CFD under the same parameters as those employed for xenon. Fig. A.4 in the appendix shows the extraction for all PHD means. Fig. 4.44 presents the PHD means of argon alongside the corresponding fit based on the model by Gilmore and Seah [113].
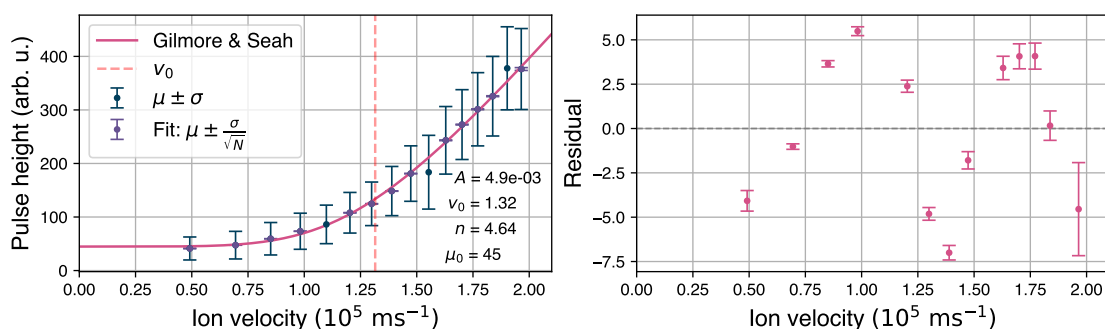
Figure 4.44: Pulse-height dependence of argon as a function of velocity.

The parameters A and v_0 are specific to the element, as the triggered electron avalanche within the MCP detector is dependent on the mass of the ion. In contrast, the parameters n and μ_0 are specific to the detector and exhibit similar values for argon and xenon (see Tab 4.7).

	Argon	Xenon
n	4.64 ± 0.87	3.32 ± 0.07
μ_0	45 ± 4	39 ± 1

Table 4.7: Comparison of the fit parameter for argon and xenon.

In the TOF spectrum, the charge states Ar^{5+}, Ar^{10+}, and Ar^{15+} overlap with the oxygen charge states O^{2+}, O^{4+}, and O^{6+}, respectively, due to identical mass-to-charge ratios. The PHDs for the charge states Ar^{5+} and Ar^{10+} could not be distinctly separated from the contributions of the oxygen ions. Conversely, in the case of Ar^{15+}, the two PHDs are sufficiently separated, enabling the estimation of the ion yield and PHD mean by fitting the combined PHD of Ar^{15+} and O^{6+} with two gamma distributions, as illustrated in Fig. 4.45.
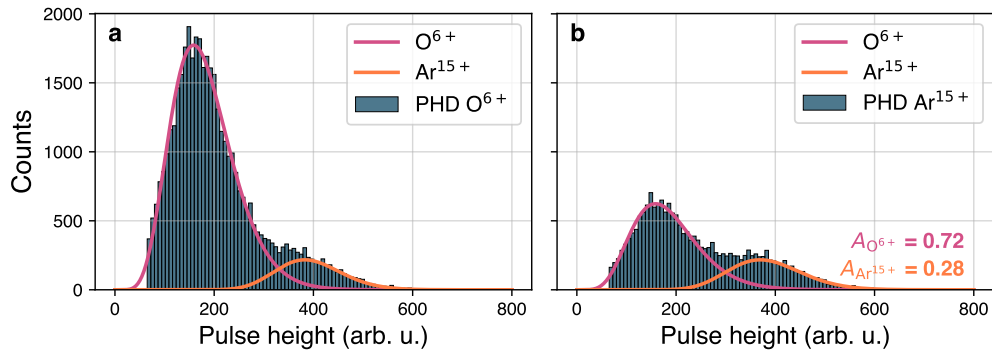
Figure 4.45: Estimation of the ion yield of Ar^{15+}.

In panel **a**, the temporal limits for generating the PHD encompass the entire oxygen peak, providing an initial guess for the fit in panel **b**, where the temporal limits are restricted to the argon peak, which is smaller ($\Delta m = 0.08$ a.u.) than for xenon. The fitted amplitude of Ar^{15+} is normalised to the sum of both amplitudes and represents the correction factor. This estimation is performed for each photon energy at which Ar^{15+} is observed.

Fig. 4.46 shows in panel **a** the pulse-height dependent TOF spectrum of argon and the calibrated argon charge state positions for 1100 eV. Panel **b** shows an example of the final CSD with all corrections applied and the corresponding errors. The error estimation was done analogously to that of xenon.
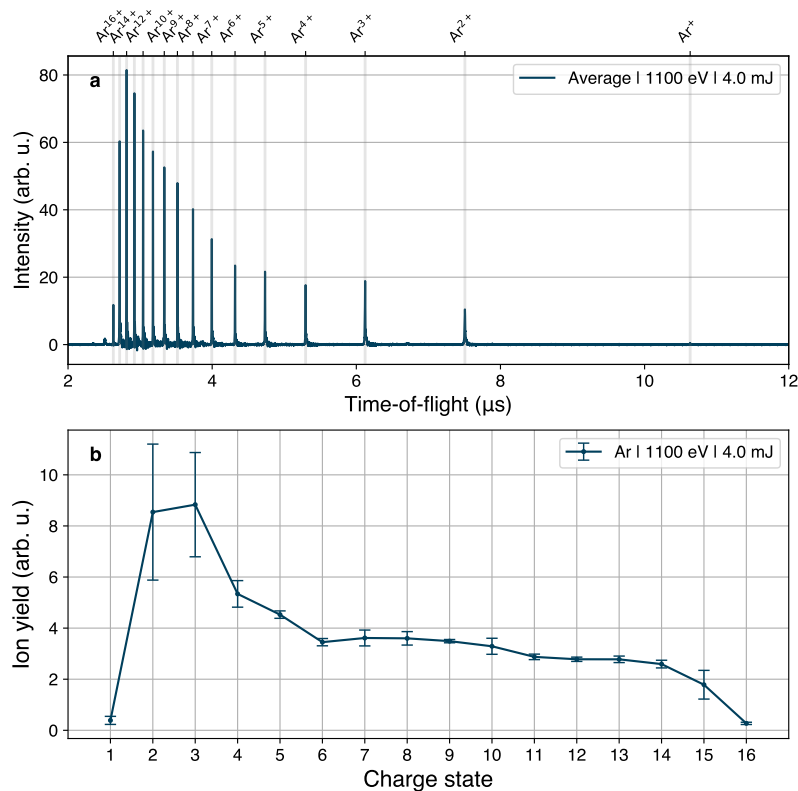
Figure 4.46: Argon TOF spectrum and CSD at 1100 eV.

4.4 Fluence distribution and saturation

Volume integration or volume averaging means weighting the local fluence values occurring in a focused X-ray beam by the spatial distribution in an experiment [119, 120]. To get the full picture of the underlying mechanisms, it is necessary to investigate the nonuniform fluence distribution of the three-dimensional X-ray beam in the focal spot. Since the Rayleigh length is much greater than the effective acceptance length of the spectrometer [Sec. 4.2], the longitudinal dependence (z direction) can be neglected, meaning that the atoms are exposed to the same fluence in the z direction. In polar coordinates, the position-dependent fluence function $F(r; F_0)$ as a function of r in the focal spot is:

$$F(r; F_0) = F_0 \exp\left(-\pi a \frac{r^2}{\Delta^2}\right), \tag{4.4}$$

with $a = \frac{4\ln(2)}{\pi}$, so that the focal size Δ becomes the FWHM of the function [120]. Fig. 4.47 **a** displays an exemplary slice of the two-dimensional fluence function along the beam diameter. The red dot marks the peak fluence, which is important to distinguish from the (local) fluence since it represents the maximum fluence value of the function.
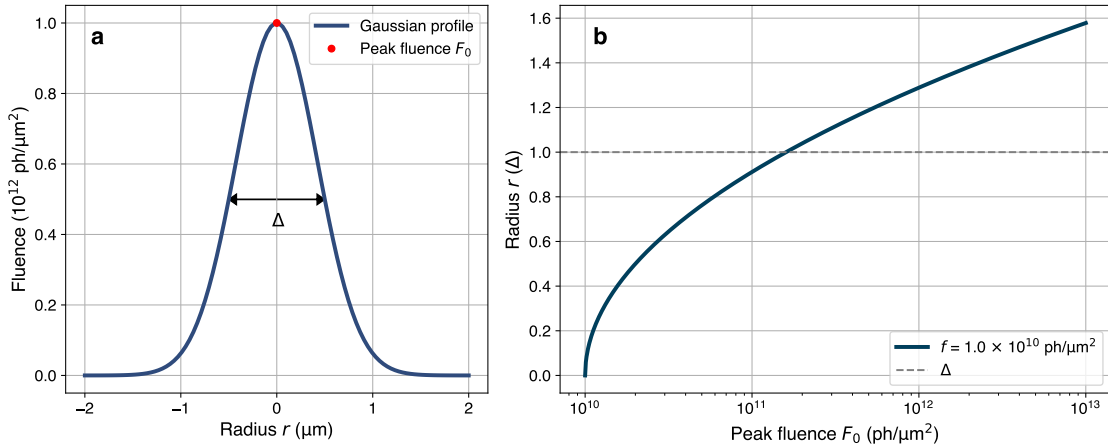
Figure 4.47: **a** Slice of a single Gaussian spatial profile at the waist of the beam ($z = 0$) in polar coordinates. The peak fluence F_0 is 1×10^{12} ph/µm^2 (red dot) and $\Delta = 1$ µm. **b** Radius as a function of peak fluence in units of the focus size Δ. The x axis is on a logarithmic scale.

From Eq. 4.4 the radius r_f of a given fluence f from a fluence function with peak fluence F_0 can be obtained and reads [57]:

$$r_f = \Delta \sqrt{\frac{\ln\left(\frac{F_0}{f}\right)}{\pi a}}. \tag{4.5}$$

Fig. 4.47 **b** displays the radius as a function of the peak fluence F_0 for the fixed and arbitrarily chosen fluence value of $f = 1.0 \times 10^{10}$ ph/µm² in units of Δ. This demonstrates that a given fluence value f moves towards the tail of the beam profile for increasing peak fluences. From theory, it is known that specific charge states are generated in a limited fluence range $[f_1, f_2]$ [57] with $f_1 < f_2$. This is shown in Fig. 4.48 for a fixed photon energy of 1325 eV for different charge states. For lower fluences beyond this range $f < f_1$, a charge state cannot be created since it requires more photons and for higher fluences $f > f_2$, the ion yield of the charge state gets depleted because it becomes further ionised and will reach a higher charge state. Consider an arbitrarily chosen fluence range $[f_1, f_2]$ in a focused X-ray beam exhibiting a Gaussian fluence distribution (Eq. 4.4): When varying the peak fluence F_0, as demonstrated in Fig. 4.47 **b** by using Eq. 4.5, the radii r_1 and r_2 ($r_2 < r_1$) of the fluence range will increase, which is demonstrated in Fig. 4.49 for fluence distributions with different peak fluences and the fluence range of 1-4$\times 10^{10}$ ph/µm², which would correspond to the fluence range in which Xe^{4+} is created, see Fig. 4.48. The annuluses ("hollow disks") covering the identical fluence range are moving away from the beam centre and getting thinner for higher peak fluences. Each beam profile is normalised on the peak fluence and looks the same for better visibility. To find out how the area A of the annuluses, covering the fluence range, change, $F(r; F_0)$ needs to be integrated between the values r_1 and r_2 with the infinitesimal area element $dA = 2\pi r dr$:

$$2\pi F_0 \int_{r_2}^{r_1} dr' \, r' \exp\left(-\pi a \frac{r'^2}{\Delta^2}\right). \tag{4.6}$$

Through a change of variables $r \mapsto f$ by using Eqs. 4.5 & 4.4 to obtain $dr = -\frac{\Delta^2}{2\pi a f r} df$, the integral condenses to:

$$A = \frac{\Delta^2}{a} \int_{f_1}^{f_2} df' = \frac{\Delta^2}{a}(f_2 - f_1),$$

which is independent of the peak fluence F_0. This means that with increasing peak fluence F_0 as long as $f_1, f_2 < F_0$ holds, and the focus geometry stays the same, the fluence range $[f_1, f_2]$ always covers the same area. This is further confirmed by the fluence distribution function shown in Fig. 4.50, showing a histogram of the fluence distribution for different peak fluences, assuming a fixed single Gaussian spatial profile. It becomes clear that an increase in peak fluence F_0 does not change the abundance of lower fluences. In addition, the fluence range 1-4$\times 10^{10}$ ph/µm² used in Fig. 4.49 is indicated to support the meaning of the consistency of the fluence range for different peak fluences.

In combination with the narrow fluence range, where a charge state, for example, Xe^{4+}, is created [Fig. 4.48], the fluence distribution [Fig. 4.50], containing all fluences up to the peak fluence, explain why the volume-integrated ion yield becomes constant above a certain saturation peak fluence. In Fig. 4.51, this is shown for the charge state Xe^{25+}, where the volume-integrated ion yield as a function of peak fluence becomes constant above the peak fluence of 7×10^{11} ph/µm², matching with the right tail of the fluence-dependent ion yield marked with pink crosses. In general, this saturation peak fluence is a function of the photon energy and the charge state and will be further investigated in the next section.
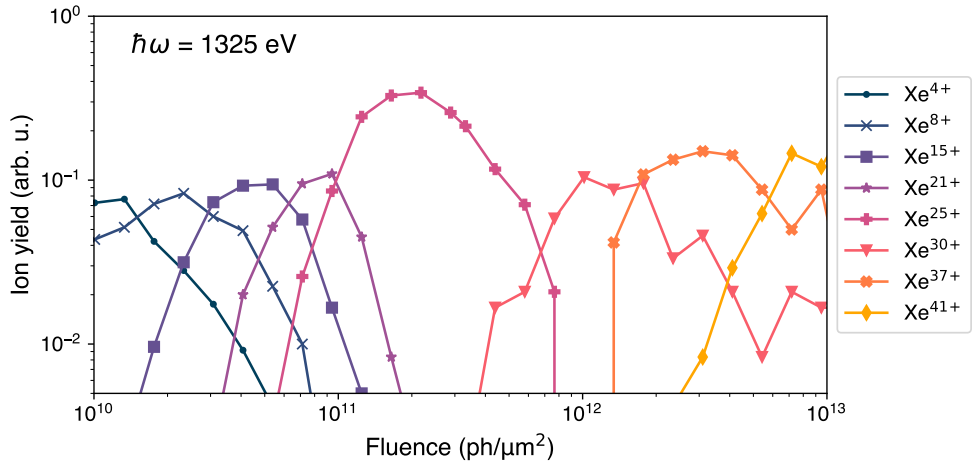
Figure 4.48: Calculated ion yields (without volume integration) for different charge states as a function of fluence at a fixed photon energy of 1325 eV.
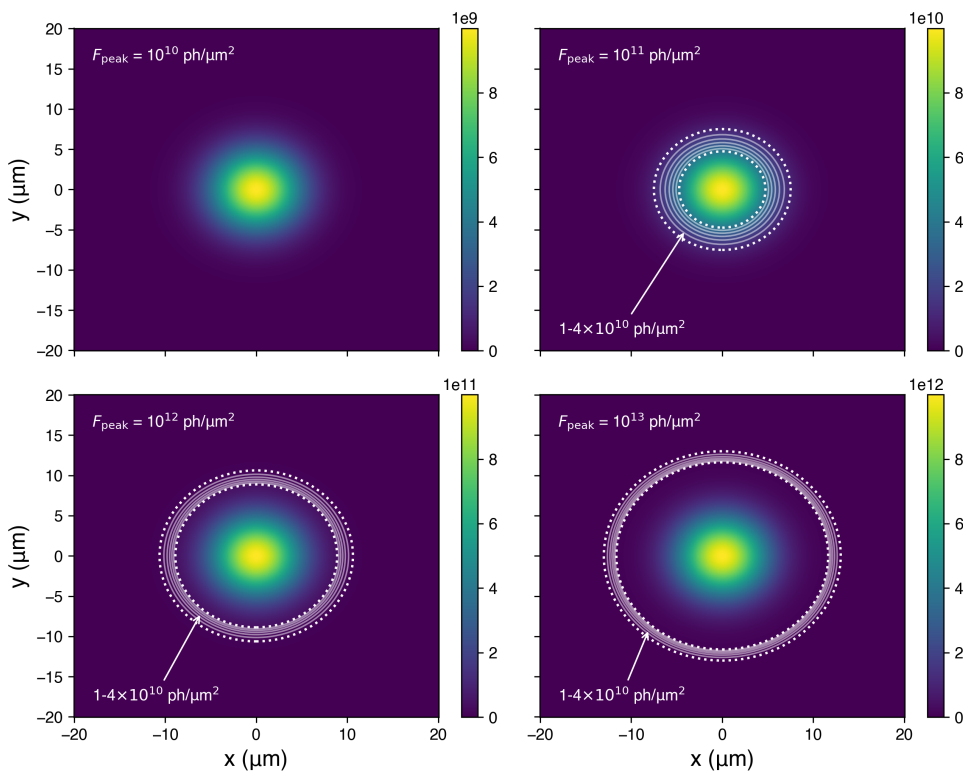
Figure 4.49: Beam profile and fluence distribution in focal spots for different peak fluences as indicated in each panel. The white dotted lines represent the local fluence values of 1.0×10^{10} ph/µm^2 and 4.0×10^{10} ph/µm^2. Additionally, the faint solid lines are shown between the two local fluences to demonstrate the movement of the area.
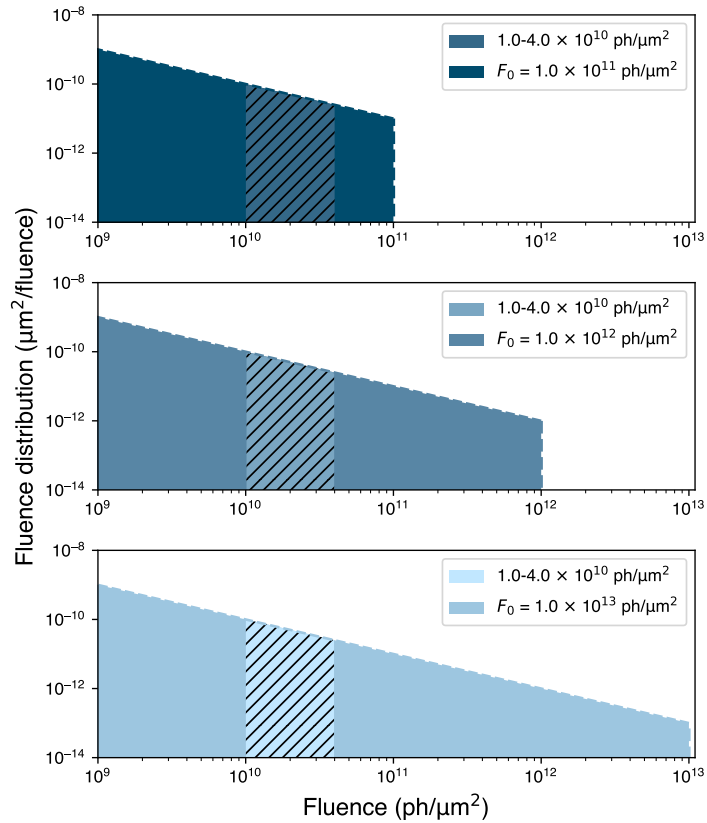
Figure 4.50: Fluence distribution function for different peak fluences. Analytic expression of the fluence distribution function can be found in Appendix E of Ref. [120].
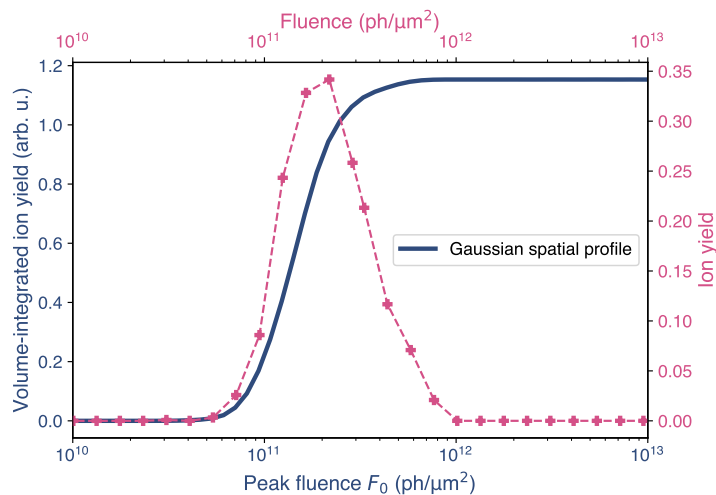
Figure 4.51: Volume integration of the ion yields of Xe^{25+} using a single Gaussian beam profile. Displayed are the volume-integrated ion yield as a function of peak fluence (dark blue line) and the ion yield as a function of fluence (pink crosses).

Assuming a double Gaussian beam profile, where the second Gaussian acts as a pedestal [120], the calculations show a slight change in slope but exhibit the same saturation behaviour. That is why only a single Gaussian profile was used. Fig. 4.52 compares the peak-fluence dependence for a single and a double Gaussian spatial profile.
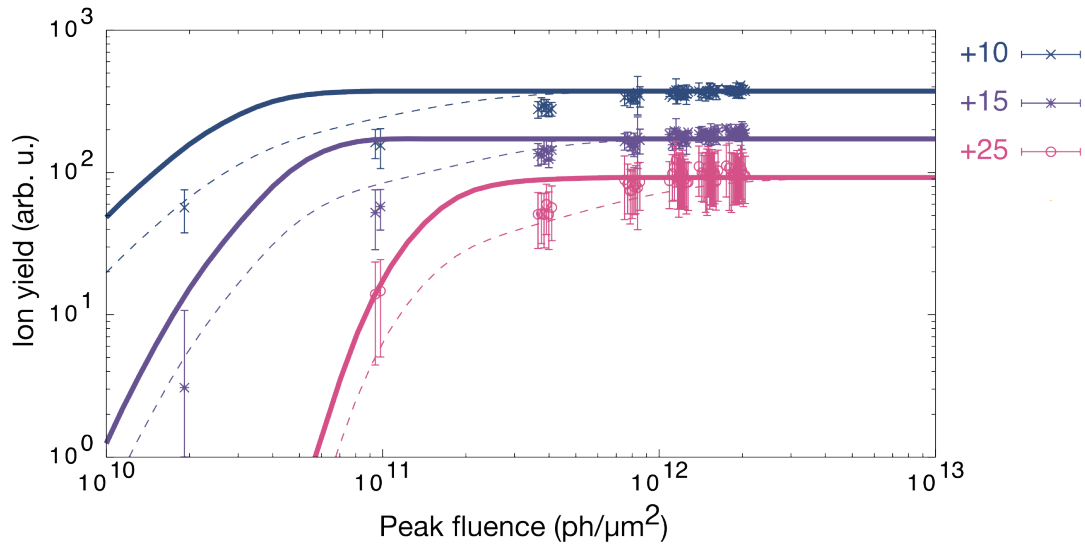
Figure 4.52: Peak-fluence dependence of the xenon ion yields at 1325 eV. Calculated ion yields are volume-integrated with a single (solid lines) and double (dashed lines) Gaussian spatial profile. Both calculated ion yields are scaled to the highest experimental ion yield. This figure was similarly published in Ref. [57].

4.5 Intensity compression

To display an extensive range of ion yields spanning over three orders of magnitude, it is necessary to compress the intensity for better visualisation. For this reason, the following formula (courtesy of Philipp Schmidt) is used:

$$I_{\mathrm{comp}} = 1 - e^{-a \cdot I_{\mathrm{init}}},$$

with I_{comp} the compressed intensity, the scaling parameter a, and the initial intensity I_{init}. Fig. 4.53 shows the ion yields without and with compression as a function of ion yield on a log-log plot and illustrates the wide-spanning ion yields. As a result, the higher ion yields get compressed towards the lower ion yields, thus lowering the overall dynamic range.
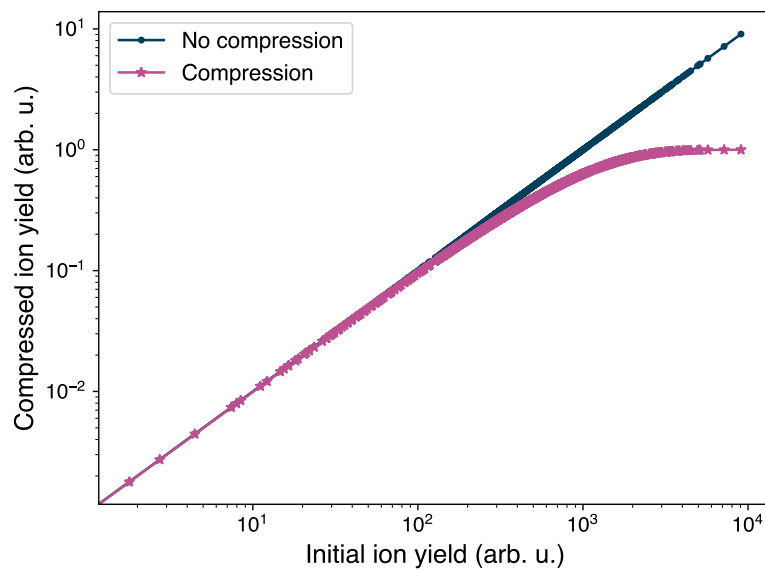
Figure 4.53: Ion-yield compression for visualisation.

4.6   Conversion TOF to kinetic energy

4.6.1   Electron TOF spectrum

The analogue electron TOF spectra employed in the investigation of DCH states in argon are processed analogously to those for xenon, as detailed in Sec. 4.1.1. Rather than evaluating the analogue signal, the background-corrected electron TOF spectra are digitised using a CFD, thereby mitigating concerns regarding pulse-height dependence.

In contrast to the xenon data, where each TOF dataset corresponds to a fixed photon energy, the photon-energy scan presented here is stored within a single data file, as the data were acquired continuously while scanning the photon energy. Consequently, it is necessary to filter the data based on photon energy.

Concerning the pulse-energy drift within the pulse train, applying pulse filtering exclusively to the first pulse did not significantly impact the electron TOF spectrum. Panel **a** of Fig. 4.54 illustrates the pulse-energy distribution at 255 eV. Panel **b** presents the average pulse energy as a function of pulse position, where the distributions for each position overlap, revealing only minor deviations as indicated by the ratio $\frac{\sigma_{\text{train}}}{\mu_{\text{train}}} \approx 3\%$. The pulse-energy distribution and pulse-position dependence are consistent across all photon energies.
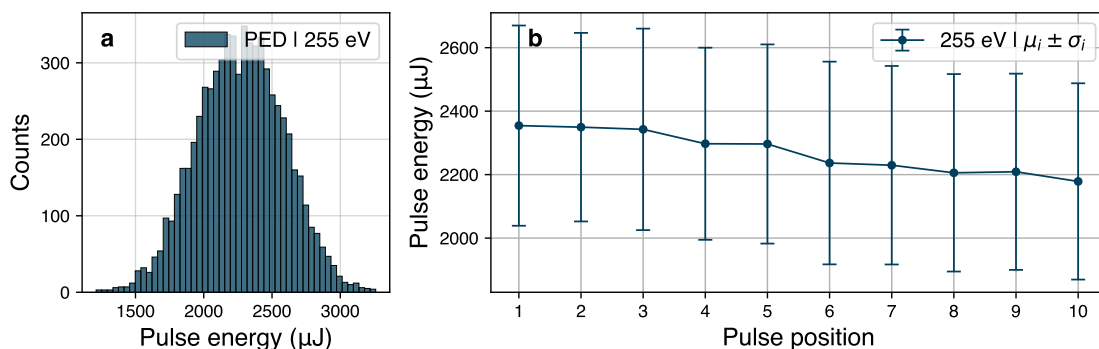
Figure 4.54: **a** Pulse-energy distribution at 255 eV. **b** Average pulse energy as a function of pulse position within the pulse train.

The electron TOF spectrum comprises 21120 digitiser samples, of which only the range 2700–3200 contains the relevant electron signal. Fig. 4.55 shows the average trace of a pulse, with the inset highlighting the region of interest, where the pink dashed line indicates the arrival of photons (prompt) at 2500. The conversion of the TOF $t - t_0$ to electron kinetic energy E_{kin} in eV is achieved using the following relationship:

$$E_{\text{kin}} = \frac{A}{(t - t_0)^2} + \frac{B}{(t - t_0)^3} + E_{\text{kin}}^{(0)}. \tag{4.7}$$

$E_{\text{kin}}^{(0)}$ represents an offset that accounts for the retardation potential. The term $\frac{A}{(t-t_0)^2}$ is derived from first principles, where $A = \frac{m_e}{2e} L^2$, whit m_e denoting the electron mass, L the length of the field-free drift tube of the spectrometer, and e the elementary charge. The term $\frac{B}{(t-t_0)^3}$ serves as an additional higher-order correction to account for

the nonuniform electric field configuration within the spectrometer. Given that the kinetic energy of the electrons is significantly lower than their rest mass, relativistic effects can be neglected in this context.
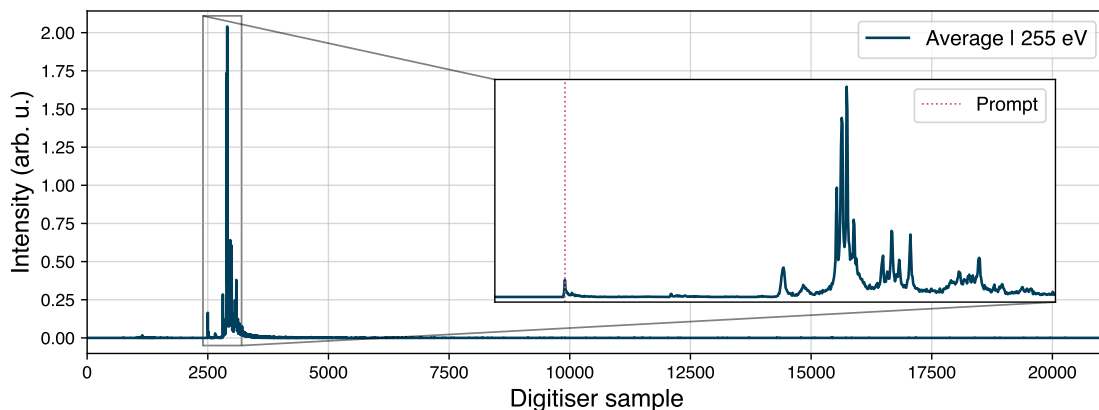
Figure 4.55: Average electron TOF spectrum at 255 eV.

The $L_{2,3}MM$ Auger-Meitner spectrum of argon was used for the energy calibration by assigning the peaks with the experimentally obtained energy values of Ref. [121]. These values were measured above the Ar $2p$ binding energy and below the Ar $2p$ shake-up states at a photon energy of 265 eV using synchrotron radiation. Fig. 4.57 shows the electron TOF spectra filtered by photon energy as a waterfall plot, with markings indicating the positions of the Auger-Meitner electrons and their corresponding kinetic energies. To determine the temporal timestamp (in units of digitiser sample), the Auger-Meitner peaks for all photon energies were fitted with a Gaussian profile to extract the mean values, which were subsequently averaged to yield a single timestamp for each kinetic energy. Fig. 4.56 shows in panel **a** the experimentally obtained timestamps along with the corresponding fit using Eq. 4.7, while panel **b** displays the residuals of this fit.
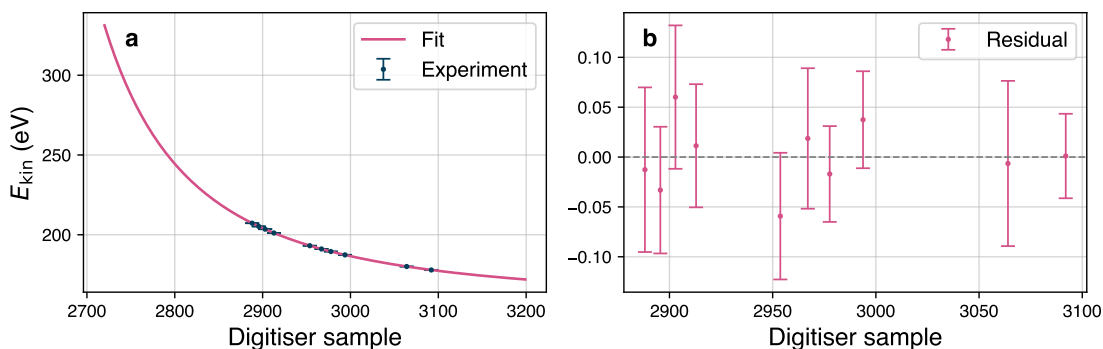
Figure 4.56: Calibration of the electron TOF spectrum.
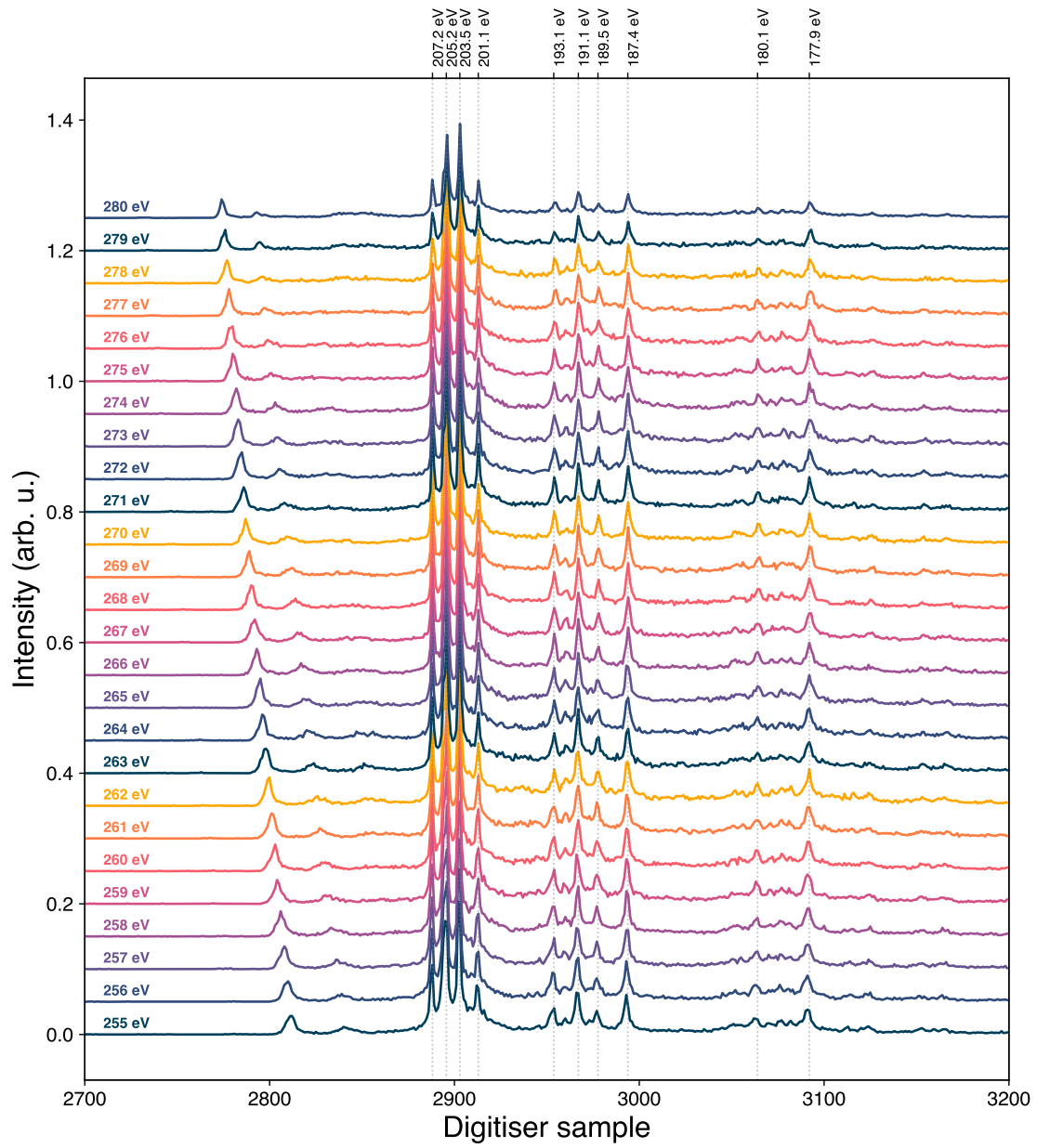
Figure 4.57: Electron TOF spectra for different photon energies.

4.6.2 Transmission function

The figure presented in Fig. 4.58 displays the spectrometer transmission function, where the blue data points represent the ratio of measured and theoretical intensity, while the red line indicates the fitted step-function-like slope. The analysis reveals that kinetic energies exceeding 205 eV exhibit a transmission approximately 60% lower than energies slightly above the retardation potential of 160 V. The fit to the data is performed using a logistic function of the form $\frac{A}{1+e^{k(x-x_0)}}$. Normalisation is applied by scaling the intensities relative to the maximum value of the data points. The data points were derived by utilising the ratio of the experimental electron yields at a photon energy of 253.25 eV to the calculated $2p$ cross sections [31], weighted by the experimental Auger-Meitner branching ratios as reported in Ref. [121].

Thus, the experimentally and theoretically derived Auger-Meitner decay spectrum ($L_{2,3}$–MM) was categorised into three groups: $L_{2,3}$–$M_{2,3}M_{2,3}$, $L_{2,3}$–$M_1M_{2,3}$, and $L_{2,3}$–M_1M_1, each characterised by distinct transition energies. Each group is represented by a single data point, corresponding to the sum of the intensities. The average electron energy of each group, weighted by the respective intensities, is assigned to the corresponding data point. The branching ratios were obtained by summing the intensities within each group and normalising the three branching ratios to unity.

Additionally, the fourth data point is derived from the ratio of the experimental $3p$ photoelectron yield at a photon energy of 253.25 eV to the calculated $3p$ cross section reported in Ref. [31]. Due to the superposition of the electron yield resulting from sequential $3p$ ionisation, the $3s$ photoelectron was excluded from this analysis.
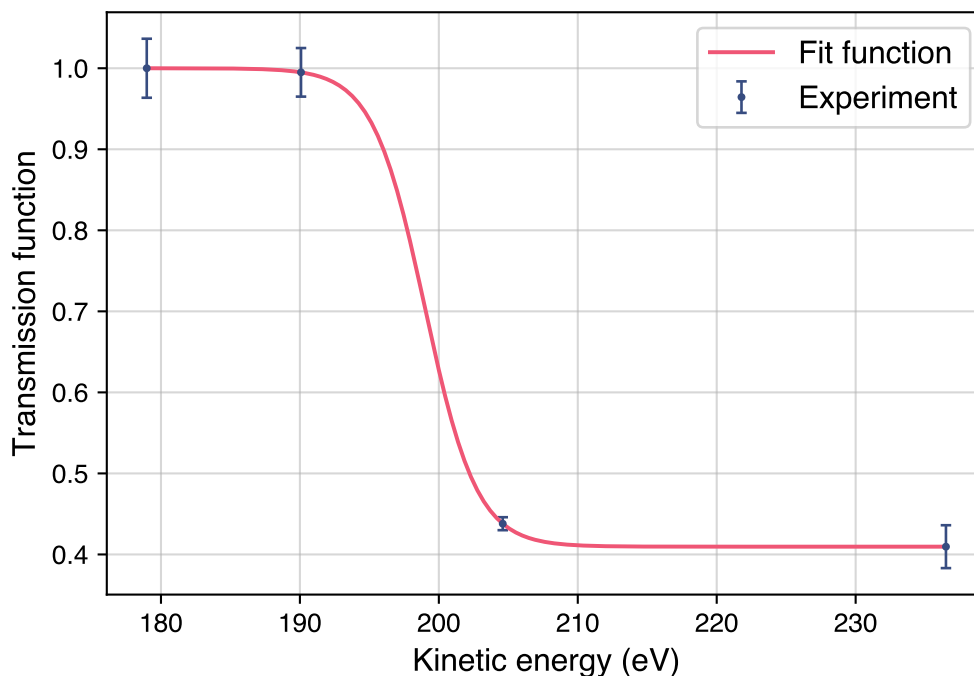
Figure 4.58: Spectrometer transmission function as a function of electron kinetic energy.

4.7 Instrument function

Due to the spectrometer's time-to-energy dispersion, the energy spread (peak width) changes as a function of kinetic energy (gets broader towards higher kinetic energies). It needs to be addressed in the modelling for displaying the calculations. For this reason, the time-to-energy calibration E_{kin} is differentiated with respect to the TOF t_{TOF} and scaled by σ_{3p} of the instrument function at the $3p$ photoelectron peak, which is assumed to be Gaussian.

$$\sigma(E) = \sigma_{3p} \cdot k \frac{\mathrm{d}E_{\text{kin}}}{\mathrm{d}t_{\text{TOF}}}\bigg|_{E_{\text{kin}}=E}$$

k is a scaling parameter making the derivative $\frac{\mathrm{d}E_{\text{kin}}}{\mathrm{d}t_{\text{TOF}}}$ to range between 0 and 1 and is equal to the derivative $\frac{\mathrm{d}E_{\text{kin}}}{\mathrm{d}t_{\text{TOF}}}$ evaluated at the kinetic energy, where the $3p$ peak is centred. The instrument function is estimated to be 2.6 eV (FWHM) and derived through deconvolution of the $3p$ photoelectron peak using a modelled Gaussian whose FWHM matches the FEL bandwidth.
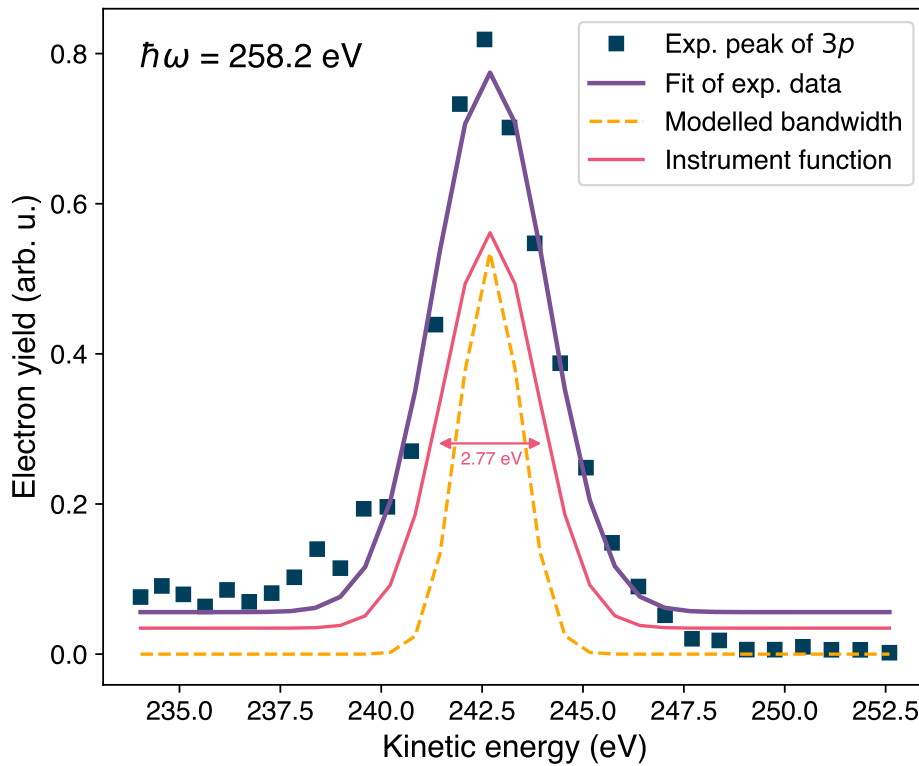
Figure 4.59: Extraction of the bandwidth of the instrument function.

Chapter 5

Multiphoton absorption in xenon

This chapter investigates the complex ionisation process of xenon atoms after multiphoton absorption under irradiation with soft X-ray pulses using a FEL by altering the photon energy. In the X-ray regime, photoabsorption generally occurs in inner shells, and multiphoton absorption is predominantly driven via a sequence of single-photon absorption events that produce inner-shell vacancies, which dominantly relax via Auger-Meitner decay cascades (s. Ch. 2). During the decay process, the atom may absorb additional photons. If the rate of additional photoabsorption exceeds that of core-hole decay, two or more core holes may be generated.

The gist of the chapter is the analysis of the photon-energy dependence of the ionisation process, explored systematically for the first time using XFEL pulses. The tunable undulators facilitate this capability at the European XFEL, allowing for variations in photon energy without altering the electron beam energy. This scanning capability mapped transient resonances in xenon across a range of 1 keV, from 700-1700 eV, which became resonantly excited during the charge-up process in the atom–XFEL interaction at a specific charge state. Previous studies [25, 50] focused on similar experiments, albeit constrained to fixed photon energies.

The role of the pulse intensity in the ionisation process will be further illuminated by introducing resonance spectra. These spectra display the ion yields of a fixed charge state as a function of photon energy for different intensities, revealing a saturation behaviour of their pattern. After a charge-state-specific peak fluence and at specific photon energies, the resonance profiles no longer change in structure, which can be viewed as "disabling" the peak fluence's impact on the ion yields. This enables studying the underlying ionisation mechanisms undisturbed in detail and exposing a different ionisation mechanism for ion yields, which do not saturate.

It will be shown that MCH states are indispensable in understanding the observed ion-yield peaks in the resonance spectra. Further, they lead to deviations of the ground-state transition energy lines and demonstrate the crucial role of the precursor charge states in the temporal evolution to a final charge state. Also, an outlook on the pulse-duration dependence, which could not yet be experimentally observed systematically, will be given.

The chapter will compare the experimental findings with calculations conducted using XATOM [53, 54] by Sang-Kil Son from the Center for Free-Electron Laser Science (CFEL) in Hamburg.

Parts of this chapter's results have been published in Nature Communications, volume 14, Article number 5738 (2023). For more information, see Ref. [57].

5.1   Experimental parameters

The experiment was conducted in October 2019 at the SQS scientific instrument at the European XFEL using the SASE3 soft X-ray variable-gap undulators and the AQS end station. Isolated xenon atoms were irradiated using ultraintense femtosecond XFEL pulses varying in photon energy from 700-1700 eV. For the measurement, xenon gas was introduced into the AQS experimental station through an effusive needle perpendicular to the X-ray propagation direction at an ambient pressure of around 3×10^{-8} mbar. The resulting ions from the interaction with the X-ray pulses were detected by the vertical TOF spectrometer of AQS (s. Sec. 3.5).

The primary experimental objective was to investigate the photon-energy dependence of the ionisation process of xenon atoms irradiated by ultraintense, femtosecond soft X-ray pulses. The secondary goal was to assess the influence of fluence (number of photons per unit area) on the ionisation process. The gap distance between the two undulator halves was varied to adjust the photon energy during the scan, while the electron energy was maintained at 14 GeV. Further, the undulator was tapered to achieve the maximum pulse energy up to 7 mJ at 700 eV and 2 mJ at 1700 eV, wherein the gap distance of the final segments varies progressively along the beam propagation axis. The tapering increases the pulse energy after saturation while preserving the resonance condition of the amplification process [74].
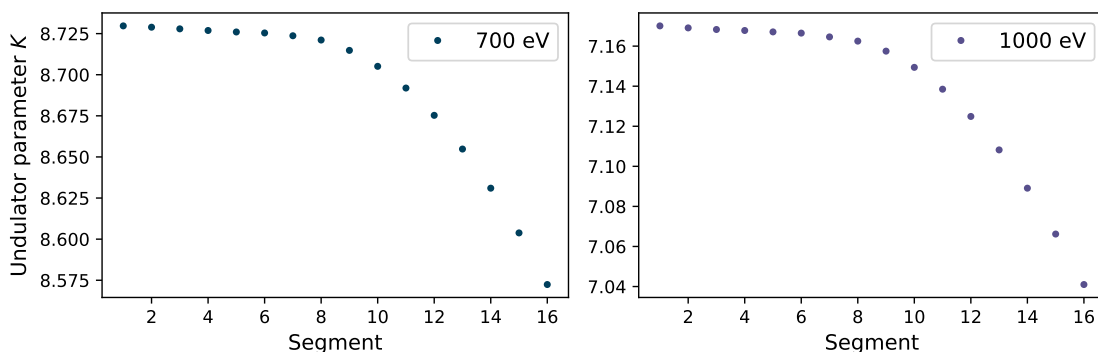
Figure 5.1: Undulator parameter K as a function of the undulator segment for the photon energy 700 eV and 1000 eV. The undulators have a quadratic tapering in both cases.

Figure 5.1 illustrates the undulator parameter K for the individual segments at photon energies of 700 eV and 1000 eV. The undulator parameter K is directly proportional to the magnetic field and decreases as the gap increases. Both settings exhibit quadratic tapering, resulting from an optimisation to gain the highest pulse energy.

The presented data in this chapter comprises only measurements recorded in SQS beamtime 2310 with the experimental specification shown in Tab. 5.1. The labelling of the fluence regimes in the interaction point is as follows:

$$100\% \equiv 1.0 \times 10^{13} \text{ photons/pulse},$$
$$50\% \equiv 0.5 \times 10^{13} \text{ photons/pulse},$$
$$10\% \equiv 0.1 \times 10^{13} \text{ photons/pulse}.$$

5.1.1 Constant number of photons on target

To carry out a photon-energy scan of 700–1700 eV in 25-eV steps to study the photon-energy dependence of the ionisation process, it is desired to keep as many parameters as possible constant during the scan to exclude other influences, such as the dominant peak-fluence (number of photons per unit area) dependence. This is generally challenging at FEL facilities since the FEL parameters are intertwined. Specifically, the pulse energy is proportional to the number of photons and photon energy. As photon energy increases, the focal spot size decreases, resulting in larger focus sizes for lower photon energies [79]. Consequently, this variation impacts the fluence within the interaction volume. Another example is the non-Fourier-limited relation between spectral bandwidth and pulse duration.

At the time of the experiment, there was no established procedure for determining the focus of the XFEL beam for every photon energy. It could only be estimated by reconstruction using a Hartmann-type wavefront sensor [122], requiring a drastic attenuation of the XFEL beam, e.g., by a gas attenuator, to operate safely, making it impractical during a beamtime and under the high intensities used for the experiment. However, the number of photons per pulse N_{ph} is controllable and considered a critical parameter since it essentially determines the fluence. The goal of this section is to describe the procedure used during the experiment to obtain a constant number of photons on target.

As mentioned earlier, the average pulse energy E_{pulse} of an XFEL pulse increases linearly with the average number of photons N_{ph} each having a central photon energy of E_{ph}:

$$E_{\mathrm{pulse}} = E_{\mathrm{ph}} \times N_{\mathrm{ph}}. \tag{5.1}$$

The word "central" refers to the fact that an XFEL pulse is not monochromatic but has a spectral bandwidth, as described in Section 3.1.2. To compensate for variations in photon energy and maintain a constant number of photons, the X-ray beam needs to be attenuated using a GATT (s. Sec. 3.4) accordingly. Taking into account the GATT transmission $T_{\mathrm{GATT}} \in [0, 1]$, where 0 means no photons pass through, and 1 all photons reach the experimental chamber, Eq. 5.1 transforms as follows:

$$N_{\mathrm{ph}} = \frac{E_{\mathrm{pulse}} \times T_{\mathrm{GATT}}}{E_{\mathrm{ph}}}. \tag{5.2}$$

This equation remains an idealisation and requires adjustment by the beamline transmission $T_{\mathrm{beamline}} \in [0, 1]$, which is a function of photon energy influenced by variations in mirror reflectivity and finite mirror sizes. This factor becomes significant for lower photon energies, where the larger focus size, attributed to increased divergence, contrasts with that of higher photon energies [79]. To measure the beamline transmission, as described in Ref. [73], and to characterise a constant number of photons in the interaction region, an additional XGM was installed downstream of the AQS end station for this experiment. The overall beamline transmission T_{beamline} represents the pulse-energy loss during the beam transport from leaving the last undulator segment to the interaction point.

The employed photon-energy range spans a wide range, necessitating adjustments to the optical configuration, as a single X-ray mirror cannot maintain consistent reflectivity across this range. Therefore, two distinct mirror configurations, differing

in pre-mirrors, as described in Sec. 3.2, were utilised to achieve optimal reflectivity for the entire range of photon energies [79]. The low-energy (LE) configuration uses a pre-mirror, which cuts at around 1500 eV with almost no reflectivity, and 13-mrad chicane for the photon-energy range 700-1175 eV. The high-energy (HE) configuration uses a pre-mirror which cuts at around 2500 eV and a 9-mrad chicane for the photon-energy range 1200-1700 eV, as described in Ref. [79]. Both configurations effectively suppress higher FEL harmonics [73], which could otherwise affect the ionisation process of xenon. For example, if employing a fundamental photon energy of 700 eV in the HE configuration, the third harmonic at 2100 eV would also be reflected by the mirror, contributing approximately 4% of the pulse energy of the fundamental [73].

Fig. 5.2 shows the measurement of the beamline transmission for the used photon-energy range and additionally displays the calculated reflectivity using the Henke online calculator[1] to demonstrate that the discontinuity at 1200 eV is inherent in the two different optical settings. For the photon energies 700-1175 eV, the data shows a further discrepancy of about 30% towards the measurement, which could be due to a "more intensive use" of the LE pre-mirror at the time of the experiment [79], which eventually led to a higher degree of attrition induced by X-ray irradiation in comparison to the HE pre-mirror.
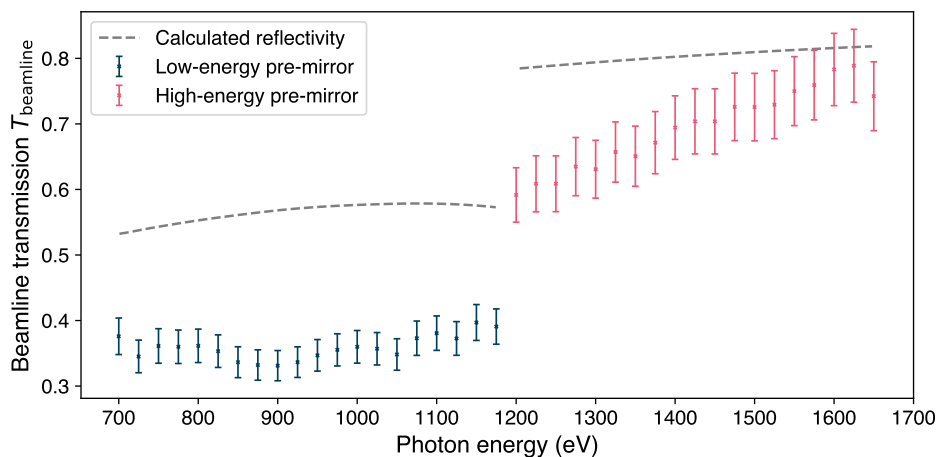
Figure 5.2: Beamline transmission for 700–1700 eV. The XGM was filled with krypton gas, leading to a resonance around 1675 eV, which makes the measurements unreliable for 1675–1700 eV and are excluded in the figure. Reflectivity was calculated using the Henke online calculator and is derived from the product of the six reflectivities of the M1-M4 and KB mirrors without accounting for mirror size.

---

[1]http://henke.lbl.gov/optical_constants/layer2.html

Taking into account T_{beamline}, the final equation reads:

$$N_{\text{ph}} = \frac{E_{\text{pulse}}}{E_{\text{ph}}} \times T_{\text{GATT}} \times T_{\text{beamline}}. \tag{5.3}$$

Another experimental condition is that the undulators lase differently for different photon energies. The increased undulator gap for higher photon energies changes the highest possible gain despite tapering, leading to lower pulse energies for higher photon energies. Fig. 5.3 depicts the initial pulse energy directly after the undulator as a function of the photon energy and shows the decreasing trend for higher photon energies. Around 1200 eV, a small jump from 1175 eV to 1200 eV is visible due to two different measurement days.
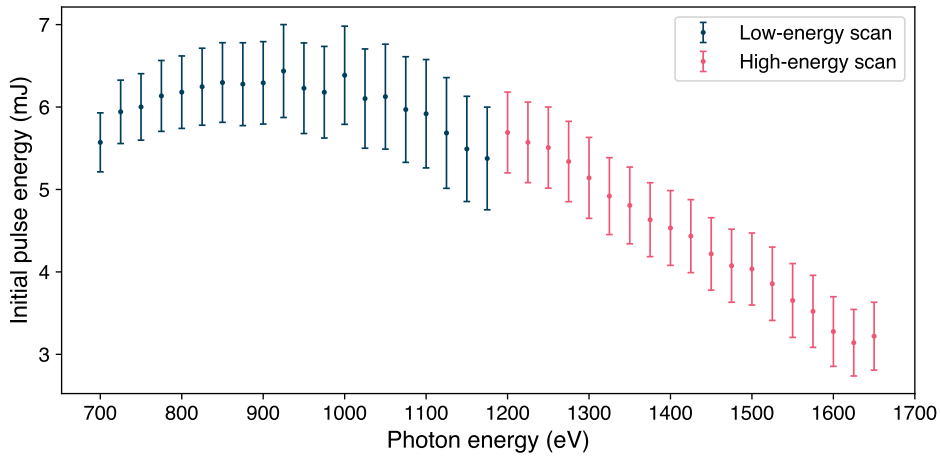
Figure 5.3: Initial pulse energies measured by the XGM in the tunnel before entering the SQS beamline.

The photon energy with the lowest pulse energy $E_{\text{pulse}}^{(\text{min})}$ occurring in the photon-energy scan defines $T_{\text{GATT}} = 1$ (no attenuation). For all other photon energies, T_{GATT} needs to be adjusted accordingly to reach a constant number of photons. Fig. 5.4 **a** shows the adjusted GATT transmission for the highest fluence regime (100%) as a function of the photon energy. The two optical settings are also reflected in the adjusted GATT transmissions. The pulse energy at 1625 eV is already at the minimal level, resulting in $T_{\text{GATT}} = 1$.
Fig. 5.4 **b** shows the number of photons on target as a function of photon energy, calculated using Eq. 5.3 and the pulse energy measured by the tunnel XGM, which was employed for pulse filtering (s. Sec. 4.1.7). At a given photon energy, the data points represent a narrow pulse-energy bin from the PED (see Sec. 4.1.7), transformed into a number-of-photons representation, with a selection limited to the bins closest to 10^{13}. The error bars indicate the width of the bin. Overall, Fig. 5.4 **b** displays an almost constant number of photons within the experimental uncertainty with a mean of $(0.93 \pm 0.02) \times 10^{13}$ photons per pulse.

As noted earlier, the focus size cannot be directly obtained; however, it can be estimated using the XCALIB toolkit [120, 123]. XCALIB is a toolkit developed to calibrate the beam profile of an XFEL by using experimental CSDs of light atoms.
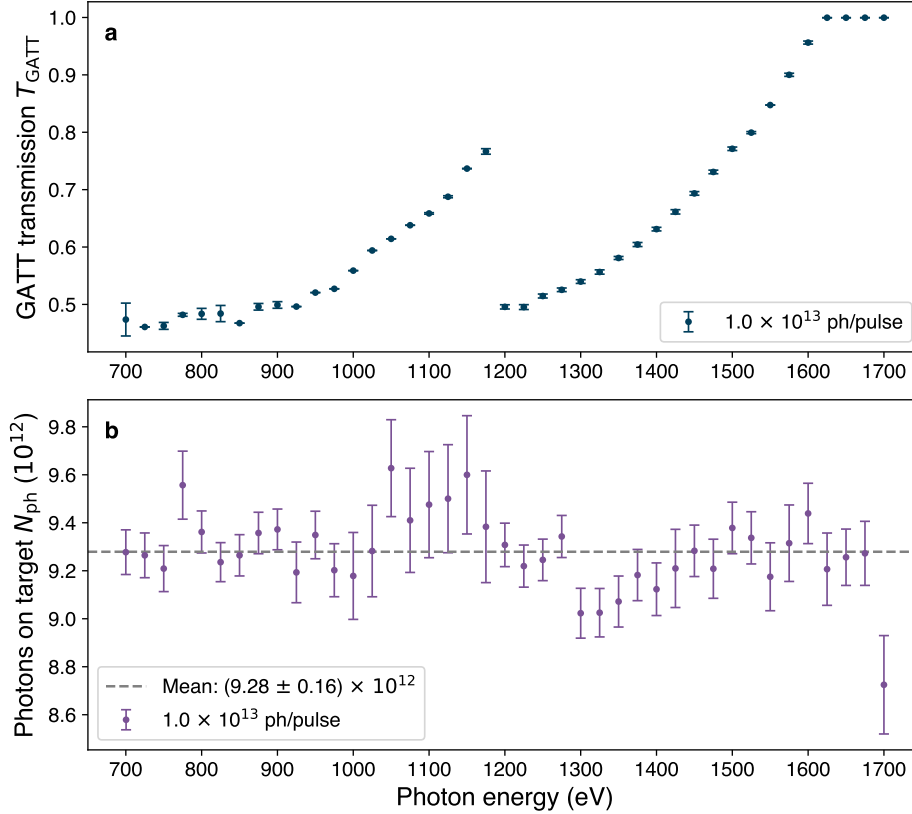
Figure 5.4: **a** Transmission settings of the GATT as a function of photon energy for the highest fluence regimes. **b** Number of photons on target as a function of photon energy for the highest fluence.

The focal spot size can be obtained by using the calibrated peak fluence and the measured number of photons. To achieve this, XCALIB requires the ion yields of a light atomic species measured under the same conditions as those of the xenon measurements. In this context, argon was selected due to its lighter atomic weight and reduced complexity in its interactions with the XFEL pulse compared to xenon. Specifically, an appropriate argon data set was recorded for each photon energy and fluence regime.

Fig. 5.5 **a** shows the peak fluences calibrated by XCALIB as a function of photon energy. The absence of error bars is because XCALIB does not provide an error estimation of the peak fluence. The discontinuity around 1200 eV due to the two optical settings can be visibly seen, revealing an almost 60% lower peak fluence for the LE than for the HE setting and corresponds to a much larger focus size for the LE setting since the number of photons is constant in both cases.

Given the peak fluence F_0 in units of ph/µm^2 and assuming a single Gaussian profile, it is possible to determine the focus size Δ (FWHM) in µm:

$$F_0 = \frac{a N_{\text{ph}}}{\Delta^2}, \tag{5.4}$$

with $a = 4\ln(2)/\pi$ [120]. Fig. 5.5 **b** shows the reconstructed focus size as a function of the photon energy in steps of 50 eV by using Eq. 5.4. The mean focus size of the LE range is almost twice as high as the HE range. In Ref. [79], Mazza et al.

reconstructed a focus size of 1.9 µm (FWHM) at a photon energy of 1050 eV from a measurement during the commissioning phase of the SQS instrument with a strongly attenuated X-ray beam by using a Hartmann-type wavefront sensor [122]. This conflicts with the obtained focus size by the calibration procedure of XCALIB at 1050 eV of 4.3 µm. However, the direct comparison must be treated with caution because the measurements are not taken at the same time period, albeit with the same optical setting but different beam properties. Further, the calibration species argon is susceptible to the spectral bandwidth due to resonances occurring in the range of 700–900 eV.
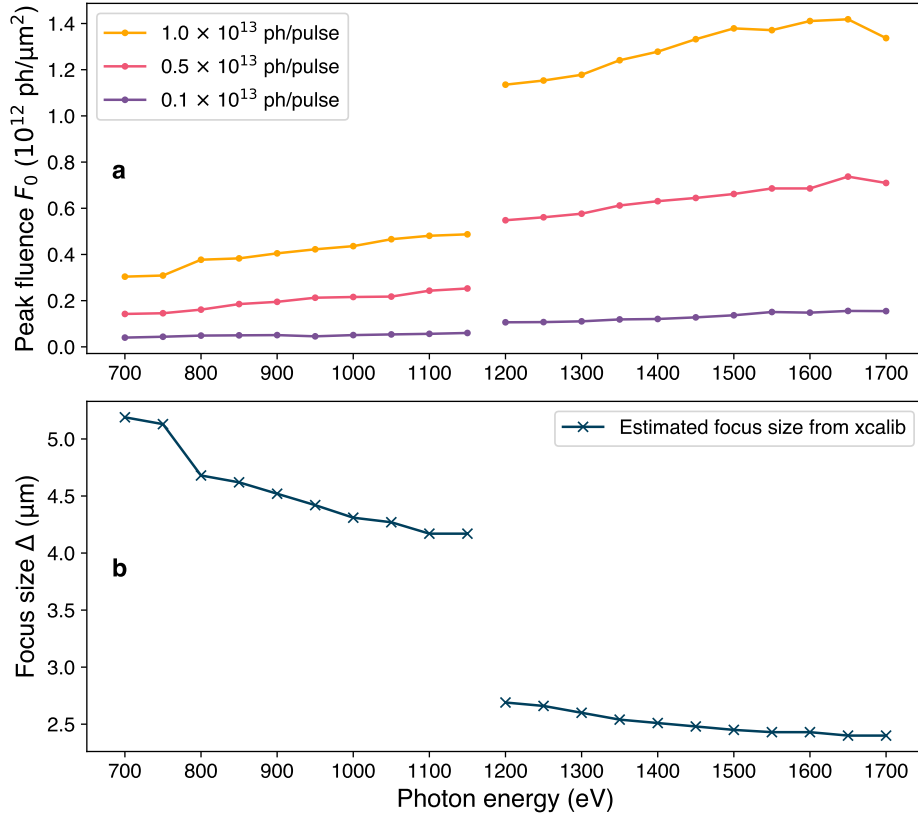
Figure 5.5: Focal parameters for the different fluence regimes. No error bars are included since XCALIB does not provide an error estimation of the peak fluence.

The peak fluence should generally be held constant during a photon-energy scan to make it comparable with the theoretical calculations. However, this was impossible because the uncontrollable focus geometry changes with photon energy and the pre-mirror setting. Ultimately, the two different pre-mirrors were necessary to suppress higher FEL harmonics, but they simultaneously caused two disparate fluence regimes, which could not be compensated.

5.1.2   Time-of-flight spectrum

Fig. 5.6 shows an averaged analogue ion TOF spectrum of xenon without any corrections at a photon energy of 1300 eV and pulse energy on target of $E_{\mathrm{pulse}} = 1.9\,\mathrm{mJ}$, where the highest charge state of Xe^{41+} was observed, for the complete time frame of $14.22\,\mu\mathrm{s}$, showcasing the measurement and the experimental conditions of the photon-energy scan.
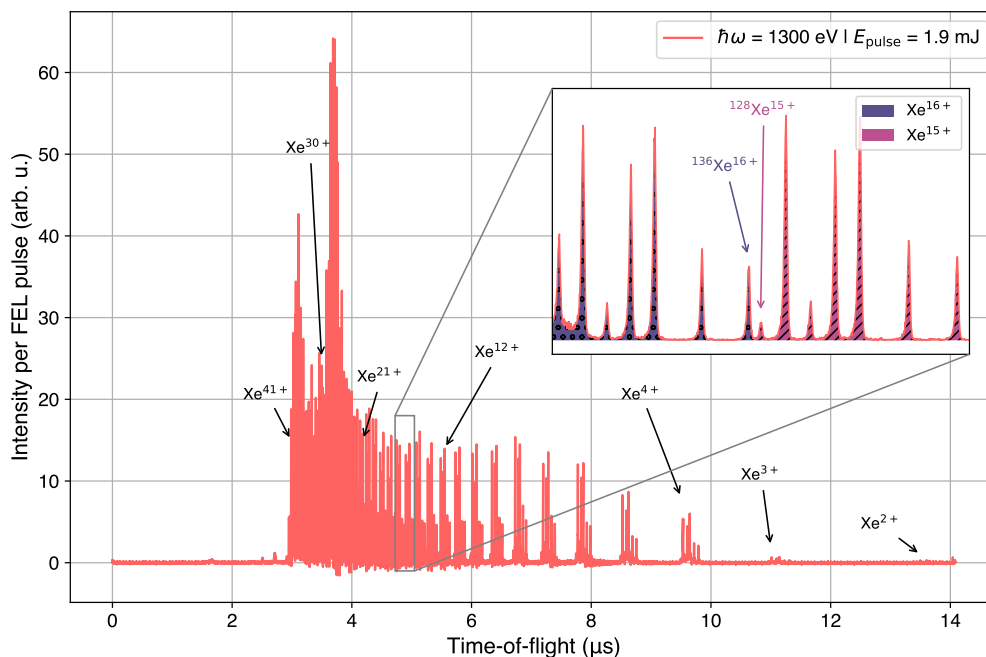
Figure 5.6: Average analogue TOF spectrum of xenon at $\hbar\omega = 1300$ eV and pulse energy of 1.9 mJ on target.

Some charge states are marked with a black arrow and serve as orientation. $^{128}\mathrm{Xe}^{41+}$ has the shortest flight time of $2.94\,\mu\mathrm{s}$ and $^{136}\mathrm{Xe}^{2+}$ the longest with $13.86\,\mu\mathrm{s}$. Until charge state Xe^{16+}, the isotopes of a given charge state Xe^{q+} do not superimpose with the isotopes of the next higher charge state $\mathrm{Xe}^{(q+1)+}$. The inset shows the charge states Xe^{15+} and Xe^{16+} in counting mode for better visibility, illustrating the almost overlapping isotopes of different charge states, e.g., $^{128}\mathrm{Xe}^{15+}$ and $^{136}\mathrm{Xe}^{16+}$.
Charge state Xe^{+} is out of range in the chosen time frame. It would have a flight time of $19.3\,\mu\mathrm{s}$ corresponding to a flight time of $5.08\,\mu\mathrm{s}$ in the consecutive spectra of the pulse train, which in turn has a similar flight time as Xe^{13+} and Xe^{14+}, albeit an almost nonexistent ion yield due to the vanishing probability to absorb only a single photon in the O shell during a pulse, which is the only available option to create Xe^{+}.
Figure 5.7 presents the integrated ion yield peaks, extracted from a given TOF spectrum, plotted on a logarithmic scale as a function of charge state across different photon energies. In each panel, the ion yields are normalised to 1, and the noise threshold is marked in grey. Sec. 4.1 cover the complete TOF $\mapsto$ CSD conversion procedure. Displayed are examples of CSDs for specific photon-energy thresholds of the neutral xenon atom, such as the $3d_{3/2}$ edge at 700 eV in panel **a**, the $3p_{3/2}$ edge at 950 eV in panel **d**, the $3p_{1/2}$ edge at 1000 eV in panel **e** or the $3s$ edge at 1150 eV

in panel **f**. Panel **g** shows the CSD with the highest observed charge state Xe^{41+} and panel **h** the CSD for the highest investigated photon energy of 1700 eV. The CSDs in **b** and **c** at 750 eV and 800 eV, respectively, are around the $3d \rightarrow nf$ resonances, with $n \geq 3$. Every CSD has a characteristic pattern with hills and valleys and hints at complex ionisation mechanisms at specific photon energies. The following section provides a compilation of all measured CSDs as a function of photon energy and will give a first overview of the complex ionisation process. A more detailed analysis will be carried out in the following sections.
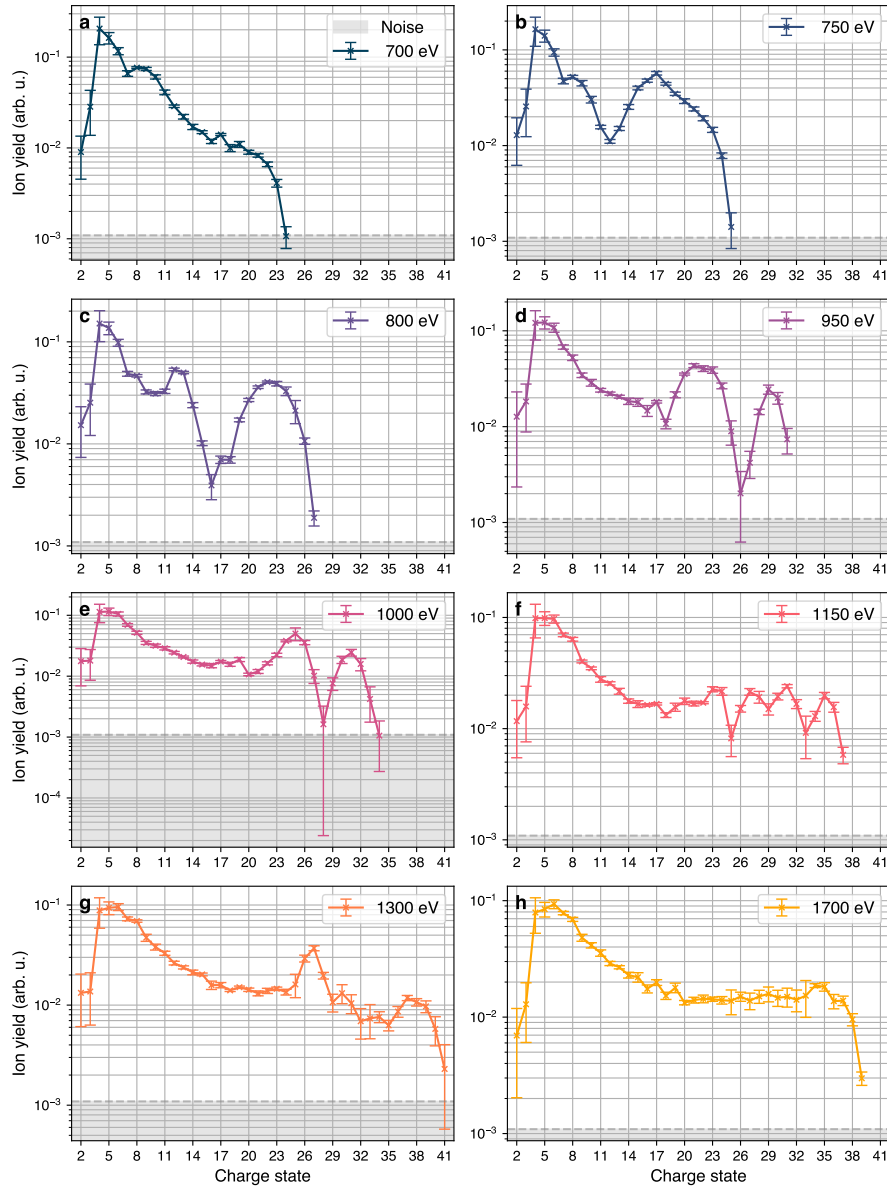
Figure 5.7: CSDs in the photon-energy range 700–1700 eV for the highest fluence regime. Panels **a-c** show CSDs around the $3d$ edge and $3d \rightarrow nf$ excitations, **d** and **e** show the CSD around the $3p$ edge, and **f** shows the CSD around the $3s$ edge. Panel **g** shows the CSD with the highest observed charge state Xe^{41+} and panel **h** the CSD for the highest investigated photon energy of 1700 eV. The ion yields (y axis) are on a logarithmic scale and normalised to 1 in each panel.

5.1.3 Summary parameters

Parameter	Low energy (LE)	High energy (HE)
Photon-energy range (25-eV steps)	700–1175 eV	1200–1700 eV
Wavelength	1.06–1.77 nm	0.73–1.03 nm
Mirror setting	LE pre-mirror + 13 mrad chicance	HE pre-mirror + 9 mrad chicance
Calc. focus size (FWHM)	4.17–5.19 µm	2.48–2.69 µm
Bandwidth	1.9–1.4%	1.4%
Beamline transmission	38–48%	61–78%
Initial pulse energy	5.4–6.4 mJ	2.0–5.7 mJ
Electron energy	14 GeV	
2nd & 3rd harmonic	0.14±0.02% & 4.4±0.4% [73]	
Undulator tapering	quadratic	
Pulse duration	$\approx$ 10 fs [Sec 5.5]	
Sample	Xenon	
TOF window	14.22 µs	
Background pressure	3×10^{-8} mbar	
Repetition rate	70.3125 kHz	
Number of bunches	25–35	
Effective acceptance length	$\pm$ 1.5 mm [Sec. 4.2]	

Table 5.1: Experimental parameters from the beamtime 2310.

5.2 Photon-energy dependence

5.2.1 Overview

The present subsection overviews the photon-energy scan and the experimentally obtained ion-yield data from complex ionisation processes. The sections that follow will offer an in-depth discussion of these ionisation processes.
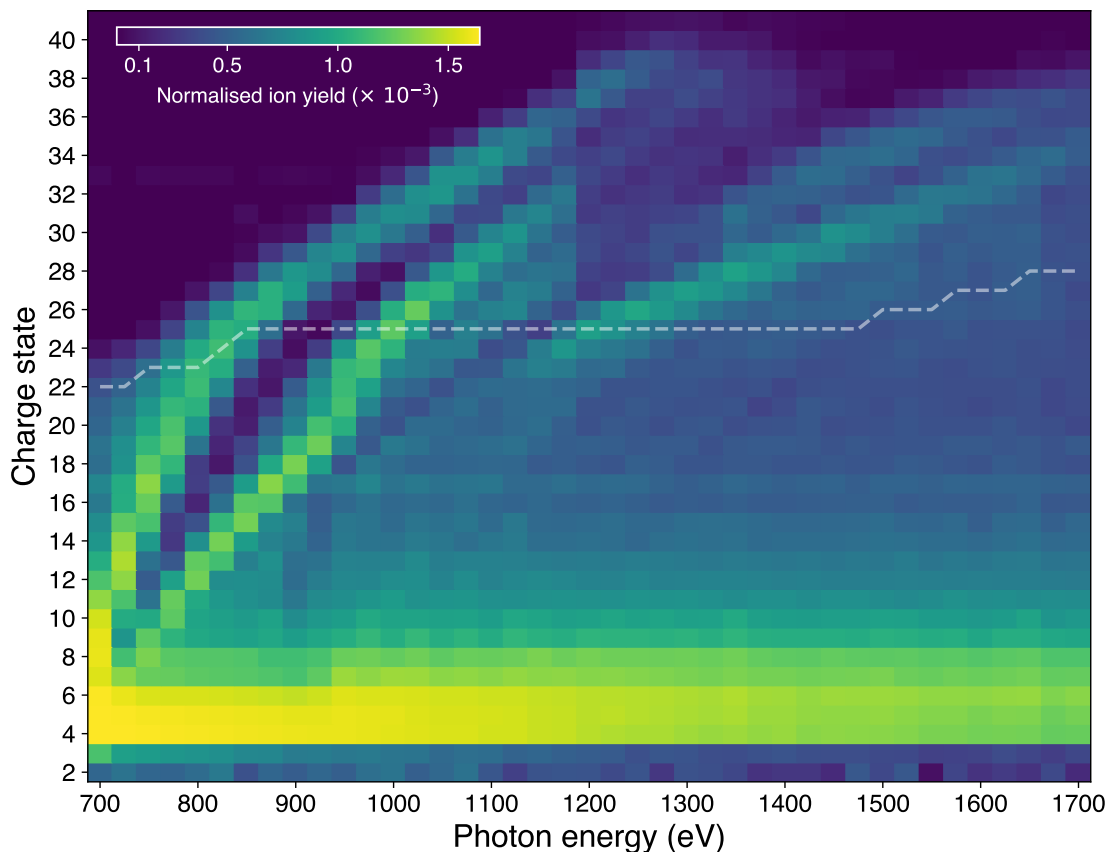
Figure 5.8: Experimental 2D colour map depicting the xenon ion yields for charge states Xe^{2+}–Xe^{41+} across photon energies ranging from 700 to 1700 eV. The white dashed line indicates the sequential direct one-photon ionisation limit. All ion yields of a respective photon energy are normalised to its prevailing gas pressure, measured by an ion gauge in the interaction chamber parallel to the data recording. The discontinuity at 1200 eV is due to a change in the beamline optics. A similar figure was published in Ref. [57].

The 2D colour map in Figure 5.8 shows the ion yields per XFEL pulse of the measured xenon CSDs between 700 and 1700 eV in steps of 25 eV for the highest fluence (100%) and exhibits the collection of all CSDs at single photon energy, as partly shown for selected photon energies in Fig. 5.7. The intensities of the ion yields span three orders of magnitude and have therefore been compressed [Sec. 4.5], such that high ion yields are saturated in colour. In Sec. 5.2.4, the ion yields of the lower charge states (Xe^{4+}–Xe^{8+}) are presented without compression.
Overall, comprehensive ion-yield minima and maxima structures can be spotted

and shift towards higher charge states as the photon energy increases. The chosen photon-energy range of 700–1700 eV covers the electron binding energies of the M shell in the neutral ground state, including the $3d$ (689 eV), $3p$ (941 eV) and $3s$ (1149 eV) subshell (see also the grey-shaded area in Fig. 5.9). Photoionisation of the K or L shell was inaccessible.

Moreover, Fig. 5.8 displays a trend of decreasing ion yields towards higher photon energies and towards higher charge states, which directly relates to a decreasing PCS and fewer remaining electrons in higher charge states, making a photoabsorption event less likely in both cases. For photon energies between 700–1300 eV, the experimental data shows a "knee" around Xe^{26+} related to an empty N and O shell in the ground state. Up to 1200 eV, the charge state with the highest ion yield is Xe^{4+}, which, along with Xe^{5+}, predominantly results from single-photon absorption [41]. For photon energies greater than 1200 eV, Xe^{6+} display the highest ion yield and is also predominantly created by single-photon absorption. Only charge states Xe^{2+} and Xe^{3+} result exclusively from single-photon absorption for the whole photon-energy range (s. Fig. 5.12).

In the sequential direct one-photon ionisation limit [25, 56, 124], indicated by the dashed white line, the highest charge state Xe^{q+} is defined by the last ionic state $Xe^{(q-1)+}$ that can be ionised with a single photon from its electronic ground state. However, charge states well beyond this limit are observed in the CSDs, with differences of up to 15 for photon energies in the 1200–1400 eV range.

The subsequent sections will present essential background information to facilitate the understanding of the experimental findings.

5.2.2   Electron binding energies

The electronic structure of neutral xenon (Xe^0) with its 54 electrons (e^-) is:

$$\underbrace{\overset{K}{1s^2}}_{2\ e^-}\ \underbrace{\overset{L}{2s^2 2p^6}}_{8\ e^-}\ \underbrace{\overset{M}{3s^2 3p^6 3d^{10}}}_{18\ e^-}\ \underbrace{\overset{N}{4s^2 4p^6 4d^{10}}}_{18\ e^-}\ \underbrace{\overset{O}{5s^2 5p^6}}_{8\ e^-}.$$
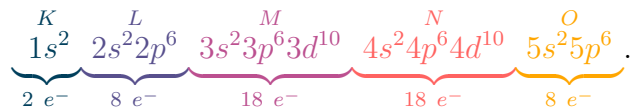
The visualisation of the calculated orbital binding energies, including fine-structure splitting, of Xe^{q+} as a function of the charge state q in ground-state configuration can be found in Fig. 5.9 and range from 12 eV ($5p_{3/2}$) to almost 35 keV ($1s$) at Xe^0. For $1s$, the binding energy has shifted to more than 41 keV at Xe^{53+}. The dots represent at least one available electron in the respective subshell in the ground state. As previously noted, the K and L shells are inaccessible at the highest experimentally employed photon energy of 1700 eV.
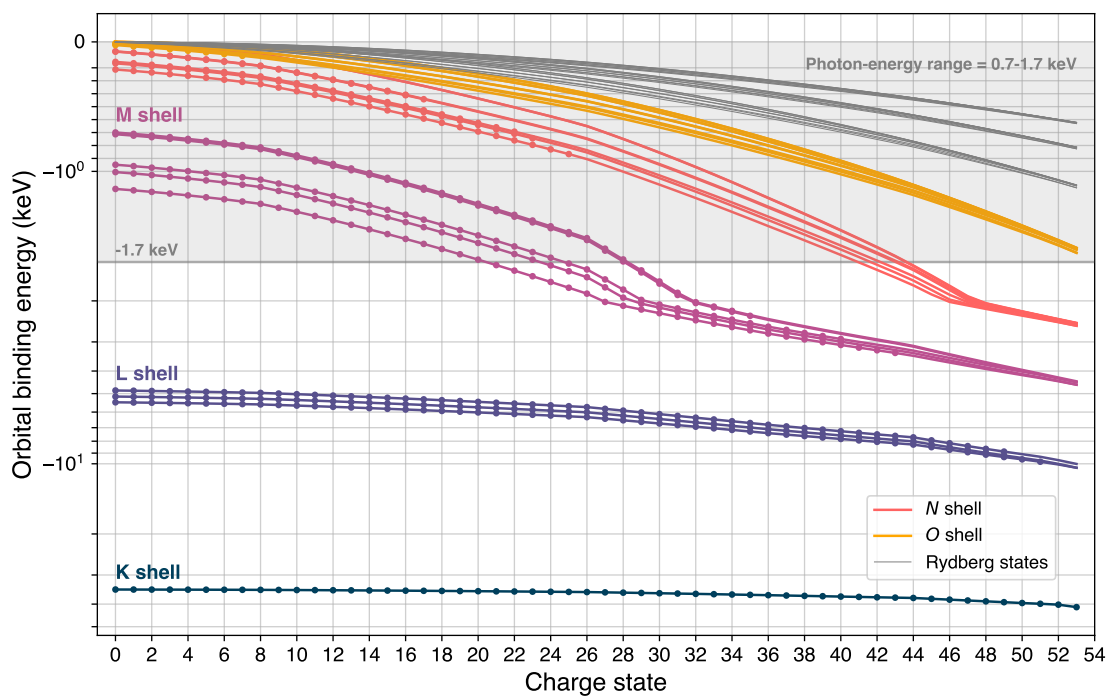
Figure 5.9: Calculated ground state electron binding energies of xenon as a function of the charge state with fine-structure splitting. The dots represent available electrons in the ground state electronic configuration of a given charge state. The y axis is on a logarithmic scale.

Multiphoton absorption of atoms happens predominantly sequentially in the soft X-ray regime [125, 126]. By initially focusing only on the required energy, a series of single-photon absorptions at a photon energy of 1700 eV can yield a maximum charge state of Xe^{29+}, as Xe^{28+} is the last charge state that can be ionised. The minimum number of absorbed photons can be estimated by dividing the accumulated ionisation potential E_{pot} up to Xe^{28+} by the photon energy of 1700 eV, yielding:

$$N_{ph}^{(min)} = \left\lceil \frac{\sum_{i=1}^{q-1} E_{pot}^{(i)}}{\hbar\omega} \right\rceil = \left\lceil \frac{13.7 \text{ keV}}{1.7 \text{ keV}} \right\rceil = 9 \text{ photons.}$$

This means that nine 1700-eV photons are needed to deliver sufficient energy to the atomic system to get Xe^{29+}. Fig. 5.10 shows the cumulated ionisation potential taken from Ref. [43] (purple line) of xenon as a function of charge state. In addition, the number of sequentially absorbed photons needed to get to a given charge state is shown (rose line). Removing all accessible electrons from the M, N, and O shells would result in a maximum observable charge state of Xe^{44+} with the configuration $1s^2 2s^2 2p^6$. It would also need a photon energy of 4500 eV to ionise the last remaining electron in the $3s$ subshell at Xe^{43+} [127].
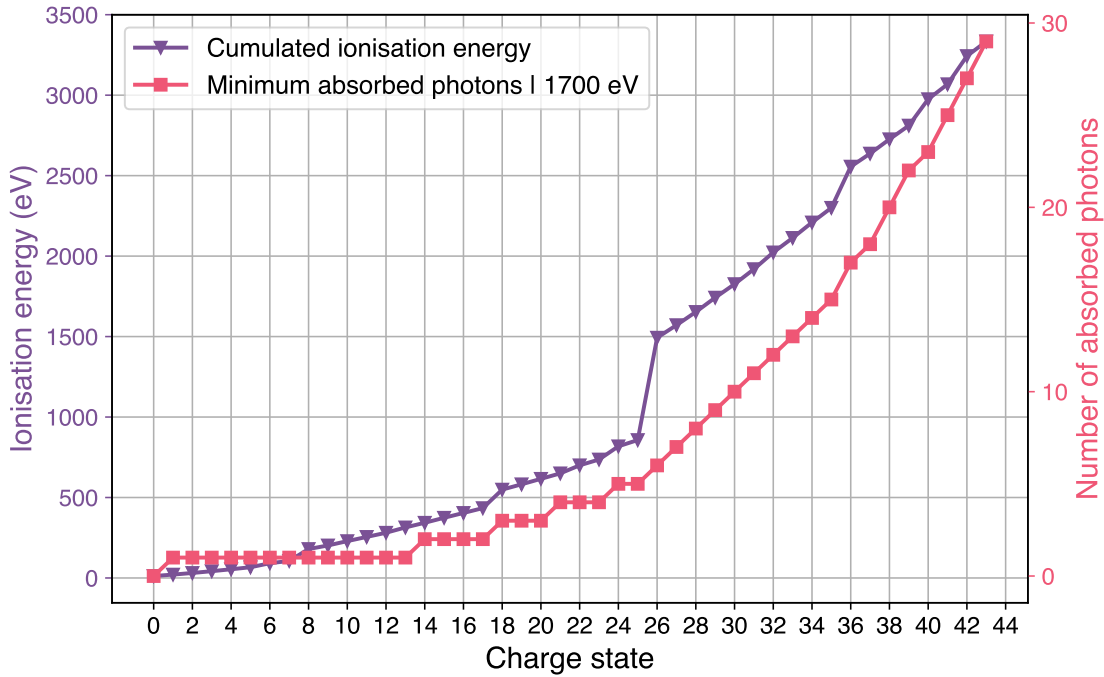
Figure 5.10: Cumulated ionisation potentials and number of the minimum absorbed photons.

5.2.3 Photoabsorption cross section

Fig. 5.11 shows the experimental PCS of the neutral xenon atom measured by Suzuki and Saito in 2003 [128] for the photon-energy range 680–1080 eV and the XATOM-calculated PCS for the photon-energy range 700–1700 eV in 4-eV steps. Moreover, it covers the entire experimentally photon-energy range, comprising the $3d$, $3p$ and $3s$ ionisation edge, and shows the decreasing trend of the PCS for higher photon energies. The PCS peaks around 700–740 eV are also reflected in the high ion yields in Fig. 5.8 at these photon energies.

The calculations start above the $3d$ ionisation edge at 700 eV, showing a constant offset towards higher photon energies with respect to the experimental data of about 25 eV, and assume a bandwidth of 1%, whereas the experimental data ranges between 0.1–1% in the range of 100–1000 eV. Further, the calculations are overestimated by roughly a factor of two at the $3d$ resonances at 700–740 eV. A similar situation between theory and experiment exists for the $4d$ "giant" resonance where theory yields an exaggerated PCS [31] compared to experiment [129].
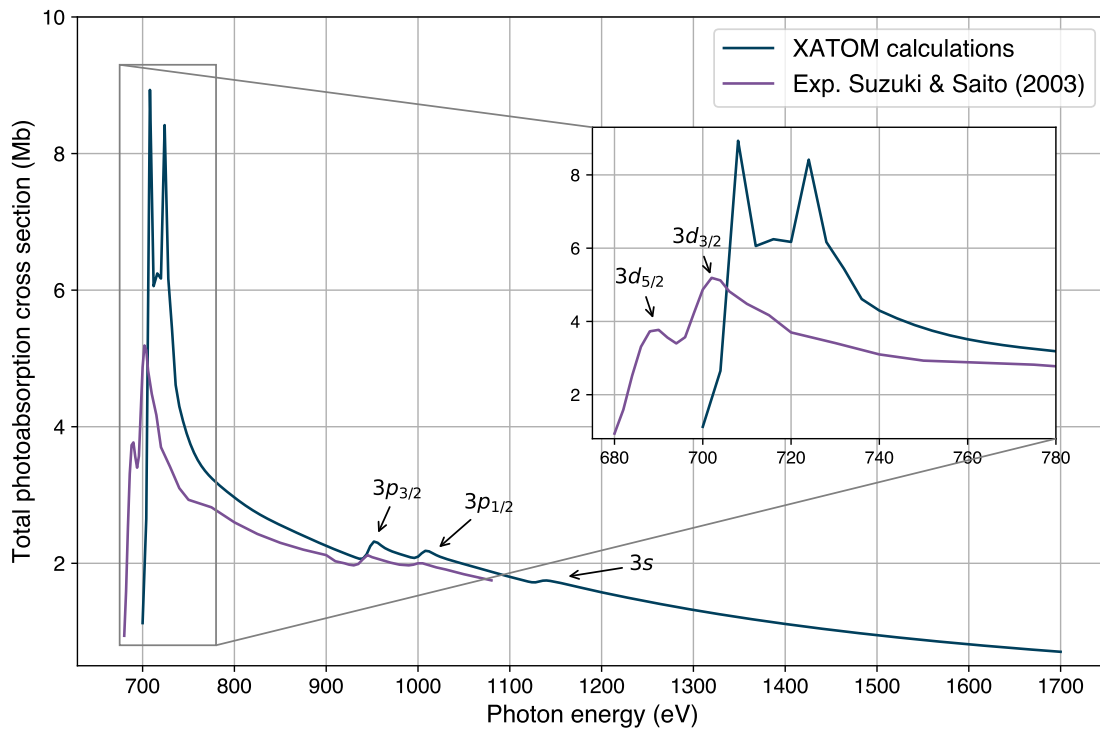
Figure 5.11: PCSs for the neutral xenon atom within the photon energy range of 700 to 1700 eV. The XATOM-calculated PCS exhibits a constant offset of approximately 25 eV towards higher photon energies. In contrast, the PCS reported by Suzuki and Saito [128] represents experimental absolute PCS measurements obtained through synchrotron radiation.

5.2.4   Single- and multiphoton absorption

This section treats the atomic response of xenon after absorbing only one X-ray photon and discusses the limit when multiphoton absorption sets in.

According to the work of Saito and Suzuki in 1992 [41], in which they experimentally studied single-photon multiple ionisation of xenon up to Xe^{8+} in the range of 650–1270 eV, a $3d$ core hole relaxes mainly to the charge states Xe^{4+} and Xe^{5+} [Tab. 1 in Ref. [41]]. Photoabsorption of a $3p$ electron becomes the second most probable process after passing the threshold of 941 eV, creating a $3p$ hole, which mainly relaxes in Xe^{7+} via consecutive Auger-Meitner decays and double Auger-Meitner decay. Yet with smaller branching ratios, a $3p$ hole also produces Xe^{5+}, Xe^{6+} and Xe^{8+} ions. At around 950 eV, the ion yields of Xe^{7+} and Xe^{8+} slightly increase due to an energetically possible shake-off process accompanying the initial photoionisation of a $3p$ electron. No further increase, however, was observed after the $3s$ threshold. Most of the Xe^+ and Xe^{2+} ion yields stem from direct N- or O-shell photoionisation. This indicates that a single soft X-ray photon, such as one with an energy of 1200 eV, suffice to induce the emission of eight electrons from a neutral xenon atom, resulting in an empty O shell in the ground state.

Figs. 5.12 **a**–**d** show the experimental ion yields as a function of photon energy for the lower charge states Xe^{2+}–Xe^{8+} at the highest fluence (100%). Except for Xe^{2+}, the charge states exhibit the decreasing trend of the $3d$ PCS. The jump around the $3p$ threshold can be seen in the ion yield of charge state Xe^{5+}–Xe^{8+} in Fig. 5.12 **d** at 950 eV and can also be found in the work of Saito and Suzuki. The ion yield of Xe^{2+} shows no dependence around the $3d$ edge and is, therefore, most probable produced by photoionisation of $4d$ electron in the N or even by sequential two-photon absorption in the O shell of $5p$ electrons.
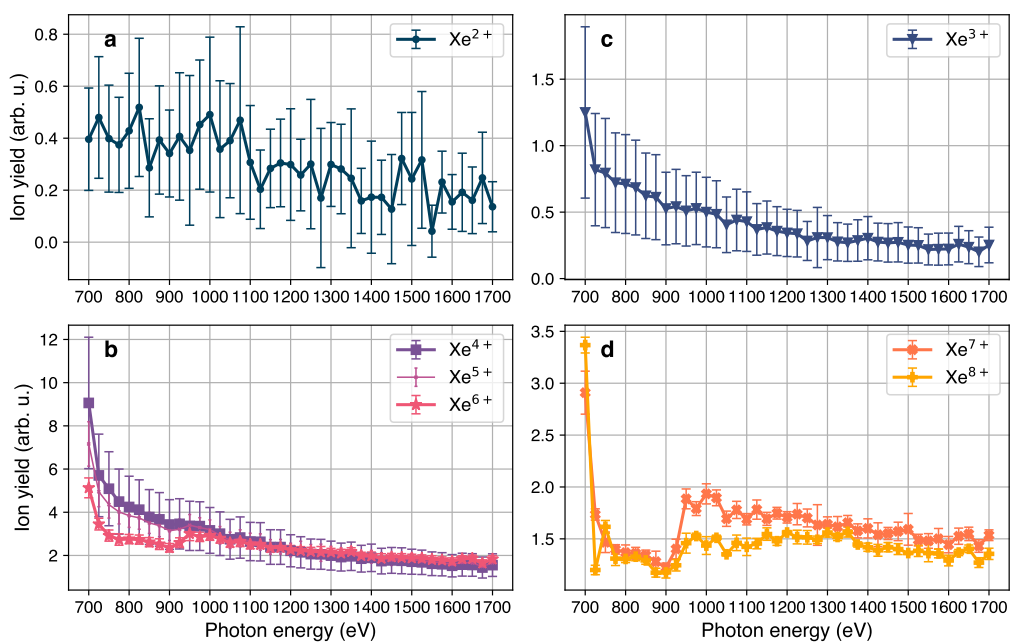
Figure 5.12: Experimental ion yields for the charge states Xe^{2+} to Xe^{8+}. The underlying data is the same as in Fig. 5.8.

Charge state Xe^{3+} shows no dependence on the $3p$ or $3s$ edge and stems mainly from the Auger-Meitner decay of the $3d$ core hole after single-photon absorption. After passing the $3s$ threshold at around 1150 eV, the highest observed ion yield shifts from Xe^{4+} to Xe^{6+}, as shown in Fig. 5.12 **b** as the $3s$ core hole become available.
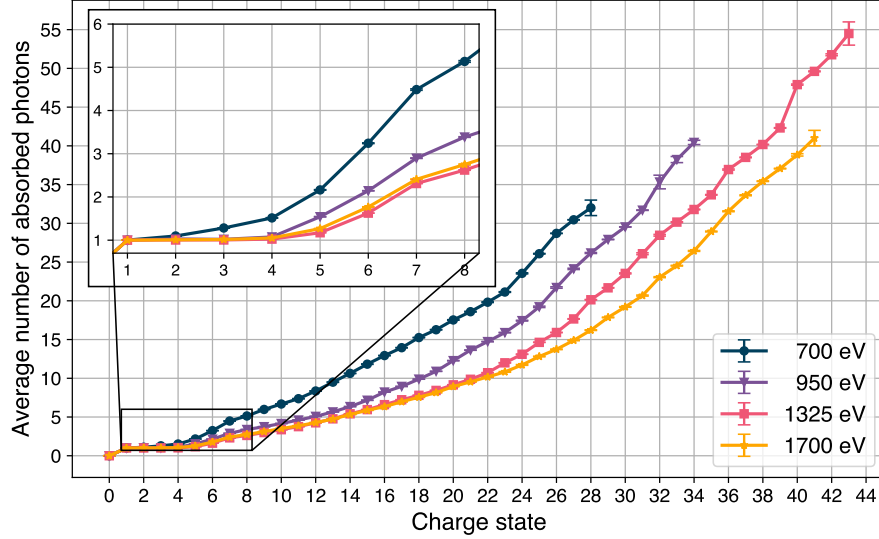
Figure 5.13: Calculated average number of absorbed photons.

Fig. 5.13 displays the calculated average absorbed number of photons as a function of the charge state for different photon energies (coloured lines). As the charge state increases, more photons are necessary to reach a given charge state since the orbital binding energy becomes more attractive due to less screening of the nucleus [Fig. 5.9]. At the same time, the average number of absorbed photons for a given charge state decreases with increasing photon energy because more energy is available for the ionisation. The inset in the upper left corner is a zoom of the x axis for the charge states Xe^+–Xe^{8+}, showing that for energies $\geq$ 950 eV, charge states $\geq Xe^{5+}$ can result from multiphoton ionisation. For 700 eV, this is already the case from Xe^{2+} onwards.

The relation (2) used by Santra and Young in Ref. [37] can be used to estimate at which peak fluence F_0 of the XFEL pulse all neutral atoms in the interaction volume absorb at least one photon because this can be considered the threshold to (sequential) multiphoton absorption. Using the conversion $1\,\mathrm{Mb} = 10^{-10}\,\mathrm{\mu m^2}$ gives the estimated saturation peak fluence $F_0^{(\mathrm{sat})}$ for single photoabsorption at $1\,\mathrm{keV}$ with $\sigma_{\mathrm{abs}} = 2\,\mathrm{Mb}$ (Fig. 5.11):

$$F_0^{(\mathrm{sat})} = \frac{1}{\sigma_{\mathrm{abs}}} = \frac{1}{2\,\mathrm{Mb}} = 0.5 \times 10^{10}\ \mathrm{ph/\mu m^2}.$$

By comparing this estimate with the measured peak fluence of $0.4 \times 10^{12}\,\mathrm{\mu m^2}$ at $1\,\mathrm{keV}$, it is clear that the absorption of at least one photon for a neutral atom in the interaction zone is inevitable under the extreme conditions of the experiment. As previously noted, the experimental data indicate that with a photon energy of 1700 eV, the charge state Xe^{39+} could be achieved [Fig. 5.7 **f**], resulting in the

emission of ten more electrons than the limit set by sequential direct single-photon ionisation, which leads to Xe^{29+}. Achieving this charge state requires a minimum of 22 photons at 1700 eV. The following section addresses the transient resonant excitations that arise at specific photon energies and charge states, which are crucial for reaching the Xe^{39+} charge state at 1700 eV.

5.2.5   Transient resonances

Despite the high photon energies, charge states no higher than Xe^{26+} were expected for a photon energy of 1500 eV when Rudek et al. in 2012 [25] investigated the ionisation process of xenon with a photon energy of 1500 eV and 2000 eV utilising the ultraintense XFEL pulses at the Linac Coherent Light Source (LCLS) at SLAC in Stanford, USA, and ion TOF spectroscopy. However, they observed a charge state of Xe^{36+} at 1500 eV, ten more ejected electrons than expected. A more detailed comparison between the two CSDs at 1500 eV can be found in A.1 of the appendix. The conclusion reached by Rudek et al. [25] is that charge states exceeding the sequential direct single-photon ionisation limit are produced through a resonance-enhanced absorption mechanism occurring in high charge states, which will be elucidated in the following.

Fig. 5.14 shows the shifting electron binding energy for Xe^{q+} as a function of the charge state in the electronic ground state configuration for the M, N, O shell and Rydberg states (grey lines). This figure is similar to Fig. 5.9 with the difference of only showing the M-O shells on a linear scale. The five coloured arrows embody energetically possible resonant excitations for selected transitions. These transitions are chosen because of their prominent role in the XFEL–xenon interaction and differ in the needed photon energy mirrored in the size of the arrow drawn to scale.
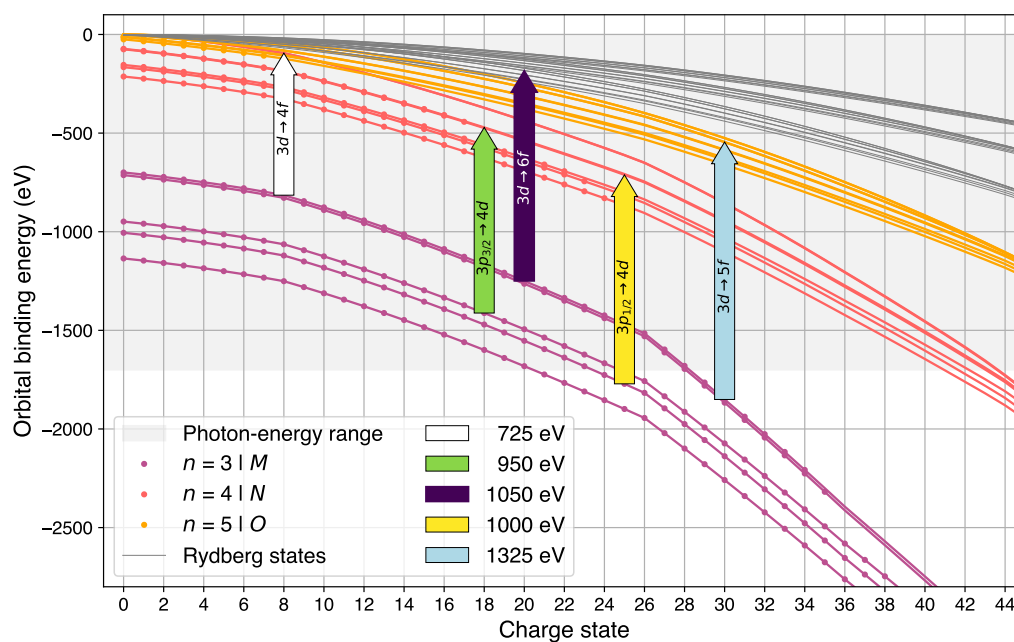
Figure 5.14: Orbital binding energies of xenon for the M, N and O shell as a function of charge state.

By satisfying the dipole selection rules, the energy difference between two orbitals becomes resonant for certain photon energies at specific charge states, enhancing the PCS. For example, the white arrow in Fig. 5.14 located at the charge state Xe^{8+} displays the energetically possible resonant excitation $3d \rightarrow 4f$ with a photon energy of 725 eV. Resonant excitations starting from the $3p_{3/2}$ (green arrow) or $3p_{1/2}$ (yellow arrow) subshell to the $4d$ subshell need at least one hole in the $4d$ subshell. This restriction does not apply to the transitions $3d \rightarrow nf$, e.g., $3d \rightarrow 5f$ (light blue) or $3d \rightarrow 6f$ (purple) in Fig. 5.14, with $n \geq 4$.

In the course of a single XFEL pulse, these resonances enable ionisations at charge states beyond the sequential direct one-photon ionisation limit [25, 56, 124], dubbed resonance-enabled or resonance-enhanced X-ray multiple ionisation (REXMI) [25, 50]. The REXMI mechanism also includes so-called "hidden" resonances, which are absent in neutral xenon atoms [130] or energetically inaccessible for low charge states, where an inner-shell electron can be excited into a newly created vacancy of a formerly filled subshell, such as the $4p$ or $5p$ subshell of xenon.

As an example of the REXMI mechanism occurring during an XFEL pulse: At a photon energy of 1300 eV and a charge state of Xe^{27+}, an energetically accessible resonant excitation promoting a firmly bound $3d$ electron to the unoccupied higher-lying Rydberg orbital $6f$ can be facilitated leading to new Auger-Meitner decay cascades, which further increases the charge state beyond the sequential direct single-photon ionisation limit. Finally, the REXMI mechanism makes a significant contribution to the highest observed charge state Xe^{41+} at the photon energies 1225–1400 eV, exhibiting a higher charge state than at 1700 eV (Xe^{39+}, s. Fig. 5.8). The following section focuses on the possible ground-state resonances for specific charge states and photon energies.

5.2.6 Transition energy lines

At certain combinations of photon energy and charge state, bound-bound transitions become resonant, leading to the energy transition lines, as shown in Fig. 5.15, which are given by:

$$E_{\mathrm{TL}}(q) = \left| E_{\mathrm{bind}}^{(nl)_{i_1}}(q) - E_{\mathrm{bind}}^{(nl)_{i_2}}(q) \right| \text{ with } i_1 \neq i_2.$$

Where $E_{\mathrm{bind}}^{(nl)}(q)$ represents the orbital binding energy as a function of the charge state q, n the principal quantum number, and l the orbital angular momentum of the respective atomic subshell. i_1 and i_2 are indices indexing a set of quantum numbers. Fig. 5.15 shows the transition energy lines as a function of the photon energy starting from the M shell ($n = 3$) to higher shells (coloured lines n=4–8) at a given charge state, whereby the stars mark more specific the $3d$ subshell, the squares the $3p$ subshell and the triangles the $3s$. The acquired lines in Fig. 5.15 resemble a phase space for resonant excitations with the coordinates charge state and photon energy and are energetically densely spaced, covering the entire photon-energy range. The lines do not include the fine-structure splitting for better visibility. Moreover, the lines only include transitions starting from the M shell because resonances from the N and O shell only become energetically possible at charge states, where in the ground state, no electrons are longer available in these shells.
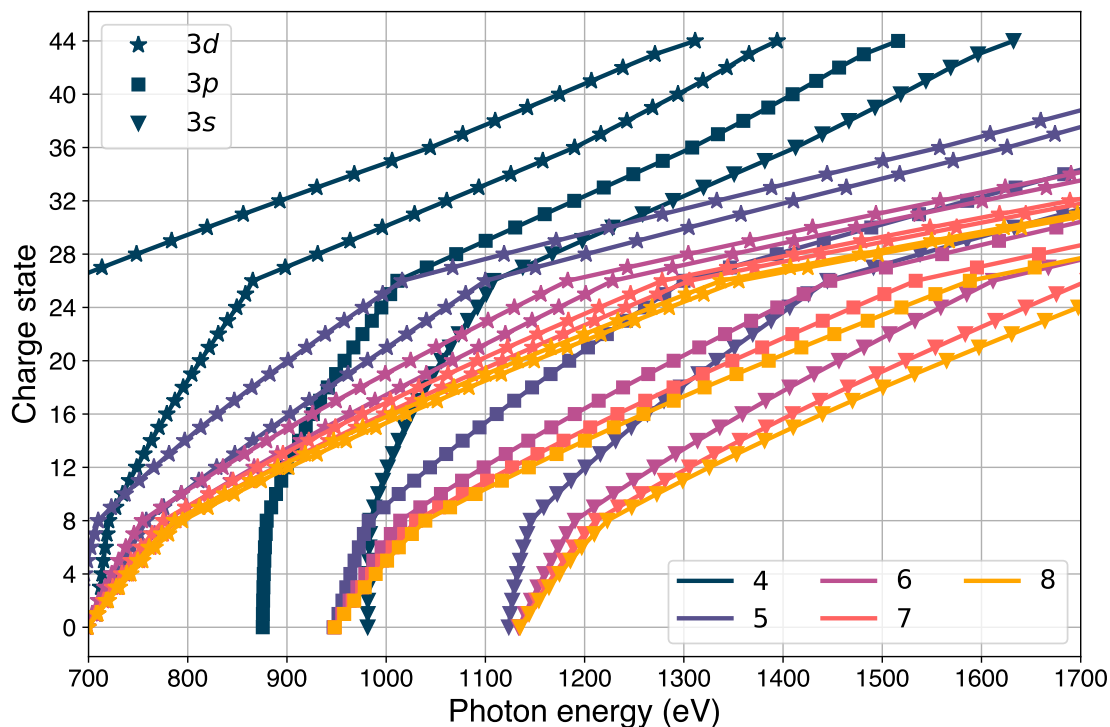
Figure 5.15: Transition energy lines starting from the $3s$ (triangle), $3p$ (square) and $3d$ (star) subshell as a function of photon energy and charge state for the photon-energy range 700–1700 eV with a step size of 25 eV and charge states Xe^0–Xe^{44+}. The lines represent energetically accessible resonant excitations to higher-lying orbitals (n=4–8), represented by different colours. For better visibility, the lines do not include the fine-structure splitting.

Calculated ground-state PCSs for different charge states, compared to the neutral atom, are shown in Fig. 5.16 displaying significantly enhanced cross sections at the charge states Xe^{15+}, Xe^{25+} and Xe^{35+} including all possible resonant excitations for that particular charge state. Only a few peaks are annotated with resonant transitions because of the better visibility. All charge states exhibit high cross sections for the transition $3d \rightarrow 4f$, shifting toward higher photon energies for higher charge states. For Xe^{35+}, the transition $3d \rightarrow 4f$ exhibit a strong shift to higher photon energies (1150 eV) compared to the position at Xe^{25+} (850 eV) with a significantly reduced PCS due to an almost empty $3d$ subshell ($1s^2 2s^2 2p^6 3s^2 3p^6 3d$) in the ground state. Most notable are the PCSs for the charge states Xe^{15+} and Xe^{25+}, whose resonances span over the whole photon-energy range, which is also reflected in the experimental data and will be further explained in the coming sections. For a photon energy of 1300 eV, a bandwidth of 1% correspond to 13 eV, allowing for various resonant excitations to take place during the pulse, particularly at the intermediate charge states.
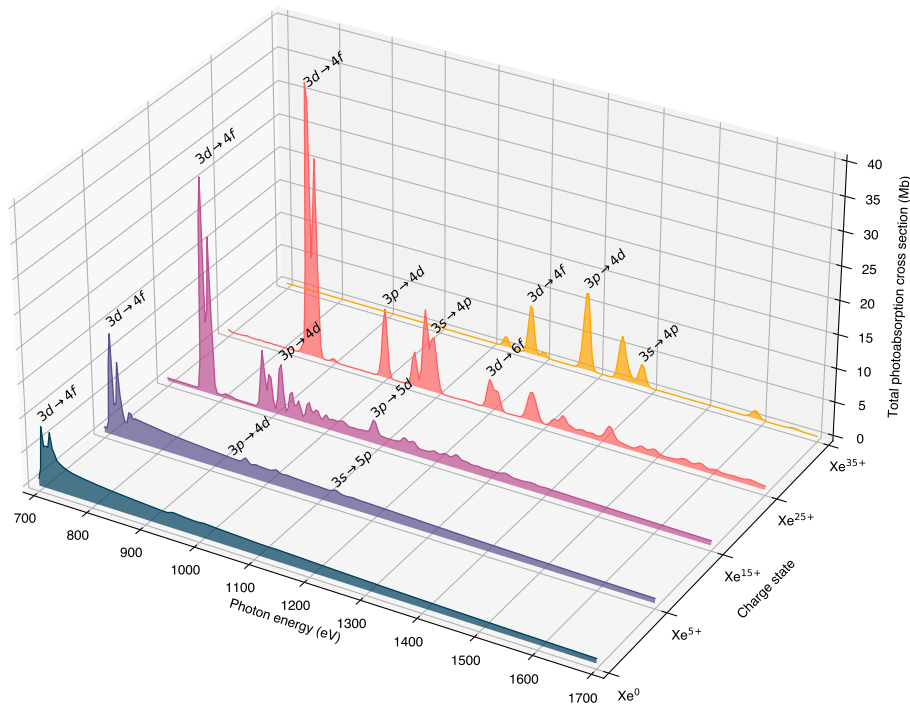
Figure 5.16: Calculated absolute PCSs for different charge states as a function of photon energy.

5.2.7 Comparison experiment and theory

This section compares the experimental findings and the calculations. Fig. 5.17 shows in **a** the same experimental data as in Fig. 5.8 and in **b** the calculated CSD as a function of photon energy for the range 700–1700 eV in 25-eV steps, performed by *ab initio* ionisation dynamics calculations [53, 54]. The calculations consider volume integration [120] because experimental ion spectra are always subject to a fluence distribution determined by the focused X-ray beam shape (s. Sec. 4.4). Further, the parameters employed are 1% bandwidth, a Gaussian temporal shape, a pulse duration of 10 fs FWHM, and no contribution from the FEL second harmonic (s. Sec. 5.6).

In both panels **a** and **b**, the five main contributing transition energy lines are shown on top, indicated by different markers. In addition, the transition energy lines have been horizontally shifted towards higher charge states by one. This reflects the preliminary assumption that the ion yield at charge state Xe^{q+} is the result of the last resonant excitation at $Xe^{(q-1)+}$.

As shown in Fig. 5.17 **b**, the theoretical CSDs reproduce the overall features of the experimental ion-yield maxima well. For both experiment and theory, the ion-yield maxima roughly follow the transition energy lines, showing a good agreement with the calculated resonances. This features the crucial role of the resonant excitations in the ion's charge-up process during the interaction with the XFEL pulse and demonstrates a good understanding of the underlying ionisation mechanism leading to the observed highly charged ions.
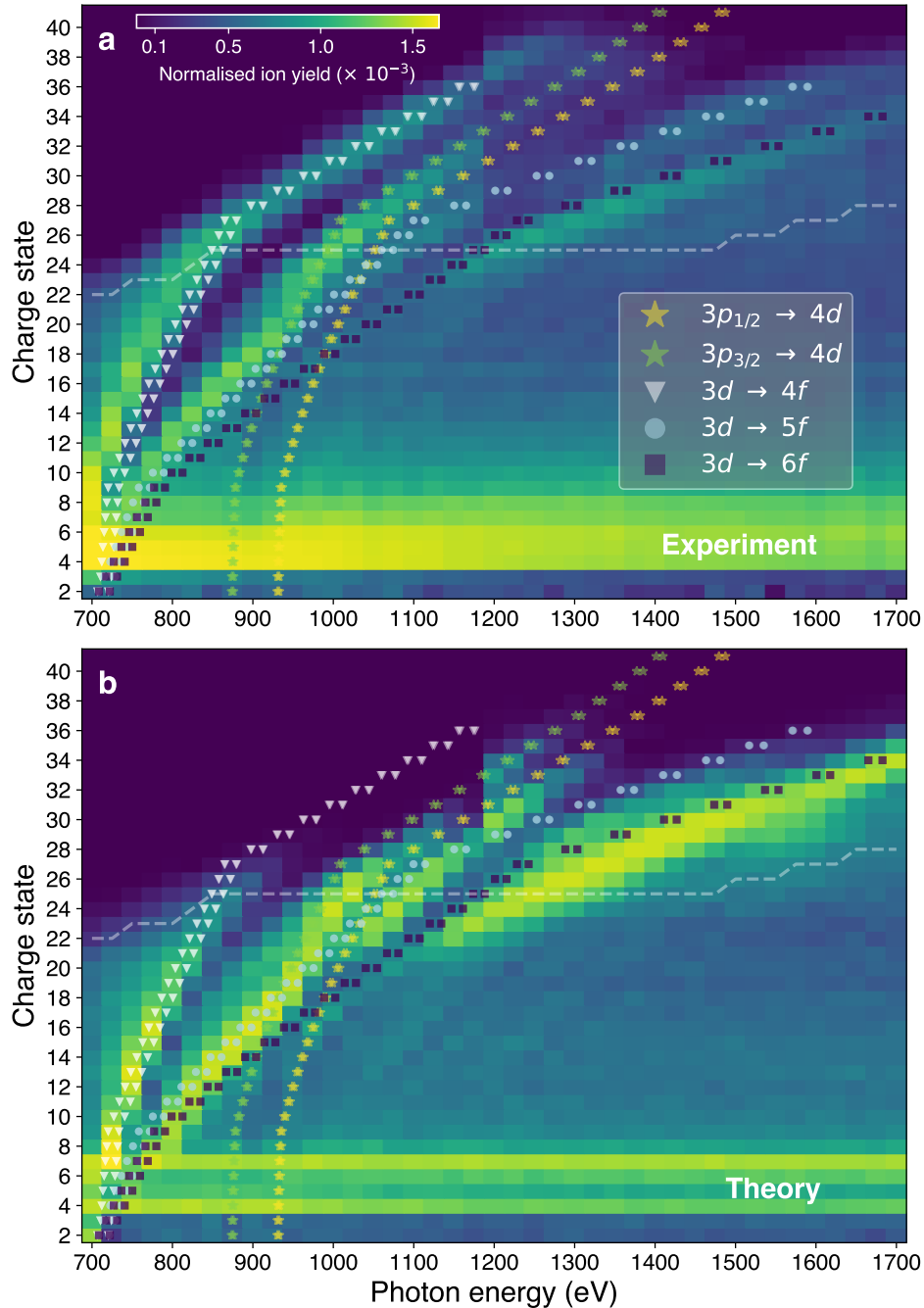
Figure 5.17: Experimental **a** and calculated **b** xenon CSDs as a function of photon energy. Coloured markers show selected resonant transition energies in the ground-state configuration of each charge state $Xe^{(q-1)+}$. In **a**, the highest fluence (100%) was used. The theoretical results in **b** were volume-integrated [120] with a peak fluence of 1.2×10^{12} ph/µm². The white dashed line in both panels indicates the sequential direct one-photon ionisation limit. The ion yields are normalised to the sum of all detected (calculated) ion yields for all photon energies in the experimental (theoretical) data set. The discontinuity at $1200\,\mathrm{eV}$ in **a** is due to a change in the beamline optics (s. Sec. 5.1.1). The colour scale in **a** also applies to **b**. This figure was similarly published in Ref. [57].

However, there are some noticeable differences. The experimental CSDs show a marked void between the two ion-yield branches around 800–1000 eV, which is less pronounced in the theoretical CSDs, and a small shift of $\sim$25 eV (similar to the PCSs in Fig. 5.11) between the experiment and theory towards higher photon energies, best seen between 700–800 eV, attributed to the finite accuracy of the electronic structure method used in XATOM. Moreover, the highest charge states observed in the experiment, around 1000–1400 eV, are missing in Fig. 5.17 **b**. As a consequence, the ion yield piles up for the intermediate charge states (Xe^{22+} to Xe^{32+}), thus enhancing structures related to the $3d \rightarrow 6f$ excitation. The highest charge states can be reproduced by increasing the peak fluence in the calculation beyond the calibrated peak fluence. On the other hand, the theoretical CSDs show a structure around Xe^{22+} to Xe^{26+} at 700–800 eV, which is absent in the experimental data. This can be attributed to a reduced peak fluence at these photon energies in the experiment.

Fig. 5.17 **a** shows a dip around 925 eV at Xe^{18+}, which corresponds to an empty $4d$ subshell, in the ion yields originating from the superposition of $3d \rightarrow 5f$ and $3p \rightarrow 4d$ lines. After this, the ion yields are mainly enhanced along the $3p_{1/2}/3p_{3/2} \rightarrow 4d$ lines until 1200 eV. For the $3d$ subshell, the shift in electron binding energy attributable to spin-orbit coupling $3d_{3/2}$ and $3d_{5/2}$ is relatively minor, in contrast to the significant shifts observed for the $3p$ subshell (s. yellow and green stars in Fig. 5.17). This highlights the necessity of incorporating relativistic effects, such as spin-orbit coupling, in the calculations [21].

It becomes visible that the experimental ion yields in **a** for photon energies 700 eV to 850 eV and charge states $< Xe^{26+}$ are shifted from the energy transition line $3d \rightarrow 4f$ towards lower energies, yet following the trend of the line and not far exceeding the sequential direct one-photon ionisation limit. This phenomenon can be explained by resonant excitations in precursor charge states distinctively lower than $Xe^{(q-1)+}$. Most of the ion yield maxima in Fig. 5.17 **a** do indeed follow the general trend of the resonant transitions, but it will become apparent in the following that a correct assignment of the resonances requires considering complicated multiple ionisation dynamics during the FEL pulse in detail.

The subshells nf, with n=4–6, are not occupied in the ground-state configuration and can be reached via resonant excitation from the $3d$ subshell independently of a formerly created vacancy. In contrast, the transitions lines $3p_{1/2}/3p_{3/2} \rightarrow 4d$ belong to the so-called "hidden" resonances [130], meaning that resonant excitations become only possible if there is at least one vacancy in the higher-lying $4d$ subshell. In the ground-state configuration, at least Xe^{9+} is needed for a vacancy in the $4d$ subshell. In the relaxed ground state of Xe^{36+}, electron excitations of the $3d$ subshell are no longer possible since no electron is left. This is the reason why the $3d \rightarrow 4f$ and $3d \rightarrow 5f$ transition lines already ends at Xe^{36+} in Fig. 5.17. However, the experimental results clearly show the enhanced ion yields along the $3d \rightarrow 4f/5f$ transition lines beyond Xe^{36+}, which indicates not relaxed core holes in the $3s$ and $3p$ subshell and a still partly occupied $3d$ subshell.

5.3   Fluence (in)dependence

The fluence dependence of the photon-energy scan was investigated for three different fluence regimes, 0.1, 0.5 and 1.0×10^{13} photons per pulse (10%, 50% and 100%).

5.3.1   Resonance spectra

The panels **a**–**d** in Figure 5.18 show three experimental data sets (100% = yellow, 50% = purple, and 10% = dark blue) and **e**–**h** theoretical ion yields for six different peak fluences (coloured lines) as a function of photon energy for four exemplary charge states Xe^{15+}, Xe^{21+}, Xe^{25+} and Xe^{37+}, dubbed resonance spectra. The charge states are selected in such a way that they represent a specific resonant behaviour. The labelling A–N in the calculations are used as identifiers for the respective peaks, which will be used in the analysis. The experimental data were additionally assigned the theoretical labels A–N by identifying the experimental equivalent, except for peak F, which is absent in the experimental data. The experimental ion yields correspond to horizontal lineouts of Fig. A.5 **a-c** and were normalised to the gas pressure.

Besides the photon-energy dependence, the resonance spectra expose another critical parameter: The peak fluence, which is generally assumed decisive for the resulting charge states in X-ray multiphoton ionisation [21, 23, 25, 50]. These resonance spectra significantly reduce the experimental data derived from three 2D colour maps. Nevertheless, they effectively visualise the dependence on fluence with clarity while preserving the relevant information. For the complete dataset, presented as the three 2D colour maps, the reader is advised to refer to Fig. A.5 in Appendix A.6.

The panels **a** and **e**, showing the resonance spectrum of Xe^{15+}, display two marked peaks in ion yield, labelled as A and B. These two peaks, A and B, are resonances and correspond to a particular resonant transition of a bound electron to a higher-lying unoccupied orbital. In this particular case, the underlying transition can be quickly identified by following the energy transition lines in Fig. 5.17 until Xe^{15+} at the photon energies 725 eV as $3d \rightarrow 4f$ (A) and 850 eV as $3d \rightarrow 5f$ (B). The deep valley between peaks A and B at 775 eV indicates a depletion of Xe^{15+}, suggesting that it is likely subject to further ionisation.

Comparing the calculations with the experimental data, the two peaks show different positions on the photon-energy axis in their respective panel. Experimental (exp.) peak A is located at 725 eV in **a** and the theoretical (theo.) equivalent at 775 eV in **e**, and exp. peak B is located at 850 eV in **a** and theo. peak B at 875 eV in **e**. The overall average offset between theory and experiment is about 25 eV towards higher photon energies, and the experimental spectral resolution is 25 eV. Despite the seemingly large difference of 50 eV for peak A for theory and experiment, the agreement is still acceptable.

Further, the resonance spectrum for Xe^{15+} in Fig. 5.18 **a** is entirely insensitive to the peak fluence as of a peak fluence of 0.50×10^{12} ph/µm² in both experiment and theory. For Xe^{21+} and Xe^{25+} in panel **b** and **c**, the overall shapes of the resonance spectra similarly remain unchanged for the experimental data sets 50% and 100% and the theoretical ion yields as of 0.50×10^{12} ph/µm². Most striking is the strongly fluence-dependent peak F around 725 eV in the calculations in panel **g**, which is absent in the experimental data, albeit consistent with a peak fluence of approximately

0.30×10^{12} ph/µm² at this photon energy, matching the fluence calibration. Only peak G is visible in the experimental data, equivalent to peak G at a peak fluence of 0.50×10^{12} ph/µm² in panel **g**.
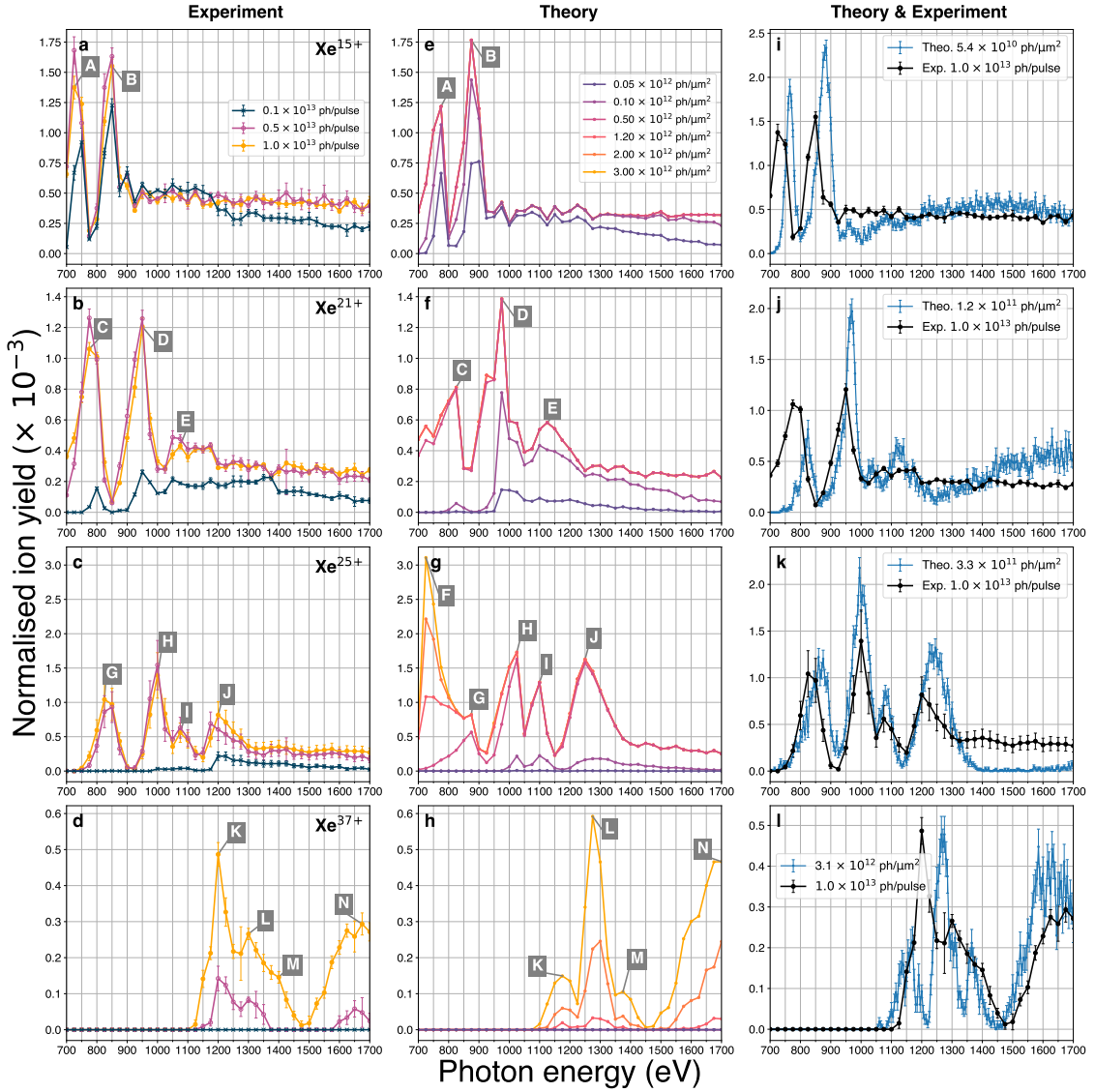
Figure 5.18: Experimental and theoretical resonance spectra for the charge states Xe^{15+}, Xe^{21+}, Xe^{25+} and Xe^{37+}. Panels **a-d** show the experimental data sets for 10%, 50%, and 100%. Panel **e-h** show volume-integrated calculations for different peak fluences in different colours. Panel **i-l** show calculations without volume integration and experimental data. Theoretical error bars indicate the statistical uncertainty. The 100% data set is normalised in the same manner as in Fig. 5.17, whereas the 50% and 10% data sets are scaled relative to the 100% data set, ensuring that the ion yield of Xe^{4+} at 1325 eV is equivalent across all three data sets. This figure was similarly published in Ref. [57] without the experimental data set corresponding to 10% and the calculated data set for 0.05 and 0.10×10^{12} ph/µm².

In Fig. 5.18 **d** and **h**, showing Xe^{37+}, the resonance spectrum shows no saturation for the complete photon-energy range in the investigated fluence regimes and instead increases nonlinearly with the peak fluence. As of Xe^{32+} (not shown here), no saturation behaviour can be observed anymore in theory and experiment for the whole photon-energy range.

To further analyse this behaviour, it is essential to investigate the underlying processes in greater detail. Using the calculations, a histogram can be generated that distinguishes between photoexcitation, photoionisation, and Auger-Meitner decay for all peaks (A–N), providing the average occurrence of each respective process. This is shown in Figure 5.19.
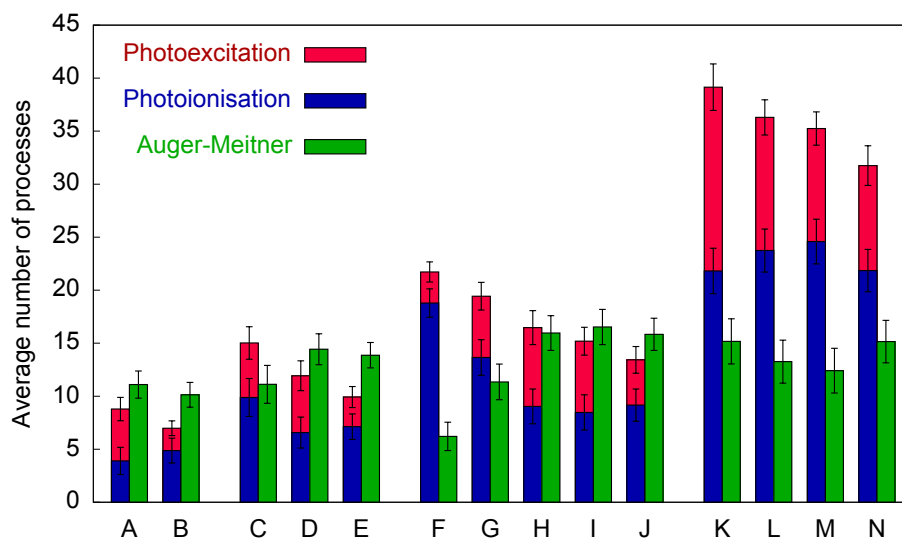
Figure 5.19: Histogram of photoabsorption and Auger-Meitner events for the peaks A–N labelled in Fig. 5.18. This figure was similarly published in the Supplementary Information of Ref. [57].

For the peaks F, G, and K–N, the number of photoionisation events surpasses the number of Auger-Meitner decay events, as illustrated in Figure 5.19. Auger-Meitner decay is the prevailing mechanism for getting to the final charge state for the remaining peaks. In case a resonant excitation occurs in the outermost shell, for instance, peaks K–N, only a few higher-lying (excited) electrons are available for relaxation, making Auger-Meitner decays less likely.

This equals a shift in the dominant ionisation mechanism because Auger-Meitner decay needs higher-lying electrons to fill a core hole. As of Xe^{26+}, the M shell becomes the valence shell in ground-state configuration, meaning that either higher-lying electrons from preceding resonant bound-bound excitations are available or electrons in partially filled N and O shells when the ion has multiple core holes in the M shell. As a reminder, in the studied photon-energy range, the theoretically maximum possible charge state is Xe^{44+}, which cannot be overcome without increasing the photon energy beyond the L-shell binding energy of xenon or drastically increasing the peak fluence to make direct multiphoton processes possible.

Consequently, the peaks K–N, F, and G demonstrate a nonlinear relationship between peak fluence and ion yield in the resonance spectra illustrated in Figure 5.18. In this context, an ionisation event requires two photons to surpass the ionisation

potential: The first photon facilitates the resonant excitation of an electron to a vacant higher-lying orbital, while the second photon is required to ionise the excited electron. In contrast, an Auger-Meitner decay process necessitates only one photon. In Figure 5.18, these peaks have not yet attained saturation and remain responsive to the X-ray fluence. Furthermore, their resonance structures correspond to the highest charge states achieved at the respective photon energies. Notably, this indicates that peaks K–N are also observed in the resonance spectra of Xe^{41+}.

This finding is critical for volume integration [Sec. 4.4] used in theoretical calculations. The independence of the peak fluence of the present data means that volume integration is not necessary to capture essential features of the data. To further demonstrate this, the corresponding resonance spectra calculated without volume integration are plotted in Figs. 5.18 **i-l**. Fixed fluences (indicated in the legends) are chosen as an average of fluences that maximise the respective ion yield for a given range of photon energies. In these panels, a smaller step size of 5 eV is used in theory, and the theoretical data are normalised such that the sum of their ion yields equals the sum of the experimental ion yields in a respective panel. In each panel of Fig. 5.18 **i-l**, the peak structure is well reproduced, displaying the same characteristics as the volume-integrated spectra in the panels **e-h**, except for Xe^{25+} in panel **k**, where peak F is missing since the selected fluence is too low. Given this drastic simplification, the agreement of the calculated charge-state-specific resonance spectra with the experiment is still surprisingly good, illustrating that each charge state selects its own local fluence.

In summary, the calculations effectively replicate the positions of the minima and maxima at specific photon energies within the spectra and reflect the overall trend for higher photon energies. However, notable deviations remain, such as peak C in panel **f** and peak F in panel **g** of Figure 5.18, along with a general shift of approximately 25 eV of the theoretical ion-yield maxima towards higher photon energies compared to the experimental results. Furthermore, Figure 5.18 demonstrates that, beyond a certain saturation threshold (in terms of the number of photons or peak fluence), the overall resonance spectra become independent of the peak fluence for individual intermediate charge states within the observed photon energy range. Saturation occurs also partly for individual peaks in the resonance spectra.

5.3.2 Pulse-energy scan for fixed photon energies

Using the GATT, pulse-energy scans for the fixed photon energies 700 eV, 950 eV, 1200 eV, and 1325 eV were performed over more than two orders of magnitude to gain more insights into the saturation behaviour of the ion yields of different charge states, as first encountered in the resonance spectra in Fig. 5.18. The section starts with the pulse-energy scan at 1325 eV, at which the highest detected charge state of Xe^{41+} was observed.
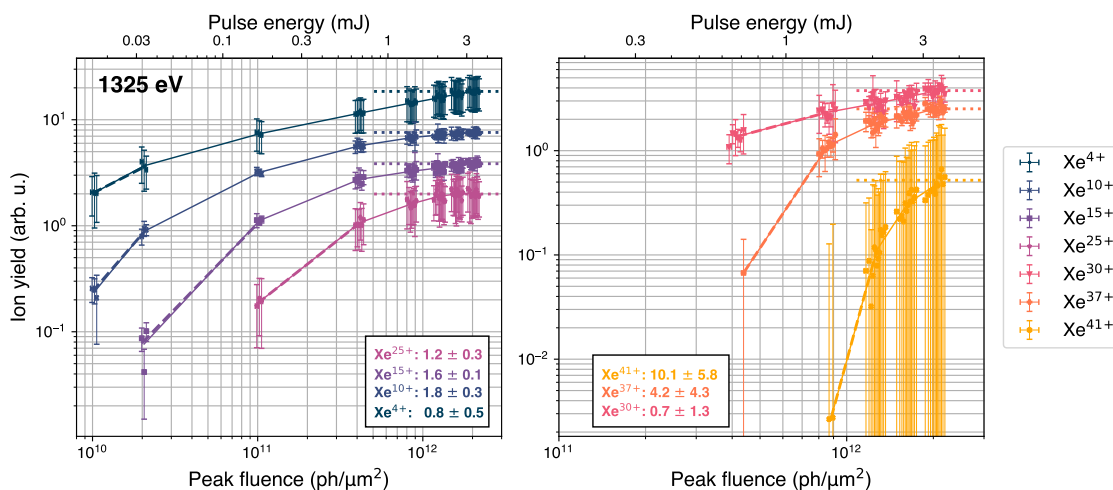
Figure 5.20: Log-log plot of the peak-fluence dependence for different charge states at 1325 eV.

Fig. 5.20 shows the experimental ion yields of several charge states as a function of peak fluence for the photon energy of 1325 eV in a log-log plot as coloured markers. In addition to the peak-fluence axis, a pulse-energy axis is depicted on top, which is the measured parameter in the experiment. The conversion of pulse energy to peak fluence was done by using Eqs. 5.3 and 5.4 and employing the calculated focus size [Fig. 5.5]. Eight groups of data points show the data, each representing a run with a different GATT transmission. Starting from left to right, these values are: 0.5%, 1%, 5%, 20%, 40%, 60%, 80%, and 100% with an initial pulse energy of 4.8 mJ.

Each run is, in turn, divided into several data points accomplished by binning the pulse-energy distribution of a respective run with a statistically sufficient amount of FEL shots in each bin. As mentioned in Sec. 4.1.7, the binning of the pulse-energy distribution must be treated with caution since two FEL shots with the same pulse energy do not automatically mean that both shots share the same set of parameters, such as the beam pointing or the pulse duration. However, this does not affect the overall dependencies between the data point groups (runs) over the full pulse-energy range.

Each group of data points is connected to the next group by linearly connecting the mean of each data point group with a solid line in the same colour as the charge-state marker to guide the eye. The horizontally dotted lines correspond to the respective charge state by colour and display the mean ion yield of the last group of data points (GATT 100%) to offer insight into the convergence of the ion yields. The tilted

dashed lines for the charge states Xe^{4+}, Xe^{10+}, Xe^{15+} and Xe^{25+} in the respective colour of the charge state represent the linear slope of the first two data point groups and correspond to the number n, which will be explained later in the text together with values in the lower right corner of the left panel.

Overall, the ion yields increase nonlinearly with increasing peak fluences and flatten at high peak fluences. The slopes of the curves also get steeper for higher charge states. The steeper-getting slopes for higher charge states, beyond the onset of saturation, is a well-known behaviour [22, 25], which can be described by LOPT, stating that the ion yield is proportional to the nth power of the peak fluence ($\propto F_0^n$), where n is the average number of sequentially absorbed photons involved in the ionisation process to reach a given charge state [37, 44]. Thereby, n does not have to be an integer since it stands for the average number of absorbed photons involved, which means that all contributions from the different ionisation processes, such as Auger-Meitner decay and photoionisation, are weighted included.

As mentioned before, at a fixed photon energy, the number of absorbed photons n increases for higher charge states, which in turn leads to a steeper slope of the ion yield on a log-log plot ($\propto n \cdot \ln\{F_0\}$). A fit with the model $Y(f) = A \cdot F_0^n$ (similar to Ref. [22]) was used to obtain n from the data. The result can be found in the lower right corner of the left panel in Fig. 5.20.

For Xe^{4+}, the obtained slope of 0.8 falls within the error margin of the energetic minimum of absorbed photons [43] and corresponds to the calculated average number of absorbed photons, denoted in the following by $\bar{N}_{\mathrm{ph}}^{(\mathrm{abs})}$, of one at 1325 eV. This average, derived from Fig. 5.13, will be referenced throughout the analysis. For Xe^{10+}, the requirement of one photon corresponds with the obtained slope of 1.8; however, $\bar{N}_{\mathrm{ph}}^{(\mathrm{abs})}$ shows a significant deviation of 3.4. The measured value of 1.6 for Xe^{15+} is also insufficient, as this charge state necessitates at least two photons for its creation, while $\bar{N}_{\mathrm{ph}}^{(\mathrm{abs})}$ approaches six. The retrieved value 1.2 for Xe^{25+} considerably diverges from the energetic minimum of seven photons and from $\bar{N}_{\mathrm{ph}}^{(\mathrm{abs})}$, which equals 14.6. The slope of the charge states Xe^{30+}, Xe^{37+}, and Xe^{41+} also exhibit significant deviations from $\bar{N}_{\mathrm{ph}}^{(\mathrm{abs})}$, with values of 23.5, 38.5, and 49.6, respectively.

These deviations demonstrate the model's inapplicability to the current data set, as the fitting model [22] is designed to approximate the initial slope far from any saturation regimes. In Fig. 5.20, the slopes for the charge states Xe^{15+} to Xe^{41+} are close to the saturation regime, as their deviations from a slope of zero – which signifies saturation – are smaller than those from $\bar{N}_{\mathrm{ph}}^{(\mathrm{abs})}$.

Fig. 5.20 shows that only charge state Xe^{25+} saturates and all other charge states have not yet reached saturation. For example, charge state Xe^{4+} show a shallow monotonical increase in ion yield without saturation. This means that the assumption of a single spatial Gaussian profile, as done in Sec. 4.4, is incorrect (see also Fig. 3 (c) in Ref. [79]). Also, a double Gaussian beam profile does not change the overall saturation behaviour, as shown in Sec. 4.4. This means that at the edges of the beam profile, the area of a fluence regime, where, for example, Xe^{4+} is created, is not constant and causes the ion yield to increase further for higher peak fluences. In contrast to Xe^{25+}, where the approximation by a spatial Gaussian profile remains applicable as the fluence range in which Xe^{25+} occurs entirely in the fluence distribution of the beam [Sec. 4.4]. The charge state Xe^{41+} does not show an onset of saturation and is consistent with the ion yield without volume integration in Fig. 4.48, where the ion yields have not yet peaked in the observed peak-fluence

range.

In summary, this supports the notion of a limited fluence range where a higher charge state, such as Xe^{25+}, gets created because lower charge states, for example, Xe^{4+}, are still increasing in ion yield and consequently available when charge state Xe^{25+} saturates. Thus, lower charge states are not responsible for the depletion of Xe^{25+}.

A peak-fluence scan at different photon energies was done to study the dependence of the saturation peak fluence compared to the calculations. Fig. 5.21 display the extended pulse-energy scan showing additionally to 1325 eV (yellow markers and lines) the photon energies 700 eV (dark blue), 950 eV (purple) and 1200 eV (red) for the charge states Xe^{15+}, Xe^{25+}, Xe^{30+}, and Xe^{37+}. Every row, comprising three columns, belongs to the labelled charge state in the first column. The first column (**a**–**d**) shows the experimental data connected similarly as in Fig. 5.20, and the second column (**e**–**h**) shows the calculated, volume-integrated ion yield as a function of the number of photons ($= \frac{F_0}{a\Delta}$, with $\Delta = 1$ µm^2). The third column (**i**–**l**) displays the ion yields without volume integration as a function of the number of photons.

All experimental ion yields were normalised to the gas pressure in the interaction volume. The calculations in **e**–**h** are normalised to the highest experimental ion yield for a respective charge state at 1325 eV and were volume-integrated with a single Gaussian beam profile. In **i**–**l**, the ion yields are normalised to one for every photon energy in a respective charge-state panel. Further, the experimental ion yields are not converted to peak fluence since the focus size was not measured but only estimated by theory and differs for each photon energy. Instead, the ion yields are a function of the number of photons on target per pulse, measured by the downstream XGM. The GATT transmissions at 700 eV were 0.1%, 0.5%, 1%, 8%, 50% and 100%; at 950 eV: 20%, 30%, 40%, 60%, 80%, and 100%; at 1200 eV: 0.1%, 0.5%, 1%, 5%, 10%, 50%, and 100%, with the initial pulse energies of 5.5 mJ, 6.6 mJ, and 4.9 mJ.

The relation of the saturation ion yields differs from the calculations for the charge states Xe^{15+} and Xe^{25+}. However, the saturation dependence in Fig. 5.21 at different photon energies supports that the resonance spectra in Fig. 5.18 become independent of the X-ray fluence as soon as the saturation regime is reached. In general, the saturation peak fluence is a function of the charge state and photon energy: It shifts for higher photon energies towards lower peak fluences and for higher charge states towards higher peak fluences. The observed saturation behaviour confirms that a given charge state is created in a narrow fluence range, as shown in panels **i**–**l**.

For 700 eV in **c**, the charge state Xe^{25+} begins to emerge at 2.0×10^{13} ph/pulse, which is consistent with peak F in the calculations in the resonance spectrum of Xe^{25+} in Fig. 5.18, albeit with a higher needed fluence. For Xe^{37+} in **e**, the ion yields of 1200 eV and 1325 eV show no saturation and reflect the general underestimation of the calculations for higher charge states.

An onset of saturation has also been measured in former multiphoton absorption studies in the soft [22, 25, 50] and hard [21] X-ray regimes. Still, the peak fluence in those experiments was insufficient to reach a constant ion yield for many charge states.
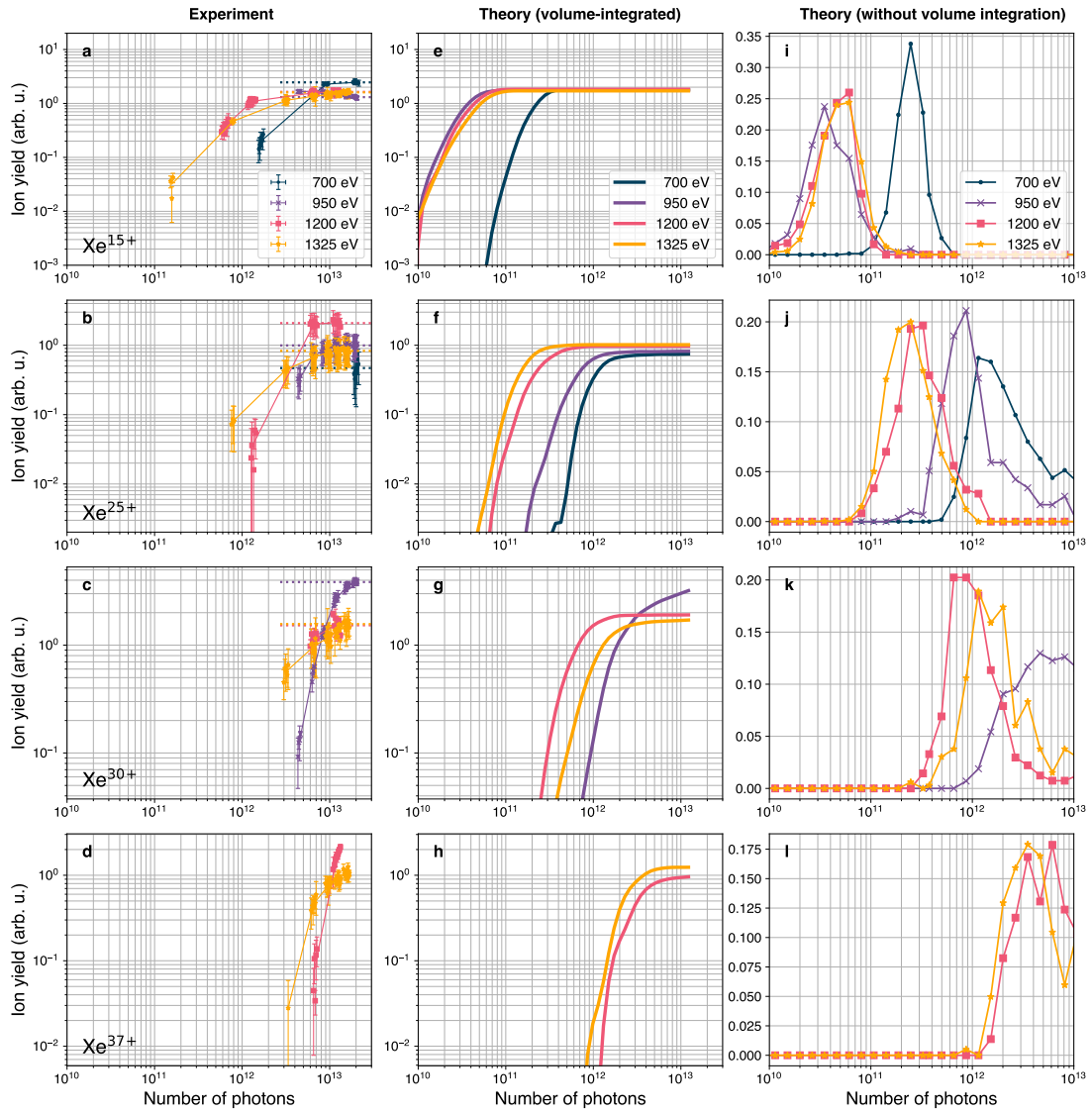
Figure 5.21: Log-log plot of the peak-fluence dependence for different charge states at 700 eV, 950 eV, 1200 eV and 1325 eV.

5.3.3 Transition assignment in ground state

In addition to the resonance spectra in Fig. 5.18, Fig. 5.22 display the experimental resonance spectra (solid coloured lines) of the 100% data set of the four charge states Xe^{q+} with q=15, 21, 25, or 37, using the same labels A–N. Additionally, the calculated PCSs (dashed coloured lines) corresponding to the respective direct precursor charge states $Xe^{(q-1)+}$ are also depicted.

The coloured vertical bars in each panel represent the energy positions of the energetically possible transitions based on the transition energy lines with the selection rules $\Delta l = \pm 1$ and $\Delta j = 0, \pm 1$. Transitions with a PCS < 1.5 Mb for Xe^{15+}, Xe^{21+}, and Xe^{25+} and PCS < 0.5 Mb for Xe^{37+} are not shown. On top of each panel are the labels of the resonant transitions. Sometimes, more than one vertical bar corresponds to a label because they resolve the spin-orbit splitting, and the annotation does not. All data of the theoretical calculations are shifted by 25 eV towards lower photon energies to compensate for the overall energy shift in the calculations.

Utilising Fig. 5.22, several peaks (except F, I, and N) in Fig. 5.18 can be attributed to resonant transitions in the precursor charge state and are listed in Tab. 5.2.

Peak	Assignment
A	$3d \to 4f$
B	$3d \to 5f$
C	$3d \to 4f$
D	$3d \to 5f$
E	$3d \to 7f$
F	-
G	$3d \to 4f$
H	$3p_{1/2} \to 4d$
I	-
J	$3d \to 7f$
K	$3d \to 4f$
L	$3p_{3/2} \to 4d$
M	$3p_{1/2} \to 4d$
N	-

Table 5.2: Resonant transition-to-peak assignments in ground state based on Fig. 5.22.

Yet, this assignment approach does not work generally. The assigned transition of peak G does not correspond to an outer shell. However, it shows the same exceeding photoionisation events towards the Auger-Metiner decay events [Fig. 5.19] as the peaks K–N, indicating a wrong transition assignment. Peak K seems to belong to the transition $3p_{3/2} \to 4d$, albeit with a difference of 75 eV, despite the compensated shift. The assignment of the resonant transitions used here will be re-evaluated in the next section, revealing a deeper analysis of the resonances by thoroughly tracing back the last resonant excitation, leading to a given final charge state to its charge state and photon energy.
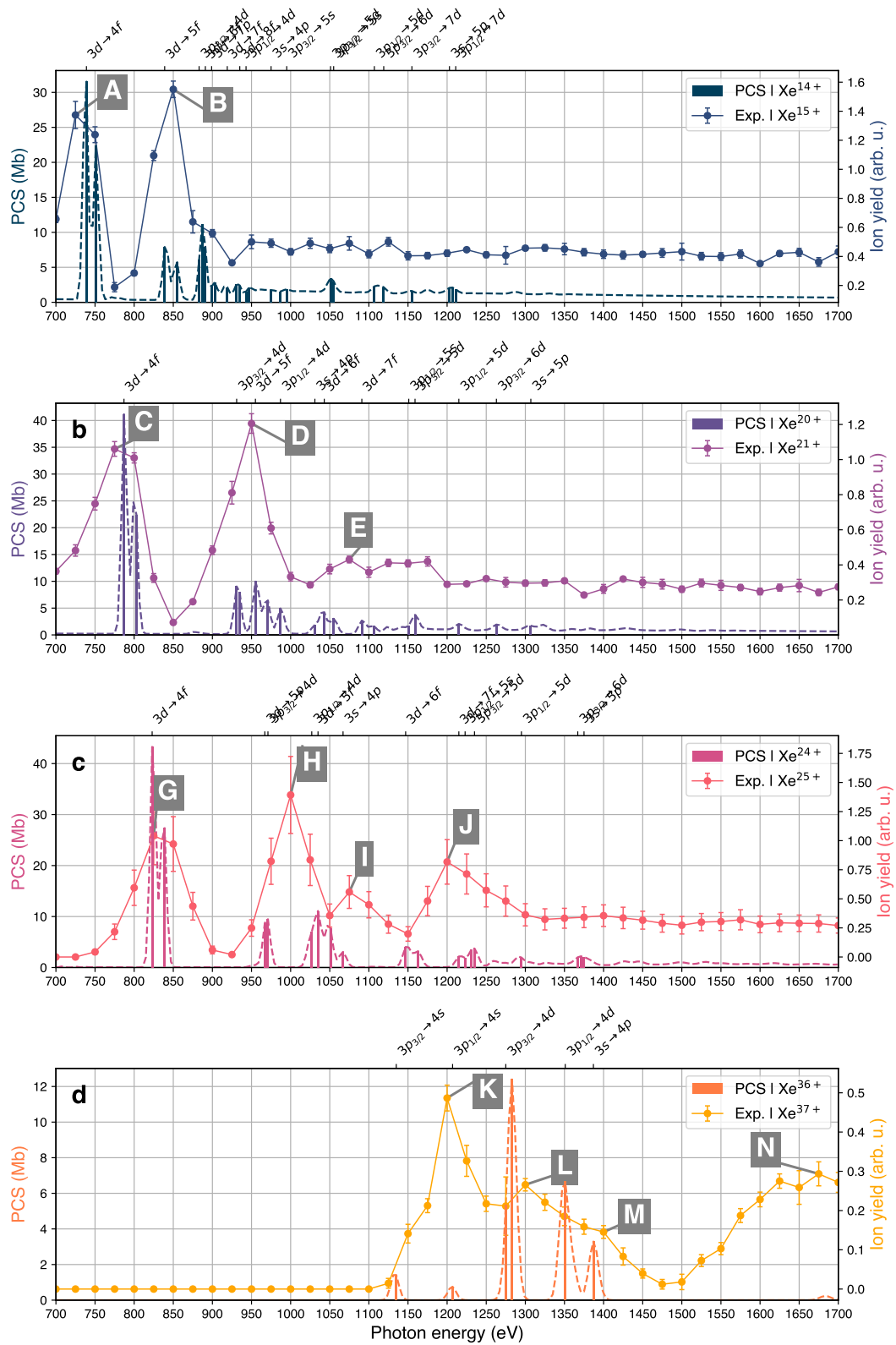
Figure 5.22: Calculated PCSs for the charge states Xe^{15+}, Xe^{21+}, Xe^{25+}, and Xe^{37+} labelled with the corresponding resonant transitions.

5.4 Multiple-core-hole states

This section investigates the temporal evolution of the charge-up process and provides proper assignments of the last resonant transitions underlying the resonance structures in Fig. 5.18.

Fig. 5.23 displays one exemplary ionisation pathway as a function of time to reach the final charge state Xe^{25+} at a photon energy of 1250 eV and corresponds to the peak J in Fig. 5.18. This particular ionisation pathway is a good example of multiple-core-hole states, exhibiting the highest number (six) of transient M-shell core holes along the charge-up process during a single XFEL pulse. The y axis marks the temporary charge state, and the grey-shaded area symbolises the temporal evolution of the XFEL pulse with a pulse duration of 10 fs (FWHM). After 25 fs, the time axes are on a logarithmic scale because the last fluorescence event happens at 1.5×10^4 fs.

The top panel shows the ionisation pathway and distinguishes between four events: photoionisation (blue vertical lines); Auger-Meitner decay, including Coster-Kronig decay (green vertical lines); resonant excitation (red dots); and fluorescence decay (orange dots). The bottom panel depicts the temporary core holes in the M shell as a function of time with the blue-shaded area. At the peak of the pulse at around 15 fs, the maximum of six simultaneous M-shell core holes, accumulating during the pulse, is reached at the charge states Xe^{17+} and Xe^{18+}, which have a calculated lifetime of 0.75 fs and 0.80 fs, respectively. The last resonant excitation $3d \rightarrow 6f$ happens at charge state Xe^{17+} after 14 fs, and the last photoabsorption at Xe^{21+} after almost 17 fs. At the time of the last resonant excitation at Xe^{17+}, the transient electronic configuration exhibits five M-shell core holes, which subsequently increases to six M-shell core holes following the last resonant excitation.

As the charge state gets relatively high, ionisations via Auger-Meitner decay become less probable because only a few higher-lying electrons remain, increasing the core-hole states' lifetime. The first photoabsorption in the ionisation path of Xe^{25+} ionises a $3s$ electron, creating an M shell core-hole which decays within a lifetime of only 0.054 fs, whereas the sextuple-core-hole state at Xe^{17+} lasts 0.75 fs. After 15 fs, the quadruple-core-hole state $3d_{3/2}^{-2}3d_{5/2}^{-2}$ created by decay of a quintuple-core-hole state at Xe^{19+} lasts 12 fs until 27 fs where Xe^{23+} decays to Xe^{24+} creating the triple-core-hole state $3d_{3/2}^{-2}3d_{5/2}^{-1}$, which lasts until 600 fs. After 617 fs, the last Auger-Meitner decay happens, and the remaining M-shell core holes relax via subsequent fluorescence events. The lifetimes of atomic species created via a sequence of core ionisation and excitation events vary by several orders of magnitude, depending on the charge state and the number of core holes.

In total, the neutral xenon atom has absorbed 14 photons consisting of four resonant excitations and ten photoionisations and underwent 15 Auger-Meitner and three fluorescence events. The relaxed ion Xe^{25+} has the final configuration $3s^23p^63d^{10}4s$. This visualisation of an ionisation pathway demonstrates that the pathway towards a final charge state Xe^{q+} is more complicated than sequentially ionising until $Xe^{(q-1)+}$. In the following, these intricate pathways will be further analysed.
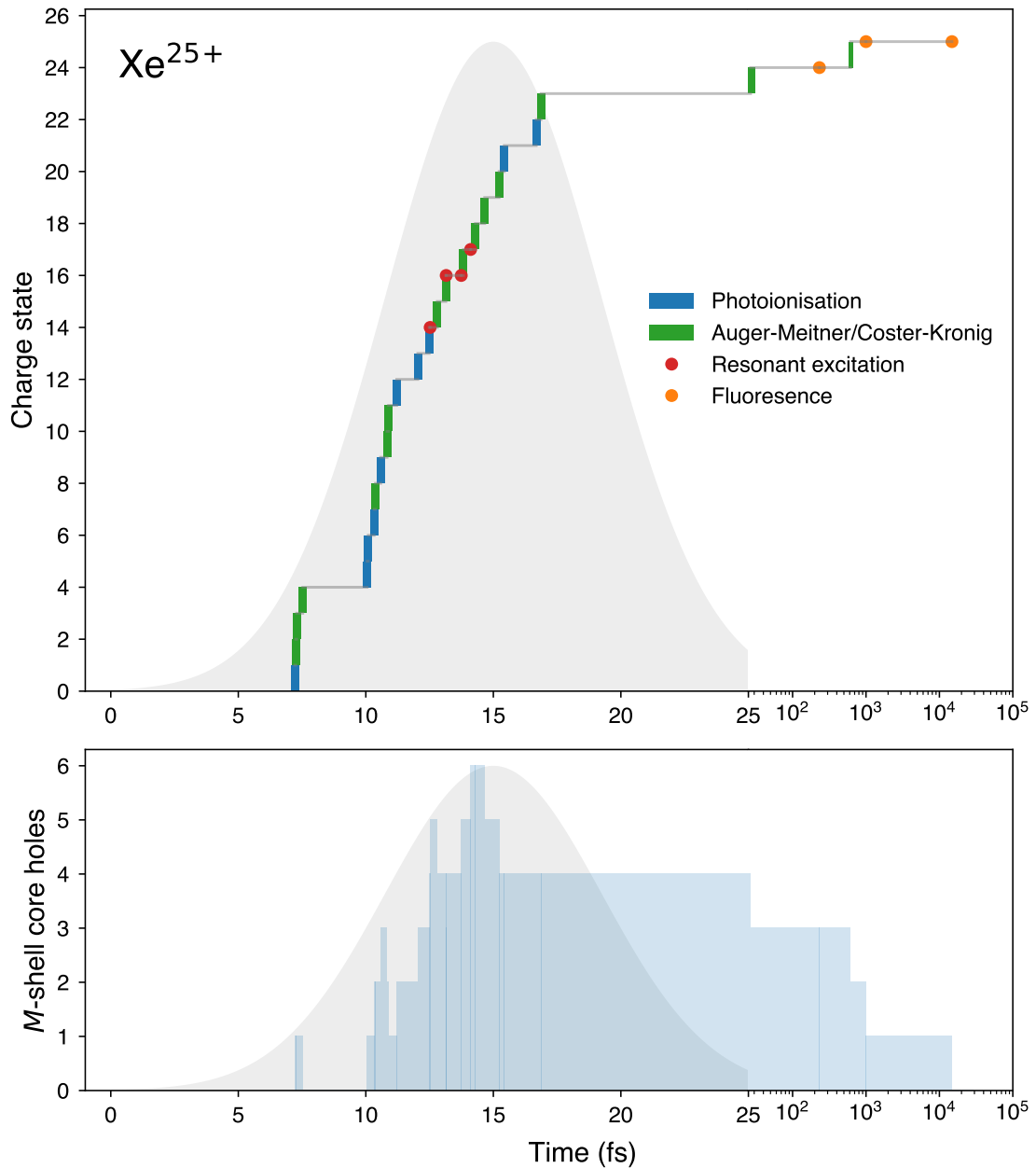
Figure 5.23: Exemplary ionisation pathway leading to charge state Xe^{25+} at 1250 eV. The grey-shaded area symbolises the temporal evolution of an XFEL pulse with a 10 fs FWHM Gaussian profile. After 25 fs, the x axis (time) is on a logarithmic scale. The figure was similarly published in Ref. [57] as Fig. 4 **b**.

Figure 5.24 shows six normalised histograms of the relative frequency of precursor charge states at which the last resonant excitation in a given ionisation pathway occurs, leading to a given final charge state Xe^{q+} within the XATOM calculations. The dominant last resonant excitation is specified in the title of each panel. Different colours indicate the number of M-shell core holes present at the time of the resonant excitations. Beyond Xe^{26+}, the M shell becomes the outermost shell; therefore, no M-shell core holes exist, as indicated by the grey colour in panel L. The selection of final charge states and photon energies rests on the maxima in the respective resonance spectra in Fig. 5.18 and are representative examples to demonstrate the wealth of information about the electronic structure and transient resonances coalesced in a peak. The labelling corresponds to the labelling in Fig. 5.18 **e-h**.
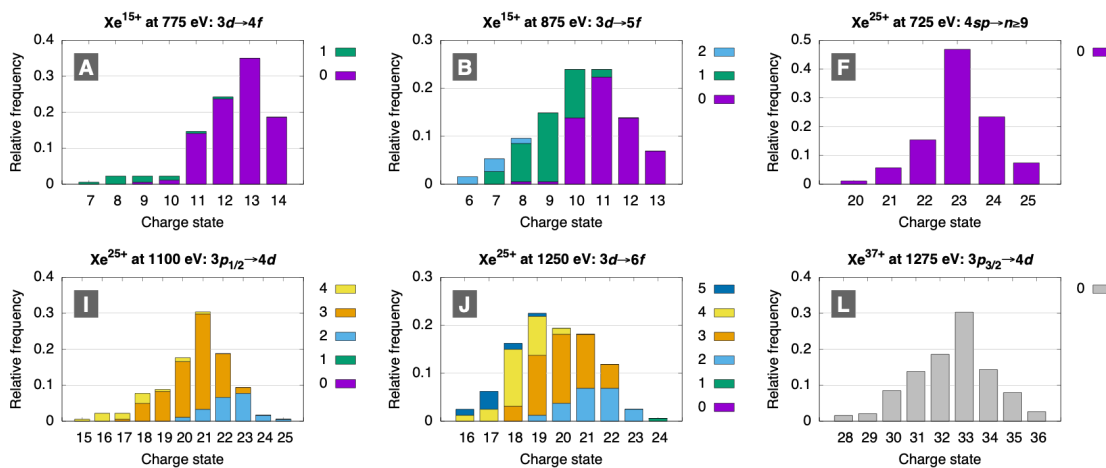
Figure 5.24: Normalised histograms of the precursor charge states at which the last resonant excitation resulting in a given final charge state occurs. The figure was published in the Supplementary Information of Ref. [57].

Panel A analyses peak A in Fig. 5.18 **e** at the photon energy of 775 eV of the charge state Xe^{15+} and shows that the resonant excitation $3d \rightarrow 4f$ leading to Xe^{15+} can already happen at a charge state as low as Xe^{7+}, having a core hole in the M shell, but will most probably take place at Xe^{13+}, having no core hole in the M shell. X-ray multiphoton ionisation dynamics calculations are described by a statistical ensemble of Monte Carlo trajectories in electronic configuration space [25, 58]. Multiple resonant excitations can occur in each trajectory, but the decisive transition for the structures in the resonance spectra of the final charge state is the last one since it is the same for most trajectories leading to this charge state. All histograms show a wide distribution of precursor charge states, demonstrating that most of the last resonant excitations do not happen at the immediate precursor charge state $Xe^{(q-1)+}$, as assumed for the tentative assignments by the transition energy lines. To appropriately assign the peaks in the resonance spectra, the Monte Carlo trajectories through electronic configuration space were initially selected based on those leading to a specific final charge state at a fixed fluence, where the corresponding ion yield is maximised (see Fig. 5.18 **i-l**). These trajectories were subsequently classified by the last resonant transition, and the resonant transition occurring most frequently among the trajectories was identified as the most probable and is depicted at the top of each panel in Fig. 5.24. Tab. 5.3, which will be detailed later in the text,

shows for all peaks A–N in Fig. 5.18 the number N_T of trajectories with the assigned transition out of a total number of trajectories N_{tot}.

As mentioned in Sec. 5.3, the peaks A and B in Xe^{15+} in Fig. 5.18 **a** can be tentatively assigned to the transition $3d \rightarrow 4f$ and $3d \rightarrow 5f$ in Xe^{14+}, respectively. However, panel A reveals that for peak A, the resonant excitation $3d \rightarrow 4f$ happens most probably at Xe^{13+} to create the final charge state Xe^{15+}. Peak B already shows a more complex picture for the creation of Xe^{15+}, as the two most contributing precursor charge states Xe^{10+} and Xe^{11+} are even lower in charge state and possess a core hole in the M shell at the time of the resonant excitation. Furthermore, it is possible that a triple-core-hole state in the M shell of the charge states Xe^{6+}-Xe^{8+} leads to Xe^{15+}. The assignment $3p_{3/2} \rightarrow 4d$ to reach Xe^{37+} in panel L matches with the transition energy line at Xe^{36+}. Again, the histogram demonstrates that this transition mostly happens at lower charge states than Xe^{36+}. For the peaks F, I and J in Xe^{25+} in Fig. 5.18 **g**, the ion-yield maxima in Fig. 5.17 do not match with any of the transition energy lines at Xe^{24+}, pointing to a dependence besides the charge state, which will be further analysed in the following.

Fig. 5.25 illustrates the dependence of the PCS on the photon energy, the charge state, and the number of core holes for the resonant excitation $3p_{1/2} \rightarrow 4d$. This transition corresponds to the assignment of peak I at 1100 eV in the resonance spectrum of Xe^{25+} (s. Fig. 5.18 **g**). The cross sections are convolved with a Gaussian profile having a photon-energy bandwidth of 1%. Panel (a) depicts the PCSs for five different charge states Xe^{21+}-Xe^{25+}, whose centres move towards higher photon energies for increasing charge states due to the more attractive orbital binding energy (see also Fig. 5.14). Panel (b) takes the PCS of Xe^{21+}, which has the highest probability to lead to Xe^{25+} [Panel **I** in Fig. 5.24] and varies the number of simultaneous $3d_{5/2}^{-n}$ core holes, with n the number of core holes up to four. Compared to the ground state, the PCS's centre moves towards higher photon energies for increasing core holes by more than 20 eV per additional core hole. Panel (c) shows the PCS of Xe^{21+} with three core holes for different electronic configurations, comparing it to the ground state. The PCS shifts to higher photon energies for an increasing number of valence electrons in the O shell or holes in the N shell.

In summary, this underscores the complexity of electron-electron correlation effects in many-electron atoms, which significantly alters the electronic energy levels. The photon energy required for a resonant transition depends on the charge state and specific electronic configuration and may markedly differ from the assignment based on the ground state.
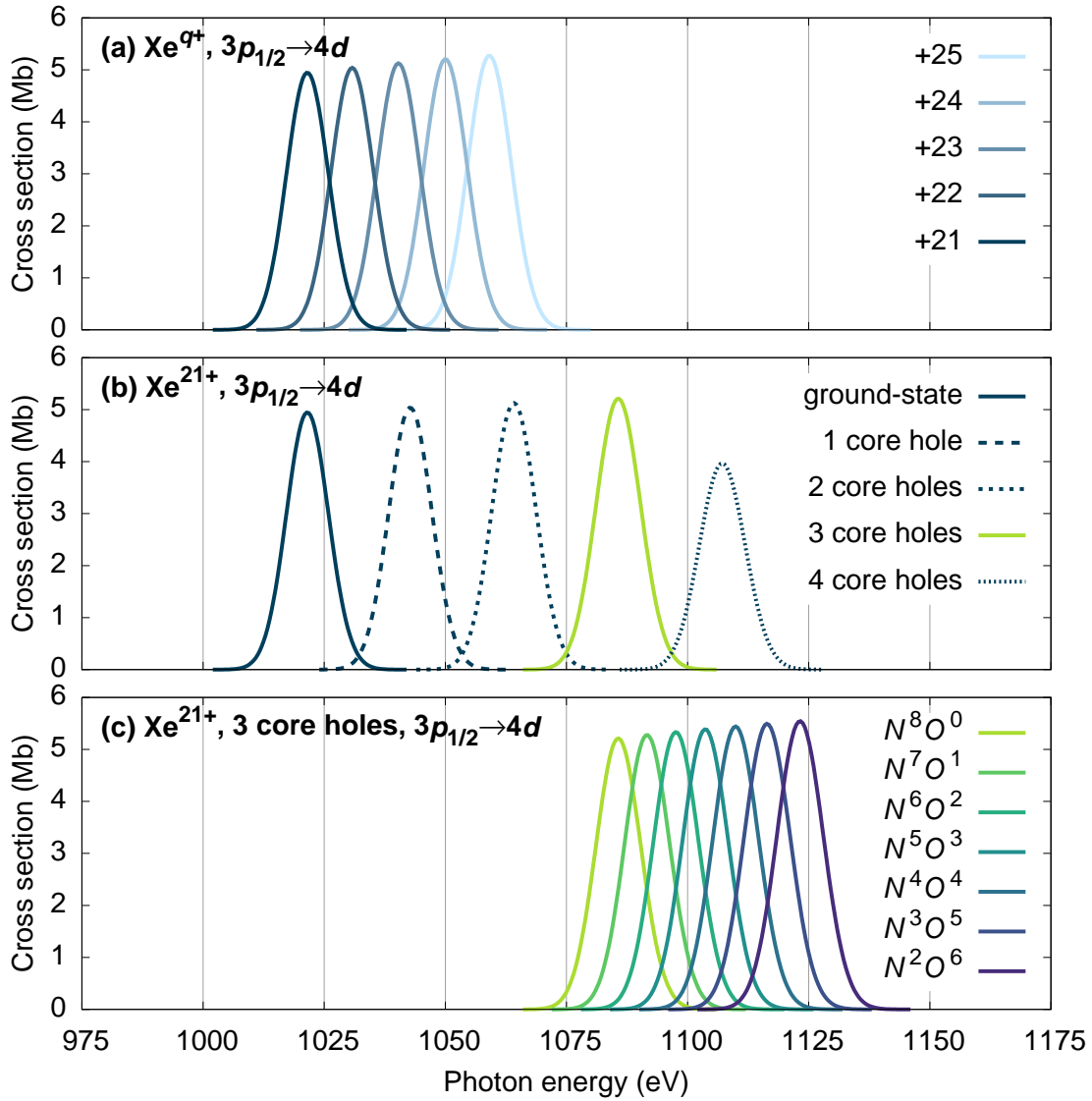
Figure 5.25: PCS for detailed electronic structure. The calculated PCS of specific $3p_{1/2} \rightarrow 4d$ transitions depends on (a) charge states (ground electronic configuration), (b) multiple core holes ($3d_{5/2}^{-n}$; n is the number of core holes), and (c) individual valence electronic configurations. PCSs were convolved with a photon-energy bandwidth of 1%. This figure was published in the Supplementary Information of Ref. [57].

The analysis of trajectories also allows the examination of transient single- or multiple-core-hole states during the charge-up. Lower precursor charge states exhibit the highest number of core holes, for example, four or five core holes at Xe^{16+}. Panels A and B demonstrate that single and double core holes are present at lower charge states when the respective resonant excitation happens, which finally leads to Xe^{15+}. In the case of Xe^{25+}, the trajectory analysis reveals that the transitions $3p_{1/2} \rightarrow 4d$ and $3d \rightarrow 6f$ are responsible for the peaks I and J in Fig. 5.18 **g**. They are created exclusively via the decay of multiple core holes, which explains why the preliminary assignment of the transition fails. Triple core holes are the overall dominant contribution for peak I, and thus also present in the most probable precursor charge state Xe^{21+}. For peak J in Xe^{25+}, up to quintuple core holes are traced for the precursor charge states Xe^{16+}-Xe^{19+}. The last excitation creates one additional M-shell hole, i.e., sextuple core holes are present after the last excitation, for example, $3d \rightarrow 6f$ in Xe^{17+} in panel J. This is an impressive demonstration of the complexity of the transient electronic structure emerging upon the interaction of matter with ultraintense X-ray pulses.

As mentioned in Sec. 5.3, the situation is different for the peaks F and L because the resonant excitations occur from the respective outermost shells of the ground-state configurations. Peak F in Xe^{25+} corresponds to a transition from the N shell (n=4), the outermost shell for $+8 \leq q < +26$. For peak L in Xe^{37+}, the M shell is the outermost shell for $q \geq +26$. When the excitation happens at the outermost shell, only a few higher-lying (excited) electrons are available. The dominant path to the final charge state is thus not through Auger-Meitner decay but via additional photoionisation events, as seen in Fig. 5.19 for peaks F and L. This is a manifestation of X-ray resonance-enabled multiphoton ionisation (XREMPI) [131], where a resonant transition excites an electron and further photoabsorption eventually ionises the excited electron. While the XREMPI process requires additional photons, Auger-Meitner decay in REXMI does not. This implies that peaks that are dominated by XREMPI depend more strongly on the X-ray fluence compared to REXMI-dominated peaks. This is consistent with the results in Figs. 5.19 and 5.18, where peaks F and L are sensitive to the peak fluence, while others are not. This demonstrates that saturation happens at lower peak fluence for multiple-core-hole-mediated processes like REXMI but requires much higher peak fluences for XREMPI processes. Tab. 5.3 lists for all labelled peaks A–N in Fig 5.18 the assigned dominant transition T, as shown in Fig. 5.24. Additionally, the tentative assignment of the resonant transition in the ground state is listed [Sec. 5.3.3]. The analysis was carried out with a fixed fluence f, maximising the ion yield of the respective peak at the photon energy $\hbar\omega$. N_{tot} is the total number of trajectories that give rise to the final charge state at the associated resonance position, and N_T is the number of trajectories for the specific transition T that dominantly occurs at the last resonant excitation among the N_{tot} trajectories.

Table 5.3: Peak assignment based on the Monte Carlo analysis for the dominant resonant excitation contrasted with the ground-state (GS) assignment. Here, N_{tot} is the total number of trajectories leading to a given final charge state, while N_T denotes the number of trajectories corresponding to the specific transition T. Fluence f is expressed in units of $\text{ph}/\mu\text{m}^2$, and photon energy $\hbar\omega$ is in eV. This table is similarly published in the Supplementary Information (Tab. S3) of Ref. [57].

q	$\hbar\omega$	Label	Fluence f	N_{tot}	N_T	Transition T	GS assignment
Xe^{15+}	775	A	5.4×10^{10}	180	177	$3d \to 4f$	$3d \to 4f$
	875	B	5.4×10^{10}	209	188	$3d \to 5f$	$3d \to 5f$
Xe^{21+}	825	C	2.2×10^{11}	120	81	$3d \to 4f$	$3d \to 4f$
	975	D	9.4×10^{10}	129	120	$3p_{3/2} \to 4d$	$3d \to 5f$
	1125	E	7.1×10^{10}	109	81	$3d \to 6f/7f$	$3d \to 7f$
Xe^{25+}	725	F	1.8×10^{12}	194	175	$4sp \to n \geq 9$	$-$
	875	G	4.4×10^{11}	106	68	$3p_{3/2} \to 4s$	$3d \to 4f$
	1025	H	2.2×10^{11}	133	113	$3p_{3/2} \to 4d$	$3p_{1/2} \to 4d$
	1100	I	1.6×10^{11}	196	181	$3p_{1/2} \to 4d$	$-$
	1250	J	1.6×10^{11}	201	160	$3d \to 6f$	$3d \to 7f$
Xe^{37+}	1175	K	3.1×10^{12}	101	76	$4f \to n \geq 12$	$3d \to 4f$
	1275	L	4.1×10^{12}	270	188	$3p_{3/2} \to 4d$	$3p_{3/2} \to 4d$
	1375	M	5.4×10^{12}	103	99	$3p_{1/2} \to 4d$	$3p_{1/2} \to 4d$
	1700	N	2.3×10^{12}	106	83	$3d \to 5f$	$-$

Fig. 5.26 shows an exemplary ionisation pathway leading to the final charge state Xe^{41+}, which is the highest observed in the present study by sequentially absorbing 51 photons. The 51 absorbed photons comprise 26 resonant excitations and 25 photoabsorption, accompanied by 16 Auger-Meitner decays and five fluorescence events.

Six M-shell core holes are generated after less than 6 fs, which remains temporally distant from the peak intensity at 15 fs. The last resonant excitation happens after 24 fs by promoting an electron in the $4f_{5/2}$ subshell, which in turn stems from the former resonant transition $3d \to 4f$ to the $9g_{7/2}$ subshell. This last resonant transition occurs much later than the peak intensity at 15 fs.

Around the peak of the XFEL pulse, in the time frame 13.7-14.6 fs, eight resonant excitations take place, and the ion has no electron left in the M shell equivalent to 18 holes. These eight resonant transitions cannot be distinguished in Fig. 5.26, because the depiction squeezes the red dots into one another. The five fluorescence events happen in the time frame 64-21346 fs and, therefore, after the last photon has passed the ion. The measured ion is fully relaxed when it reaches the detector since the ion TOF is in the order of µs corresponding to 10^9 fs.
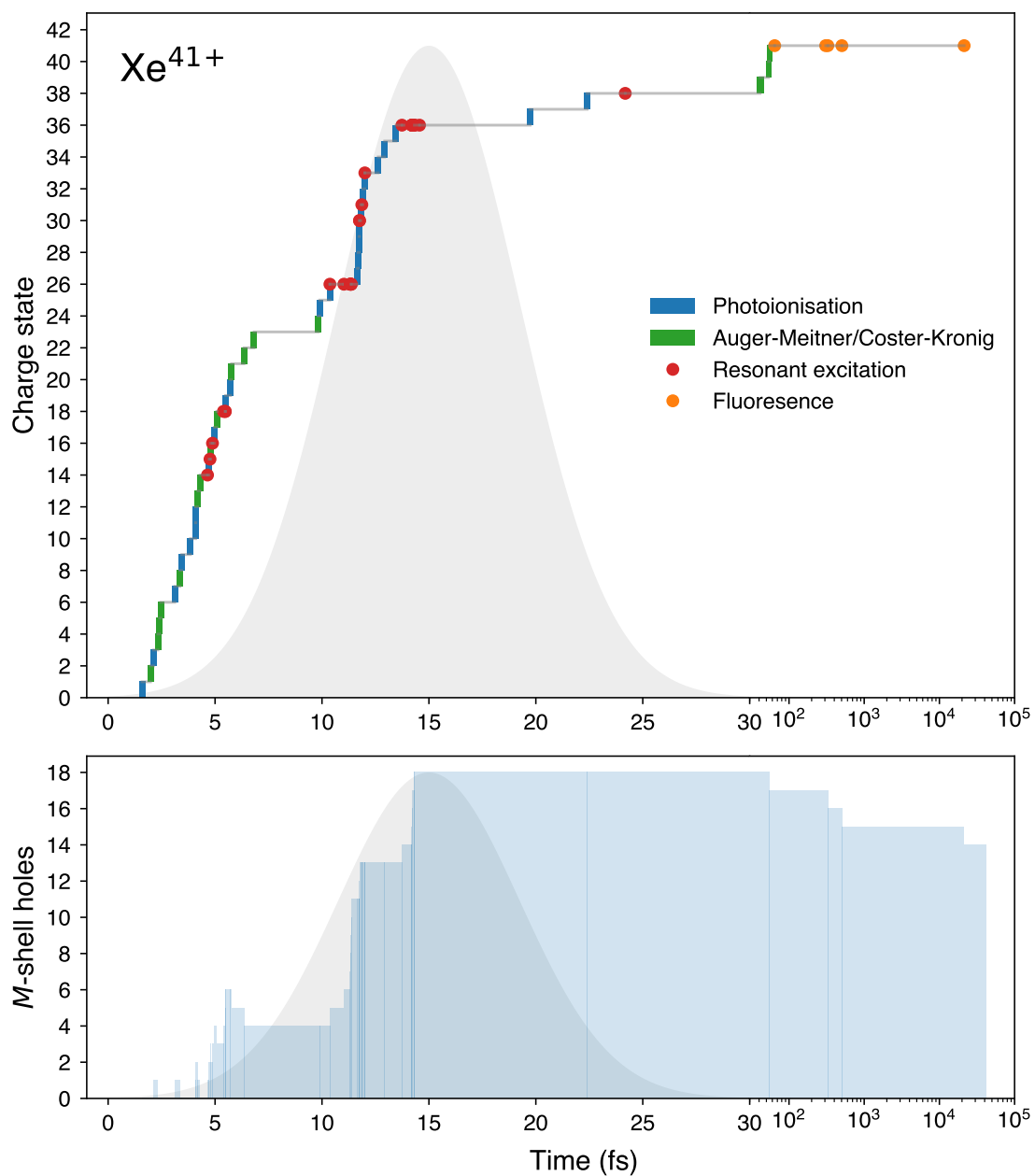
Figure 5.26: Ionisation pathway leading to the highest observed charge state Xe^{41+}.

5.5   Pulse-duration dependence

This section investigates the pulse-duration dependence of the resonance spectra based on XATOM calculations for different pulse durations. The correlation between the peak structure and multiple-core-hole states in the calculations suggests that the resonance spectra of intermediate charge states, e.g., Xe^{25+}, should be sensitive to the pulse duration.

Despite the possibility of producing short pulses as low as 700 as, which can be characterised by an angular streaking scheme [132], there was, at the time of the experiment, no established, noninvasive diagnostic for characterising pulse durations in the order of 10 fs on a shot-to-shot basis at the European XFEL. Thus, no direct measurement of the X-ray pulse duration had been carried out in this study. Therefore, the investigation of the pulse duration of the resonance profiles is only theoretical and confirmation by experiments is still pending.

The calculated upper limit of the X-ray pulse duration is 25 fs derived from an electron bunch charge of 250 pC in the accelerator [133]. Indirect measurements at the European XFEL using Hanbury Brown and Twiss (HBT) interferometry indicate an average pulse duration of 12.8 ± 1.5 fs with a quadratic tapering of the SASE3 undualtor [134]. Further indirect measurements were conducted using spectral fluctuations [135], spectral profiles in XREMPI [131], and dedicated pulse-duration calibration with argon CSD [123]. Based on these indirect measurements, it can be assumed that the average pulse duration is 10 fs.

Figure 5.27 displays calculated resonance spectra of **a** Xe^{15+}, **b** Xe^{25+}, and **c** Xe^{37+} for the different pulse durations 3 fs, 10 fs, and 30 fs. The peak fluences (indicated in each panel) are selected such that the resonance spectra of Xe^{15+} and Xe^{25+} are saturated, and the not-yet saturated peaks, peak C at 725 eV in Xe^{25+} and all peaks in Xe^{37+} have sufficient ion yields.

Each peak in the spectra shows a characteristic pulse-duration dependence. For the two peaks A and B in Xe^{15+} and the three peaks H, I, and J in Xe^{25+}, the minima and maxima of the resonance spectra shift towards higher photon energies (blueshift) as the pulse duration gets shorter. This reflects the fact that more core holes shift the resonant transitions to higher photon energies due to reduced electronic screening (see Fig. 5.25). Opposite to that, peak F in Xe^{25+} in **b** moves towards lower photon energies (redshift) for shorter pulse durations, which is consistent with the observation in XREMPI [131].

Generally, at short pulse durations, the time between two photoabsorptions can be shorter than the Auger-Meitner-decay lifetimes, suppressing the formation of higher charge states. The same resonant excitations can already happen at lower charge states, at which the resonant excitation needs less energy [Fig. 5.25].
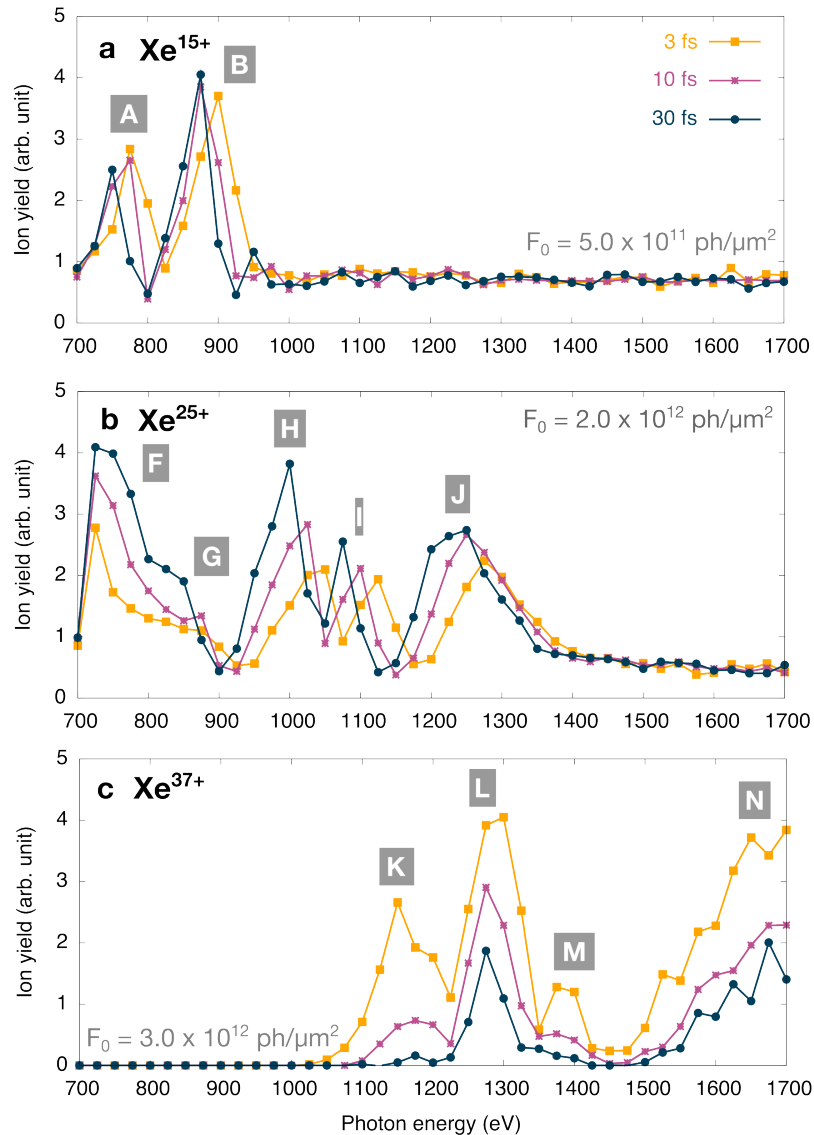
Figure 5.27: Calculated resonance spectra of the charge states Xe^{15+}, Xe^{25+}, and Xe^{37+} for three different pulse durations.

For shorter pulse durations, the overall heights of the peaks in Xe^{25+} in **b** decreases, whereas they strongly increase for Xe^{37+} in **c**. This enhancement at short pulse durations signifies the breakdown of frustrated absorption in heavy atoms subjected to extremely high intensities [124]. The phenomenon of "frustrated absorption" [126] states that the yield of highly charged ions is decreased for shorter pulse durations at extremely high fluences due to the formation of hollow atoms, rendering atoms transparent for X-ray photons [23].

In panel **b**, the ion yields decrease with shorter pulse durations for all peaks except peak G, which displays an ambiguous dependence. Furthermore, the peaks A and B in panel **a** display contrasting behaviours concerning their peak heights. These phenomena may be attributed to various influences stemming from the pulse parameters, which can be challenging to identify. The following section will explore the impact of different pulse parameters on the CSD.

5.6   Influence of various pulse parameters

Fig. 5.28 compares the experimentally obtained CSD at 1200 eV with theoretical equivalents (with volume integration) calculated for various pulse parameters, including pulse duration, spectral bandwidth, photon energy, second FEL harmonic, and temporal pulse shape, thereby illustrating their distinct influences on the CSD. All panels in the first column are calculated with a peak fluence of 1.41×10^{12} ph/µm^2 and a double Gaussian fluence distribution, while those in the second column are calculated with double this peak fluence.
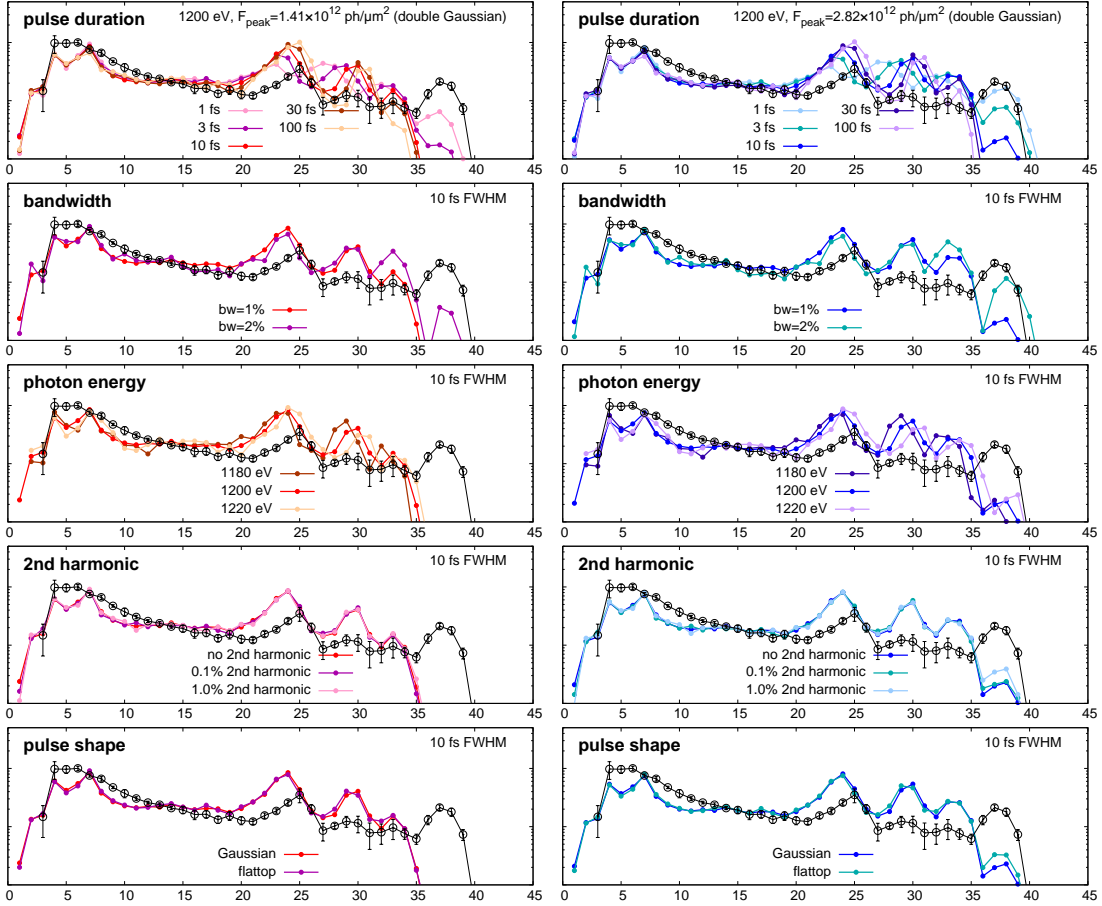
Figure 5.28: Comparison of experimental and theoretical CSD at 1200 eV for various pulse parameters – including pulse duration, spectral bandwidth, photon energy, second FEL harmonic, and pulse shape – across two distinct peak fluences with a double Gaussian spatial profile used in volume integration. Each curve is normalised to one. Aside from the values specified in the respective legends, the x-ray parameters employed are a photon energy of 1200 eV, a 1% bandwidth, a Gaussian temporal shape, a pulse duration of 10 fs FWHM, and no contribution from the second harmonic.

Overall, the experimental CSD exhibits several ion-yield peaks as of Xe^{20+}, where the last peak around Xe^{37+} determines the highest charge state Xe^{39+}. This peak is particularly sensitive to the peak fluence and pulse duration, which aligns with the resonance structures presented in Figs. 5.18 and 5.27. The red solid line in the first panel of the left column, corresponding to calculations using a pulse duration of 10 fs,

reflects the parameters employed for the calculated 2D colour map in Fig. 5.17 **b**. By doubling the peak fluence (as seen in the right column) while maintaining a fixed pulse duration of 10 fs, the calculated CSD reproduces the higher charge states $\geq Xe^{35+}$. This is evident in the peak-fluence-sensitive peaks, specifically peaks K–N in the resonance spectrum of Xe^{37+} [Fig. 5.18], where XREMPI-like processes appear to dominate.

Moreover, a shorter pulse duration of 1 fs, coupled with a higher peak fluence of 2.82×10^{12} ph/µm², further improves the alignment between calculations and experimental data, as illustrated in the first panel of the right column. Nevertheless, simultaneously, as higher charge states get created, the local maxima positions of the intermediate charge states shift with pulse duration, which distorts the match. It is imaginable that certain regions of the CSD are dominated by pulses of varying durations and/or individual SASE spikes due to the stochastic nature of SASE FEL pulses. For instance, the experimental peak around Xe^{25+} may arise from longer-duration pulses or multiple SASE spikes that are temporally separated, while the highest charge states might be generated primarily by the shortest pulses consisting of one or a few spikes.

The second row addresses the spectral bandwidth, comparing 1% to 2%, reflecting the measured experimental conditions of 1.4-1.9%. An increased bandwidth of 2% primarily impacts the higher charge states ($>Xe^{30+}$) and, in conjunction with a higher peak fluence, improves the match between experimental and theoretical CSD. Slight variations (± 20 eV) around the central photon energy of 1200 eV in the third row illustrate how the last two local maxima shift towards higher charge states with increasing photon energy as the specific resonant transition occurs at different charge states under the altered conditions.

The fourth row illustrates that this second harmonic has a minor impact on the CSD. Generally, the contribution of the second harmonic is smaller than that of the third harmonic [73]. In conjunction with the mirror settings, the FEL harmonics are not expected to influence the experiment significantly.

The fifth row shows the impact of the temporal pulse shape: Gaussian and flattop. Only for the highest peak fluence a minor enhancement for charge states $\geq Xe^{35+}$ can be observed, which justifies the usage of a Gaussian temporal profile. Further, it has been demonstrated [48] that the statistical enhancement factor in x-ray multiphoton ionisation is much smaller than expected in the optical domain and becomes close to one. However, spectral spikiness [136] was not investigated and could potentially enhance specific resonances.

In the calculations, an increase in fluence is effectively equivalent to a higher PCS, while a shorter pulse duration corresponds to a reduced relaxation rate. This also indicates the necessity for accurately validating the atomic data used in the calculations, particularly for multiply excited ions in the soft X-ray regime. The electronic structure method employed in the calculations is based on a mean-field approach, and the resonance positions are expected to benefit from improved electronic-structure theory [137].

5.7 Conclusion

In conclusion, this chapter investigates the multiphoton multiple ionisation processes of isolated xenon atoms interacting with ultraintense soft X-ray FEL pulses, exploring the dependence on photon energy across three different fluence regimes. The overall result is a map of resonant features as a function of photon energy and charge state. On this map, photon-energy- and charge-state-dependent transition energy lines belonging to a specific resonant excitation could be identified by comparison with theoretical calculations. However, assuming only the ground state, the transition energy lines reveal regions of significant deviation from the experimentally observed ion yields. A deeper analysis of the calculated ionisation pathways reveals the involvement of multiple-core-hole states, which shifts the energy at which the photon energy becomes resonant. This shift is crucial for understanding the resonance structures.

The findings also reveal that resonance spectra become constant in ion yield beyond a specific saturation point, making them insensitive to the peak fluence and, thus, the influence of the beam's focus size. This peak-fluence insensitivity makes studying resonance features occurring in particular charge states in a pure form possible. It sets the stage for future experiments focusing on the impact of pulse duration, an essential pulse property besides peak fluence in multiphoton interaction with XFELs. In the experimental methodology, a high constant number of photons in the interaction volume could be achieved for every photon energy, ranging from 700 eV to 1700 eV, covering the energy for M-shell ionisation in the neutral atom and up to an ionic state of Xe^{28+} in ground-state configuration. The capability to scan the photon energy of an XFEL while delivering nearly 10^{13} photons per pulse onto the target has not been accomplished before within this scope.

Future experiments could complement ion TOF spectroscopy with fluorescence spectroscopy to validate the calculations, particularly at high charge states. If higher peak fluence regimes become experimentally accessible, this study can be extended to investigate the transition from sequential to direct multiphoton absorption and the potential of strong-field effects. Investigating the pulse duration at high peak fluences would yield further insights into forming multiple-core-hole states and could pave the way for a pulse-duration diagnostic based on ion TOF spectroscopy.

Chapter 6

Double-core-hole state in argon

This study aims to investigate the dynamics of resonant DCH excitation of the $2p$ subshell of argon through sequential absorption of two X-ray photons – a phenomenon that remains relatively unexplored to date. The experimental findings will be presented and compared with MCDHF calculations conducted using the JAC program performed by Stephan Fritzsche at the Helmholtz Institute Jena, alongside calculations using FAC.

The term "resonant" indicates that following the initial photoionisation of a core electron, creating a SCH, a second core electron gets resonantly excited to an unoccupied, higher-lying orbital by a subsequent photon. The initial SCH causes a temporary imbalance in the electronic cloud, which is bound to relax within several femtoseconds. This means the second photon must be absorbed before the SCH decays to create a DCH state.

The study of DCH states, including their formation and relaxation, has become an ever-increasing field of scientific interest since the first theoretical investigation by Cederbaum et al. in 1986. Measurements involving DCH states are particularly interesting since core electrons are not involved in the chemical bonding but are sensitive to their chemical environment. Thus, the decay of the short-living DCH state provides information about the molecule's chemical properties before the chemical bonds start to break after photoionisation [138]. Atoms with multiply core-excited states are of fundamental interest due to their strong electron-electron correlations [139, 140] and are an excellent probe for theoretical models. Moreover, understanding the formation of MCH states in atoms and molecules is a crucial ingredient in interpreting the results of light–matter interaction with ultraintense X-ray free-electron laser pulses [57].

Resonant DCH states occurring in the K shell of argon have been infrequently studied experimentally [141] and theoretically [142]. However, neon has served as a more favourable system for DCH examination, both experimentally [143–146] and theoretically [142, 147], revealing a comparatively straightforward energy-level structure characterised by the empty $1s$ subshell and the excited electron in a np subshell with $n \geq 2$, resulting in a total of two final energy levels.

In stark contrast, resonant DCH states within the $2p$ subshell favourably arise from the excitation of a $2p$ electron to an unoccupied $3d$ orbital, leading to a significantly greater complexity manifested by the coupling between the partially occupied $2p$ and $3d$ subshells, giving rise to a total of 28 final energy levels. The exploration of resonant DCH states within the $3d$ subshell, e.g., of xenon with the favourable resonant

excitation $3d \rightarrow 4f$, further accentuates the intricate nature of DCH phenomena, as the interaction between the partially filled $3d$ and $4f$ subshell results in a total of 81 final energy levels. However, nonresonant DCH states in the $4d$ subshell of xenon have been examined by Fushitani et al. [148] in 2020, demonstrating a similar complexity in the decay cascade as observed in the current study.

Besides, in neon, the K shell is empty after two core holes and thus unsuitable for studying the phenomenon of MCH states, as encountered in the previous chapter, where MCH were considered essential in forming intermediate charge states during the X-ray–xenon interaction. Electron spectroscopy of MCH decay in the $3d$ subshell of xenon is assumed to gain more profound insights into MCH formation. However, this is technically extremely difficult to realise since too many electrons are involved in the decay cascade, dramatically hampering the distinction between electron kinetic energies. Therefore, investigating resonant DCH states within the $2p$ subshell is a crucial step in approaching MCH formation and decay. This step introduces the next layer of complexity after DCH states in the K shell of neon [143–146] and before MCH in the M shell of xenon.

The controlled generation of a DCH state within the $2p$ subshell of argon is realised via nonlinear X-ray absorption, facilitated by ultraintense X-ray pulses from an XFEL and has not been previously accomplished. This advancement has been made possible by the European XFEL's unique operational capabilities to tune the electron energy in the accelerator to 8 GeV to achieve photon energies as low as approximately 250 eV while maintaining ultrahigh intensities. This photon-energy range is essential for investigating the $2p$ subshell of argon, as the $2p$ ionisation edges in neutral argon are located at 248.5 eV and 250.6 eV [40]. The DCH state is detected by analysing emitted electrons during the subsequent Auger-Meitner decay, employing resonant Auger-Meitner electron TOF spectroscopy. The experimental results are compared with JAC calculations to elucidate the resonant excitations and decays.

Historically, photon-induced DCH formation in the $2p$ subshell of argon has been investigated indirectly [149–151], typically as an intermediate state within decay cascades following $1s$ ionisation by a single photon. Linusson et al. successfully generated a $2p$-DCH state in argon via single-photon double ionisation using synchrotron radiation with photon energies ranging from 534 to 562 eV [149]. Žitnik et al. [150] indirectly created a $2p^{-2}$ state through the decay of an initially generated $1s$ single core hole using synchrotron radiation at 3215 eV at SOLEIL, France. However, their study focused on the two-electron–one-electron transition, whereby two valence electrons filled the double core vacancy in the $2p$ subshell resulting in the emission of a single Auger-Meitner electron, primarily possessing a kinetic energy of 458.7 eV. Mailhiot et al. [151] performed a comparable experiment at SOLEIL focusing on the dominant decay pathways of the $2p^{-2}$ state of argon. They employed a multi-coincidence setup that included a MBES coupled with an ion TOF spectrometer, thereby facilitating detailed tracking of the Auger-Meitner decay cascade.

6.1 Experimental parameters

The experiment was conducted at the SQS scientific instrument at the European XFEL during the commissioning phase in August 2022 using the AQS end station. The accelerator's electron energy was 8 GeV, which is a rarely used operation mode of the European XFEL. Adjusting the undulator gaps and employing this electron energy enabled a tunable photon-energy range of 250–300 eV, with an average pulse energy of approximately 100 µJ before entering the KB mirrors. The European XFEL delivered ten pulse trains per second, each containing ten pulses with a temporal spacing of 5.31 µs, corresponding to a repetition rate of 188 kHz. With an electron bunch charge of 250 pC, the maximum pulse duration is estimated to be 25 fs. The XFEL pulses were focused by mirrors configured in a KB arrangement to attain a nominal focus diameter of approximately 2.5 µm [79] at the centre of the ultra-high vacuum chamber within AQS. Gaseous argon was introduced into the AQS chamber at a sample density of 1 mbar against a background pressure of 5×10^{-8} mbar via an effusive gas needle. Following interaction with the XFEL pulses, the emitted electrons were measured by a spectrometer positioned at the "magic angle" of $\theta = 54.7°$ using a negative retardation potential of 160 V.

During the experiment, the photon energy was nominally set by changing the gap of the undulators within the photon-energy range of 259–283 eV, with an increment of 1 eV, resulting in the acquisition of 25 electron spectra. To facilitate a more accurate comparison between experimental findings and theoretical calculations in the data analysis, this photon-energy range was adjusted by a constant offset of 1.75 eV towards lower photon energies, which accounts for the uncertainty associated with the absolute electron energy of the accelerator. The offset was determined using the calibrated electron TOF spectrum (s. Sec. 4.6.1) to determine the kinetic energy of the argon $3p$ photoelectron, which is not used for calibration. Subsequently, the binding energy of the Ar $3p$ level of 15.7 eV [40] was added to the experimentally determined kinetic energy to yield the actual photon energy. The difference between the nominal and actual photon energy provided the offset. This procedure was systematically applied to all 25 spectra, consistently resulting in an offset of 1.75 eV.

Tab. 6.1 displays experimental and calculated K-, L- and M-shell electron binding energies of argon relative to the vacuum level and additionally the lifetimes of L-shell core holes, including the spin-orbit coupling. This table serves, on the one hand, to provide an overview of the needed ionisation energy and, on the other hand, to give an impression of the accuracy of the JAC calculations, which will be discussed in the following sections.

shell	subshell	$E_{\text{bind}}^{(\text{exp.})}$ (eV) [40, 152]	$E_{\text{bind}}^{(\text{calc.})}$ (eV)	$\tau_{\text{SCH}}^{(\text{exp.})}$ (fs) [153]	$\tau_{\text{SCH}}^{(\text{calc.})}$ (fs)
K	$1s$	3205.90 ± 0.50	-	-	-
L	$2s$	326.30 ± 0.10	335.02	-	5.45
	$2p_{1/2}$	250.56 ± 0.07	256.86	5.58 ± 0.19	4.39
	$2p_{3/2}$	248.45 ± 0.07	254.71	5.58 ± 0.19	4.37
M	$3s$	29.30 ± 0.10	33.53	-	-
	$3p_{1/2}$	15.94 ± 0.01	14.95	-	-
	$3p_{3/2}$	15.76 ± 0.01	14.76	-	-

Table 6.1: Comparison of the experimental and JAC-calculated electron binding energies of argon for the K, L and M shell and SCH lifetimes for the L shell. The experimental lifetime is obtained by the conversion $\tau_{\text{SCH}}^{(\text{exp.})} = \frac{\hbar}{\Gamma}$, where Γ is the experimental linewidth.

In the investigated photon energy range of 257.2–281.2 eV, photons can ionise the $2p$, $3s$, and $3p$ subshell; however, they do not suffice to ionise a $2s$ electron nor a $1s$ electron. Photoabsorption in the $2p$ subshell is dominant, with the corresponding PCSs being, on average, approximately 15 times larger than those for the $3p$ subshell and around 50 times larger than for the $3s$ subshell [31].
Furthermore, Tab. 6.1 indicates that the second photon must be absorbed within the lifetime τ_{SCH} of 5.6 fs before the initial $2p$ core hole relaxes via Auger-Meitner decay [121, 154, 155]. The sequential absorption of the second photon exhibits a significantly smaller cross-section than single-photon absorption. Consequently, the process of absorbing a second photon requires a short pulse duration and an ultraintense X-ray beam ($\sim 10^{16}$ W/cm^2) with an extremely high number of photons per pulse ($\sim 10^{12}$ ph/pulse). Such high intensities are typically available at XFEL facilities.

6.2 Theoretical background

6.2.1 Resonant DCH formation and decay

This section describes the photon-initiated DCH formation and subsequent decay in more detail for the specific case of the $2p$ subshell of argon.
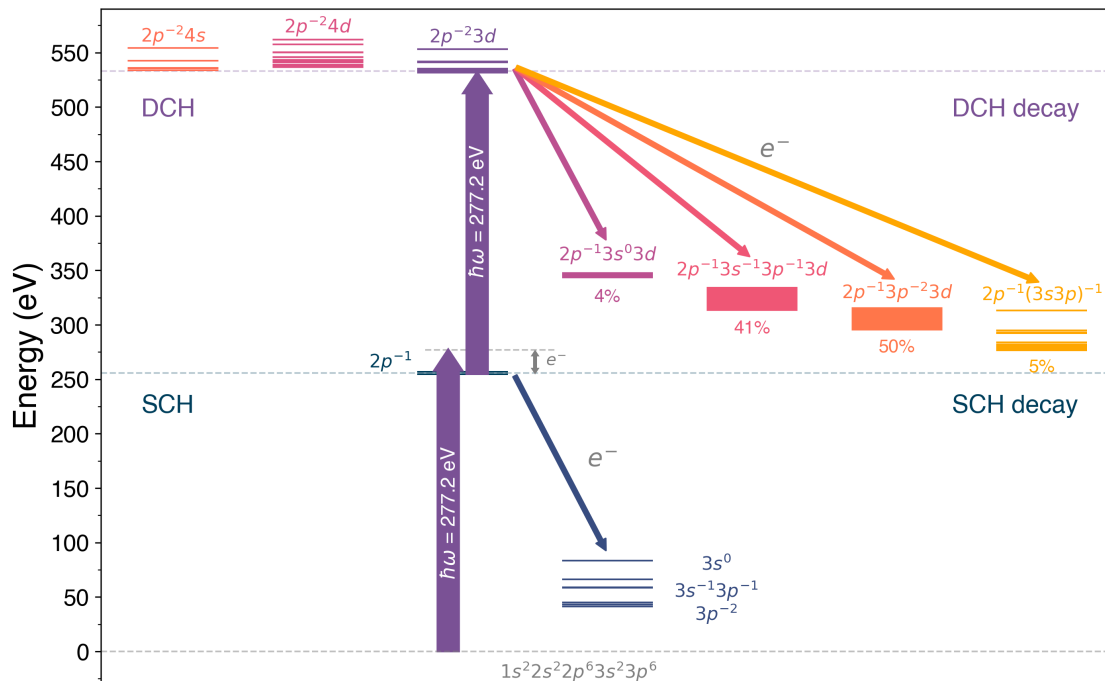
Figure 6.1: Illustration of the JAC-calculated energy-level diagram showcasing the electronic states involved in the formation and decay of the $2p$-DCH state in singly charged and excited argon. Photons with an energy of 277.2 eV, highlighted by the broad purple arrows, trigger the resonant transitions, particularly emphasising the dominant $2p \rightarrow 3d$ transition. The Auger-Meitner decay pathways, indicated by thin coloured arrows, unravel the intricate decay channels, leading to distinct final configurations following both SCH and DCH decays. The two final configuration $2p^{-1}3p^{-1}$ and $2p^{-1}3s^{-1}$ corresponding to the participator decay are summarised by $2p^{-1}(3s3p)^{-1}$ in yellow.

Fig. 6.1 displays the calculated energy-level diagram of the electronic states associated with DCH formation and decay. The energy levels are presented with respect to the ground-state level ($^1S_0$), marked with the grey dashed line at 0. In its ground-state configuration, neutral argon contains 18 electrons distributed in five subshells:

$$1s^2 2s^2 2p^6 3s^2 3p^6.$$

In the following, full subshells in the electronic configurations will be omitted. The first photon ($\hbar\omega$) ionises a neutral argon atom (Ar^0), creating a singly charged ion (Ar^+) with a $2p$ core hole, denoted by the superscript -1, equivalent to $2p^5$. The two

states $^2P_{1/2}$ and $^2P_{3/2}$ belonging to the SCH are denoted by the blue dashed line.

$$\mathrm{Ar}^0 + \hbar\omega \rightarrow \mathrm{Ar}^+(2p^{-1}) + e^-_{\mathrm{ph}}$$

e^-_{ph} represents the photoelectron emitted into the continuum carrying the excess energy between ionisation potential and photon energy. By focusing exclusively on the absorption processes within the $2p$ subshell, the second photon can be absorbed either nonresonantly or resonantly while remaining within the lifetime of the $2p$-SCH state. Nonresonant absorption refers to the scenario in which the second photon knocks off an additional $2p$ electron into the continuum, thereby forming a doubly charged ion.

$$\mathrm{Ar}^+(2p^{-1}) + \hbar\omega \rightarrow \mathrm{Ar}^{2+}(2p^{-2}) + e^-_{\mathrm{ph}}$$
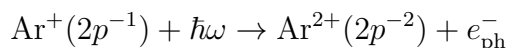
For a resonant DCH formation, the second photon excites a $2p$ electron to an unoccupied orbital of a higher-lying subshell $n_d d$ or $n_s s$ with $n_d \geq 3$ and $n_s \geq 4$, leaving the ion in an excited, singly charged state. Whereby the photon energy (purple arrow) must correspond to the difference between the $2p$ and excited state within the margins of the photon-energy bandwidth of the XFEL pulse.

$$\mathrm{Ar}^+(2p^{-1}) + \hbar\omega \rightarrow \mathrm{Ar}^{+*}(2p^{-2}n_d d, n_s s)$$
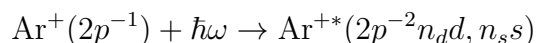
Above the SCH energy levels depicted in Fig. 6.1 are the energy levels associated with the resonant DCH configuration ($2p^{-2}3d$), which are generated by resonant $2p \rightarrow 3d$ transitions starting from the SCH configuration. These levels are the primary focus of this study and represent the energetically lowest pathway for producing a DCH state in the $2p$ subshell. The energy levels of the transitions $2p \rightarrow 4d$ and $2p \rightarrow 4s$ are also shown on the left side. However, the transition $2p \rightarrow 4d$ is only marginally reached within the bandwidth of the highest photon energy. Further, the oscillator strength of the transition $2p \rightarrow 3d$ is roughly ten times stronger than the transition $2p \rightarrow 4s$, and its decay spectra do not significantly contribute to the electron spectra, albeit some of the energy levels of the configuration $2p^{-2}4s$ are energetically accessible with the photon-energy range.

The $2p^{-2}3d$ configuration in argon has 28 different energy levels. The calculations indicate that a total of 34 resonant $2p \rightarrow 3d$ transitions can occur in the photon-energy range 272–300 eV starting either from the $^2P_{1/2}$ or the $^2P_{3/2}$ level of the $2p$-SCH. Tab. 6.2 presents the three most dominant resonant transitions involved in forming a DCH in the $2p$ subshell of argon. The approach for retrieving these transitions will be explained based on Fig. 6.2.

transition	energy (eV)	lifetime (fs)
$2p^{-1}$ $(^2P_{1/2}) \rightarrow 2p^{-2}$ $(^3P_1)$ $3d$ $(^2P_{3/2})$	277.13	1.80
$2p^{-1}$ $(^2P_{3/2}) \rightarrow 2p^{-2}$ $(^1D_2)$ $3d$ $(^2D_{5/2})$	278.29	1.79
$2p^{-1}$ $(^2P_{3/2}) \rightarrow 2p^{-2}$ $(^1D_2)$ $3d$ $(^2P_{3/2})$	278.36	1.80

Table 6.2: JAC calculations of the energies and lifetimes corresponding to the strongest excitation probabilities for the resonant transition $2p^{-1} \rightarrow 2p^{-2}3d$ leading to a DCH state in the singly charged argon ion.

Fig. 6.2 **a** presents all possible calculated resonant transitions associated with the $2p^{-2}3d$ configuration. These transitions can be categorised into three groups based on their electronic coupling within the $2p$ subshell. Panel **b** illustrates the experimentally determined transmission as a function of photon energy, showing that the first group exhibits non-constant transmission (will be explained in the next section) and that the photon-energy range does not encompass the resonances of the second and third groups.
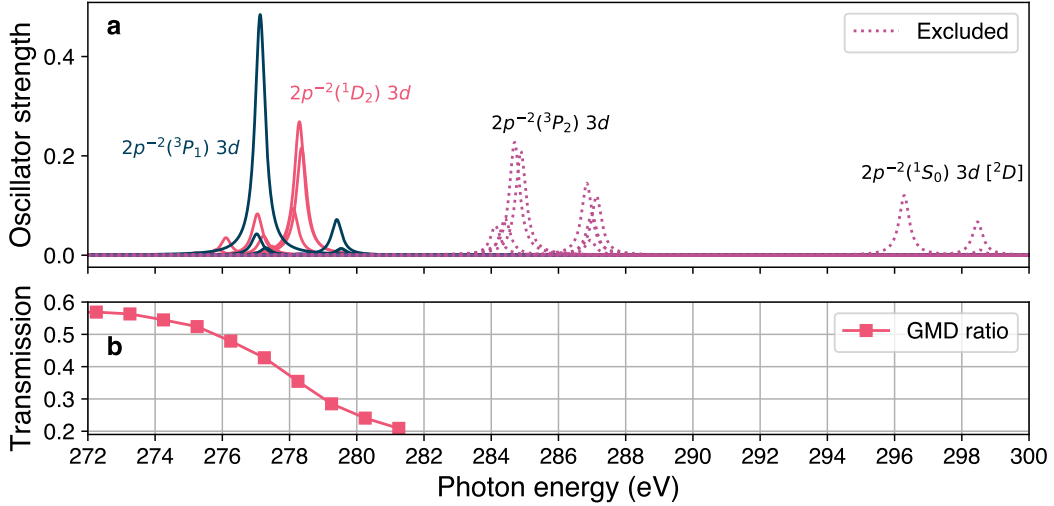
Figure 6.2: **a** JAC calculated resonant $2p \rightarrow 3d$ transitions leading to the formation of a resonant DCH state in the $2p$ subshell of argon in the photon-energy range 272–300 eV. The linewidth is based on the average DCH lifetime of 1.8 fs and is equal for all transitions. **b** Experimental beamline transmission for the photon-energy range 272.2–281.2 eV. The transmission is determined based on the ratio between the tunnel XGM and the XGM before the KB mirrors.

1) The rightmost group on the energy axis belongs exclusively to the transition to the doublet ^2D state with the four $2p$ electrons in the singlet $^1S_0$ state. The experimental photon-energy range does not cover the energy range in which they occur and exhibits relatively minor oscillator strengths. Thus, these transitions will be neglected in the analysis.

2) The central group (ca. 284–288 eV) is associated with the triplet state $^3P_2$ in the $2p$ subshell. This range lies outside the experimental photon-energy range and will not be considered. Additionally, preliminary photon-energy scans conducted during the experimental phase revealed no resonant characteristics within this energy range.

3) The leftmost group on the energy axis predominantly comprises the states $^3P_1$ and $^1D_2$, while the state $^3P_0$ exhibits negligible oscillator strength. When summing the oscillator strengths of all transitions, only six transitions contribute more than 5% to the total. Finally, three out of the six resonant transitions with the strongest oscillator strength, accounting together for 68% of the total sum, were chosen because including more transitions had no impact on the final decay spectra.

The resonant DCH state predominantly relaxes through a cascade of nonradiative Auger-Meitner decays [151]. The initial decay step results in five distinct final electronic configurations, collectively accounting for 314 possible final energy levels derived from the JAC calculations. These configurations can be categorised into resonant spectator decay [Sec. 2.2], wherein an electron in the $3d$ orbital acts as a spectator and contributes to 95% of the final energy levels, and resonant participator decay [Sec. 2.2], in which the excited electron in the $3d$ subshell participates in the decay, accounting for the remaining 5% of final energy levels. On the right side of Fig. 6.1, the final energy levels are illustrated and grouped by the final electronic configuration, where the final energy levels of the resonant participator decay are summarised by $2p^{-1}(3s3p)^{-1}$. The percentages indicate the proportion of final energy levels.

$$
\begin{aligned}
\mathrm{Ar}^{+*}(2p^{-2}3d) \quad &\rightarrow \mathrm{Ar}^{2+*}(2p^{-1}3p^{-2}3d) &&+e^-_{\mathrm{AM}} \ (50\%) \\
&\rightarrow \mathrm{Ar}^{2+*}(2p^{-1}3s^{-1}3p^{-1}3d) &&+e^-_{\mathrm{AM}} \ (41\%) \\
&\rightarrow \mathrm{Ar}^{2+*}(2p^{-1}3s^03d) &&+e^-_{\mathrm{AM}} \ \ (4\%) \\
&\rightarrow \mathrm{Ar}^{2+}(2p^{-1}3p^{-1}) &&+e^-_{\mathrm{AM}} \ \ (3\%) \\
&\rightarrow \mathrm{Ar}^{2+}(2p^{-1}3s^{-1}) &&+e^-_{\mathrm{AM}} \ \ (2\%)
\end{aligned}
$$
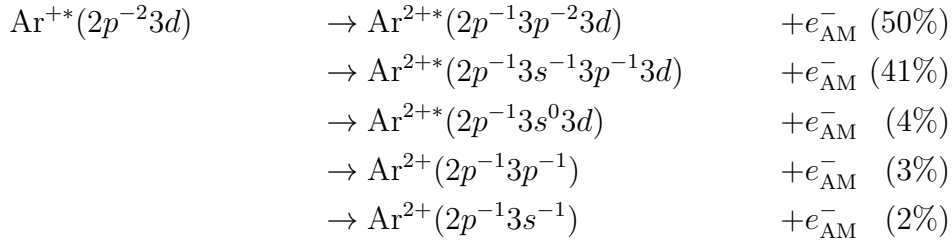
All decay channels increase the charge state of the ion by one, predominantly leaving the ion with a SCH in the $2p$ subshell. According to JAC calculations, about 5-10% of the $3d$ orbitals are shaken up to $4d$ during DCH decay. This small relaxation pathway will be omitted in the subsequent analysis since the pure $2p^{-2}3d$ decay spectrum provides a satisfactory approximation to the experimental findings. The second step of the decay cascade can start from any of the five electronic configurations, leading to 16 final configurations, as presented below:

$$
\begin{aligned}
\mathrm{Ar}^{2+*}(2p^{-1}3p^{-2}3d) \quad &\rightarrow \mathrm{Ar}^{3+*}(3s^{-1}3p^{-3}3d) &&+e^-_{\mathrm{AM}} \ (51\%) \\
&\rightarrow \mathrm{Ar}^{3+*}(3p^{-4}3d) &&+e^-_{\mathrm{AM}} \ (21\%) \\
&\rightarrow \mathrm{Ar}^{3+*}(3s^03p^{-2}3d) &&+e^-_{\mathrm{AM}} \ (20\%) \\
&\rightarrow \mathrm{Ar}^{3+}(3s^{-1}3p^{-2}) &&+e^-_{\mathrm{AM}} \ \ (5\%) \\
&\rightarrow \mathrm{Ar}^{3+}(3p^{-3}) &&+e^-_{\mathrm{AM}} \ \ (4\%) \\
\mathrm{Ar}^{2+*}(2p^{-1}3s^{-1}3p^{-1}3d) \quad &\rightarrow \mathrm{Ar}^{3+*}(3s^{-1}3p^{-3}3d) &&+e^-_{\mathrm{AM}} \ (64\%) \\
&\rightarrow \mathrm{Ar}^{3+*}(3s^03p^{-2}3d) &&+e^-_{\mathrm{AM}} \ (25\%) \\
&\rightarrow \mathrm{Ar}^{3+}(3s^{-1}3p^{-2}) &&+e^-_{\mathrm{AM}} \ \ (7\%) \\
&\rightarrow \mathrm{Ar}^{3+}(3s^03p^{-1}) &&+e^-_{\mathrm{AM}} \ \ (4\%) \\
\mathrm{Ar}^{2+*}(2p^{-1}3s^03d) \quad &\rightarrow \mathrm{Ar}^{3+*}(3s^03p^{-2}3d) &&+e^-_{\mathrm{AM}} \ (93\%) \\
&\rightarrow \mathrm{Ar}^{3+}(3s^03p^{-1}) &&+e^-_{\mathrm{AM}} \ \ (7\%) \\
\mathrm{Ar}^{2+}(2p^{-1}3p^{-1}) \quad &\rightarrow \mathrm{Ar}^{3+}(3s^{-1}3p^{-2}) &&+e^-_{\mathrm{AM}} \ (27\%) \\
&\rightarrow \mathrm{Ar}^{3+}(3p^{-3}) &&+e^-_{\mathrm{AM}} \ (17\%) \\
&\rightarrow \mathrm{Ar}^{3+}(3s^03p^{-1}) &&+e^-_{\mathrm{AM}} \ \ (7\%) \\
\mathrm{Ar}^{2+}(2p^{-1}3s^{-1}) \quad &\rightarrow \mathrm{Ar}^{3+}(3s^{-1}3p^{-2}) &&+e^-_{\mathrm{AM}} \ (80\%) \\
&\rightarrow \mathrm{Ar}^{3+}(3s^03p^{-1}) &&+e^-_{\mathrm{AM}} \ (20\%)
\end{aligned}
$$
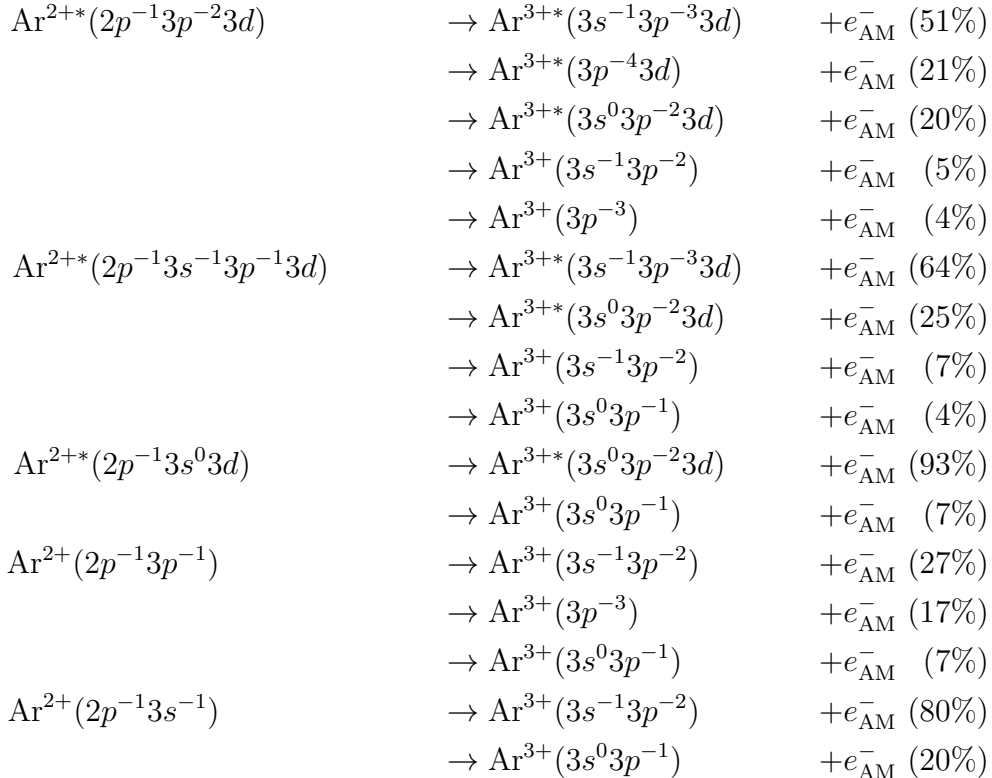
The listing above highlights the intricate nature of the DCH decay cascade despite excluding shake-up or shake-off processes that may occur during decay, potentially giving rise to satellite structures (s. Sec. 2.2) in the electron spectrum.

6.2.2   Resonant SCH in doubly charged argon

This section describes the resonant transition $2p \rightarrow 3d$ in doubly charged argon ($3p^{-2}$), which arises from the shift in the orbital binding energies as discussed in the previous chapter (Ch. 5). These doubly charged ions originate from the SCH decay within the $2p$ subshell, leading to three final configurations:

$$\begin{aligned}
\mathrm{Ar}^+(2p^{-1}) &\rightarrow \mathrm{Ar}^{2+}(3p^{-2}) & +e^-_{\mathrm{AM}}, \\
&\rightarrow \mathrm{Ar}^{2+}(3s^{-1}3p^{-1}) & +e^-_{\mathrm{AM}}, \\
&\rightarrow \mathrm{Ar}^{2+}(3s^0) & +e^-_{\mathrm{AM}}.
\end{aligned}$$
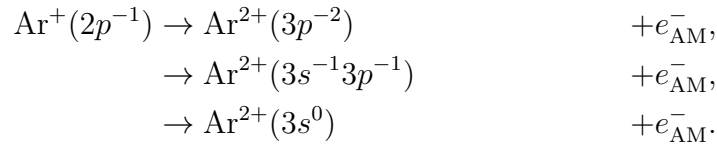
This section exclusively focuses on the configuration $3p^{-2}$ as it emerges as the most abundant final configuration after the Auger-Meitner decay [121]. $3p^{-2}$ has five different energy levels, namely $^3P_{2,1,0}$, $^1D_2$, and $^1S_0$, each associated with a particular branching ratio. The configuration $2p^{-1}3p^{-2}3d$ formed after $2p \rightarrow 3d$ resonant excitation includes 158 distinct energy levels; when combined with the five initial energy levels, this results in a total of 381 possible resonant transitions.
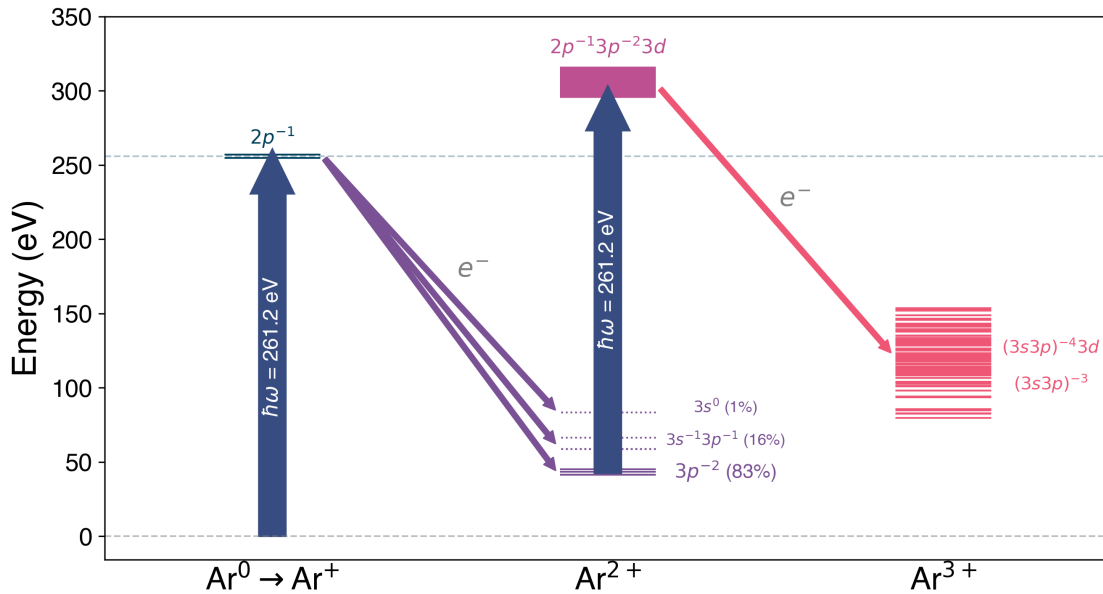
Figure 6.3: Energy-level diagram illustrating the formation and decay of the SCH states in Ar^{2+*}. The branching ratios are taken from the experimental values of Ref. [121]. The blue arrows indicate the photon energy, representing the average energy required to create the state.

Fig. 6.3 displays the energy level diagram representing the stages involved in the formation of a resonant SCH in Ar^{2+}. Initially, a SCH in the neutral argon atom is created by a photon (indicated by the thick blue arrow) decaying in a second step to Ar^{2+} (indicated with the thin purple arrows). A successive photon now resonantly excites a $2p$ electron to an unoccupied $3d$ orbital, creating Ar^{2+*}. This excited state relaxes (indicated by the red thin arrow) to one of 141 distinct final states in Ar^{3+} by Auger-Meitner decay, including spectator and participator decay.

Out of the 381 potential resonant transitions, the four most prominent were selected to approximate the experimental finding. Prior to this selection process, each transition was weighted by the corresponding branching ratio of their initial state, determined by the preceding Auger-Meitner decay [Intensities of Tab. 1 in Ref. [121]]. Fig. 6.4 provides a visual representation of the calculated oscillator strengths of the resonant $2p \to 3d$ transitions in Ar^{2+}, coloured in blue, along with the selected transitions highlighted in red.
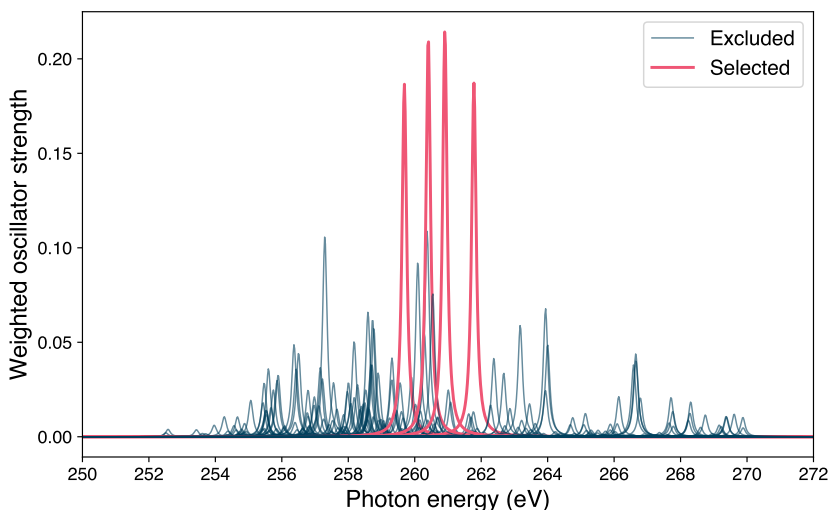
Figure 6.4: JAC-calculated, weighted (s. Text) oscillator strength as a function of the photon energy of the resonant transitions from $2p$ to $3d$ in Ar^{2+} ($3p^{-2}$), created by previous $2p$-SCH Auger-Meitner decay. The selected transitions are highlighted in red, while the nonconsidered transitions are indicated in blue.

The respective energies, where the transitions become resonant, are listed in Tab. 6.3. It is noted that the inclusion of more than these four transitions results in no significant change in the shape of the calculated feature.

transition	JAC energy (eV)
$3p^{-2}$ ($^1D_2$) $\to$ $2p^{-1}3p^{-2}3d$ ($J = 3$)	259.69
$3p^{-2}$ ($^1D_2$) $\to$ $2p^{-1}3p^{-2}3d$ ($J = 3$)	260.41
$3p^{-2}$ ($^1S_0$) $\to$ $2p^{-1}3p^{-2}3d$ ($J = 1$)	260.91
$3p^{-2}$ ($^1D_2$) $\to$ $2p^{-1}3p^{-2}3d$ ($J = 2$)	261.78

Table 6.3: Calculated energies with the strongest transition rates for the resonant transition $3p^{-2} \to 2p^{-1}3p^{-2}3d$ in doubly charged argon. J is the total angular momentum.

6.3   Results

A preliminary photon-energy scan from 253.2–298.2 eV in 1-eV steps was conducted during the experiment. This scan aimed to identify resonant excitations below the $2p^{-2}$ ionisation threshold. The scan showed a broad resonant feature around a photon energy of 277.2 eV and a smaller one around 261.2 eV. However, around the carbon $1s$ edge of 284.2 eV [40], the beamline transmission decreased significantly due to carbon contamination of the mirrors. This contamination rendered the photon-energy range greater than 281.0 eV experimentally unexploitable. As a result, the photon-energy range 257.2–281.2 eV was chosen for a more detailed analysis.

Fig. 6.5 presents the 2D colour map, dubbed resonance map, of the experimental electron-emission spectra in panel **a** and the theoretical equivalent in panel **c** as a function of photon energy, ranging from 257.2 eV to 281.2 eV. Panel **a** features two distinct linearly increasing photolines corresponding to the electron emissions from the $3s$ (226.9–250.6 eV) and $3p$ (240.4–264.1 eV) subshells, indicated by translucent white lines. Below these lines, two resonant structures are observed: One centred around 261.2 eV and the other around 277.2 eV. Additionally, minor features between these two resonant structures are nearly indistinguishable from the background.

In panel **a**, the vertical kinetic energy range of 160.0 eV to 210.0 eV is predominantly characterised by the $L_{2,3}MM$ Auger-Meitner electron emission spectrum, exhibiting a reduction by a factor of 20 relative to the region from 210 eV to 280 eV. By comparing these observations with the resonant transition energies from the JAC calculations in panel **b**, the bright yellow region in Fig. 6.5 **a**, encompassing the photon energies of 275.2–280.2 eV and kinetic energies of 210.0–228.0 eV, is identified as the $2p$-DCH feature, which is further discussed in Sec. 6.3.1. The flat region centred around the photon energies of 258.2–263.2 eV and kinetic energies of 214.0–222.0 eV in panel **a** corresponds to the Ar^{2+*} SCH feature, which will be examined in detail in Sec. 6.3.2.
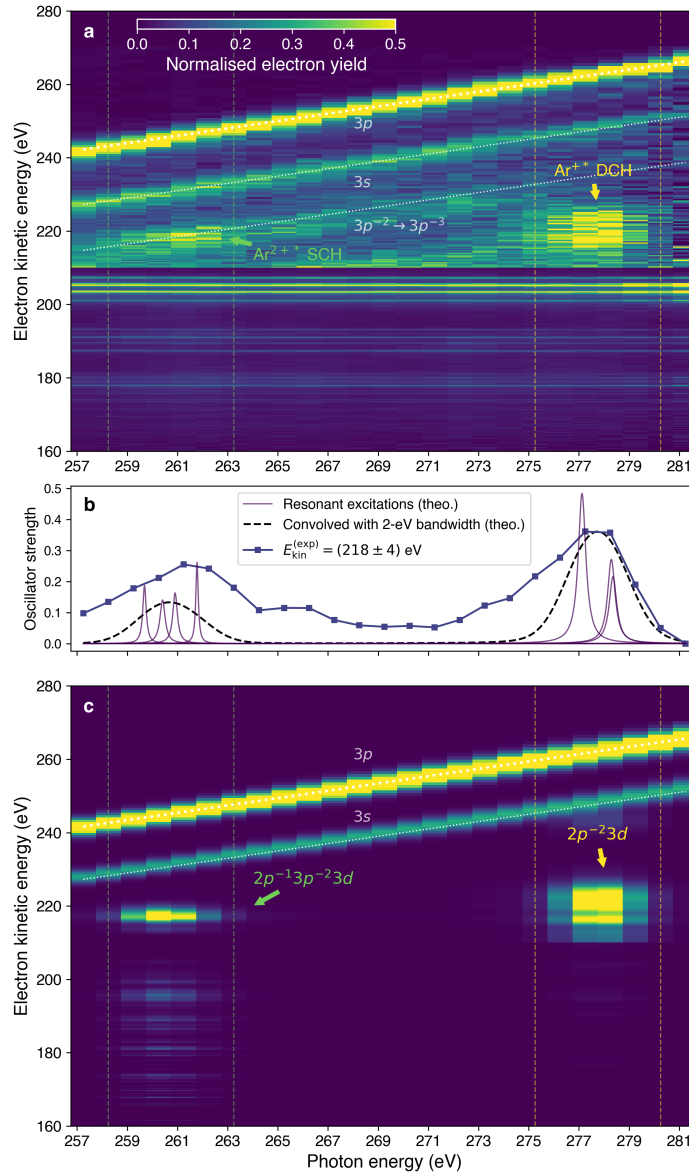
Figure 6.5: Panel **a** presents the experimental and **c** the theoretical 2D colour map of the electron-emission spectra as a function of photon energy, spanning the range of 257.2–281.2 eV with a step size of 1 eV. The theoretical map, derived from JAC calculations, includes two photolines for the $3s$ and $3p$ electrons, which are not part of the original JAC calculations and are scaled to match the experimental $3p$-to-DCH ratio in electron yield. In both panels, the intensity between the electron kinetic energies of 210.0–280.0 eV is amplified by a factor of 20. Each experimental and theoretical spectrum is normalised to the electron yield of the $3p$ photoelectron. Panel **b** displays the JAC-calculated oscillator strengths of selected resonances, alongside their summed values, convolved with an FEL bandwidth of 0.7%, featuring a higher resolution with 500 data points instead of 25. Additionally, a horizontal cutout of the experimental electron energies at 218.0 eV (blue squares), integrated within $\pm$ 4 eV limits and normalised to the maximum of the convolved spectrum, is provided as an experimental comparison.

In the presence of a DCH feature, other two-photon processes, such as sequential ionisation, are highly probable. The kinetic energy of the emitted electron following the sequential ionisation of a $3p$ electron, which has a binding energy of 27.6 eV [43], in singly charged argon ($3p^{-1}$), is comparable to that resulting from the ionisation of a $3s$ electron, with a binding energy of 29.3 eV [40], in neutral argon. Further, electrons involved in single-photon ionisation or sequential ionisation are susceptible to the FEL's bandwidth, which appears correspondingly broad in the resonance map in contrast to Auger-Meitner electrons, resulting from electron correlations and do not interact with the photons directly. Consequently, both lines lie on each other and cannot be separated. The dotted white line labelled $3p^{-2} \rightarrow 3p^{-3}$ indicates the sequential ionisation process of the $3p$ electron, with a binding energy of 40.7 eV [43], in doubly charged argon, resulting from Auger-Meitner decay of $2p^{-1}$.

The $L_{2,3}MM$ spectrum in the kinetic-energy range of 160.0–210.0 eV complicates the differentiation of superimposed electrons from other decay channels, such as DCH or sequentially ionised ions with an SCH and a valence hole, as it cannot be subtracted from the spectrum. Nonetheless, an attempt to estimate the underlying processes is made in the two following subsections by comparing the two on-resonance spectra with an off-resonance spectrum, which is overlaid with the respective calculated spectrum and the modelled $L_{2,3}MM$ spectrum.

The electron-emission spectra in **a** comprise the electron yield as a function of the electron kinetic energy from 160.0 eV to 280.0 eV in counting mode (s. Sec. 4.1.5) and are vertically aligned to form a 2D colour map. Each spectrum is normalised to the electron yield of the $3p$ electron to account for the varying pulse energies (s. panel **b** in Fig. 6.2). Moreover, the intensities of the spectra are corrected by the transmission function of the spectrometer (s. Sec. 4.6.2), which depends on the electron kinetic energy. For the kinetic energy representation, the intensities were additionally compensated by the Jacobian of the TOF-to-electron-kinetic-energy conversion (s. Sec. 4.6.1).

By comparing the electron yield of the DCH to the electron yield of the $3p$ photoelectron scaled by the ratio of the calculated $2p$ and $3p$ partial photoabsorption cross sections [31] in the limits 275.2–280.2 eV, the SCH-to-DCH ratio can be estimated to be 8:1.

Fig. 6.5 **c** shows the calculated resonance map exhibiting the exact data-point resolution as the experimental equivalent. The JAC-calculations are shifted by 4.5 eV towards lower photon energies to match the experimental spectra. The calculations comprise two data sets: The resonant DCH feature in singly charged argon (Ar^{+*}) and the resonant SCH feature in doubly charged argon (Ar^{2+*}). The two data sets are relatively scaled to each other such that the ratio of the integrated electron yields of the two features above 210 eV is equal to the experimentally obtained ratio. For the scaling, the experimental electron yields were integrated horizontally between 275.2–280.2 eV and vertically between 210.0–228.0 eV for the Ar^{+*} DCH feature, and for the Ar^{2+*} SCH feature, the electron yields were horizontally integrated between 258.2–263.2 eV and vertically between 214.0–222.0 eV.

The individual electron spectra were modelled in two steps: First, an emission spectrum was created encompassing all the calculated Auger-Meitner decay transitions originating from the final states of the chosen resonant transitions. Each decay process was modelled by a Gaussian profile centred at the calculated electron

energy, where the Auger-Meitner rate serves as the amplitude, further weighted by
the corresponding oscillator strength of the resonant transition and the variance
determined by the energy-dependent instrument function (s. Sec. 4.7). Secondly,
this emission spectrum is distributed into 25 electron spectra weighted by the convo-
luted resonance spectrum, similar to Panel **b**, but with the experimental resolution.
Additionally, the spectra are multiplied by the calculated partial cross section for
the $2p$ subshell [31], which slightly varies within the photon-energy range, to account
for the initial $2p$-photoionisation.

The two photolines corresponding to the emission of a $3s$ or $3p$ electron are not part
of the JAC calculations and are supposed to provide an orientation in the spectra
for better comparison with the experimental resonance map. Both photolines ($3s$
and $3p$) are modelled by Gaussian distributions. Their amplitudes scale with the
respective calculated partial cross sections taken from Ref. [31]. The utilised variance
($\sigma_{\mathrm{photo}}^2$) is formulated as a convolution of two Gaussian functions, being the sum
of the instrument function variance (σ_{I}^2) and the bandwidth variance (σ_{BW}^2). To
ensure consistency between theory and experiment, the JAC calculations are adjusted
relative to the electron yield of $3p$, aligning it with the experimental ratio of $3p$
electron yield to the DCH electron yield within the energy range of 275.2–280.2 eV
before normalisation. This energy range is intentionally chosen to encompass a wider
span than the DCH features due to a slight offset between the experimental and
theoretical electron peak positions along the photon-energy axis, thereby enabling
equal integration limits. Finally, each spectrum is normalised based on the yield of
the $3p$ photoelectron.

In Figure 6.5 **b**, the calculated oscillator strengths (s. Tab. 6.2 and 6.3) are presented
in greater detail. The solid lines in the plot represent the individual selected resonant
transitions, each characterised by a Lorentzian line profile. Additionally, the dashed
line signifies the convolution of these resonant transitions with a bandwidth of 2 eV.
This bandwidth value corresponds approximately to the average of the FEL band-
width (0.7%) across the photon-energy range under consideration. The Lorentzian
line profiles of the individual transitions are modelled with the scale parameter
$\gamma = \frac{\hbar}{2\tau e}$, where τ denotes the calculated lifetime (FWHM) of the final state ($2p^{-2}3d$),
e the elementary charge, and 2γ the equivalent to the FWHM of a Gaussian profile.
Additionally, a horizontal cutout from panel **a** at a fixed electron kinetic energy of
218.0 eV, plotted as a function of photon energy, serves as an experimental analogue
to the convolved oscillator strengths. This cutout is selected to encompass the two
resonant features: Ar^{2+*} SCH and Ar^{+*} DCH, and is integrated within $\pm$ 4 eV limits.
It is normalised to the maximum of the convolved spectrum.

Overall, both the experimental resonance map and the calculated resonance map
demonstrate good agreement, successfully reproducing the two resonant features,
Ar^{+*} DCH and Ar^{2+*} SCH, by accounting for only three and four resonant transitions,
respectively. The subsequent sections provide a more detailed analysis of these two
resonant features.

6.3.1 Resonant DCH excitation and decay

For a more comprehensive comparison, this section analyses the integrated experimental emission spectrum with the integrated calculated emission spectrum in the limits 275.2–280.2 eV, where the DCH feature occurs. The integration is based on the data presented in Fig. 6.5 from the previous section. These limits are indicated by the yellow dashed lines in Fig. 6.5.

Panel **a** shows the integrated experimental electron spectrum (black) and the theoretical counterpart (red) calculated using JAC for the truncated kinetic energy range 170–270 eV. Additionally, the transition rates corresponding to the final configurations $2p^{-1}3p^{-2}3d$ (blue), $2p^{-1}3s^{-1}3p^{-1}3d$ (green) and the participator decay summarised into a single representation (yellow) are shown, illustrating the complexity of the DCH decay process. The configuration $2p^{-1}3s^{-2}3d$ is not shown here, as the contributions are too minor.

The experimental spectrum is additionally contrasted with the modelled Auger-Meitner spectrum (dashed red line and labelled "Pulkkinen et al.") stemming from the $2p$ SCH decay, based on the energies and intensities of Ref. [121] using the experimental resolution. Both spectra are normalised to the arbitrarily chosen peak at 178.0 eV. This comparison serves as an estimation of how the decay of the DCH affects the Auger-Meitner spectrum stemming from pure SCH decay since the pure experimental $L_{2,3}MM$ spectrum cannot be subtracted from the experimental spectrum due to the lack of a reference spectrum. The minor deviations of the experimental spectrum compared to the modelled $L_{2,3}$–MM Auger-Meitner spectrum for kinetic energies lower than 210 eV will be discussed together with panel **b**.

The simulations presented in panel **a** successfully replicate the experimental observations of the DCH feature centred around 220 eV, indicating a general understanding of the underlying mechanisms. Moreover, the simulations reveal that the experimentally DCH feature predominantly arises from decays resulting in the final configuration of $2p^{-1}3p^{-2}3d$. This implies that both the core-filling electron and the ejected electron in the Auger-Meitner decay originate from the $3p$ subshell, which is also the preferred decay pathway of the pure SCH configurations [121]. Moreover, the simulations reveal the minimal impact of the participator decay pathways on the DCH feature. Specifically, at approximately 243 eV, participator decay influences only the yield of the $3s$ photoelectron, which is not discernible in the experimental spectrum due to background noise exacerbated by integration.

Collectively, the three selected resonant transitions [Tab. 6.2] encompass a total of 942 (3×314) decay transitions: Transitions to the final configuration $2p^{-1}3p^{-2}3d$ account for 468, $2p^{-1}3s^{-1}3p^{-1}3d$ for 390, $2p^{-1}3s^{0}3d$ for 36, and the participator decay accounts for 48 transitions. This complexity can be discerned only theoretically due to the closely spaced transition energies, which overlap due to their natural line widths. Furthermore, the limitations of the spectrometer function exacerbate this overlap.

Despite the overall agreement, the discrepancy of 4.5 eV between the experimental data and the JAC calculations is considerable, particularly given that inaccuracies in the calculations are expected to lie within the range of 2–3 eV. Comparable calculations presented in panel **b**, conducted using FAC (to be discussed later), also exhibit a similar deviation of 4.5 eV. The calibration uncertainty is estimated to be no greater than 0.5 eV. Consequently, a satisfactory explanation for this discrepancy remains elusive.
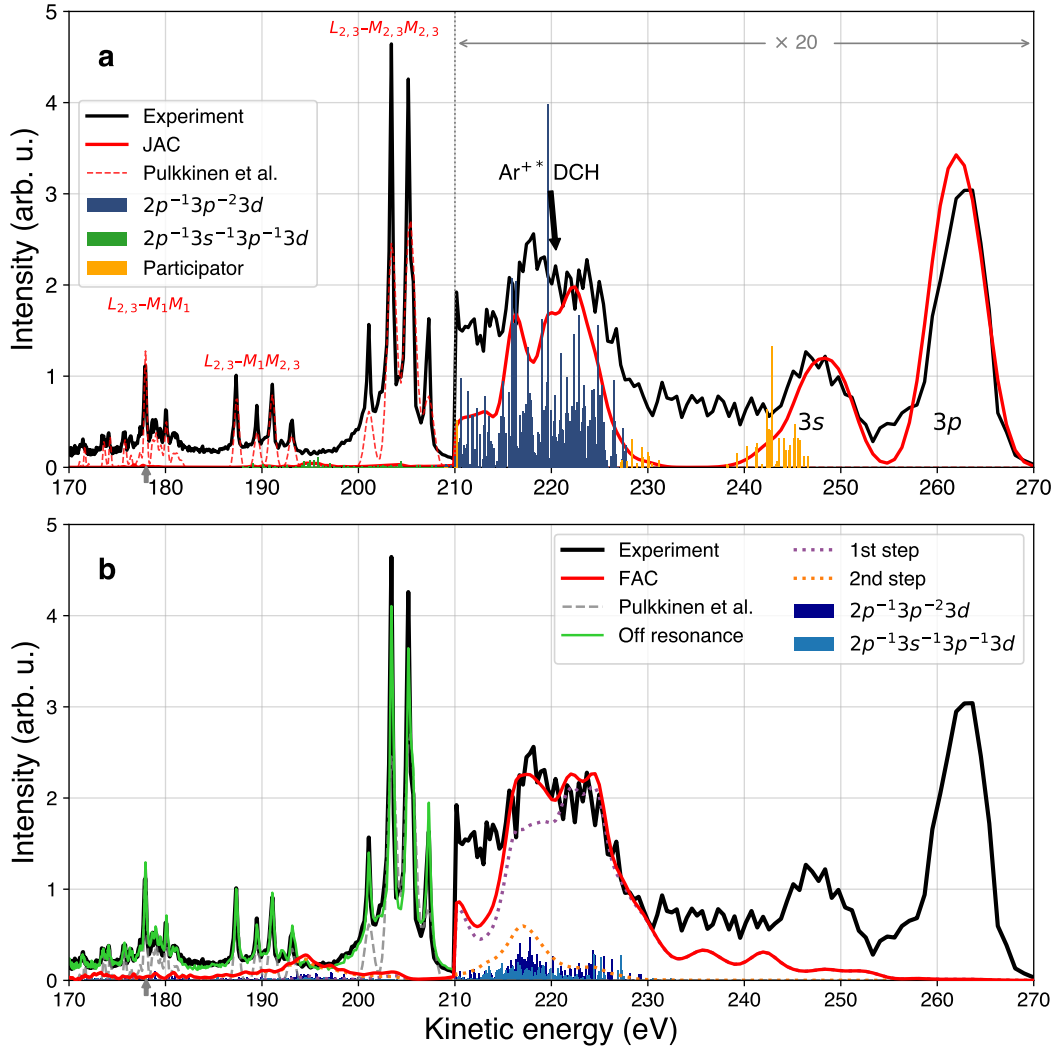
Figure 6.6: Comparison between theory and experiment focusing on the resonant DCH feature. Panel **a** displays the integrated experimental spectrum (black) and the corresponding JAC-calculated spectrum (solid red). Both spectra exhibit the integration of the data illustrated in Fig. 6.5 within the photon-energy range of 275.2–280.2 eV. From 160 eV to 210 eV, the modelled Auger-Meitner spectrum (red dashed line) resulting from the $2p$-SCH decay is shown. The minor grey arrow positioned at 178.0 eV signifies the normalisation peak for the experimental and modelled spectrum in both panels. Further, the JAC-calculated transition rates weighted by the oscillator strength of the selected resonant transitions for DCH decay are shown. The decay transitions are colour-coded according to the final configuration. In panel **b**, the experimental and the modelled Auger-Meitner spectrum are the same as in panel **a**. Here, the solid red line displays FAC calculations of the DCH decay cascade and shows, in addition to the first step (dotted purple line), the second step (yellow solid line) and is normalised to the experimental DCH feature. The colour-coded transition rates belong to the second decay step, and the labels display the initial configuration of the decay. FAC calculations are also shifted by 4.5 eV towards lower energies.

Panel **b** illustrates the influence of the second step of the decay cascade on the spectrum. The calculations, conducted using FAC, include the DCH decay cascades down to Ar^{3+}, as detailed in Sec. 6.2.1, and are represented by the solid red line. The calculated transition rates are weighted by the oscillator strengths and branching ratios from the first step. Specific parts of the FAC calculations are highlighted: The dotted purple line represents only the first step of the DCH decay cascade, while the dotted orange line depicts solely the subsequent second step. The FAC calculations are shifted by 4.5 eV towards lower kinetic energies and normalised to the integrated electron yield of the experimental DCH feature. In contrast to panel **a**, the labels of the transition spectra (blue and dark blue) correspond to the initial configurations of the transitions. The experimental spectrum (solid black line) remains unchanged from panel **a**, while the modelled $L_{2,3}MM$ spectrum is displayed as a dashed grey line. Additionally, panel **b** presents an "off-resonance" spectrum, corresponding to a single spectrum at 257.2 eV, scaled to the arbitrarily chosen peak at 178.0 eV, marked by the grey arrow.

The FAC-calculated first step yields a comparable result as the JAC calculations in panel **a**. Furthermore, the FAC calculations indicate that the second step of the DCH decay releases electrons with kinetic energies comparable to those emitted during the first step. The combined FAC calculations mirror the experimental findings more closely, displaying a two-peak structure and decay electrons in the energy range below 210 eV. As a result, the decay cascade following the DCH decay cannot be disregarded, as it generates electrons within the same energy range.

Incorporating the cascade's second step also helps elucidate certain residual discrepancies between the experiment and modelled spectrum in the SCH Auger-Meitner spectrum, particularly regarding contributions below a kinetic energy of 210 eV. Besides a noticeable noisy background, the peak group associated with the $L_{2,3}$–$M_{2,3}M_{2,3}$ transitions shows a distinct deviation in intensity from the pure SCH decay spectrum. The off-resonance spectrum serves as an experimental reference, expected to be free from contributions beyond the SCH decay, and reveals a similar deviation when compared to the "on-resonance" spectrum of the $L_{2,3}$–$M_{2,3}M_{2,3}$ peak group. This suggests that the observed differences arise from the second step of the decay cascade, thereby enhancing the understanding of the experimental observations below 210 eV.

6.3.2   Resonance in doubly charged argon

The observed resonant feature around 261.2 eV corresponds to the resonant excitation of the $2p \rightarrow 3d$ transition in doubly charged argon ions with an electronic configuration $3p^{-2}$, resulting from the relaxation of a previous $2p$-SCH state, as indicated by the JAC calculations. The calculations in this section are exclusively done using JAC.
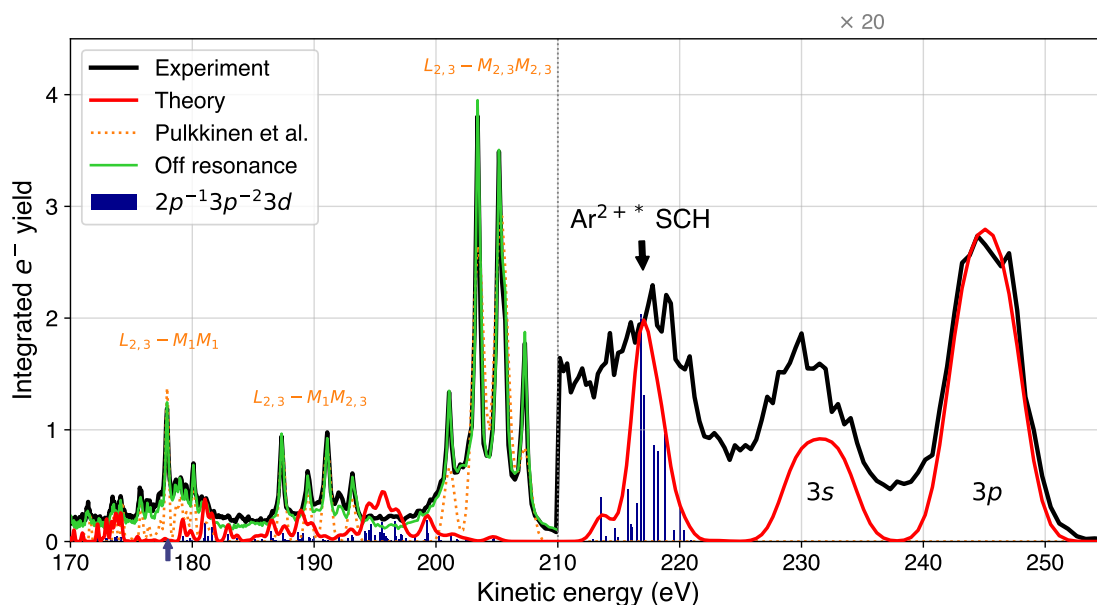

Figure 6.7: Comparison between theory and experiment of the resonant SCH formation in doubly charged argon for the kinetic energies 170–255 eV. Panel **a** shows the experimental spectrum (black) alongside the JAC-calculated spectrum (red), encompassing integrated electron spectra of the data illustrated in Fig. 6.5 for the photon energies 258.1–262.1 eV, where the SCH feature of Ar^{2+*} is observed. Similar to Fig. 6.6, the modelled Auger-Meitner spectrum, resulting from the $2p$-SCH decay, is shown by the dashed red line, and the green solid line shows the off-resonance spectrum. The minor blue arrow positioned at 178.0 eV signifies the normalisation peak for the experimental, modelled, and off-resonance spectra.

Fig. 6.7 displays the integrated experimental and theoretical spectra along the photon-energy axis from 258.1 to 262.1 eV from the data illustrated in Fig. 6.5. The experimental feature spans 214.0–224.0 eV, whereas the calculated spectrum ranges from 212.0 to 221.0 eV and exhibits a notably smaller peak. Adding more than four resonant transitions did not lead to a broadening of the calculated peak. It is likely a result of the superposition of the $3p$ photoelectron yield, resulting from the sequential ionisation of the relaxed $3p^{-2}$ configuration to $3p^{-3}$, with an ionisation energy of 40.7 eV [43] in Ar^{2+}. The increased peak in the $3s$ photoelectron yield around 230.0 eV is probably superimposed with the sequential ionisation of a $3p$ electron in $3p^{-1}$ to $3p^{-2}$, given that the ionisation energy of a $3p$ electron in Ar^{+} (27.6 eV [43]) is comparable to that of a $3s$ electron in neutral argon (29.3 eV [40]). Overall, the calculations reasonably explain the resonant feature at 218.0 eV.
Fig. 6.7, analogous to Fig. 6.6, further displays the modelled SCH decay (dashed red line) and the off-resonance spectrum (solid green line). This comparison reveals

minor differences between the on- and off-resonance spectra in the kinetic energy range of 180–200 eV, which can be attributed to the contribution of the Ar^{2+*} SCH decay for kinetic energies below 210 eV.

In analogy to similar experiments on neon and water [156], the presence of a distinct resonant peak at 261.2 eV was initially thought to be linked to the decay of a DCH state formed through resonant excitation of a $2p$ electron to a $3s$ vacancy, triggered by a conjugated shake-up process promoting a $3s$ electron to an unoccupied $3d$ orbital during the initial photoionisation process and effectively leads to the same DCH state discussed above. This mechanism resembles an alternative DCH state formation pathway in isolated water molecules, as documented by Ismail et al. in 2023 [156], involving a similar valence electron shake-up.

According to the JAC-calculations, the probability of a conjugated shake process, where a $3s$ electron transitions to an unoccupied bound $3d$ orbital, is estimated to be approximately 1-2% during the photoionisation of a $2p$ electron, requiring a photon energy of at least 288 eV to occur. In contrast, the resonant transition $2p \rightarrow 3s$ from the $2p^{-1}3s^{-1}3d$ configuration to the $2p^{-2}3d$ configuration requires a photon energy of approximately 257 eV, indicating that the photon energy required for the resonant transition $2p \rightarrow 3s$ is insufficient to enable the initial formation of the $2p$ core hole and the conjugated shake-up process. Furthermore, the calculations reveal that approximately 2% of $3s$ orbitals experience a monopole shake-up, transitioning to an unoccupied bound $4s$ orbital during photoionisation, requiring comparable photon energies as the conjugated shake-up process to manifest.

As a result, the JAC calculations reveal the energetic impossibility of this alternative pathway for DCH state formation within the $2p$ subshell of argon using two photons of identical energy.

6.3.3 Pulse-energy dependence of the DCH

To explore the intensity-dependent nonlinearity of the DCH, which is crucial for the validity of a two-photon process, a pulse-energy scan was performed at the fixed photon energy of 277.2 eV, spanning from 66 to 790 µJ prior to the KB mirrors. For the scan five different runs were measured, each characterised by different GATT transmissions. The pulses from a given run, exhibit a Gaussian pulse-energy distribution (s. Sec. 4.1.7). This distribution is subdivided into pulse-energy bins containing sufficient pulses ($\sim$3000) to generate an electron TOF spectrum and provide more continuous data points. Subsequently, the pulses of a bin are averaged to generate an electron spectrum. The pulse-energy distribution has already undergone pre-filtering, which only considers the first pulse of a train to rule out effects originating from deviations within a pulse train. From a bin's averaged spectrum, the data points corresponding to the yield of the DCH feature and the $3p$-photoelectron are extracted by integration along the kinetic-electron-energy axis.
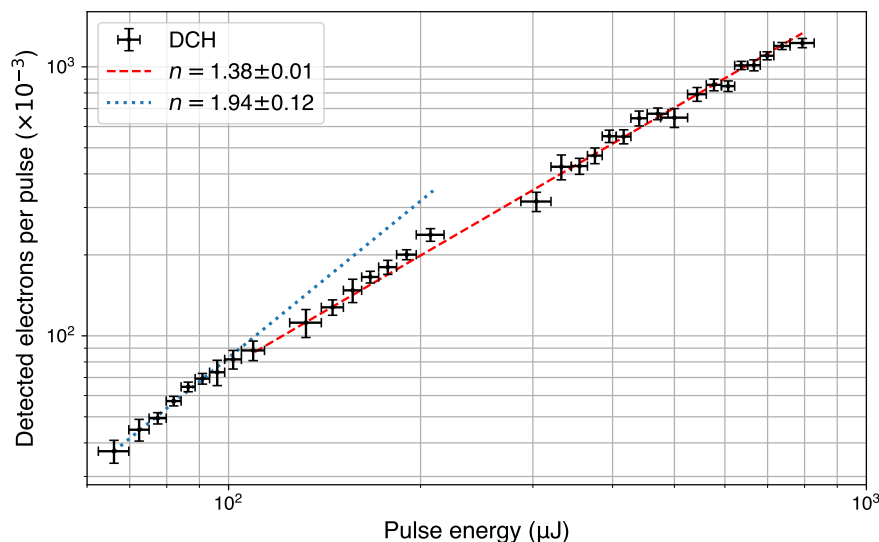
Figure 6.8: Pulse-energy dependence of the electron yield from DCH decay and $3p$ photoelectron yield.

Fig. 6.8 presents the integrated DCH yield as a function of pulse energy, displayed in black on a log-log plot. According to Ref. [22], the electron yield on a log-log plot is proportional to the number of absorbed photons n, indicated by the slope of a straight line. Assuming that the yields of $3p$ photoelectrons are linear, the data are aligned to correspond with a straight line of slope 1, thereby accounting for variations in pulse energy and serving as a reference for a linear process. This alignment results in an individual correction factor for each data point, which is similarly applied to the DCH data points. This approach is justified under the assumption that the ionisation yield of a $3p$ electron represents a linear one-photon process. It is important to note that this represents an approximation, as the $3p$ photoelectron and the DCH feature originate from different source volumes, with their respective processes occurring under different fluence regimes of the XFEL beam, as discussed in Sec. 5.3.

The analysis of the overall slope (dashed red line) yields a value of 1.4, suggesting a nonlinear process that is approaching saturation. According to LOPT, the formation of DCH is characterised as a nonlinear process, with an anticipated slope of 2, attributable to the absorption of two photons. By examining only the first six data points, the observed slope (dotted blue line) is 1.9, further indicating a nonlinear process consistent with $n = 2$. This finding supports the assertion that the electron yield reaches saturation beyond 100 µJ. Additionally, the influence of a linearly increasing background, which includes contributions from residual and sample gases, remains unclear due to the lack of estimation methods and may potentially impact the slope.

6.4 Conclusion

This study presented experimental evidence of a resonant $2p$-DCH state in singly charged argon induced by the absorption of two photons. Based on JAC calculations, the transition of a $2p$ electron to an unoccupied $3d$ orbital in singly charged argon, exhibiting an SCH in the $2p$ subshell, could be identified, and the calculated relaxation processes align with experimental observations. Moreover, further analysis via FAC demonstrated that the second step of the DCH decay cascade emits electrons within the same energy range as the first step, thereby improving the agreement between theoretical predictions and experimental results. In addition to the DCH feature, an SCH feature in doubly charged argon could be observed, which could only be identified by JAC calculations.

Given that the experiment was performed during the commissioning phase of the SQS instrument and under given time constraints, the experimental conditions were not ideal. Several improvements are recommended to enhance the conditions for similar future experiments. Firstly, additional measurements should be performed at a retardation of 200 V to better resolve the DCH feature. Secondly, expanding the photon-energy range to exceed 280 eV would facilitate searching for additional resonances, particularly those associated with the $2p^{-2}3d$ state, thereby confirming theoretical calculations. Furthermore, it is essential to record calibration spectra for both energy and transmission measurements to ensure accurate data. Finally, improving the signal-to-noise ratio would significantly enhance the quality of the experimental results.

Chapter 7

Conclusion and Outlook

In summary, the first part investigates the multiphoton multiple ionisation processes of isolated xenon atoms interacting with ultraintense soft XFEL pulses, focusing on how these processes depend on photon energy across three distinct peak fluence regimes. Employing ion TOF spectroscopy, a CSD was extracted from the experimental data for each photon energy across the photon-energy range of 700 to 1700 eV. The key outcome is a map of resonant structures as a function of photon energy and charge state. The map comprises the vertical aligned CSDs across the photon-energy range. By slicing this resonance map horizontally, resonance spectra can be rendered, illustrating the ion yield of selected charge states as a function of photon energy. The theoretical analysis of the ionisation pathways further reveals that specific peaks in the resonance spectra are exclusively formed through configurations involving two or more core holes. This investigation identifies photon-energy- and charge-state-dependent transition energy lines specific to resonant excitations. It demonstrates the creation and probing of extremely short-lived and unusually long-lived highly charged ions in exotic electronic configurations through intense soft XFEL pulse interactions. Such unusual atomic species may also arise from collisions in outer space [19, 157], potentially serving as candidates for unidentified X-ray emission lines in astrophysical contexts [20, 158]. However, significant deviations between the transition energy lines and the experimentally observed ion yields emerge when considering only the ground state. A deeper analysis of the ionisation pathways indicates that the involvement of MCH states leads to shifts in energy at which the photon energy becomes resonant, enhancing the understanding of the resonance structures.

Moreover, this investigation introduces a novel form of nonlinear spectroscopy that exploits fully saturated yields of individual xenon ion charge states. This advancement is made possible by the wide tunability of photon energy through ultraintense, femtosecond XFEL pulses, operating stably across the photon-energy range. The combination of advanced photon diagnostics and fast attenuation techniques ensures the constant number of photons on target during the scan. It is demonstrated that the resonance spectra become insensitive to peak fluence beyond a specific saturation peak fluence, enabling the isolation of X-ray beam parameters that the dominant fluence dependence would otherwise complicate. This insensitivity facilitates the characterisation of transient resonant excitations during the charge-up process, even without requiring volume integration in theoretical models.

The second part of this thesis examines the nonlinear absorption of two soft X-ray photons within the $2p$ subshell of argon, resulting in the formation of a DCH state. This work elucidates the complexity of atomic DCH states and provides experimental evidence for a resonant $2p$-DCH state in singly charged argon induced by the absorption of two photons by using electron TOF spectroscopy. Through theoretical calculations, the transition of a $2p$ electron to an unoccupied $3d$ orbital in singly charged argon, exhibiting a SCH in the $2p$ subshell, was identified, with calculated relaxation processes aligning closely with experimental observations. Further analysis revealed that the second step of the DCH decay cascade emits electrons within the same energy range as the first step, enhancing the agreement between theoretical predictions and experimental results. In addition to the DCH feature, an resonant SCH feature in doubly charged argon was observed. The calculations indicate that this feature belongs to the resonant transition $2p \rightarrow 3d$, revealing high complexity.

The two employed spectroscopic techniques for ions and electrons represent straightforward approaches to exploring the intricate pathways of multiphoton multiple ionisation while providing profound insights into their complexity. Future experiments may enhance these methods with high-resolution fluorescence measurements – despite representing only a minority of all electronic transitions involved – to validate theoretical calculations or combine them in coincidence measurements to track Auger-Meitner decay cascades using a MBES. Notably, the resonant DCH formation in the $2p$ subshell of argon, serving as a first approximation to MCH states, exemplifies the complexity of DCH formation beyond that observed in the K shell. Investigating DCH formation in xenon's $3d$ subshell or the phenomenon of triple-core-hole formation will necessitate coincidence methods to disentangle the electron spectra due to overlapping emission lines. Additionally, at high degrees of ionisation – up to 41 electrons emitted from a single atom – Coulomb interactions among ejected electrons invariably broaden the emission lines.
Consequently, ion spectroscopy remains advantageous for probing the dynamics of multiphoton multiple ionisation under ultraintense XFEL pulses. Techniques such as seeding and X-ray pump / X-ray probe schemes may be employed to systematically investigate the evolution of transient resonances in the spectral and temporal domain. In addition to the photon energy, upcoming possibilities of tuning the pulse duration at high peak fluences will provide deeper insights into forming MCH states and pave the way for diagnostics concerning the pulse duration based on ion TOF spectroscopy.

The data analysis of the multiphoton investigation in xenon demonstrated that the domain of ultraintense XFEL interactions with atoms requires modifications of the data evaluation, in contrast to established ion TOF analysis. Moreover, the analysis of the PHD revealed a method to differentiate between two species with identical mass-to-charge ratios, a consideration of significance in multiphoton investigations involving molecules, such as Coulomb explosion imaging (CEI), where the detected constituents exhibit only slight variations in their mass-to-charge ratios.

Appendix A

Appendix

A.1 Experimental comparison with Rudek et al. in 2012

In Fig. 1 of Ref. [25], Rudek et al. note that the peak fluence at 1500 eV was approximately halved compared to the peak fluence of 82-89 µJ/µm² at 2000 eV. This suggests a peak fluence of roughly 43 µJ/µm², corresponding to a photon flux of 1.79×10^{11} ph/µm², at which they observed Xe^{36+} as the highest charge state. In contrast, Fig. A.1 indicates that in the present study, at a comparable peak fluence of 1.4×10^{11} ph/µm², the highest observed charge state is Xe^{30+}, which contradicts Rudek et al.'s findings. It need a roughly five times higher peak fluence to observe Xe^{36+} in the present study. This difference can have multiple causes: an overestimated focus size or incorrect estimated peak fluence or an shorter pulse duration than estimated.
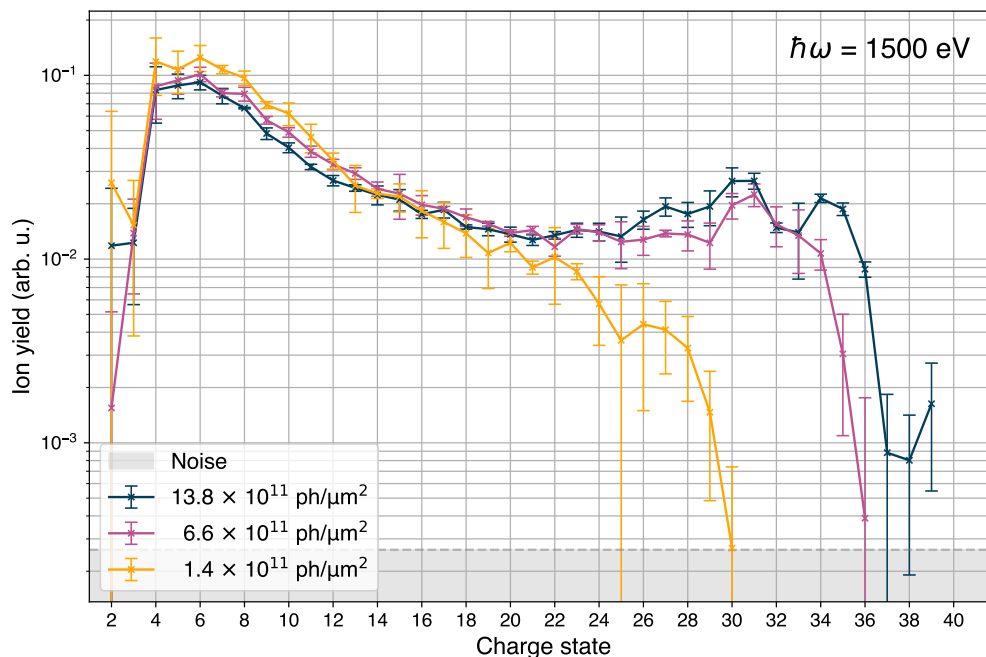
Figure A.1: CSD of 1500 eV at three different peak fluences.
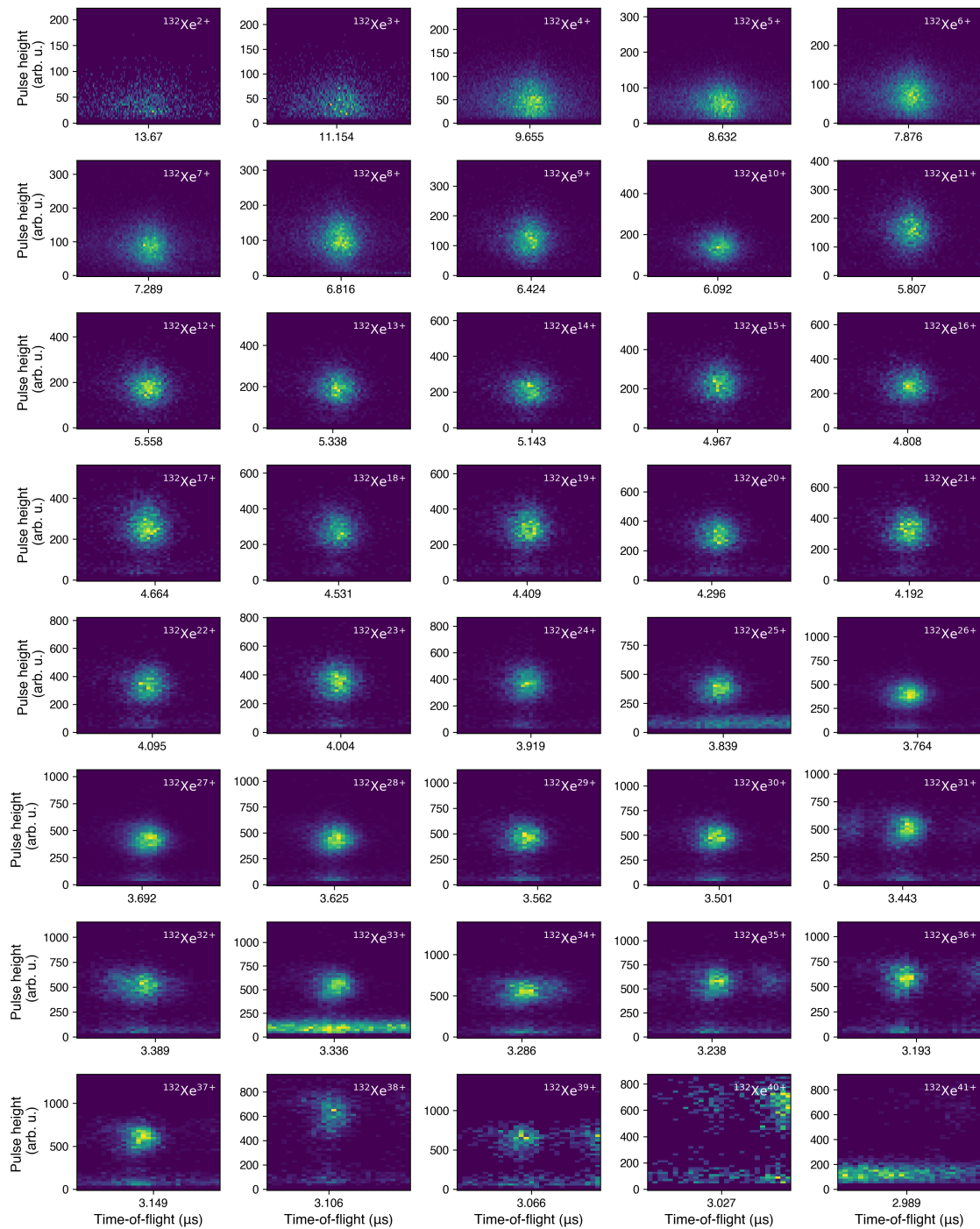
A.2   Xenon PHDs

Figure A.2: 2D colour map of PHD as a function of TOF for the charge states Xe^{2+}–Xe^{41+} extracted from Fig. 4.18.
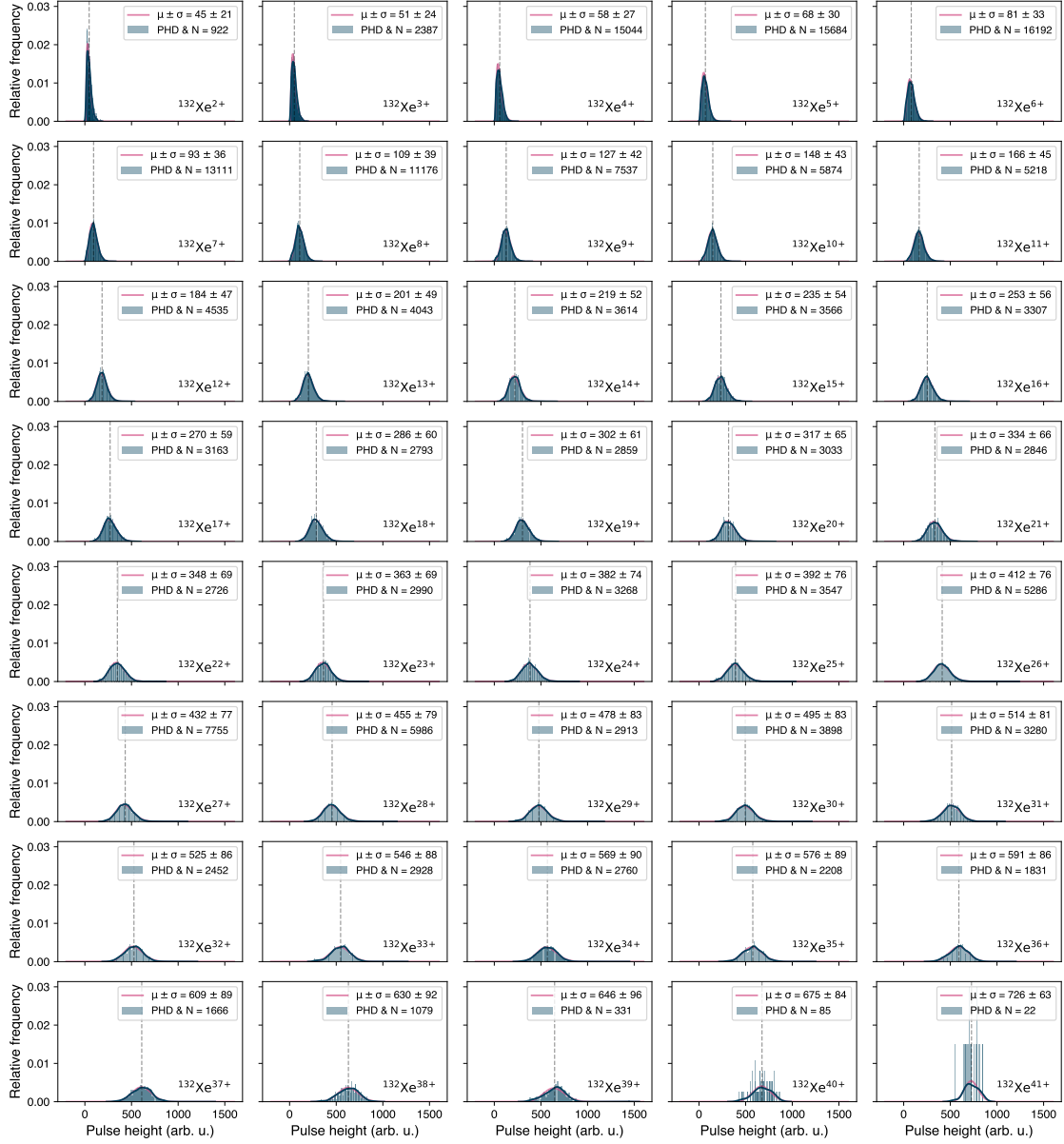
Figure A.3: Peak fitting of individual PHDs using a gamma distribution function to extract the mean.

A.3   Argon PHDs

Figure A.4: PHDs of argon at reduced gas pressure. The photon energy is 1100 eV, and the pulse energy on target is 3.2 mJ.

A.4   Multiphoton multiple ionisation of xenon at 93-eV

The phenomenon of a higher charge state than the direct sequential single-photon ionisation limit was first observed by Sorokin et al. [22] in 2007 at FLASH by using ion TOF spectroscopy on xenon atoms irradiated with a maximum intensity of 7.8 $\times 10^{15}$ W/cm^2. They detected charge states up to Xe^{21+} at a photon energy of 93 eV near the so-called $4d$ giant resonance, which would require an overall absorption of 56 photons. Including Auger-Meitner decay cascades of an initial $4d$ core hole, Xe^{7+} is supposed to be the highest charge state with a photon energy of 93 eV, according to the ionisation potentials of xenon in Ref. [43]. Further, Sorokin et al. excluded:

- Plasma effects of neighbouring atoms due to the insensitivity of the gas pressure on the observed TOF spectrum (no line broadening),

- nonperturbative strong-field phenomena, which can be neglected due to the weak ponderomotive potential of 0.13 eV and a first ionisation energy of 12.1 eV for xenon, and

- nonsequential direct multiphoton ionisation because of the shallow cross section for direct two-photon absorption in the XUV regime and the necessity of absorbing seven photons in the last ionisation of Xe^{20+}.

This unexpected observation sparked a "controversial" discussion about the role of the $4d$ giant resonance in multiphoton ionisation of xenon and whether a strong electron correlation within the $4d$ subshell leads to a collective resonance [159]. Not least because the first theoretical approach considered a sequence of single- and multiphoton absorptions comprising 19 ionisation steps equivalent to 19 coupled rate equations and 19 corresponding single- or multiphoton absorption cross sections partly known from experiment and the unknown are obtained by scaling and variation to match the experimental data [160, 161]. In a not-yet peer-reviewed study (as of April 2024), Palutke et al. provide an alternative explanation of the high charge states of Xe^{21+} by thoroughly tracing the complex resonant excitations involved in the ionisation process [162]. A chronological list of publications that followed this first experiment in 2007 can be found in Appendix A.4. Just as a note, a charge state of Xe^{21+} means an empty O shell, an empty $4d$ subshell and a half-filled $4p$ subshell, which is remarkable since the photon energy of 93 eV is already far off the $4p$ ionisation threshold of the ground state of around 146 eV and has in addition a lower PCS than $4d$. Access to the $4p$ subshell is only possible for resonant excitations within the N shell, which is a perfect match of photon energy and the energy difference between the subshells.

- **November 2004** *Santra and Greene* Theoretical rate-equation-based description of VUV multiphoton ionisation of Xe atoms and ions with 12.7-eV photons → Reproduction of the experimentally observed Xe^{6+}. However, theory indicates that treating a single active electron does not suffice. [163]

- **May 2007** *Sorokin et al.* Investigation of He and Ne → Multiphoton absorption is mainly sequential. [125]

- **November 2007** *Sokokin et al.* Investigation of Xe → Observation of Xe^{21+}. [22]

- **November 2008** *Popruzhenko et al.* Nonrelativistic analytical expression without resonances and one active electron for the ionisation rate of atoms and ions → Multielectron mechanisms may play an important role

- **January 2009** *Makris et al.* Theoretical study of Xe^{21+} observed by Sorokin et al. → Development of semi-empirical formalism for multiphoton perturbation theory explaining the charge states up to Xe^{15+} [160].

- **April 2009** *Richter et al.* Investigation of Xe with 90.5 eV → Suspicion of a collective electronic behaviour involving the giant $4d$ resonance of xenon [164].

- **June 2010** *Richardson et al.* Direct two-photon absorption (ATI) of a $4d$ electron of xenon with 93-eV photons → Observation of a nonlinear process in the soft X-ray regime by electron spectroscopy [165].

- **September 2010** *Richter et al.* Investigation of multiphoton ionisations of atoms, including Xe, with soft X-ray pulses → Inner-shell resonances might play a significant role in creating Xe^{21+} [159].

- **March 2011** *Richter* Theoretical nonperturbative approach by plasma excitation → Model reproduce high charge states but with overestimation of charge states as of Xe^{20+} [166].

- **June 2011** *Lambropoulos et al.* Theoretical parametric study of the conditions leading to Xe^{21+} → $4d$ giant resonance do not contribute to the high charge states of xenon and shows no collective behaviour at intensities above 5×10^{15} W/cm² [167].

- **May 2014** *Gerken et al.* Time-dependent multiphoton ionisation of xenon with 93-eV photons → Tracing back the multiphoton multiple ionisation route up to Xe^{10+} [168].

- **October 2020** *Hadjipittas* Xenon interacting with attosecond XUV pulses → Sequential ionisation leading to Xe^{5+} involves a direct two-photon absorption process [169].

- **October 2022** *Palutke et al.* Scanning xenon along the $4d$ giant resonance → Reaching Xe^{21+} by "multi-resonant ladder of predominantly $4p - 4d$ excitations" [162].

A.5 Sequential ionisation approach in xenon

The study of Saito and Suzuki [41] illustrates a high degree of ionisation after single-photon absorption. Based on this, the study of Schippers et al. [170] can be used to deduce what happens after a two-photon process. Now, considering absorptions of more than two photons, the ionisation pathways are becoming less understandable, and theory is needed to shed light on the underlying ionisation mechanisms.
Schippers et al. [170] extended the study on neutral xenon of Saito and Suzuki [41] in 2014 by measuring the absolute photoionisation cross sections of the xenon ions Xe^+ to Xe^{5+} in the photon-energy range of 500–1200 eV and observed enhanced PCS resulting from $3d \rightarrow nf$ resonant excitations in the range of 650-750 eV with an ionisation degree of up to Xe^{9+}. Summarising in a reaction equation similar to Eq. (5) in [170] yields:

$$\hbar\omega + Xe^{i+} \rightarrow Xe^{r+} + (r-i)e^-$$

With Xe^{i+} the initial (i=1-5) and Xe^{r+} (r=4-9) the resulting charge state. By using the results of Schippers et al. [170], a second photoabsorption in the predominantly created charge states Xe^{4+} and Xe^{5+} (after previous single photon absorption) with a photon energy around the $3d$ edge triggers the $3d \rightarrow nf$ transition leading mainly to Xe^{6+}, Xe^{7+} and Xe^{7+}, Xe^{8+}, respectively. As a result, the resonant absorption of a second photon significantly increases the ion yield of Xe^{6+}-Xe^{8+} in a narrow photon-energy range around 700 eV, which can partly be observed by the subsequent, rapid decline (50-60%) of the ion yields of Xe^{6+}-Xe^{8+} in Fig. 5.12 **d** after passing 750 eV.

A.6   Fluence dependence of the 2D colour map
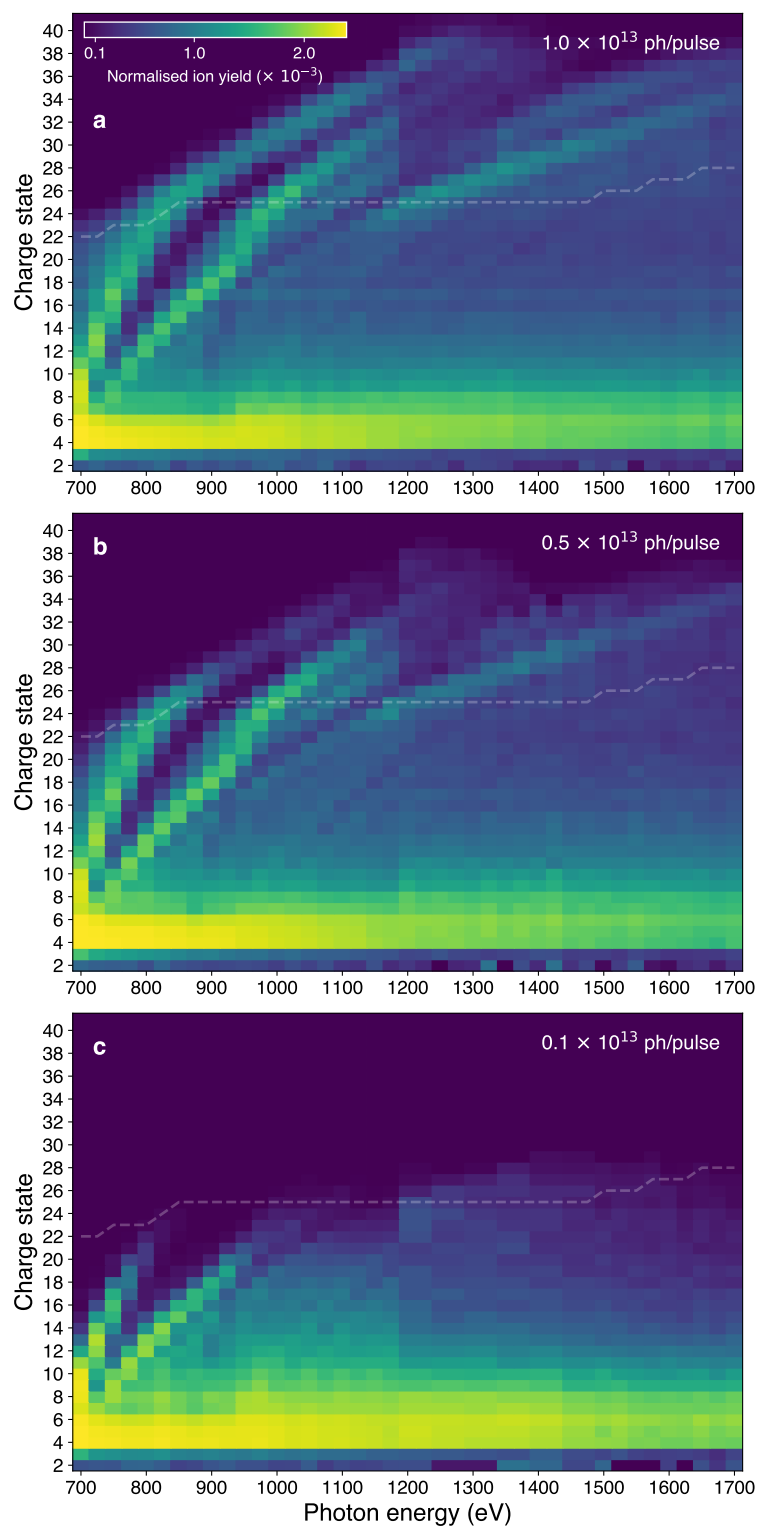
Figure A.5: Photon-energy-dependent CSD of xenon for three different fluence regimes **a** 0.1, **b** 0.5 and **c** 1.0×10^{13} photons per pulse. Panel **a** equals to Fig. 5.8. The underlying data was normalised to the gas pressure.
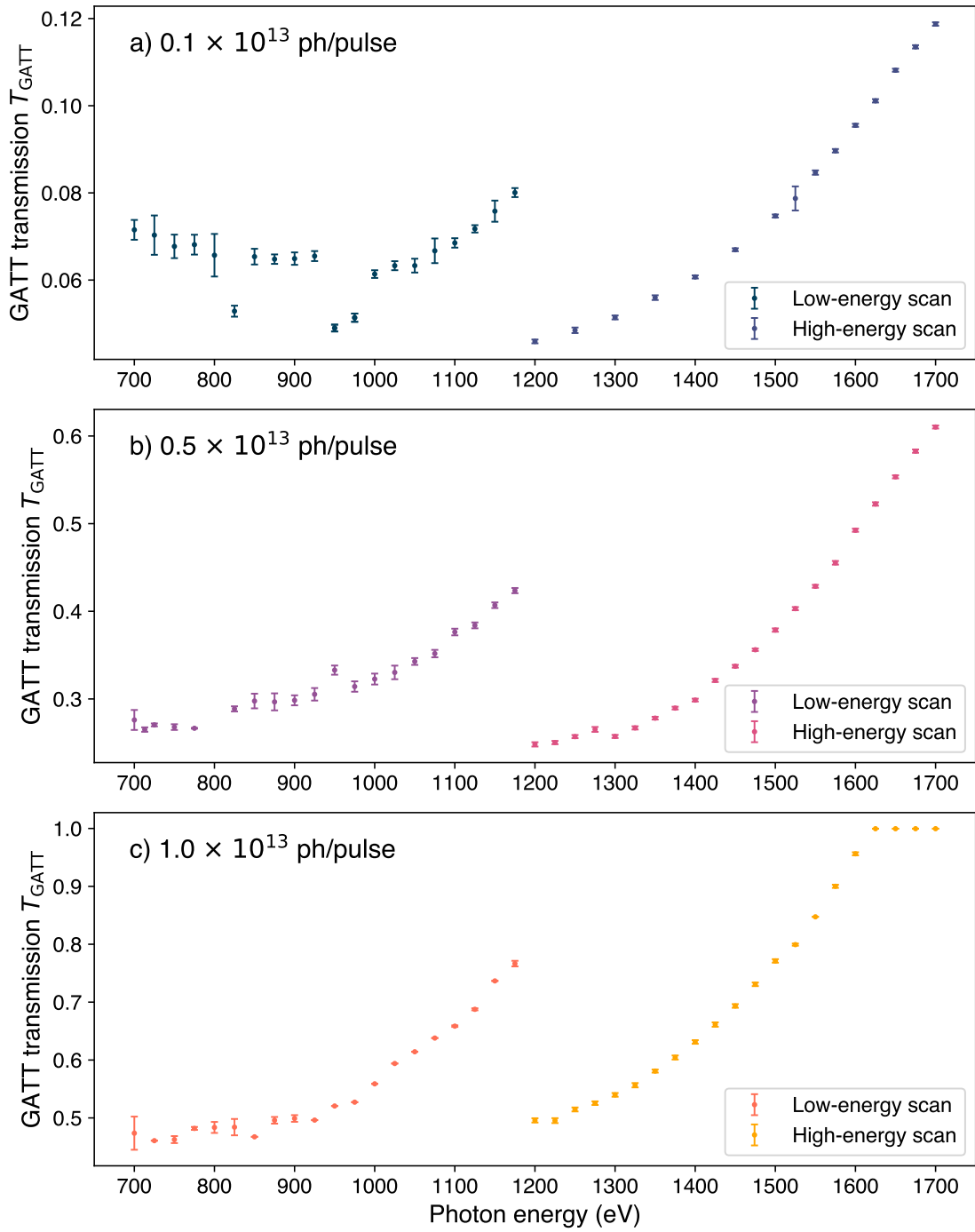
Figure A.6: Transmission settings of the GATT as a function of photon energy for the three different fluence regimes.
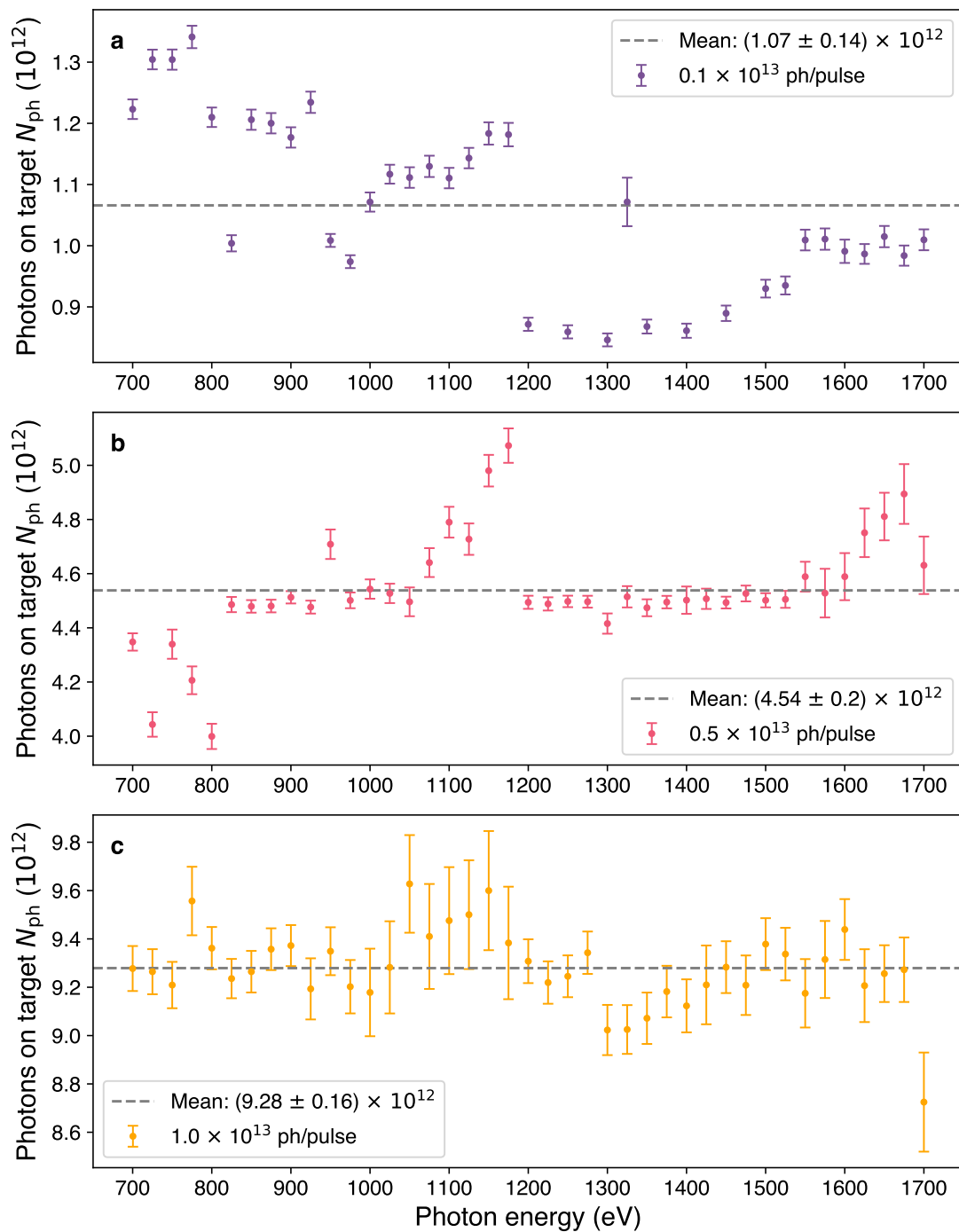
Figure A.7: Number of photons on target as a function of photon energy.

A.7   Partial PCS of xenon

Fig. A.8 shows the calculated partial photoabsorption cross section for xenon's subshells in the neutral state to visualise, The subshell of N and O are summarised in a single line, showing that PCS for the $3d$ subshell is an order of magnitude higher than for $3s$ and will be much in evidence for the resonant excitations. Also, the resonant excitation starting from the $3p$ subshell will be less pronounced than $3d$.
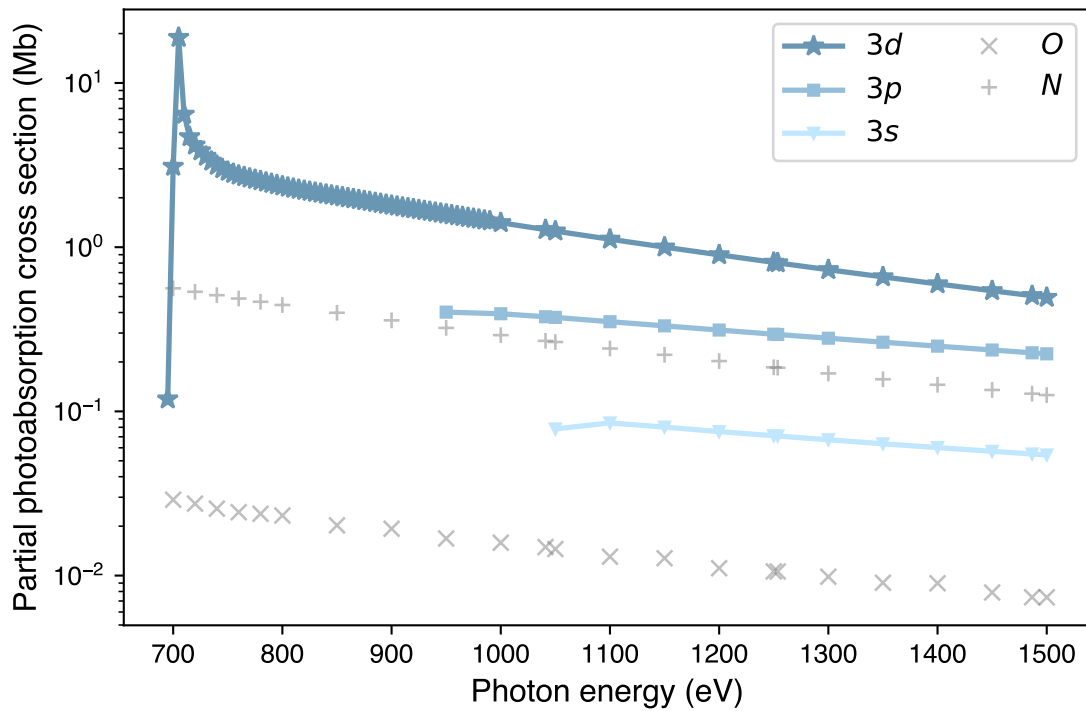

Figure A.8: Calculated partial PCSs of xenon for the subshell $3d$ (star), $3p$ (square), $3s$ (triangle), shown as coloured lines, together with the summarised subshells of the O (x) and N (plus) shell shown in grey markers. The underlying calculated data stems from Ref. [31] and can be easily accessed via `https://vuo.elettra.eu/services/elements/`.

A.8   Alternative TOF spectrum representations

The following TOF spectra show the truncated TOF spectra ($t_{\mathrm{TOF}} = 2.8$ to $10.0\,\mu s$) for five different photon energies taken from the 100% photon-energy scan and normalised to the ion yield of charge state Xe^{12+}.

The TOF scales down quadratically for higher charge states q due to the $\sqrt{\frac{m}{q}}$ compression, and leads to higher peak heights despite an equal ion yield. To better illustrate the photon-energy dependence of the spectrum, the mass-over-charge calibration is done in Fig. A.10, as described in Sec. 4.1.2. However, the ion yields are squeezed in a small TOF range, making it an almost useless representation. Further improvement is achieved in Fig. A.11 by a logarithmic scale of the TOF axis with the advantage of losing the mass dependence and gaining equidistant peak widths. Fig. A.12 shows the deconvolved TOF spectrum, which is put on a logarithmic scale in Fig. A.13. The final representation is illustrated in Fig. A.14, where additionally the intensity correction is applied reversing the MCP detection efficiency, as explained in Sec. 4.1.5.
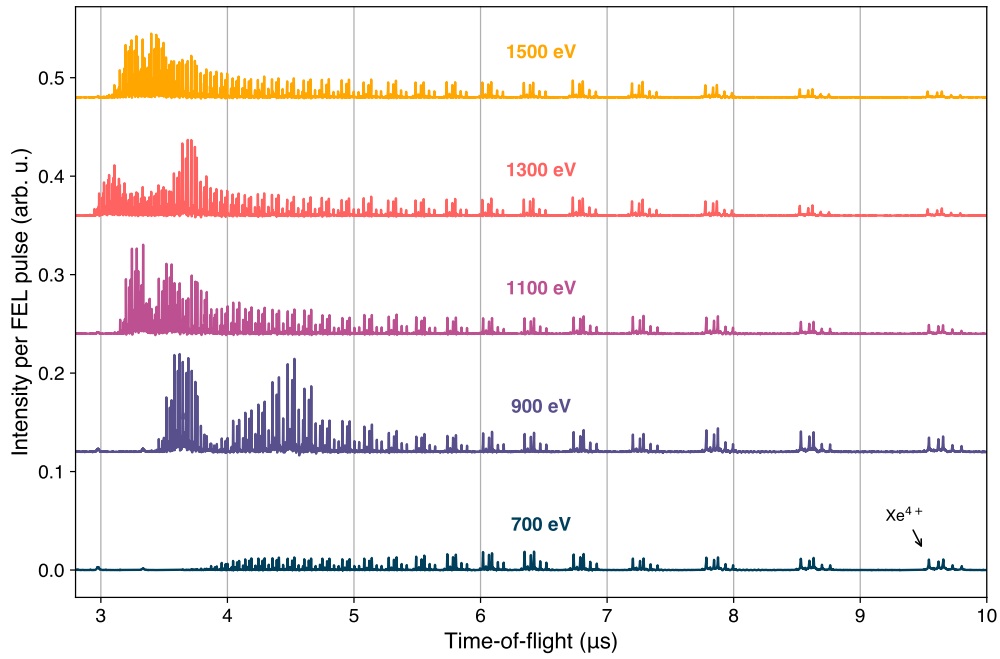
Figure A.9: Truncated TOF spectra of xenon for the photon energies 700-1500 eV for the flight times 2.8-10.0 µs. The spectra are normalised to the ion yield of charge state Xe^{12+}.
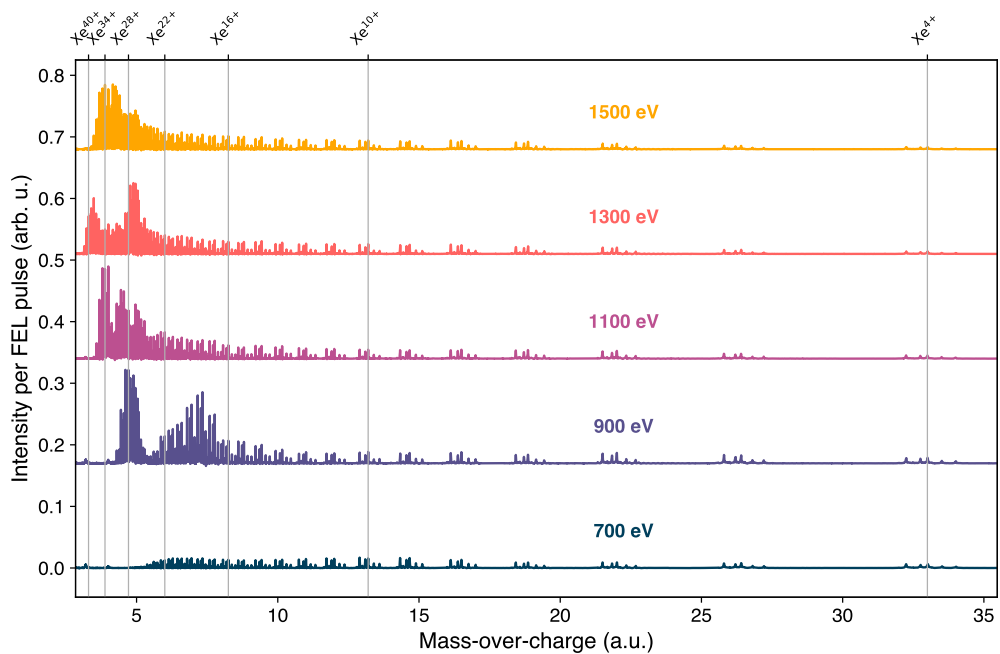
Figure A.10: Calibrated mass-over-charge spectra for the photon energies 700-1500 eV.

Figure A.11: TOF spectra of xenon on a logarithmic scale for different photon energies.

Figure A.12: Deconvolved TOF spectra of xenon for different photon energies.

Figure A.13: Deconvolved TOF spectra of xenon on a logarithmic scale for different photon energies.

Figure A.14: Deconvolved TOF spectra of xenon for different photon energies on a logarithmic scale with corrected intensity due to the MCP detection efficiency.

A.9 Comparison of the SCH decay between JAC and Pulkinnen et al. [121]

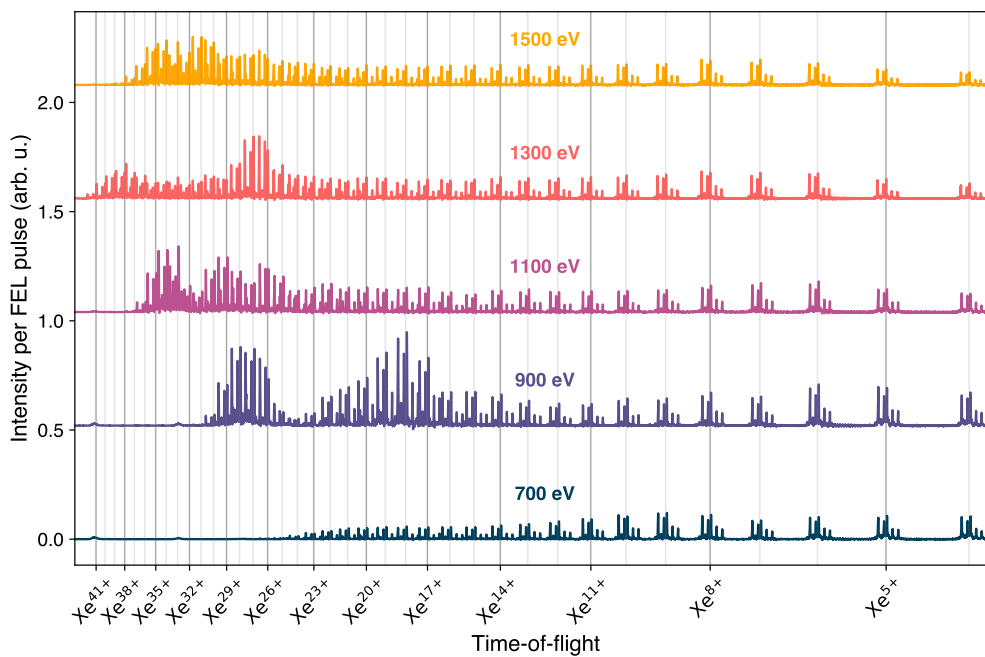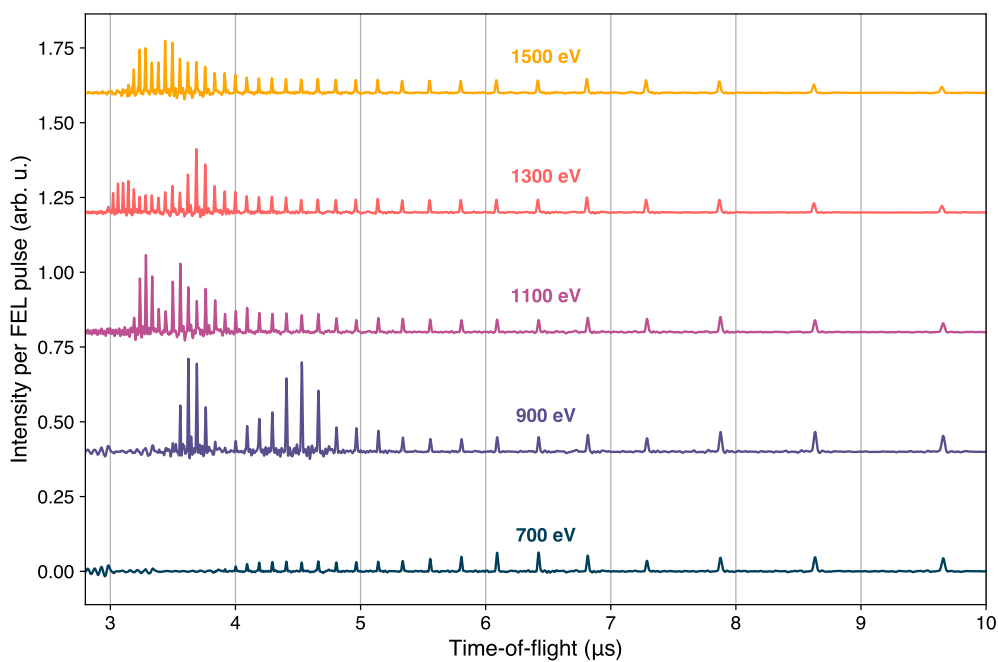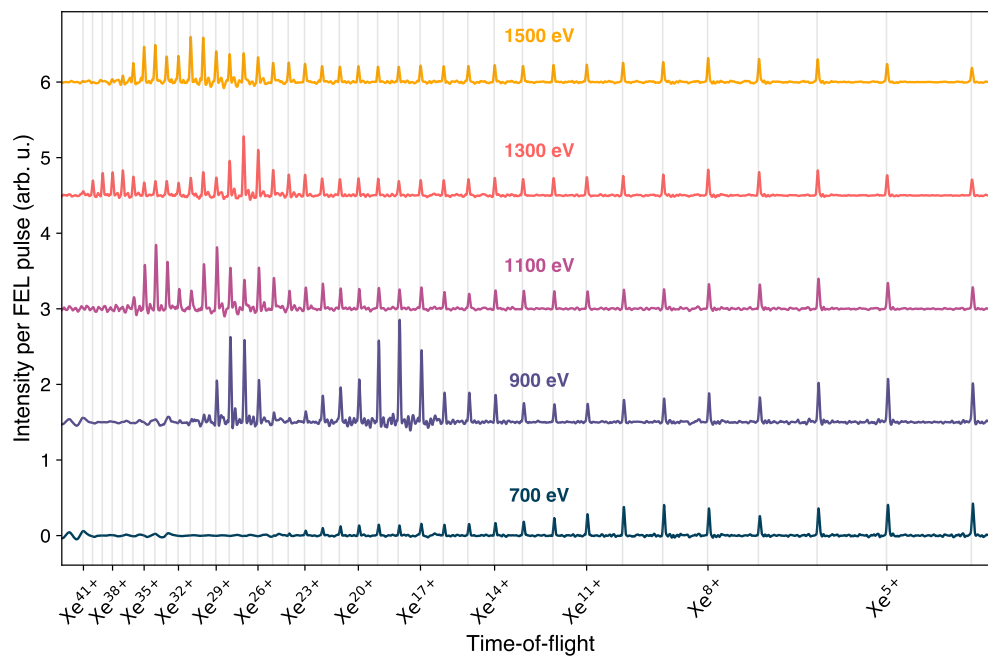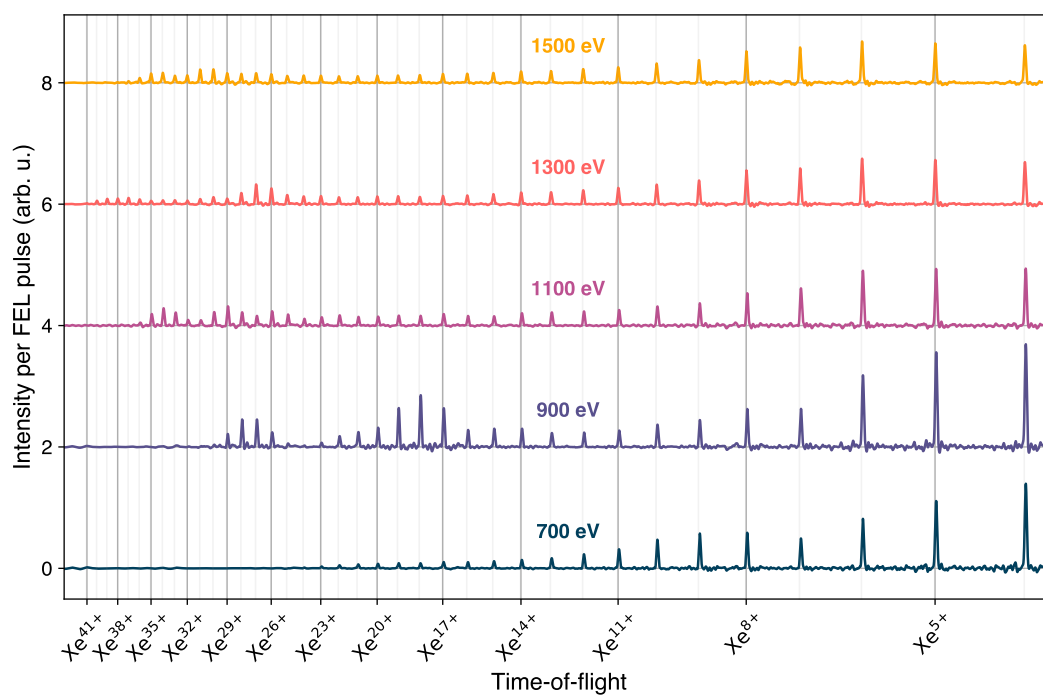| Configuration	Term symbol	$E_{\text{kin}}^{\text{(JAC)}}$ (eV)	$I^{\text{(JAC)}}$	$E_{\text{kin}}^{\text{(lit.)}}$ (eV) [121]	$I^{\text{(lit.)}}$ [121]
$2p^{-1} \to 3s^0$	$^2P_{3/2}^o \to {}^1S_0$	165.25	35.2	177.95	66.6
$2p^{-1} \to 3s^0$	$^2P_{1/2}^o \to {}^1S_0$	167.50	15.1	180.09	30.1
$2p^{-1} \to 3s^{-1}3p^{-1}$	$^2P_{3/2}^o \to {}^1P_1^o$	182.23	174.7	187.39	71.2
$2p^{-1} \to 3s^{-1}3p^{-1}$	$^2P_{1/2}^o \to {}^1P_1^o$	184.48	74.9	189.50	39.2
$2p^{-1} \to 3s^{-1}3p^{-1}$	$^2P_{3/2}^o \to {}^3P_1^o$	189.91	31.3	190.95	11.3
$2p^{-1} \to 3s^{-1}3p^{-1}$	$^2P_{3/2}^o \to {}^3P_2^o$	190.05	145.9	191.09	76.5
$2p^{-1} \to 3s^{-1}3p^{-1}$	$^2P_{1/2}^o \to {}^3P_0^o$	192.10	24.0	193.07	18.1
$2p^{-1} \to 3s^{-1}3p^{-1}$	$^2P_{1/2}^o \to {}^3P_1^o$	192.17	46.3	193.13	23.9
$2p^{-1} \to 3p^{-2}$	$^2P_{3/2}^o \to {}^1S_0$	203.46	100.0	201.11	100.0
$2p^{-1} \to 3p^{-2}$	$^2P_{3/2}^o \to {}^1D_2$	205.28	475.6	203.50	389.7
$2p^{-1} \to 3p^{-2}$	$^2P_{1/2}^o \to {}^1S_0$	205.72	50.0	203.26	50.0
$2p^{-1} \to 3p^{-2}$	$^2P_{3/2}^o \to {}^3P_0$	207.18	38.1	205.08	26.1
$2p^{-1} \to 3p^{-2}$	$^2P_{3/2}^o \to {}^3P_1$	207.24	142.8	205.10	73.2
$2p^{-1} \to 3p^{-2}$	$^2P_{3/2}^o \to {}^3P_2$	207.38	404.5	205.24	261.3
$2p^{-1} \to 3p^{-2}$	$^2P_{1/2}^o \to {}^1D_2$	207.53	209.4	205.65	202.3
$2p^{-1} \to 3p^{-2}$	$^2P_{1/2}^o \to {}^3P_0$	209.43	46.9	207.20	30.3
$2p^{-1} \to 3p^{-2}$	$^2P_{1/2}^o \to {}^3P_1$	209.49	116.3	207.25	87.6
$2p^{-1} \to 3p^{-2}$	$^2P_{1/2}^o \to {}^3P_2$	209.63	54.7	207.39	37.5

Table A.1: Comparison of SCH decays between JAC and Pulkinnen et al. [121]. Intensity is normalised to the line with the (JAC) energy 203.46 eV as done in the literature.

Bibliography

[1] Sietmann, R. False Attribution. *Physics Bulletin* **39,** 316–317 (1988).

[2] Meitner, L. Über die Entstehung der β-Strahl-Spektren radioaktiver Substanzen. *Zeitschrift für Physik* **9,** 131–144 (1922).

[3] Auger, P. Sur Les Rayons β Secondaires Produits Dans Un Gaz Par Des Rayons X. *CR Acad. Sci. (F)* **177,** 169 (1923).

[4] Auger, P. L'effet Photoélectrique Composé. *Annales de Physique* **10,** 183–253 (1926).

[5] Duparc, O. H. Pierre Auger – Lise Meitner: Comparative Contributions to the Auger Effect. *International Journal of Materials Research* **100,** 1162–1166 (2009).

[6] Matsakis, D., Coster, A., Laster, B. & Sime, R. A Renaming Proposal: "The Auger–Meitner Effect". *Physics Today* **72,** 10–11 (2019).

[7] Auger, P. Sur l'effet Photoélectrique Composé. *Journal de Physique et le Radium* **6,** 205–208 (1925).

[8] Auger, P. The Auger Effect. *Surface Science* **48,** 1–8 (1975).

[9] Decking, W. *et al.* A MHz-repetition-rate Hard X-ray Free-Electron Laser Driven by a Superconducting Linear Accelerator. *Nature Photonics* **14,** 391–397 (2020).

[10] Shintake, Tsumoru. *Review of the Worldwide SASE FEL Development* in *2007 IEEE Particle Accelerator Conference (PAC)* (IEEE, Albuquerque, NM, 2007), 89–93.

[11] Stankus, B. *et al.* Ultrafast X-ray Scattering Reveals Vibrational Coherence Following Rydberg Excitation. *Nature Chemistry* **11,** 716–721 (2019).

[12] Wolf, T. J. A. *et al.* Probing Ultrafast $\Pi\pi$*/Nπ* Internal Conversion in Organic Chromophores via K-edge Resonant Absorption. *Nature Communications* **8,** 29 (2017).

[13] Wilson, C. T. R. On an Expansion Apparatus for Making Visible the Tracks of Ionising Particles in Gases and Some Results Obtained by Its Use. *Proceedings of the Royal Society of London. Series A, Containing Papers of a Mathematical and Physical Character* **87,** 277–292 (1912).

[14] Jahnke, T. *et al.* Inner-Shell-Ionization-Induced Femtosecond Structural Dynamics of Water Molecules Imaged at an X-Ray Free-Electron Laser. *Physical Review X* **11,** 041044 (2021).

[15] Garman, E. F. & Weik, M. Radiation Damage to Biological Samples: Still a Pertinent Issue. *Journal of Synchrotron Radiation* **28,** 1278–1283 (2021).

[16] Erk, B. *et al.* Ultrafast Charge Rearrangement and Nuclear Dynamics upon Inner-Shell Multiple Ionization of Small Polyatomic Molecules. *Physical Review Letters* **110,** 053003 (2013).

[17] Nass, K. Radiation Damage in Protein Crystallography at X-ray Free-Electron Lasers. *Acta Crystallographica Section D Structural Biology* **75,** 211–218 (2019).

[18] Henke, B., Gullikson, E. & Davis, J. X-Ray Interactions: Photoabsorption, Scattering, Transmission, and Reflection at E = 50-30,000 eV, Z = 1-92. *Atomic Data and Nuclear Data Tables* **54,** 181–342 (1993).

[19] Gu, L. *et al.* Detection of an Unidentified Soft X-ray Emission Feature in NGC 5548. *Astronomy & Astrophysics* **665,** A93 (2022).

[20] Ezoe, Y., Ohashi, T. & Mitsuda, K. High-Resolution X-ray Spectroscopy of Astrophysical Plasmas with X-ray Microcalorimeters. *Reviews of Modern Plasma Physics* **5,** 4 (2021).

[21] Rudek, B. *et al.* Relativistic and Resonant Effects in the Ionization of Heavy Atoms by Ultra-Intense Hard X-rays. *Nature Communications* **9,** 4200 (2018).

[22] Sorokin, A. *et al.* Photoelectric Effect at Ultrahigh Intensities. *Physical Review Letters* **99,** 213002 (2007).

[23] Young, L. *et al.* Femtosecond Electronic Response of Atoms to Ultra-Intense X-rays. *Nature* **466,** 56–61 (2010).

[24] Doumy, G. *et al.* Nonlinear Atomic Response to Intense Ultrashort X Rays. *Physical Review Letters* **106,** 083002 (2011).

[25] Rudek, B. *et al.* Ultra-Efficient Ionization of Heavy Atoms by Intense X-ray Free-Electron Laser Pulses. *Nature Photonics* **6,** 858–865 (2012).

[26] Brown, G. S., Chen, M. H., Crasemann, B. & Ice, G. E. Observation of the Auger Resonant Raman Effect. *Physical Review Letters* **45,** 1937–1940 (1980).

[27] in. *Soft X-Rays and Extreme Ultraviolet Radiation: Principles and Applications* (ed Attwood, D.) 1–23 (Cambridge University Press, Cambridge, 1999).

[28] Veigele, W. J. Photon Cross Sections from 0.1 keV to 1 MeV for Elements Z = 1 to Z = 94. *Atomic Data and Nuclear Data Tables* **5,** 51–111 (1973).

[29] Carlson, T. A. *Photoelectron and Auger Spectroscopy* (Springer US, Boston, MA, 1975).

[30] Saito, N. & Suzuki, I. H. Multiple Photoionization in Ne, Ar, Kr and Xe from 44 to 1300 eV. *International Journal of Mass Spectrometry and Ion Processes* **115,** 157–172 (1992).

[31] Yeh, J.-J. *Atomic Calculation of Photoionization Cross-sections and Asymmetry Parameters* (Gordon & Breach Science, Publishers, 1993).

[32] Martin, W. & Wiese, W. in *Springer Handbook of Atomic, Molecular, and Optical Physics* (ed Drake, G.) 175–198 (Springer, New York, NY, 2006).

[33] Atkins, P. W. *Molecular Quantum Mechanics. 1* Reprint (Clarendon Press, Oxford, 1977).

[34] Kochur, A. G. & Popov, V. A. The Relative Role of Shake-up and Shake-off Processes in Additional Monopole Excitation of L and M Electrons Due to Inner Atomic Shell Ionization. *Optics and Spectroscopy* **100,** 645–651 (2006).

[35] Krause, M. O. Atomic Radiative and Radiationless Yields for K and L Shells. *Journal of Physical and Chemical Reference Data* **8,** 307–327 (1979).

[36] Chattarji, D. *The Theory of Auger Transitions* (Academic Press, London New York, 1976).

[37] Santra, R. & Young, L. in *Synchrotron Light Sources and Free-Electron Lasers* (eds Jaeschke, E. J., Khan, S., Schneider, J. R. & Hastings, J. B.) 1233–1260 (Springer International Publishing, Cham, 2016).

[38] Coster, D. & L. Kronig, R. D. New Type of Auger Effect and Its Influence on the X-Ray Spectrum. *Physica* **2,** 13–24 (1935).

[39] Svensson, S. Soft X-Ray Photoionization of Atoms and Molecules. *Journal of Physics B: Atomic, Molecular and Optical Physics* **38,** S821 (2005).

[40] *Photoemission in Solids I: General Principles* (eds Cardona, M. & Ley, L.) (Springer-Verlag, Berlin, 1978).

[41] Saito, N. & Suzuki, I. H. Yields of Multicharged Xe Ions in the M-shell Transition Region. *Journal of Physics B: Atomic, Molecular and Optical Physics* **25,** 1785 (1992).

[42] Bransden, B. H. & Joachain, C. J. *Physics of Atoms and Molecules* 1st ed. (Longman, London, 1983).

[43] Kramida, A. & Ralchenko, Y. *NIST Atomic Spectra Database, NIST Standard Reference Database 78* 1999.

[44] Lambropoulos, P. & Nikolopoulos, G. M. Multiple Ionization under Strong XUV to X-ray Radiation. *The European Physical Journal Special Topics* **222,** 2067–2084 (2013).

[45] Lambropoulos, P. & Tang, X. Multiple Excitation and Ionization of Atoms by Strong Lasers. *JOSA B* **4,** 821–832 (1987).

[46] Guichard, R. Distinction of Direct and Sequential Multiple Ionization of Neon by Intense Soft XUV Femtosecond Pulses. *The European Physical Journal D* **68,** 320 (2014).

[47] Orfanos, I. *et al.* Non-Linear Processes in the Extreme Ultraviolet. *Journal of Physics: Photonics* **2,** 042003 (2020).

[48] Rohringer, N. & Santra, R. X-Ray Nonlinear Optical Processes Using a Self-Amplified Spontaneous Emission Free-Electron Laser. *Physical Review A* **76,** 033416 (2007).

[49] Sytcheva, A., Pabst, S., Son, S.-K. & Santra, R. Enhanced Nonlinear Response of Ne^{8+} to Intense Ultrafast x Rays. *Physical Review A* **85,** 023414 (2012).

[50] Rudek, B. *et al.* Resonance-Enhanced Multiple Ionization of Krypton at an x-Ray Free-Electron Laser. *Physical Review A* **87,** 023413 (2013).

[51] Kruit, P. & Read, F. H. Magnetic Field Paralleliser for 2π Electron-Spectrometer and Electron-Image Magnifier. *Journal of Physics E: Scientific Instruments* **16,** 313 (1983).

[52] Cooper, J. & Zare, R. N. Angular Distribution of Photoelectrons. *The Journal of Chemical Physics* **48,** 942–943 (1968).

[53] Son, S.-K., Young, L. & Santra, R. Impact of Hollow-Atom Formation on Coherent x-Ray Scattering at High Intensity. *Physical Review A* **83,** 033402 (2011).

[54] Jurek, Z., Son, S.-K., Ziaja, B. & Santra, R. XMDYN and XATOM: Versatile Simulation Tools for Quantitative Modeling of X-ray Free-Electron Laser Induced Dynamics of Matter. *Journal of Applied Crystallography* **49,** 1048–1056 (2016).

[55] Santra, R., Kryzhevoi, N. V. & Cederbaum, L. S. X-Ray Two-Photon Photoelectron Spectroscopy: A Theoretical Study of Inner-Shell Spectra of the Organic Para-Aminophenol Molecule. *Physical Review Letters* **103,** 013002 (2009).

[56] Toyota, K., Son, S.-K. & Santra, R. Interplay between Relativistic Energy Corrections and Resonant Excitations in X-Ray Multiphoton Ionization Dynamics of Xe Atoms. *Physical Review A* **95,** 043412 (2017).

[57] Rörig, A. *et al.* Multiple-Core-Hole Resonance Spectroscopy with Ultraintense X-ray Pulses. *Nature Communications* **14,** 5738 (2023).

[58] Fukuzawa, H. *et al.* Deep Inner-Shell Multiphoton Ionization by Intense X-Ray Free-Electron Laser Pulses. *Physical Review Letters* **110,** 173005 (2013).

[59] Fritzsche, S. A Fresh Computational Approach to Atomic Structures, Processes and Cascades. *Computer Physics Communications* **240,** 1–14 (2019).

[60] Gu, M. F. The Flexible Atomic Code. *Canadian Journal of Physics* **86,** 675–689 (2008).

[61] Margaritondo, G. & Rebernik Ribic, P. A Simplified Description of X-ray Free-Electron Lasers. *Journal of Synchrotron Radiation* **18,** 101–108 (2011).

[62] He, A., Yang, L. & Yu, L. in *Synchrotron Light Sources and Free-Electron Lasers* (eds Jaeschke, E. J., Khan, S., Schneider, J. R. & Hastings, J. B.) 149–190 (Springer International Publishing, Cham, 2020).

[63] Huang, Z. & Kim, K.-J. Review of X-Ray Free-Electron Laser Theory. *Physical Review Special Topics - Accelerators and Beams* **10,** 034801 (2007).

[64] *XFEL, the European X-ray Free-Electron Laser: Technical Design Report* tech. rep. (DESY XFEL Project Group [u.a.], Hamburg, 2006).

[65] Tschentscher, T. *et al.* Photon Beam Transport and Scientific Instruments at the European XFEL. *Applied Sciences* **7,** 592 (2017).

[66] Dwersteg, B., Flöttmann, K., Sekutowicz, J. & Stolzenburg, C. RF Gun Design for the TESLA VUV Free Electron Laser. *Nuclear Instruments and Methods in Physics Research Section A: Accelerators, Spectrometers, Detectors and Associated Equipment. Free Electron Lasers 1996* **393,** 93–95 (1997).

[67] Krasilnikov, M. *et al.* Experimentally Minimized Beam Emittance from an *L*-Band Photoinjector. *Physical Review Special Topics - Accelerators and Beams* **15,** 100701 (2012).

[68] Brinker, F. *Commissioning of the European XFEL Injector* in *Proc. of International Particle Accelerator Conference (IPAC'16), Busan, Korea, May 8-13, 2016* Busan, Korea. doi:10.18429/JACoW-IPAC2016-TUOCA03 (JACoW, Geneva, Switzerland, 2016), 1044–1047.

[69] Brinkmann, R. *et al. TESLA XFEL: First Stage of the X-ray Laser Laboratory. Technical Design Report. Pt. 7: Supplement* tech. rep. (DESY, Hamburg, 2002).

[70] Sargsyan, A. A., Sahakyan, V. V. & Decking, W. Parallel Operation of SASE1 and SASE3 Undulator Sections of European XFEL. *Journal of Physics: Conference Series* **874,** 012021 (2017).

[71] Liu, S. *et al.* Parallel Operation of SASE1 and SASE3 at the European XFEL. *Proceedings of the 39th Free Electron Laser Conference* **FEL2019,** 4 pages, 1.353 MB (2019).

[72] Casalbuoni, S. *et al.* Superconducting Undulator Activities at the European X-ray Free-Electron Laser Facility. *Frontiers in Physics* **11** (2023).

[73] Baumann, T. M. *et al.* Harmonic Radiation Contribution and X-ray Transmission at the Small Quantum Systems Instrument of European XFEL. *Journal of Synchrotron Radiation* **30,** 662–670 (2023).

[74] Pellegrini, C., Marinelli, A. & Reiche, S. The physics of x-ray free-electron lasers. *Reviews of Modern Physics* **88,** 015006 (2016).

[75] Kuster, M. *et al.* The 1-Megapixel pnCCD Detector for the Small Quantum Systems Instrument at the European XFEL: System and Operation Aspects. *Journal of Synchrotron Radiation* **28,** 576–587 (2021).

[76] Li, X. *et al.* Coulomb Explosion Imaging of Small Polyatomic Molecules with Ultrashort X-Ray Pulses. *Physical Review Research* **4,** 013029 (2022).

[77] De Fanis, A. *et al.* High-Resolution Electron Time-of-Flight Spectrometers for Angle-Resolved Measurements at the SQS Instrument at the European XFEL. *Journal of Synchrotron Radiation* **29,** 755 (2022).

[78] Agåker, M. *et al.* A 1D Imaging Soft X-ray Spectrometer for the Small Quantum Systems Instrument at the European XFEL. *Journal of Synchrotron Radiation* **31,** 1264–1275 (2024).

[79] Mazza, T. *et al.* The Beam Transport System for the Small Quantum Systems Instrument at the European XFEL: Optical Layout and First Commissioning Results. *Journal of Synchrotron Radiation* **30,** 457–467 (2023).

[80] Meyer, M. *Conceptual Design Report: Scientific Instrument SQS* tech. rep. (European XFEL, 2011).

[81] Mazza, T., Zhang, H. & Meyer, M. *Technical Design Report: Scientific Instrument SQS* tech. rep. (European XFEL, 2012).

[82] Grychtol, P. *et al.* Timing and X-ray Pulse Characterization at the Small Quantum Systems Instrument of the European X-ray Free Electron Laser. *Optics Express* **29,** 37429–37442 (2021).

[83] Rivas, D. E. *et al.* High-Temporal-Resolution X-ray Spectroscopy with Free-Electron and Optical Lasers. *Optica* **9,** 429–430 (2022).

[84] Serkez, S. *et al.* Opportunities for Two-Color Experiments in the Soft X-ray Regime at the European XFEL. *Applied Sciences* **10,** 2728 (2020).

[85] Tiedtke, K. *et al.* Gas Detectors for X-Ray Lasers. *Journal of Applied Physics* **103,** 094511 (2008).

[86] Dommach, M. *et al.* The Photon Beamline Vacuum System of the European XFEL. *Journal of Synchrotron Radiation* **28,** 1229–1236 (2021).

[87] *Performance of the SASE3 Monochromator Equipped with a Provisional Short Grating. Variable Line Spacing Grating Specifications* (ed Gerasimova, N.) (European X-Ray Free-Electron Laser Facility GmbH, Schenefeld, 2018).

[88] Brown, K. L. & Tautfest, G. W. Faraday-Cup Monitors for High-Energy Electron Beams. *Review of Scientific Instruments* **27,** 696–702 (1956).

[89] Maltezopoulos, T. *et al.* Operation of X-ray Gas Monitors at the European XFEL. *Journal of Synchrotron Radiation* **26,** 1045–1051 (2019).

[90] Yang, B., Wu, J., Raubenheimer, T. O. & Feng, Y. Fluid Dynamics Analysis of a Gas Attenuator for X-ray FELs under High-Repetition-Rate Operation. *Journal of Synchrotron Radiation* **24,** 547–559 (2017).

[91] Pollock, C. *et al.* Fast Plasma Investigation for Magnetospheric Multiscale. *Space Science Reviews* **199,** 331–406 (2016).

[92] Hauf, S. *et al.* The Karabo Distributed Control System. *Journal of Synchrotron Radiation* **26,** 1448–1461 (2019).

[93] de Waele, A. T. A. M. Basics of Joule–Thomson Liquefaction and JT Cooling. *Journal of Low Temperature Physics* **186,** 385–403 (2017).

[94] Wiley, W. C. & McLaren, I. H. Time-of-Flight Mass Spectrometer with Improved Resolution. *Review of Scientific Instruments* **26,** 1150–1157 (1955).

[95] Valkiers, S., Aregbe, Y., Taylor, P. D. P. & De Bièvre, P. A Primary Xenon Isotopic Gas Standard with SI Traceable Values for Isotopic Composition and Molar Mass. *International Journal of Mass Spectrometry and Ion Processes* **173,** 55–63 (1998).

[96] Murthy, Z. V. P. in *Encyclopedia of Membranes* (eds Drioli, E. & Giorno, L.) 1–3 (Springer Berlin Heidelberg, Berlin, Heidelberg, 2015).

[97] Mazza, T. *private communication* 2024.

[98] Fraser, G. W. The Ion Detection Efficiency of Microchannel Plates (MCPs). *International Journal of Mass Spectrometry. Detectors and the Measurement of Mass Spectra* **215,** 13–30 (2002).

[99] De Fanis, A. *SIMION simulations* 2020.

[100] Sigaud, L., de Jesus, V. L. B., Ferreira, N. & Montenegro, E. C. A Novel Double-Focusing Time-of-Flight Mass Spectrometer for Absolute Recoil Ion Cross Sections Measurements. *Review of Scientific Instruments* **87,** 083112 (2016).

[101] Takahashi, N., Hosokawa, S., Saito, M. & Haruyama, Y. Measurement of Absolute Detection Efficiencies of a Microchannel Plate Using the Charge Transfer Reaction. *Physica Scripta* **T144,** 014057 (2011).

[102] Lindhard, J. & Scharff, M. Energy Dissipation by Ions in the Kev Region. *Physical Review* **124,** 128–130 (1961).

[103] Baragiola, R., Alonso, E., Ferron, J. & Oliva-Florio, A. Ion-Induced Electron Emission from Clean Metals. *Surface Science* **90,** 240–255 (1979).

[104] Hagstrum, H. D. Theory of Auger Ejection of Electrons from Metals by Ions. *Physical Review* **96,** 336–365 (1954).

[105] Cano, G. L. Secondary Electron Emission from Au, Mo, and CuBe by High-charge-number Laser-produced Metal Ions. *Journal of Applied Physics* **44,** 5293–5300 (1973).

[106] Hasselkamp, D. *et al. Particle Induced Electron Emission II* (Springer Berlin / Heidelberg, Berlin, Heidelberg, 1992).

[107] Töglhofer, K., Aumayr, F. & Winter, H. P. Ion-Induced Electron Emission from Metal Surfaces — Insights from the Emission Statistics. *Surface Science* **281,** 143–152 (1993).

[108] Parilis, E. S. & Kishinevskii, L. M. The Theory of Ion-Induced Emssion. *Sov Phys-Solid State* **3,** 885 (1960).

[109] Meier, R. & Eberhardt, P. Velocity and Ion Species Dependence of the Gain of Microchannel Plates. *International Journal of Mass Spectrometry and Ion Processes* **123,** 19–27 (1993).

[110] Rajopadhye, N. R., Bhoraskar, S. V. & Chakravorty, D. Electron Emissive Properties of Pb and Bi Containing Glasses. *Journal of Non-Crystalline Solids* **105,** 179–184 (1988).

[111] Mroz, W., Fry, D., Prokopuik, A., Stockli, M. & Walch, B. *Calibration of the Galileo Micro Channel Plate with the Xe^{7+} to Xe^{43+} Ions in the Energy Range from 2 keV/1 up to 154 keV/q* in *12th International Conference on High-Power Particle Beams. BEAMS'98. Proceedings (Cat. No.98EX103)* **1** (1998), 487–490 vol.1.

[112] Mróz, W., Fry, D., Stöckli, M. P. & Winecki, S. Micro Channel Plate Gains for Ta^{10+}–Ta^{44+} Ions, Measured in the Energy Range from 3.7 keV/q up to 150.7 keV/q. *Nuclear Instruments and Methods in Physics Research Section A: Accelerators, Spectrometers, Detectors and Associated Equipment* **437,** 335–345 (1999).

[113] Gilmore, I. S. & Seah, M. P. Ion Detection Efficiency in SIMS:: Dependencies on Energy, Mass and Composition for Microchannel Plates Used in Mass Spectrometry. *International Journal of Mass Spectrometry* **202,** 217–229 (2000).

[114] Gershman, D. J. *et al.* The Parameterization of Microchannel-Plate-Based Detection Systems. *Journal of Geophysical Research: Space Physics* **121,** 10, 005–10, 018 (2016).

[115] Yagi, S. *et al.* Relative Counting Efficiencies of Ion Charge-States by Microchannel Plate. *Nuclear Instruments and Methods in Physics Research Section B: Beam Interactions with Materials and Atoms* **183,** 476–486 (2001).

[116] Oberheide, J., Wilhelms, P. & Zimmer, M. New Results on the Absolute Ion Detection Efficiencies of a Microchannel Plate. *Measurement Science and Technology* **8,** 351 (1997).

[117] Liénard, E. *et al.* Performance of a Micro-Channel Plates Position Sensitive Detector. *Nuclear Instruments and Methods in Physics Research Section A: Accelerators, Spectrometers, Detectors and Associated Equipment* **551,** 375–386 (2005).

[118] Emsley, J. *The Elements* (Oxford : Clarendon Press ; New York : Oxford University Press, 1998).

[119] Posthumus, J. H. The Dynamics of Small Molecules in Intense Laser Fields. *Reports on Progress in Physics* **67,** 623–665 (2004).

[120] Toyota, K. *et al.* Xcalib : A Focal Spot Calibrator for Intense X-ray Free-Electron Laser Pulses Based on the Charge State Distributions of Light Atoms. *Journal of Synchrotron Radiation* **26,** 1017–1030 (2019).

[121] Pulkkinen, H., Aksela, S., Sairanen, O.-P., Hiltunen, A. & Aksela, H. Correlation Effects in the $L_{2,3}$ - MM Auger Transitions of Ar. *Journal of Physics B: Atomic, Molecular and Optical Physics* **29,** 3033 (1996).

[122] Keitel, B. *et al.* Hartmann Wavefront Sensors and Their Application at FLASH. *Journal of Synchrotron Radiation* **23,** 43–49 (2016).

[123] Breckwoldt, N. *et al.* Machine-Learning Calibration of Intense x-Ray Free-Electron-Laser Pulses Using Bayesian Optimization. *Physical Review Research* **5,** 023114 (2023).

[124] Son, S.-K., Boll, R. & Santra, R. Breakdown of Frustrated Absorption in X-Ray Sequential Multiphoton Ionization. *Physical Review Research* **2,** 023053 (2020).

[125] Sorokin, A. A., Wellhöfer, M., Bobashev, S. V., Tiedtke, K. & Richter, M. X-Ray-Laser Interaction with Matter and the Role of Multiphoton Ionization: Free-electron-laser Studies on Neon and Helium. *Physical Review A* **75,** 051402 (2007).

[126] Hoener, M. *et al.* Ultraintense X-Ray Induced Ionization, Dissociation, and Frustrated Absorption in Molecular Nitrogen. *Physical Review Letters* **104,** 253002 (2010).

[127] Son, S.-K. & Santra, R. Monte Carlo Calculation of Ion, Electron, and Photon Spectra of Xenon Atoms in x-Ray Free-Electron Laser Pulses. *Physical Review A* **85,** 063415 (2012).

[128] Suzuki, I. H. & Saito, N. Absolute Photoabsorption Cross-Sections of Ne and Xe in the Sub-keV X-ray Region. *Journal of Electron Spectroscopy and Related Phenomena* **129,** 71–79 (2003).

[129] Samson, J. A. R. & Stolte, W. C. Precision Measurements of the Total Photoionization Cross-Sections of He, Ne, Ar, Kr, and Xe. *Journal of Electron Spectroscopy and Related Phenomena. Determination of Cross-Sections and Momentum Profiles of Atoms, Molecules and Condensed Matter* **123,** 265–276 (2002).

[130] Kanter, E. P. *et al.* Unveiling and Driving Hidden Resonances with High-Fluence, High-Intensity X-Ray Pulses. *Physical Review Letters* **107,** 233001 (2011).

[131] LaForge, A. C. *et al.* Resonance-Enhanced Multiphoton Ionization in the X-Ray Regime. *Physical Review Letters* **127,** 213202 (2021).

[132] Funke, L. *et al. Capturing Nonlinear Electron Dynamics with Fully Characterised Attosecond X-ray Pulses* 2024.

[133] Saldin, E., Schneidmiller, E. & Yurkov, M. Statistical Properties of the Radiation from VUV FEL at DESY Operating at 30nm Wavelength in the Femtosecond Regime. *Nuclear Instruments and Methods in Physics Research Section A: Accelerators, Spectrometers, Detectors and Associated Equipment* **562,** 472–486 (2006).

[134] Khubbutdinov, R. *et al.* High Spatial Coherence and Short Pulse Duration Revealed by the Hanbury Brown and Twiss Interferometry at the European XFEL. *Structural Dynamics* **8,** 044305 (2021).

[135] Lutman, A. A. *et al.* Femtosecond X-Ray Free Electron Laser Pulse Duration Measurement from Spectral Correlation Function. *Physical Review Special Topics - Accelerators and Beams* **15,** 030705 (2012).

[136] Hartmann, N. *et al.* Attosecond time–energy structure of X-ray free-electron laser pulses. *Nature Photonics* **12,** 215–220 (2018).

[137] Budewig, L., Son, S.-K. & Santra, R. Theoretical Investigation of Orbital Alignment of X-Ray-Ionized Atoms in Exotic Electronic Configurations. *Physical Review A* **105,** 033111 (2022).

[138] Cederbaum, L. S., Tarantelli, F., Sgamellotti, A. & Schirmer, J. On Double Vacancies in the Core. *The Journal of Chemical Physics* **85,** 6513–6523 (1986).

[139] Cederbaum, L. S. Many-Body Theory of Multiple Core Holes. *Physical Review A* **35,** 622–631 (1987).

[140] Kabachnik, N., Fritzsche, S., Grum-Grzhimailo, A., Meyer, M. & Ueda, K. Coherence and Correlations in Photoinduced Auger and Fluorescence Cascades in Atoms. *Physics Reports* **451,** 155–233 (2007).

[141] Püttner, R. *et al.* Argon 1s-2 Auger Hypersatellites. *Journal of Physics B: Atomic, Molecular and Optical Physics* **54,** 024001 (2020).

[142] Carniato, S. Theoretical Simulation of K-2V Inner-Shell Processes in Ne and Ar. *Journal of Electron Spectroscopy and Related Phenomena* **239,** 146931 (2020).

[143] Frasinski, L. J. *et al.* Dynamics of Hollow Atom Formation in Intense X-Ray Pulses Probed by Partial Covariance Mapping. *Physical Review Letters* **111,** 073002 (2013).

[144] Goldsztejn, G. *et al.* Double-Core-Hole States in Neon: Lifetime, Post-Collision Interaction, and Spectral Assignment. *Physical Review Letters* **117,** 133001 (2016).

[145] Goldsztejn, G. *et al.* Experimental and Theoretical Study of the Double-Core-Hole Hypersatellite Auger Spectrum of Ne. *Physical Review A* **96,** 012513 (2017).

[146] Mazza, T. *et al.* Mapping Resonance Structures in Transient Core-Ionized Atoms. *Physical Review X* **10,** 041056 (2020).

[147] Kiselev, M. D., Gryzlova, E. V., Burkov, S. M., Zatsarinny, O. & Grum-Grzhimailo, A. N. Mechanisms of 1s Double-Core-Hole Excitation and Decay in Neon. *Atoms* **9,** 114 (2021).

[148] Fushitani, M. *et al.* Multielectron-Ion Coincidence Spectroscopy of Xe in Extreme Ultraviolet Laser Fields: Nonlinear Multiple Ionization via Double Core-Hole States. *Physical Review Letters* **124,** 193201 (2020).

[149] Linusson, P., Fritzsche, S., Eland, J. H. D., Mucke, M. & Feifel, R. Single-Photon Multiple Ionization Forming Double Vacancies in the $2p$ Subshell of Argon. *Physical Review A* **87,** 043409 (2013).

[150] Žitnik, M. *et al.* Two-to-One Auger Decay of a Double L Vacancy in Argon. *Physical Review A* **93,** 021401 (2016).

[151] Mailhiot, M. *et al.* Multielectron Coincidence Spectroscopy of the Ar^{2+} $(2p^{-2})$ Double-Core-Hole Decay. *Physical Review A* **107,** 063108 (2023).

[152] Fuggle, J. C. & Mårtensson, N. Core-level binding energies in metals. *Journal of Electron Spectroscopy and Related Phenomena* **21,** 275–281 (1980).

[153] Jurvansuu, M., Kivimäki, A. & Aksela, S. Inherent lifetime widths of Ar $2p^{-1}$, Kr $3d^{-1}$, Xe $3d^{-1}$, and Xe $4d^{-1}$ states. *Phys. Rev. A* **64,** 012502 (1 2001).

[154] Mehlhorn, W. & Stalherm, D. Die Auger-Spektren der L_2- und L_3-Schale von Argon. *Zeitschrift für Physik A Hadrons and nuclei* **217,** 294–303 (1968).

[155] Werme, L. O., Bergmark, T. & Siegbahn, K. The $L_{2,3}$ MM Auger Spectrum of Argon. *Physica Scripta* **8,** 149–153 (1973).

[156] Ismail, I. *et al.* Alternative Pathway to Double-Core-Hole States. *Physical Review Letters* **131,** 253201 (2023).

[157] Cumbee, R. S. *et al.* Charge Exchange X-Ray Emission Due to Highly Charged Ion Collisions with H, He, and H_2 : Line Ratios for Heliospheric and Interstellar Applications. *The Astrophysical Journal* **852,** 7 (2017).

[158] Hell, N. *et al.* Highly Charged Ions in a New Era of High Resolution X-ray Astrophysics. *X-Ray Spectrometry* **49,** 218–233 (2020).

[159] Richter, M., Bobashev, S. V., Sorokin, A. A. & Tiedtke, K. Multiphoton Ionization of Atoms with Soft X-Ray Pulses. *Journal of Physics B: Atomic, Molecular and Optical Physics* **43,** 194005 (2010).

[160] Makris, M. G., Lambropoulos, P. & Mihelič, A. Theory of Multiphoton Multielectron Ionization of Xenon under Strong 93-eV Radiation. *Physical Review Letters* **102,** 033002 (2009).

[161] Martins, M., Meyer, M., Richter, M., Sorokin, A. A. & Tiedtke, K. in *Atomic Processes in Basic and Applied Physics* (eds Shevelko, V. & Tawara, H.) 307–330 (Springer, Berlin, Heidelberg, 2012).

[162] Palutke, S. *et al. Climbing the N-shell Resonance Ladder of Xenon* 2022.

[163] Santra, R. & Greene, C. H. Multiphoton Ionization of Xenon in the Vuv Regime. *Physical Review A* **70,** 053401 (2004).

[164] Richter, M. *et al.* Extreme Ultraviolet Laser Excites Atomic Giant Resonance. *Physical Review Letters* **102,** 163002 (2009).

[165] Richardson, V. *et al.* Two-Photon Inner-Shell Ionization in the Extreme Ultraviolet. *Physical Review Letters* **105,** 013001 (2010).

[166] Richter, M. Atomic Plasma Excitations in the Field of a Soft X-Ray Laser. *Journal of Physics B: Atomic, Molecular and Optical Physics* **44,** 075601 (2011).

[167] Lambropoulos, P., Papamihail, K. G. & Decleva, P. Theory of Multiple Ionization of Xenon under Strong XUV Radiation and the Role of the Giant Resonance. *Journal of Physics B: Atomic, Molecular and Optical Physics* **44,** 175402 (2011).

[168] Gerken, N. *et al.* Time-Dependent Multiphoton Ionization of Xenon in the Soft-X-Ray Regime. *Physical Review Letters* **112,** 213002 (2014).

[169] Hadjipittas, A., Banks, H. I. B., Bergues, B. & Emmanouilidou, A. Sequential Single-Photon and Direct Two-Photon Absorption Processes for Xe Interacting with Attosecond XUV Pulses. *Physical Review A* **102,** 043108 (2020).

[170] Schippers, S. *et al.* Absolute Cross Sections for Photoionization of Xe^{q+} Ions $(1 \leq q \leq 5)$ at the 3d Ionization Threshold. *Journal of Physics B: Atomic, Molecular and Optical Physics* **47,** 115602 (2014).

Acknowledgement

First of all, I'm grateful to my supervisor, Michael Meyer, for your guidance and for the many things you taught me. I especially appreciate our engaging and, at times, lengthy discussions and your constant support during our weekly meetings throughout the thesis writing process. I'm grateful for the opportunity to pursue my doctorate at SQS.

To my co-supervisor, Robin Santra, thank you for your insightful comments that helped refine our xenon paper and for contributing your interdisciplinary expertise to this work.

I extend my sincere appreciation to Rebecca Boll for both the scientific and personal support you provided during my doctoral studies. Thank you for guiding me, particularly through the xenon experiments and for imparting so much knowledge along the way.

Tommaso Mazza, thank you for your detailed and constructive feedback on my presentations, posters, and thesis. I learned a great deal from our discussions, and I greatly benefited from your expertise in data analysis and experimental techniques.

Sang-Kil Son, I'm grateful for your constant availability to address my questions. Your support, along with the XATOM calculations and scientific interpretations, were essential to this work.

I'd also like to thank Alberto De Fanis for assisting me in understanding the electron spectrometer and for providing the necessary characterisations.

Philipp Schmidt, thank you for your support with data analysis and for the valuable Python skills I gained.

I'd like to acknowledge Michael Martins for serving on my committee and for the insightful beamtimes we shared at FLASH.

Stephan Fritzsche, thank you for our discussions regarding the argon data and the JAC calculations.

I'm also grateful to Stefan Schippers for facilitating my connection to Michael Meyer and SQS and for travelling from Gießen to Hamburg to be part of the committee.

Eidesstattliche Versicherung

Hiermit versichere ich an Eides statt, die vorliegende Dissertationsschrift selbst verfasst und keine anderen als die angegebenen Hilfsmittel und Quellen benutzt zu haben.

Sofern im Zuge der Erstellung der vorliegenden Dissertationsschrift generative Künstliche Intelligenz (gKI) basierte elektronische Hilfsmittel verwendet wurden, versichere ich, dass meine eigene Leistung im Vordergrund stand und dass eine vollständige Dokumentation aller verwendeten Hilfsmittel gemäß der Guten wissenschaftlichen Praxis vorliegt. Ich trage die Verantwortung für eventuell durch die gKI generierte fehlerhafte oder verzerrte Inhalte, fehlerhafte Referenzen, Verstöße gegen das Datenschutz- und Urheberrecht oder Plagiate.

_____   _____

Datum   Unterschrift